A Neural Network Framework to Uncover Cosmology from Radio Observations of the Early Universe

Ph.D Thesis

by

Anshuman Tripathi
Roll No. 2001121001

Under the Supervision
of
Prof. Abhirup Datta & Dr. Suman Majumdar

Department of Astronomy, Astrophysics and Space Engineering,
Indian Institute of Technology Indore,
Khandwa Road, Simrol, Indore - 453552, India

A Neural Network Framework to Uncover Cosmology from Radio Observations of the Early Universe

A THESIS

Submitted in partial fulfillment of the requirements for the award of the degree

of

DOCTOR OF PHILOSOPHY

by

Anshuman Tripathi

Department of Astronomy, Astrophysics and Space Engineering,
Indian Institute of Technology Indore,
Khandwa Road, Simrol, Indore - 453552, India

INDIAN INSTITUTE OF TECHNOLOGY INDORE

I hereby certify that the work which is being presented in the thesis entitled **A Neural Network Framework to Uncover Cosmology from Radio Observations of the Early Universe** in partial fulfillment of the requirements for the award of the degree of **DOCTOR OF PHILOSOPHY** and submitted in the **DEPARTMENT OF ASTRONOMY, ASTROPHYSICS, AND SPACE ENGINEERING**, Indian Institute of Technology Indore, is an authentic record of my own work carried out during the time period from **August, 2020** to **July, 2025** under the supervision of **Prof Abhirup Datta, Professor, and Dr. Suman Majumdar, Associate Professor, Indian Institute of Technology Indore.**

The matter presented in this thesis has not been submitted by me for the award of any other degree of this or any other institute.

Anshuman
16/12/2025
Signature of the student with date
(ANSHUMAN TRIPATHI)

This is to certify that the above statement made by the candidate is correct to the best of my/our knowledge.

Signature of Thesis Supervisors with date

17/12/25
(PROF. ABHIRUP DATTA)

Suman Majumdar 16/12/2025
(Dr. SUMAN MAJUMDAR)

ANSHUMAN TRIPATHI has successfully given his/her Ph.D. Oral Examination held on **December 5, 2025**.

Signature of Thesis Supervisors with date

17/12/25
(PROF. ABHIRUP DATTA)

Suman Majumdar 16/12/2025
(Dr. SUMAN MAJUMDAR)

Dedicated

to

My Family

"Research is what I'm doing when I don't know what I'm doing."
— Wernher von Braun

Acknowledgements

A Ph.D. is not just a degree; it is a journey of perseverance, growth, and the collective strength of those who walk alongside you. Behind every completed thesis lies a community of mentors, peers, and loved ones who believed in the journey, even when the path was unclear.

I would like to express my heartfelt gratitude to my Ph.D. supervisors, Prof. Abhirup Datta and Dr. Suman Majumdar, for their unwavering support, insightful guidance, and constant encouragement throughout this journey. Their expertise and mentorship have been instrumental in shaping my research and fostering my development as an independent researcher. I am sincerely thankful for the valuable discussions, constructive feedback, and the numerous opportunities they provided over the years. I would also like to thank the members of my Ph.D. Student Progress Committee (PSPC), Dr. Siddharth Malu, Prof. Subhendu Rakshit, and Dr. Manoneeta Chakraborty, for their thoughtful suggestions and consistent evaluation of my research progress, which greatly enriched my work. A special note of appreciation goes to my senior, Dr. Madhurima Choudhury, whose guidance during the early stages of my Ph.D. was immensely helpful. Her thesis served as a foundational resource and significantly influenced the direction of my own research.

Over the past five years, I have encountered many challenges. I am deeply grateful to my lab mates and seniors, Arnab, Majidul, Ramij, Sumanjit, Deepthi, Aishrila, Sarvesh, and Akriti, for creating a collaborative, supportive, and friendly environment. They never made me feel like a junior and were always ready to help, especially during my initial days. I have learned a great deal from them, both technically and personally. I would also like to thank my fellow batchmates, Harsha, Swarna, Hemapriya, Sushmita, Gourab, Argyadeep, Chandrani, Souman, Chandrashekhar, and Prateek, for their camaraderie and for making this journey feel like one shared with family. Your friendship has been invaluable. My sincere thanks go to other members of the DAASE department, Sriya, Parul, Unnati, Sayan, and Kamran, for fostering a collegial and welcoming atmosphere, and for always being approachable and supportive. To my juniors, Samit, Bhuvnesh, Rashmi, Nasmi, Prajnal, Keshav, Pritam, Eeshan, and Riya, thank you for the positive energy you brought to the lab. It has been a pleasure working alongside you and learning through our interactions. I would like to sincerely thank Abhijeet for his constant support with official documentation and logistics, both within the laboratory and beyond. He has also been a close friend, a sports enthusiast, and a much-enjoyed badminton partner. I am equally grateful to my oldest friends, Maya and Shraddha, for being by my side throughout the years and for continually encouraging me to become a better version of myself. I have learned a great deal from them, both personally and professionally.

I also wish to acknowledge the faculty and staff members of the department for cre-

ating a supportive academic environment and for always being open to discussions, suggestions, and help whenever needed. I am grateful to IIT Indore for providing the institute fellowship, as well as national and international travel grants and access to essential computational facilities. Special thanks to the academic office staff for their consistent support, which made all academic processes smooth and hassle-free. I would also like to thank ANRF SERB ITS for supporting my participation in the SKA conference in Beijing. My appreciation also goes to my junior Ph.D. colleagues, who were always willing to help and engage in thoughtful discussions and feedback.

I am particularly thankful to the M.Sc. and intern students, Gursharnjit, Akash, Eeshan, Aniket, and Bisheswar, for showing faith in me, giving me the opportunity to co-supervise their work, and bringing fresh perspectives and challenges that enriched our collaborative experience.

Finally, and most importantly, I extend my deepest thanks to my parents and entire family, especially my grandparents, for their unconditional love, faith, and encouragement throughout every phase of this journey. Their constant support has been the foundation that made this achievement possible.

Abstract

The cosmic dawn (CD) and the epoch of reionization (EoR) mark critical periods in the early Universe, characterized by the formation of the first luminous sources and the subsequent heating and ionization of the intergalactic medium (IGM). Despite their significance, the physical conditions of the IGM during these epochs remain poorly constrained due to observational challenges. The redshifted HI 21-cm signal offers a unique window into these periods, and several experiments, such as EDGES, SARAS, MWA, and the forthcoming SKA, are actively targeting the detection of this signal. However, the signal is obscured by dominant foregrounds, instrumental systematics, and ionospheric distortions, further complicating by direction-dependent and frequency-dependent variations in antenna beam patterns, particularly at low radio frequencies.

This thesis focuses on addressing these challenges by developing a robust, end-to-end data analysis pipeline that leverages machine learning (ML) and Bayesian statistical techniques. Traditional inference methods become computationally expensive as the dimensionality of the problem grows, necessitating scalable and adaptive approaches. We systematically investigate each major observational obstacle, such as foreground contamination and ionospheric effects, and train artificial neural networks (ANNs) to recover global 21-cm signal parameters from all-sky averaged spectra. The trained ANN achieves a signal parameter recovery accuracy of 96–97%, exhibiting resilience to static and slowly time-varying ionospheric conditions. Additionally, the performance of the ANN framework remains consistent across different sets of signal simulation datasets using different input parameter distributions.

To enhance the generalization and stability of the ANN models, we evaluate various sampling strategies for efficiently exploring the high-dimensional signal parameter space. Specifically, we compare random sampling, Latin hypercube (stratified) sampling, and Hammersley sequence (quasi-Monte Carlo) sampling methods. Our analysis reveals that, while a sufficient sample size is essential for effective ANN training, the Hammersley sequence method yields superior robustness relative to the other techniques. The sample size requirements scale with both the number of free parameters and the intrinsic complexity of the data.

Furthermore, we extend our methodology by developing a hybrid inference framework that integrates ANN-based inference with Bayesian methods to address the influence of systematics expected in future experiments like SKA-Low. This framework is used to quantify the impact of gain calibration errors and sky model positional uncertainties on the extracted power spectrum and astrophysical parameters. Through detailed simulations, we quantify the sensitivity of the inferred parameters to these systematics and determine threshold levels beyond which signal recovery becomes significantly compromised. Our results indicate that to achieve optimal signal extraction, gain calibration errors must be constrained below 0.001%. Furthermore, sky model positional inaccuracies exceeding 0.048 arcseconds result in residual foreground contamination that effectively obscure the cosmological 21-cm signal.

In summary, this thesis demonstrates the efficacy of machine learning techniques in overcoming critical observational limitations in both global signal and interferometric 21-cm experiments. By facilitating accurate and efficient inference in the presence of complex systematics, this study paves the way for robust signal extraction in the upcoming era of precision cosmology.

List of Publications

A. Published:

1. **Anshuman Tripathi**, Abhirup Datta, Madhurima Choudhury, Suman Majumdar, "Extracting the Global 21cm signal from Cosmic Dawn and Epoch of Reionization in the presence of Foreground and Ionosphere"; Published in MNRAS; [arXiv.2401.01935]; DOI: https://doi.org/10.1093/mnras/stae078
2. **Anshuman Tripathi**, Gursharanjit Kaur, Abhirup Datta, Suman Majumdar; "Comparing sampling techniques to chart parameter space of 21 cm Global signal with Artificial Neural Networks"; Published in JCAP; [arXiv:2406.15832]; DOI: https://iopscience.iop.org/article/10.1088/1475-7516/2024/10/041
3. **Anshuman Tripathi**, Abhirup Datta, Aishrila Mazumder, Suman Majumdar; "*Impact of Calibration and Position Errors on Astrophysical Parameters of the HI Signal*"; Published in JCAP; [arxiv.org/abs/2502.20962]; DOI: https://iopscience.iop.org/article/10.1088/1475-7516/2025/10/035

C. Other Publications:

1. Aishrila Mazumder, Abhirup Datta, Mayuri Sathyanarayana Rao, Arnab Chakraborty, Saurabh Singh, **Anshuman Tripathi**, Madhurima Choudhury; "*Synthetic observations with the Square Kilometre Array: Development towards an end-to-end pipeline*"; Published in JoAA; [arXiv:2211.04302]; DOI: 10.1007/s12036-022-09906-8
2. Harsha Avinash Tanti, Tiasha Biswas, Abhirup Datta and **Anshuman Tripathi**; "*Development of a Machine Learning based Radio source localisation algorithm for Tri-axial antenna configuration*"; Published in JoAA; [arXiv.2409.20209];
3. **Anshuman Tripathi**, Abhirup Datta, Gursharanjit Kaur; "*Comparing the Performance of Various ML Regression Models for Parameter Extraction in Global 21cm Signal Experiments*", Accepted for publication in JOAA; [arXiv.2512.09361];
4. G. Akash, **Anshuman Tripathi**, Abhirup Datta "*Extracting the redshifted Global HI 21cm Signal using Quantum Neural Networks*"; Submitted in SN Computer Science, Springer Nature (Under review);

5. A. Bonaldi, et al. including **Anshuman Tripathi**; "*Square Kilometre Array Science Data Challenge 3a: foreground removal for an EoR experiment*", Submitted in MNRAS; [arXiv.2503.11740]

N.B: Entries A1-A3 are parts of my thesis.

Table of Contents

List of Figures

List of Tables

List of abbreviations

BB	Big Bang
HI	Neutral Hydrogen
CMB	Cosmic Microwave Background
CD	Cosmic Dawn
EoR	Epoch of Reionization
IGM	Intergalactic Medium
TEC	Total Electron Content
DLAs	Damped Lyman α Systems
DGSE	Diffuse Galactic Synchrotron Radiation
RFI	Radio Frequency Interference
GMRT	Giant Metrewave Radio Telescope
LOFAR	Low Frequency Array
MWA	Murchison Widefield Array
HERA	Hydrogen Epoch of Reionization Array
SKA	Square Kilometre Array
PS	Power Spectrum
ML	Machine Learning
ANN	Artificial Neural Network
PCA	Principal Component Analysis
SVD	Singular Value Decomposition
GMCA	Generalized Morphological Component Analysis
ICA	Independent Component Analysis
GPR	Gaussian Process Regression
MCMC	Markov Chain Monte Carlo
LHS	Latin Hypercube Sampling
HSS	Hammersley Sequence Sampling

Chapter 1

Introduction

1.1 Timeline of the Cosmos

The Universe is a fascinating and complex place, with many mysteries still to be explored. According to the standard model of cosmology, the Universe began about 13.8 billion years ago with the Big Bang. It started as an extremely hot and dense point, with incredibly high temperature and energy. After the Big Bang, the Universe began expanding and cooling, passing through different stages of development. In the first few moments, basic particles like protons, neutrons, electrons, neutrinos, and photons were formed. About 100 seconds after the Big Bang, when the temperature dropped to around 10^{10} K, conditions became right for nuclear fusion to occur. Protons and neutrons started combining to form light elements such as deuterium and helium, in a process known as Big Bang Nucleosynthesis. At this stage, the Universe was not yet transparent. Photons, or particles of light, were constantly interacting with free electrons and other charged particles, getting scattered in all directions. Because of this, light couldn't travel freely, and the Universe appeared like a hot, glowing fog.

With the ongoing expansion of the Universe, its temperature gradually decreased. Eventually, the rate at which photons scattered off free electrons became slower than the rate of expansion. Around 380,000 years after the Big Bang (at a redshift of $z \sim 1100$, and a temperature of about ≈ 3000 K), The Universe cooled sufficiently to allow electrons and protons to recombine into neutral hydrogen atoms. This process is known as *recombination.* Once neutral atoms formed, photons could travel freely through space without being constantly scattered. This moment is called the *decoupling* of matter and radiation. The leftover light from this time has been traveling through the Universe ever since and is now observed as the Cosmic Microwave Background Radiation (CMBR) [14,15]. Today, this radiation has cooled to a temperature of about 2.7 K [14]. Studying the CMBR, especially its small temperature variations (anisotropies), has greatly improved our understanding of the Universe. These observations form the foundation of the standard cosmological model, known as ΛCDM. Over time, various space missions have measured the CMBR, with the *Planck* satellite providing the most accurate and detailed results so far [16].

Following recombination, the Universe became almost entirely neutral, composed primarily of baryonic matter, about 75% in the form of neutral hydrogen (HI) and 25% as neutral helium by mass. The absence of significant radiation sources caused the Cosmic Dark Ages, which persisted until about $z \sim 30$ and was primarily characterized by the lack of typical radiation emitters. During this time, baryons fell into gravitational wells formed by collapsing dark matter halos, leading to the creation of the first structures: the first stars and galaxies. This event marked the

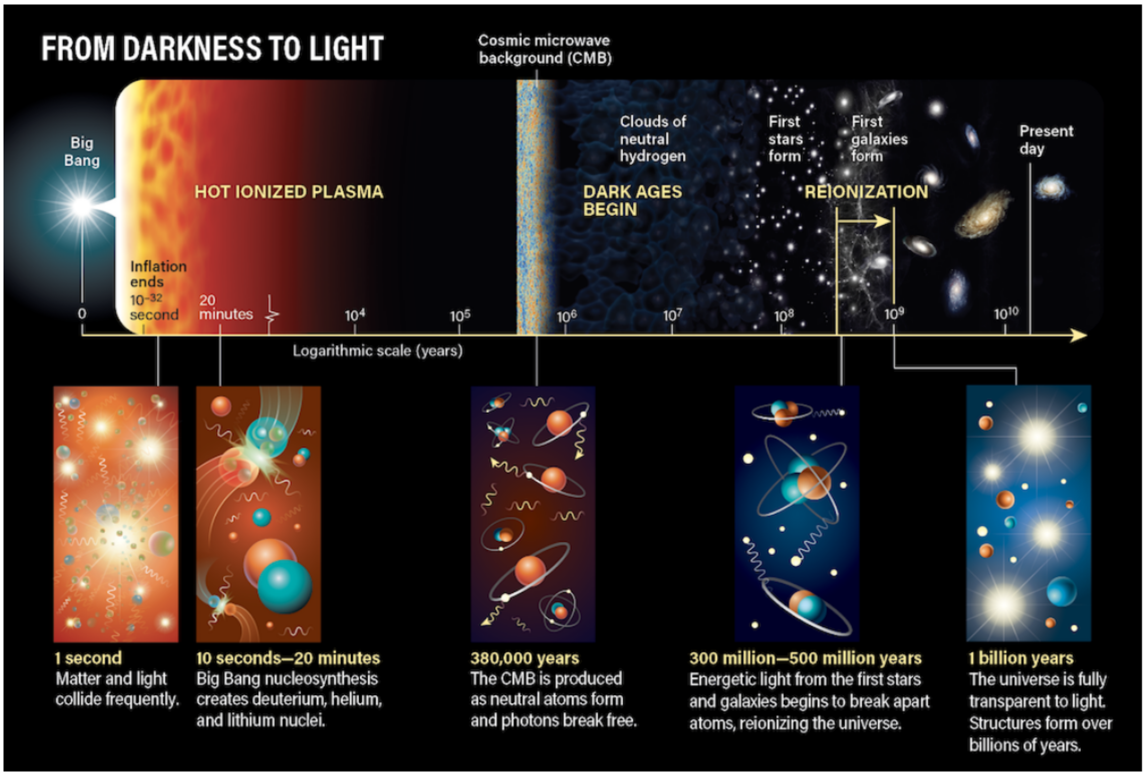

Figure 1.1: A chronological overview of the Universe's major evolutionary epochs. Image credit: Astronomy, Roen Kelly.

transition from the Dark Ages to the Cosmic Dawn (CD), typically associated with the redshift range $30 < z < 12$. The earliest luminous sources in the Universe, including the first generations of stars, galaxies, quasars, and potentially dark matter decay or annihilation processes, emitted significant amounts of ultraviolet (UV) and X-ray radiation. UV photons with energies exceeding > 13.6 eV were sufficiently energetic to ionize the intergalactic medium (IGM), which was initially composed primarily of neutral hydrogen (HI) [17]. This transition marked the start of the Epoch of Reionization (EoR).

These key phases of cosmic evolution are illustrated in Figure 1.1. Observational constraints on reionization come from several sources, including absorption features in high-redshift quasar spectra [18–20] and measurements of the Thomson scattering optical depth from the CMB [21]. Together, these suggest that the EoR occurred over the redshift range $12 \gtrsim z \gtrsim 6$.

However, observations of the Lyman-α forest in quasar (QSO) absorption spectra reveal that by redshift z $\sim$ 5, the diffuse hydrogen gas in the intergalactic medium was fully ionized. This implies a cosmic transition: from a neutral to a fully ionized Universe, during the epoch known as reionization, which occurred between redshifts 1100 and 5. The precise timing and duration of this epoch remain active areas of research in modern cosmology.

Hydrogen, although comprising only a small fraction of the total matter content of the Universe, is the most abundant baryonic element and plays a foundational role in cosmic structure formation. Its evolution is intricately linked to a broad range of astrophysical processes, including the birth of the first stars, the assembly of galaxies, and the emergence of large-scale structure. Understanding the distribution and thermodynamic state of hydrogen provides critical insight into the physical conditions that enabled the formation of complex structures and, ultimately, intelligent life.

In the present-day Universe, however, the majority of hydrogen resides in the intergalactic medium (IGM), where it has remained predominantly ionized since the end of reionization. Neutral atomic hydrogen (HI) and molecular hydrogen (H_2) are found primarily within galaxies, but they constitute only a small fraction of the total baryonic hydrogen content; even within galactic environments, a significant portion of the interstellar medium (ISM) is ionized. The neutral component (HI) can be probed via the 21-cm hyperfine transition line, which, when redshifted, provides a powerful observational window into different epochs of cosmic history. Measurements of this signal, either in absorption or emission, allow HI to serve as a tracer of the thermal and ionization state of the IGM and the underlying matter distribution.

The 21-cm line is especially promising for exploring the early Universe, including the CD and the EoR period that remain largely unconstrained observationally. As a result, 21-cm cosmology has emerged as a frontier in observational astrophysics, capable of addressing several fundamental questions:

Key Scientific Questions Addressed by 21-cm Cosmology:

- At what cosmic epoch did the first stars form, and what physical processes governed their formation?
- What were the intrinsic properties of these primordial stars, their masses, chemical compositions, lifespans, and spectral characteristics?
- How did dark matter and the formation of early black holes influence the assembly and evolution of the first galaxies?
- Through what mechanisms did the IGM transition from a cold, neutral state to a hot, ionized medium during the Epoch of Reionization?
- What were the relative contributions of ionizing sources, such as Population III stars, star-forming galaxies, and quasars, to reionization?
- How did the thermal and ionization history of the IGM evolve across cosmic time, particularly during the Cosmic Dawn?
- What role did radiative feedback mechanisms, including X-ray heating and Lyman-α coupling, play in shaping the global 21-cm signal and its fluctuations?
- To what extent can spatial fluctuations in the 21-cm brightness temperature constrain the nature of dark matter, the characteristics of early luminous sources, and the formation of large-scale structure?
- Can the 21-cm signal reveal signatures of exotic physics, such as dark matter, baryon interactions, or imprints of non-standard inflationary dynamics, in the early Universe?

1.2 Observational Indicators for Investigating the CD and EoR

The CD and EoR exploration relies on direct and indirect observational probes, supported by comparisons with theoretical models to understand their evolution. Direct probes target the redshifted

21-cm signal to trace neutral hydrogen, while indirect probes, such as quasar spectra, CMB features, Ly-α emission, galaxy UV luminosities, and metal absorption lines, provide complementary constraints on the timing and nature of reionization[22].

1.2.1 CMB Anisotropies

CMB temperature and polarization anisotropies can provide an additional observational constraint on the reionization process and its evolution [23–25]. Although the majority of CMB photons last scattered at a redshift of approximately z $\sim$ 1100, a small fraction of less than 10 % underwent secondary scattering during the EoR. The detection and analysis of this signal offer valuable constraints on the mean redshift and the temporal boundaries of the EoR. In particular, measurements of the Thomson scattering optical depth from the CMB serve as a robust, model-independent probe of the reionization history. The scattering of CMB photons during the EoR introduces two primary observational effects: first, the free electrons generated during reionization suppress the primary CMB anisotropies and produce additional polarization anisotropies at large angular scales; second, secondary anisotropies are imprinted onto the CMB radiation field through subsequent scattering processes [23, 24]. The secondary anisotropies have a minimal effect on the temperature fluctuations of the CMB. However, they significantly influence the polarization angular power spectrum, producing a distinctive 'reionization bump' at large angular scales (corresponding to scales larger than the horizon size during the EoR), as illustrated in Figure 1.2.

1.2.2 Sunyaev-Zel'dovich (kSZ) Effect

The CD and EoR can also be investigated through the kinetic Sunyaev-Zel'dovich (kSZ) effect. In this phenomenon, CMB photons scatter off free electrons that possess a bulk motion relative to the comoving frame. Unlike the thermal Sunyaev-Zel'dovich effect, the kSZ effect does not induce any spectral distortion in the CMB; instead, it leads to either an increase or decrease in the observed temperature. The kSZ effect generates secondary anisotropies in the CMB on small angular scales, arising from the patchy distribution of ionized regions during reionization. These anisotropies serve as a valuable probe of the reionization process. Using the latest Planck 2018 data [26], the Thomson scattering optical depth was measured as $\tau = 0.054 \pm 0.007$, corresponding to a midpoint of reionization around z $\sim$7.7. This implies that reionization was largely complete by z $\sim$6 and likely did not begin earlier than z $\sim$9.

1.2.3 Quasars as Probes of Reionization

Quasars, among the brightest objects in the Universe, are active galactic nuclei powered by supermassive black holes (10^6–10^9 $M_\odot$) surrounded by accretion disks. Their smooth spectra can be used to probe the intergalactic medium (IGM) along the line of sight. The Gunn-Peterson (GP) effect refers to the resonant absorption of Lyman-α photons by neutral hydrogen, producing a characteristic trough in quasar spectra beyond the reionization epoch [27]. This absorption feature directly constrains the evolution of the IGM's ionization state.

The first Gunn-Peterson (GP) trough was observed in a quasar at redshift $z = 6.28$ [28]. Analysis of Sloan Digital Sky Survey (SDSS) quasars in the redshift range $5.74 < z < 6.42$ suggested that the Universe was nearly fully ionized by $z \sim 6$ [18]. More recent observations of quasar J1007+2115 at $z = 7.5$ indicated that reionization was still ongoing at $z \gtrsim 7$, with a volume-averaged neutral hydrogen fraction of $\langle x_{\rm HI} \rangle = 0.39^{+0.22}_{-0.13}$ and evidence for patchy reionization from a weak Lyα

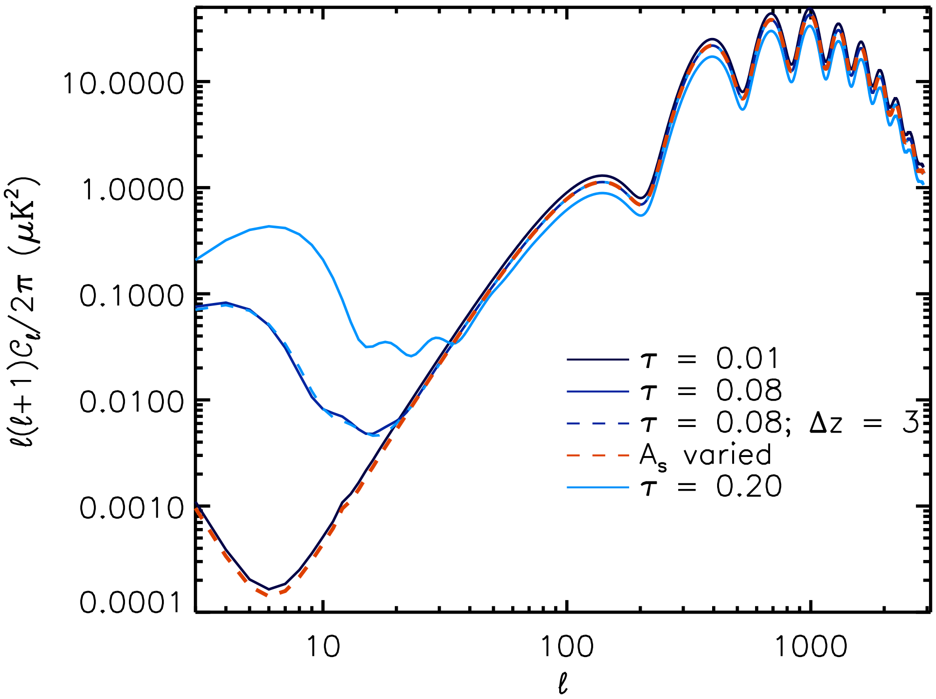

Figure 1.2: The E-mode (curl-free) polarization power spectrum of the CMB displays excess power at low multipoles (corresponding to large angular scales), primarily caused by Thomson scattering between free electrons and the CMB quadrupole. The strength of this signal varies with the optical depth, as illustrated by the different solid curves. A key advantage of the polarization spectrum is that its amplitude and optical depth are not degenerate, meaning changes in one cannot mimic the effects of the other. For instance, an increase in the overall amplitude (indicated by the red dotted line) does not reproduce the distinctive bump observed at low multipoles. This figure is adapted from [1].

damping wing [29]. A Bayesian damping wing analysis of four $z \gtrsim 7$ quasars—DES J0252−0503 ($z = 7.00$), J1007+2115 ($z = 7.51$), ULAS J1120+0641 ($z = 7.09$), and ULAS J1342+0928 ($z = 7.54$) which incorporates uncertainties in the intrinsic quasar emission and IGM morphology, found $\langle x_{\rm HI} \rangle \approx 0.25$–$0.34$ individually and a combined constraint of 0.49 ± 0.11 at $z = 7.29$, supporting the picture of ongoing and patchy reionization [2].

1.2.4 Additional indirect probes

Apart from these, additional observational probes include dark pixel analysis [30], the Lyα emitter fraction [31], the luminosity function of Lyα emitters [32–35], and observations of Lyman-break galaxies at $z = 7$ [36] and $z = 7.6$ [37]. These results are summarized in Figure 1.3.

However, indirect observations fail to resolve several fundamental aspects of the CD and EoR, including the formation and evolution of early luminous sources (e.g., stars, galaxies, quasars), their impact on the intergalactic medium (IGM), the topology of ionized regions, and the precise starting and ending points of this era in cosmic time.

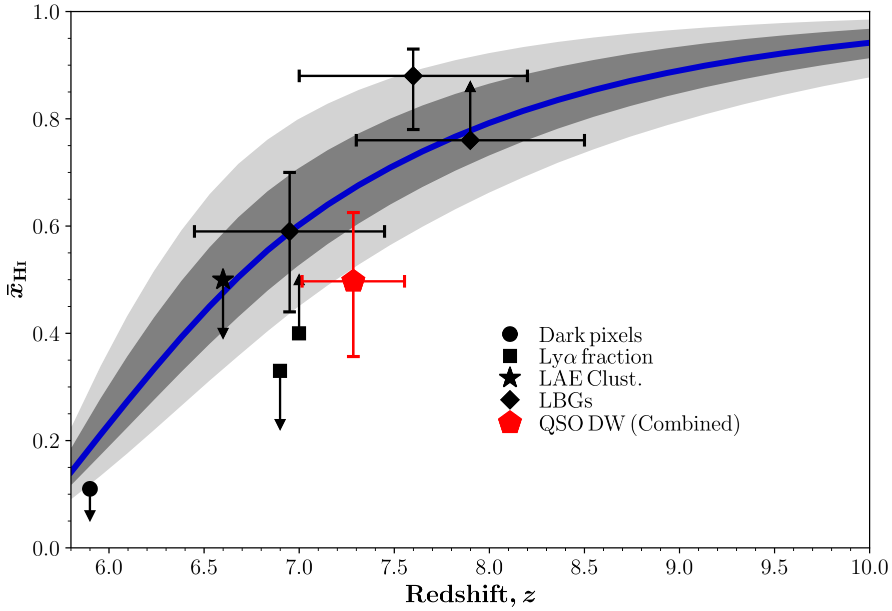

Figure 1.3: Constraints on the neutral hydrogen fraction in the intergalactic medium ($x_{\rm HI}$) across different redshifts. The data points represent estimates derived from dark pixel analysis, Ly emitter fractions, LAE clustering, and observations of Lyman-break galaxies (LBGs). The red pentagon indicates the combined damping wing constraint from four $z \gtrsim 7$ quasars [2]. The blue curve and shaded regions represent the median and $1\sigma/2\sigma$ bounds from reionization modeling [3]. This figure is adapted from [2]

1.2.5 Redshifted neutral hydrogen (HI) 21cm signal

The redshifted 21-cm signal serves as one of the key observational probes for investigating the CD and EoR. Atomic hydrogen (HI), which is the most abundant element in the Universe, emits 21-cm radiation due to the spin-flip transition of the electron-proton system in its ground state. Although this transition is forbidden with a spontaneous emission coefficient of $A_{10} = 2.85 \times 10^{-15}\,\mathrm{s}^{-1}$ (corresponding to an emission time of 11 million years for a 21-cm photon from HI) [38], the 21-cm signal remains abundant since approximately 75% of the baryons in the Universe consist of HI. The radiation initially emitted at a frequency of 1420 MHz gets redshifted to lower frequencies ($\nu_{\rm obs} = \frac{1420\,\mathrm{MHz}}{(1+z)}$) as it travels through the expanding Universe. Consequently, this signal encodes information about the IGM at the time of its emission. Several ongoing and upcoming independent efforts aim to detect the redshifted 21-cm signal, including single-dish experiments such as EDGES [39], SARAS [40], REACH [41], PRIZM [42], and LEDA [43]. In parallel, radio interferometric experiments like GMRT [44], LOFAR [45], MWA [46], HERA [47], and the SKA [48,49] are designed to trace the evolution of this signal over cosmic time. A detailed discussion will be presented in the upcoming Chapter 2.

From an observational perspective, the primary challenge lies in detecting an extremely faint signal, with a peak amplitude of only a few hundred millikelvin, which is overwhelmed by contributions from significantly stronger unwanted sources. These contaminants include astrophysical foregrounds, ionospheric disturbances, radio frequency interference, and instrumental systematics. The details for these individual challenge dicuss deatils in the Chapter 2. Significant efforts are ongoing to efficiently mitigate foreground contamination, correct for ionospheric distortions, and identify and remove instrumental systematics in both single-dish radiometer and interferometric experiments. Several independent analysis techniques have been developed, including polynomial fitting, Singular Value Decomposition (SVD), Principal Component Analysis (PCA), Generalized Morphological Component Analysis (GMCA), and machine learning-based methods. However, each of these approaches involves trade-offs between signal preservation, computational efficiency, and robustness against contaminants, highlighting the inherent challenges in reliably extracting the faint cosmological 21-cm signal. In this thesis, we introduce an alternative 21-cm signal extraction method based on the application of artificial neural networks, which will be discussed in detail in the following chapters of this thesis.

1.3 Objective of the thesis

This thesis is focused on developing computationally efficient and statistically robust pipelines for the recovery of the redshifted 21-cm signal, which serves as a critical probe of the early Universe, including the CD and the EoR. The primary objective is to construct an ML-based framework capable of recovering the global 21-cm signal in the presence of realistic observational effects, including bright astrophysical foregrounds, frequency-dependent ionospheric distortions, beam chromaticity, and instrumental thermal noise.

In addition to the global signal analysis, the methodology is extended to interferometric observations. To this end, we develop hybrid frameworks that couple neural network emulators with Bayesian inference schemes, enabling efficient and accurate recovery of the 21-cm power spectrum along with constraints on the underlying astrophysical parameters. These models are specifically designed to account for a range of instrumental systematics, including calibration errors and residual foreground contamination, and are tailored for application to data from current and forthcoming interferometric arrays such as the SKA, MWA, and HERA. This work contributes to advancing the data analysis capabilities within 21-cm cosmology and provides insights into the impact of systematic effects on signal reconstruction and parameter estimation.

1.4 Thesis Arrangement

This thesis is structured into seven chapters. Chapter 1 presents the background, motivation, and objectives of the study. Chapter 2 is divided into two parts: Part A offers an overview of the redshifted HI 21cm signal, emphasizing its scientific importance, current observational facilities, and approaches for setting upper limits on its detection. Part B addresses the observational challenges in detecting the HI 21cm signal and reviews various mitigation techniques. Chapter 3 describes the machine learning methodologies employed in this work, including data preparation and preprocessing steps critical for effective model training. The final chapter summarizes the key findings and outlines potential directions for future research. A brief summary of each chapter is provided below:

- **Chapter 4:**

  Tripathi A. et al. 2024, [50], *Monthly Notices of the Royal Astronomical Society, vol 528, 2, 1945–1964*

  In this chapter, we developed and presented an artificial neural network (ANN) based framework for extracting the global 21-cm signal along with its associated astrophysical and observational parameters. The ANN was trained on a composite sky spectrum comprising contributions from the HI signal, foreground emission, and ionospheric effects. Our ionospheric model incorporates the effects of refraction, absorption, and thermal emission, each dependent on the total electron content (TEC) and electron temperature (T_e).

The framework was designed to infer a total of 13 parameters: seven related to the global 21-cm signal, four describing the foregrounds, and two characterizing ionospheric conditions. Under scenarios with slowly varying ionospheric behavior, the trained ANN achieved a prediction accuracy between 96% and 97%. For model training, the ionospheric parameters were varied within a range of ±1 around their mean values. When tested against time-dependent ionospheric conditions, the ANN model accurately recovered the ionospheric parameters, closely matching the expected mean values, demonstrating its robustness and predictive reliability in realistic observational scenarios.

- **Chapter 5:**

  Tripathi A. et al. 2024, [51], *Journal of Cosmology and Astroparticle Physics, vol OCT 2024, 041*

  Due to the scarcity of observational data, our understanding of the Intergalactic Medium (IGM) during these epochs remains limited, resulting in a broad and largely unconstrained parameter space for the global 21cm signal. In the context of Simulation-Based Inference, exploring this entire parameter space effectively becomes essential. However, navigating a high-dimensional parameter space poses significant computational challenges. This work focuses on determining efficient sampling strategies suited to the large dimensionality and volume inherent in the 21cm signal parameter space. The sampling approach is used to generate training datasets for Artificial Neural Network (ANN) models to infer parameters from global signal experiments. We examine and compare three sampling methods: random sampling, Latin hypercube sampling (a stratified approach), and Hammersley sequence sampling (a quasi-Monte Carlo method). Our analysis shows that achieving robust and accurate ANN model performance requires a sufficiently large number of training samples, irrespective of the sampling technique. The necessary sample size is primarily governed by data complexity and the number of free parameters, with more free parameters demanding more realizations. Among the methods tested, ANN models trained with datasets generated using Hammersley sequence sampling exhibit superior robustness compared to those trained with Latin hypercube or random sampling techniques.

- **Chapter 6:**

  Tripathi A. et al. 2025, [52], *Journal of Cosmology and Astroparticle Physics, vol OCT 2025, 035*

  In this chapter, we have employed Artificial Neural Networks (ANNs) as emulators to model the observed 21-cm power spectrum, incorporating the effects of telescope layout. This work utilizes the 21cm End-to-End (E2E) pipeline, developed by our research group, to generate synthetic observations from simulated sky models that include both the redshifted 21-cm signal and astrophysical foregrounds. A hybrid framework was constructed by integrating ANNs with Bayesian inference methods to extract astrophysical parameters from the measured power spectrum directly. This approach eliminates the need for explicit corrections related to the interferometric array layout, directly inferring the astrophysical parameters for the upcoming interferometric observation.

  The study further investigates how gain calibration and sky model position errors impact the recovery of the redshifted 21-cm power spectrum. We also evaluated how these errors propagate to the inference of astrophysical parameters and established tolerances required for reliable signal recovery. Our results show that gain calibration errors must be nearly 0.001% to avoid significant signal distortion. Additionally, if sky position errors exceed 0.048 arcseconds, residual foreground contamination can dominate the observed spectrum, rendering the target cosmological signal indistinguishable.

Chapter 2

Probing Early Universe with Redshifted 21cm Signal

2.1 Cosmological HI 21cm Signal

Following the recombination epoch, the Universe became neutral and dark, entering a phase commonly referred to as the ”Dark Ages,” during which baryonic matter was predominantly composed of neutral hydrogen. Over time, the Universe underwent significant transitions, leading to the birth of the first stars approximately 0.1 billion years after the Big Bang, corresponding to redshifts between 30 and 15. This era is known as the ”Cosmic Dawn.” Gravitational instabilities primarily drove the formation of the earliest structures, although gas dynamics, cooling and heating processes, radiative interactions, and feedback mechanisms increasingly influenced the development of the first galaxies. These galaxies hosted the earliest stellar populations, initially dominated by metal-free Population III stars, followed by the emergence of metal-enriched Population II stars and black hole-driven sources.

The emergence of the first luminous sources produced ultraviolet (UV) radiation capable of ionizing the surrounding intergalactic medium (IGM), initiating a gradual transition from a neutral to an ionized state. This event marks the last major phase transition in the thermal and ionization history of the Universe, referred to as the Epoch of Reionization (EoR). The 21-cm line arises from the hyperfine transition between the hydrogen atom’s ground state’s singlet and triplet spin states. In its ground state, a neutral hydrogen (HI) atom consists of a proton and an electron, both possessing intrinsic spin. The magnetic interaction between their spins causes a slight energy splitting of the $1s$ level into two hyperfine states. The higher-energy state corresponds to parallel spin alignment, while the lower-energy state corresponds to anti-parallel spin alignment. The energy difference between these two levels is $\Delta E \approx 5.9\ \mu$eV, leading to the emission or absorption of a photon with a rest-frame wavelength of 21 cm (or frequency of 1420 MHz) during a spin-flip transition, as illustrated in Fig. 2.1.

Although the spontaneous emission from this transition is extremely rare, having a lifetime of approximately 11 million years, it remains a valuable cosmological probe. This is primarily because the 21-cm signal is sourced by the abundant neutral hydrogen, which constitutes about 75% of the Universe’s baryonic matter during the CD and EoR. The intensity of 21cm radiation is determined by the spin temperature

The brightness of the 21-cm radiation is governed by the spin temperature, T_s, which is defined

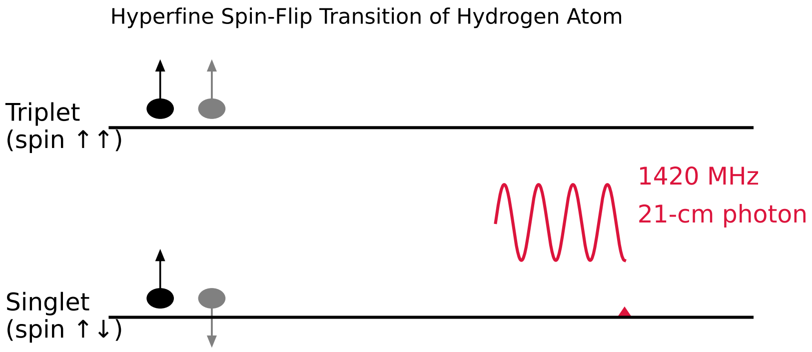

Figure 2.1: Illustration of the 21-cm spin-flip transition in neutral hydrogen, where the electron shifts from a parallel (high-energy) to antiparallel (low-energy) spin state, emitting a 1420 MHz photon.

by [53]:

$$\frac{n_1}{n_0} = 3\exp\left(-\frac{T_*}{T_s}\right), \tag{2.1}$$

Here, n_0 and n_1 represent the populations of the singlet and triplet hyperfine states of neutral hydrogen, respectively. The parameter $T^* = 0.0682\,\mathrm{K}$ corresponds to the temperature equivalent of the 21-cm transition energy, given by $h\nu_{21\mathrm{cm}} = 2k_B T^* = 5.87 \times 10^{-6}\,\mathrm{eV}$. The factor of 3 arises due to the degeneracy of the triplet state. The intensity of 21-cm emission from an H I cloud is governed by the spin temperature T_s, which sets the population ratio between the two hyperfine states.

The radiation intensity $I(\nu)$ can be described using the brightness temperature under the Rayleigh-Jeans approximation as:

$$I(\nu) = \frac{2\nu^2}{c^2} k_B T_b, \tag{2.2}$$

where ν represents the radiation frequency, c is the speed of light, and k_B denotes Boltzmann's constant.

As the Universe expands, the wavelength λ of radiation emitted at a cosmological redshift z stretches to $\lambda(1+z)$, causing the observed wavelength to be longer than the emitted one. The optical depth for 21-cm radiation from an HI cloud with a uniform spin temperature T_s, observed at a wavelength of $21(1+z)$ cm, is given by [54]:

$$\tau(z) = \frac{3c\lambda_{21}^2 h_p A_{10} n_{\mathrm{HI}}}{32\pi k_B T_s (1+z)\left(\frac{\partial v_r}{\partial r}\right)} \tag{2.3}$$

where h_p is Planck's constant, $A_{10} = 2.85 \times 10^{-15}\ \mathrm{s}^{-1}$ is the spontaneous emission coefficient associated with the hyperfine transition, and $\partial v_r/\partial r$ denotes the radial velocity gradient along the line of sight, with v_r representing the physical radial velocity and r the comoving distance.

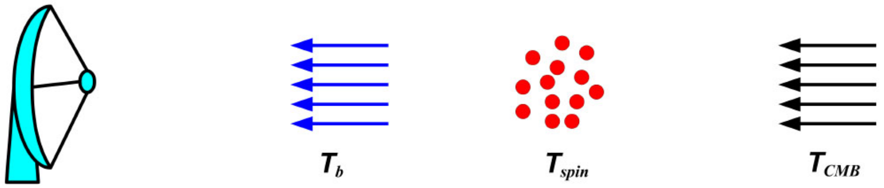

Figure 2.2: Schematic illustrating the radiative transfer setup: CMB background radiation passes through a hydrogen cloud at spin temperature T_S, resulting in an observed brightness temperature T_b. This figure is adapted from `https://ned.ipac.caltech.edu/level5/March14/Zaroubi/Zaroubi4.html`.

The term n_{HI} refers to the number density of neutral hydrogen atoms. In a fully neutral and homogeneous Universe, $n_{\mathrm{HI}} = \bar{n}_{\mathrm{H}}(z)$, and the velocity gradient reduces to $\partial v_r/\partial r = H(z)/(1+z)$, where $H(z)$ is the Hubble parameter.

Radio telescopes measure the contrast between the brightness temperature T_b of the 21-cm radiation emitted by neutral hydrogen (HI) in the intergalactic medium (IGM) and the cosmic microwave background (CMB) temperature T_{CMB} as shown in Fig. 2.2 This contrast, referred to as the differential brightness temperature or 21-cm fluctuation, is defined as [38, 54–56]:

$$\delta T_b = T_b - T_{\mathrm{CMB}}.$$

$$\begin{aligned} \delta T_b(\nu) &= \frac{T_s - T_{\mathrm{CMB}}}{1+z} e^{-\tau} \approx \frac{T_s - T_{\mathrm{CMB}}}{1+z} \tau \\ &\approx 26.8\,\mathrm{mK} \left(\frac{\Omega_b h}{0.0327} \right) \left(\frac{\Omega_m}{0.307} \right)^{-1/2} \left(\frac{1+z}{10} \right)^{1/2} \left(\frac{T_s - T_{\mathrm{CMB}}}{T_s} \right) \end{aligned} \tag{2.4}$$

where x_{HI} is the fraction of neutral hydrogen, and T_s is the spin temperature of the HI gas. Ω_b and Ω_M are the baryon and total matter density parameters, respectively, expressed relative to the critical density. The Hubble parameter at redshift z is given by $H(z)$, while $T_{\mathrm{CMB}}(z)$ denotes the CMB temperature at that epoch. The dimensionless Hubble parameter is h, defined in units of 100 km s^{-1} Mpc^{-1}, and $\partial_r v_r$ refers to the radial velocity gradient along the line of sight. In this equation 2.4, the optical depth $\tau \ll 1$. This also shows that the 21-cm signal can only be detected when the spin temperature (T_s) of the gas differs from the CMB temperature (T_{CMB}). This is expected, as $T_s = T_{\mathrm{CMB}}$ implies thermal equilibrium between the background and the gas, resulting in no absorption or emission above the background. Equation 2.4 also indicates that T_s determines whether the signal is observed in absorption or emission against the CMB.

2.2 Thermal history

The differential brightness temperature δT_b, observed either as an absorption or emission feature, as shown in Fig. 2.3, is primarily controlled by the relationship between the spin temperature T_S and the background CMB temperature T_{CMB}. Because T_S is also affected by the gas kinetic temperature T_K (as indicated in Eq. 2.5), understanding how these temperatures evolve with redshift is crucial for decoding the observed 21-cm signal. A key observational approach for studying the thermal history of the early intergalactic medium (IGM) involves tracking the global (sky-averaged)

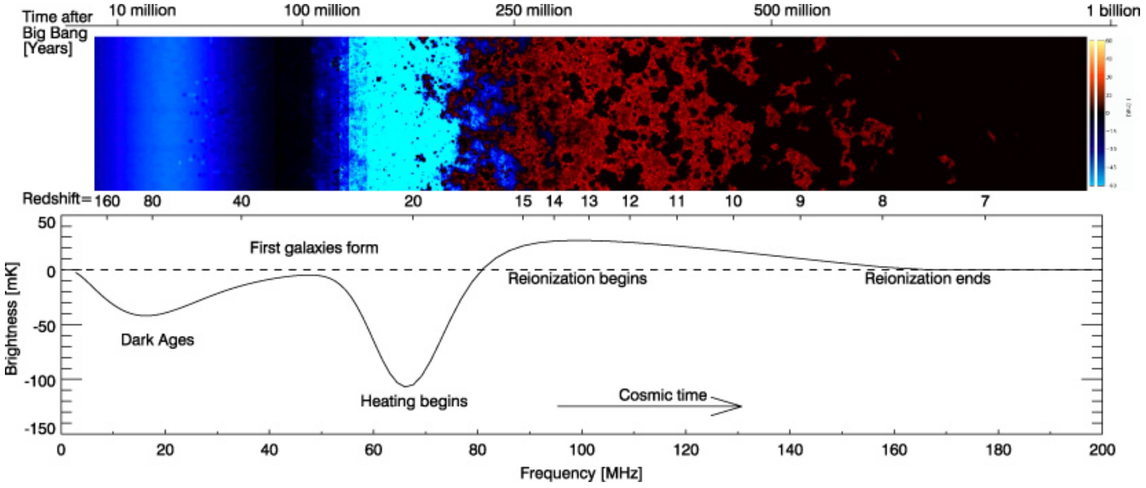

Figure 2.3: The figure illustrates the redshift evolution of the spin, CMB, and kinetic temperatures, highlighting how their interplay is governed by different cosmic mechanisms. This figure is adapted from [4]

21-cm signal across a broad frequency range. This method utilizes a single-element radiometer to observe the sky-averaged differential brightness temperature δT_b as a function of redshift (or its corresponding frequency). The global 21-cm signal manifests as either an absorption or emission feature depending on the evolution of the spin temperature T_S. The influence of T_S across cosmic time, from the early Universe at $z \sim 200$ to the completion of reionization around $z \sim 6$, is outlined below (for further discussion, see [4, 57, 58]).

The spin temperature T_S is determined by a weighted combination of the CMB temperature T_{CMB} and the kinetic temperature T_K, modulated by coupling coefficients x_k (collisional coupling) and x_α (Lyman-α coupling), and is given by:

$$T_S = \frac{T_{\mathrm{CMB}} + x_k T_K + x_\alpha T_K}{1 + x_k + x_\alpha} \tag{2.5}$$

where x_k and x_α represent the collisional and Lyman-α coupling coefficients, respectively. The term x_k arises from collisional excitation of the 21-cm hyperfine transition, while x_α originates from the Wouthuysen–Field effect, in which Lyman-α photons excite hydrogen atoms via electronic transitions. Both coupling coefficients depend on the respective rates of collisions and Lyman-α scattering within the neutral hydrogen gas.

As indicated by Eq. 2.4, the global 21-cm signal provides meaningful insight into the intergalactic medium only when the spin temperature differs from the CMB temperature. The evolution of the global signal reflects a complex interaction between cosmological and astrophysical processes, whose relative impacts vary across different epochs, shaping the observed brightness temperature accordingly. The following section provides a brief overview of this evolution. At redshifts $z \gtrsim 200$, residual free electrons efficiently couple the gas kinetic temperature T_K to the CMB temperature T_γ through **Compton scattering**, enabling energy exchange between photons and electrons. As a result, the temperatures remain tightly coupled, and the spin temperature T_s stays equal to T_γ during this epoch. Consequently, no observable 21-cm signal exists during this epoch. As the Universe expands and cools ($z \sim 30 - 200$), the ionization fraction and density decrease, reducing the coupling between T_k and T_γ. The gas cools adiabatically as $(1+z)^2$, faster than the CMB which cools as $(1+z)$, resulting in $T_k < T_\gamma$, as illustrated in Fig. 2.4. However, collisions are still

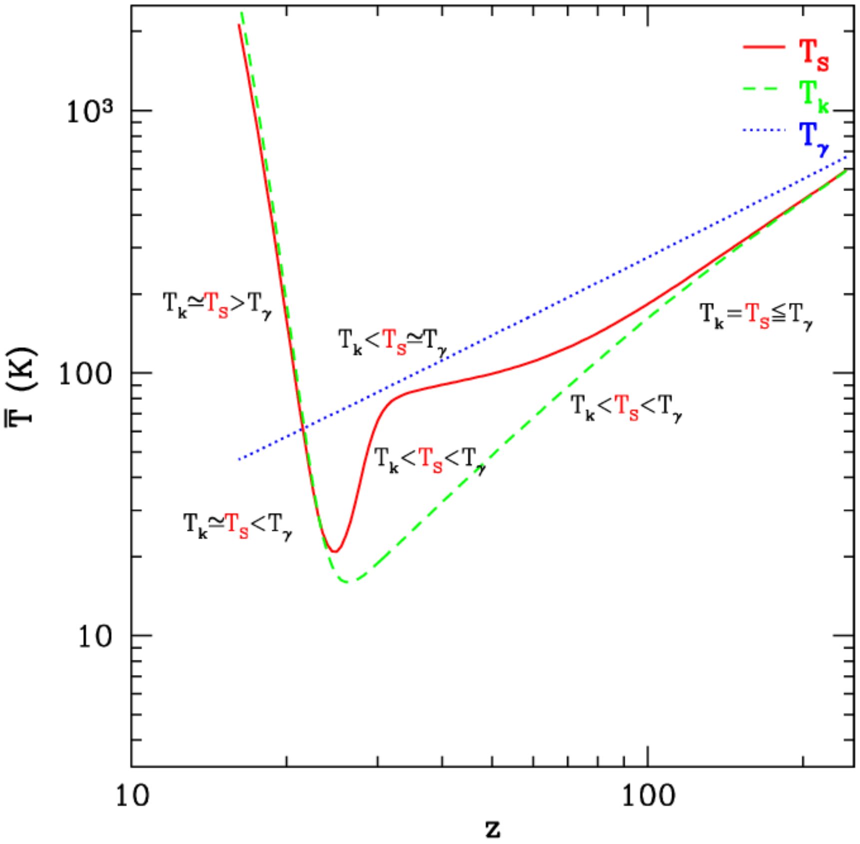

Figure 2.4: The figure illustrates the redshift evolution of the spin, CMB, and kinetic temperatures, highlighting how their interplay is governed by different cosmic mechanisms. This figure is adapted from [5].

efficient enough to couple T_s to T_k, allowing the 21-cm line to appear in absorption against the CMB.

In the subsequent redshift range ($z \sim 20 - 30$), the gas becomes too diffuse for collisions alone to maintain the coupling, and T_s starts approaching T_γ, weakening the 21-cm signal. This epoch, known as the *Cosmic Dawn*, signifies the formation of the first luminous sources. Lyman-α photons from these sources can re-establish the coupling between T_s and T_k through the Wouthuysen-Field effect, potentially leading to localized 21-cm absorption signals. X-rays and other high-energy radiation from these sources may heat the IGM above the CMB temperature, creating spatial variations in the signal including regions of absorption, emission, or no signal. Between redshifts $z \sim 6 - 20$, additional heating mechanisms such as Lyman-α scattering, X-ray heating from early galaxies and black holes, and weak shocks from structure formation raise the IGM temperature (T_k) above the CMB. As reionization progresses, ionized regions (HII bubbles) begin to dominate, and the 21-cm signal becomes increasingly complex, reflecting the morphology of these ionized zones. Post-reionization ($z \lesssim 6$), the IGM becomes almost fully ionized, and neutral hydrogen is too scarce to produce a detectable 21-cm signal.

2.3 21-cm Signal Detection: Methods and Observational Campaigns

Significant progress in astronomical instrumentation over recent decades has made it feasible to detect the faint H I 21-cm signal from the CD and EoR. This signal can be explored through two main approaches: the global (sky-averaged) signal and the power spectrum. Global signal experiments typically use single-dish instruments or total power radiometers, whereas interferometers are employed for power spectrum measurements.

2.3.1 Global 21-cm Signal: Detection Strategy

The global 21-cm signal, representing the sky-averaged differential brightness temperature of neutral hydrogen during the cosmic dawn and the epoch of reionization, offers a powerful probe of the early evolution of the thermal and ionization of the Universe. Unlike interferometric observations that target spatial fluctuations, global signal experiments measure the absolute radio spectrum in the ∼40–200 MHz range using single-element radiometers. Extracting the cosmological signal—typically tens to hundreds of mK, requires precise calibration, robust foreground subtraction, and careful modeling of instrumental systematics. Several global signal experiments, both operational and in development, aim to detect this faint signal across different redshift intervals, from the Dark Ages to the end of Reionization. This thesis focuses on the CD and the EoR. Notable efforts include EDGES [39], SARAS [40], REACH [41], LEDA [43], SCI-HI [59], and BIGHORNS [60]. However, terrestrial observations are hindered by radio frequency interference (RFI) and ionospheric effects, motivating proposals for lunar-based experiments.

A probable discovery of the global 21-cm signal with an unusually deep absorption trough was reported by the EDGES collaboration [61], challenging standard cosmological predictions and spurring a wave of theoretical and experimental scrutiny. Independent results from the SARAS experiment [62], however, rejected the EDGES profile with 95.3% confidence, reaffirming consistency with standard models. As of now, no other experiment has confirmed a detection, and the quest to uncover the true global 21-cm signal continues.

2.3.2 Power Spectrum Measurements of the 21-cm Signal

Global signal experiments target the detection of the sky-averaged 21-cm brightness temperature, whereas power spectrum analyses are designed to probe spatial variations in the signal across redshift. These fluctuations arise because of inhomogeneities in the distribution of neutral hydrogen, ionizing sources, and the underlying matter density field. The 21-cm power spectrum, typically expressed as a function of comoving wavenumber k or angular scale and redshift (or frequency), captures the statistical properties of these fluctuations and serves as a powerful tool for probing the physics of the CD and EoR. Interferometric arrays such as the Giant Meterwave Radio Telescope (GMRT [44]), Low Frequency Array (LOFAR) [63], Murchison Widefield Array (MWA) [46], Hydrogen Epoch of Reionization Array (HERA) [47], and the upcoming Square Kilometre Array (SKA) [64] are designed to measure the 21-cm power spectrum over a range of redshifts and scales. These instruments correlate signals from multiple antenna elements to achieve the sensitivity required to detect faint 21-cm fluctuations buried beneath the foreground that are several orders of magnitude brighter.

Power spectrum measurements offer key insights into the timing and topology of reionization, the properties of the first galaxies and black holes, and potentially even fundamental physics such as non-standard heating mechanisms or exotic dark matter scenarios. However, accurate foreground subtraction, calibration, and modeling of instrumental response remain major challenges for these experiments. The fundamental observable in 21-cm interferometric experiments is the power spectrum of brightness temperature fluctuations, $P_T(k,z)$. Under the assumption that these fluctuations constitute a statistically homogeneous and isotropic random field, the power spectrum is defined through the two-point correlation of the Fourier components of the brightness temperature field as:

$$\langle \Delta T_b(\mathbf{k}, z)\, \Delta T_b^*(\mathbf{k}', z)\rangle = (2\pi)^3 \delta^3(\mathbf{k} - \mathbf{k}')\, P_T(k, z), \tag{2.6}$$

where $\tilde{\delta T}_b(\mathbf{k}, z)$ is the Fourier transform of the brightness temperature fluctuation field, and δ_D is the Dirac delta function ensuring statistical independence between different modes. The H I power spectrum, $P_{\mathrm{HI}}(k,z)$, is related to the temperature fluctuation power spectrum $P_T(k,z)$ as described in [65].

$$P_T(k, z) = \overline{T}_b^2(z)\, P_{\mathrm{HI}}(k, z) \tag{2.7}$$

Here, $\overline{x}_{\mathrm{HI}}$ denotes the average neutral hydrogen fraction, which can be related to the cosmological H I density parameter $\Omega_{\mathrm{HI}}(z)$ via an appropriate conversion. The quantity $\overline{T}_b$ represents the characteristic brightness temperature, given by:

$$\overline{T}_b(z) \approx 0.39\,\mathrm{mK} \times \left(\frac{\Omega_{\mathrm{HI}}(z)}{10^{-3}}\right) \left[\frac{0.29}{\Omega_m + \Omega_\Lambda (1+z)^{-3}}\right]^{1/2} \left(\frac{1+z}{2.5}\right)^{1/2} \tag{2.8}$$

Here, $\Omega_{\mathrm{HI}}(z)$ represents the cosmological abundance of neutral hydrogen at redshift z. The H I power spectrum can be related to the underlying matter power spectrum through the following expression:

$$P_{\mathrm{HI}}(k, z) = b^2(k, z)\, P(k, z), \tag{2.9}$$

The measurement of the 21-cm power spectrum (PS) offers the advantage of capturing spatial fluctuations in the signal, unlike the global signal which represents a sky-averaged quantity. Although the 21-cm signal is significantly non-Gaussian and the PS does not capture all the spatial information, it still contains substantial insight into the underlying astrophysics. Moreover, from an observational standpoint, the PS is more accessible and less complex to measure than higher-order statistical estimators.

The 21-cm power spectrum serves as a sensitive probe of early-Universe astrophysics. The brightness temperature fluctuations arise from perturbations in key physical quantities, including the matter density, ionization fraction, Lyman-α coupling, and line-of-sight peculiar velocities, as described in Eq. 2.10 [66].

$$\delta_{21} \propto A_b\, \delta_b + A_x\, \delta_x + A_\alpha\, \delta_\alpha + A_T\, \delta_T - \delta_{\partial v}, \tag{2.10}$$

Each δ in the above expression represents the fractional perturbation of a specific physical parameter influencing the 21-cm signal. Specifically, δ_b captures the fluctuations in the baryonic matter density, δ_α denotes variations in the Lyman-α coupling coefficient x_α, δ_x reflects fluctuations in the neutral hydrogen fraction, δ_T corresponds to perturbations in the kinetic temperature T_K,

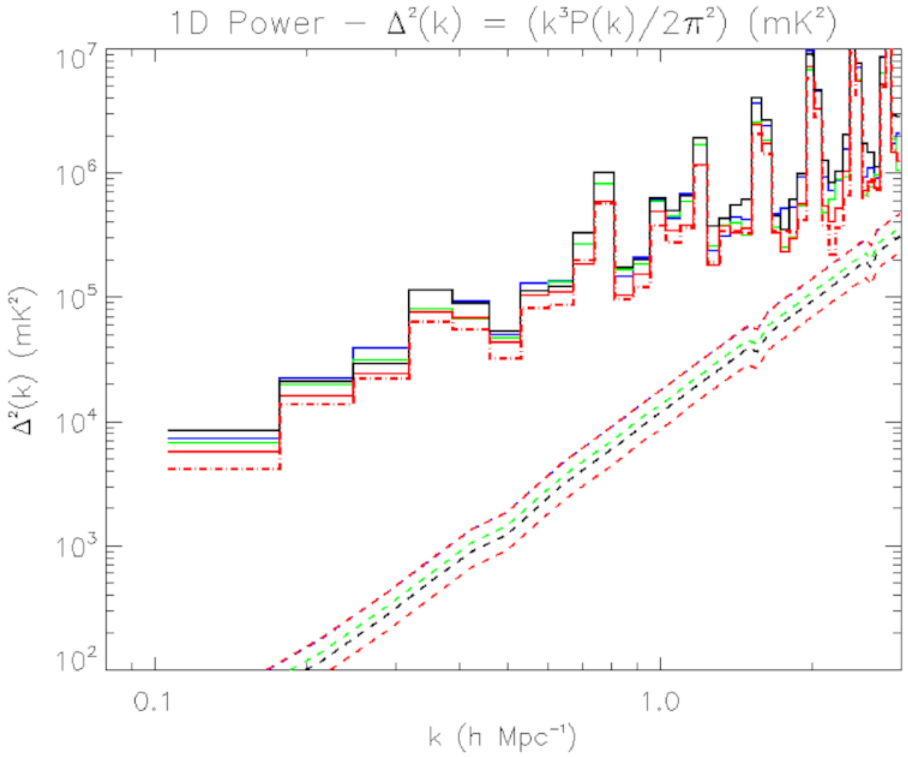

Figure 2.5: The Murchison Widefield Array (MWA) has provided current upper limit on the 21-cm power spectrum from the EoR. This figure is adapted from [6].

and $\delta_{\partial v}$ accounts for the gradient of the peculiar velocity along the line of sight. The coefficients A_i quantify the relative contribution of each physical effect to the total brightness temperature fluctuations. These components collectively modulate the amplitude and shape of the 21-cm power spectrum, encoding rich astrophysical information about the processes governing the IGM during the CD and the EoR. Consequently, precise measurements and modeling of each term are essential for accurate interpretation of future 21-cm observations.

Although a direct detection of the 21-cm power spectrum remains elusive, several interferometric experiments have placed increasingly stringent upper limits on the signal, especially during the EoR. These constraints provide valuable insights into the ionization state of the IGM and the properties of early astrophysical sources. Recent interferometric observations have progressively tightened upper limits on the 21-cm power spectrum during the Epoch of Reionization. The MWA has placed a 2σ upper limit on the 21-cm power spectrum of $\Delta^2_{21} < (43.9\ \mathrm{mK})^2$ at redshift $z \approx 6.5$ and wave number $k = 0.15\ h\,\mathrm{cMpc}^{-1}$ [6] (see Fig. 2.5). The most stringent constraints to date have been achieved by HERA, which reports $\Delta^2_{21} < (21.4\ \mathrm{mK})^2$ at $z \approx 7.9$ and $k = 0.34\ h\,\mathrm{cMpc}^{-1}$, and $\Delta^2_{21} < (59.1\ \mathrm{mK})^2$ at $z \approx 10.4$ with $k = 0.36\ h\,\mathrm{cMpc}^{-1}$ [7] (see Fig. 2.6). The LOFAR-EoR project has also significantly advanced these constraints, recently reporting upper limits of $\Delta^2_{21} < (68.7\ \mathrm{mK})^2$ at $z \approx 10.1$, $\Delta^2_{21} < (54.3\ \mathrm{mK})^2$ at $z \approx 9.1$, and $\Delta^2_{21} < (65.5\ \mathrm{mK})^2$ at $z \approx 8.3$, all measured near $k \approx 0.076$–$0.083\ h\,\mathrm{cMpc}^{-1}$ [8] (see Fig. 2.7).

While none of these measurements have yet achieved a detection, they have successfully constrained the parameter space of theoretical models describing the ionizing photon budget, source properties, and heating history of the IGM. With continued improvements in calibration, foreground subtraction, and sensitivity, upcoming observations from HERA and the future Square Kilometre Array

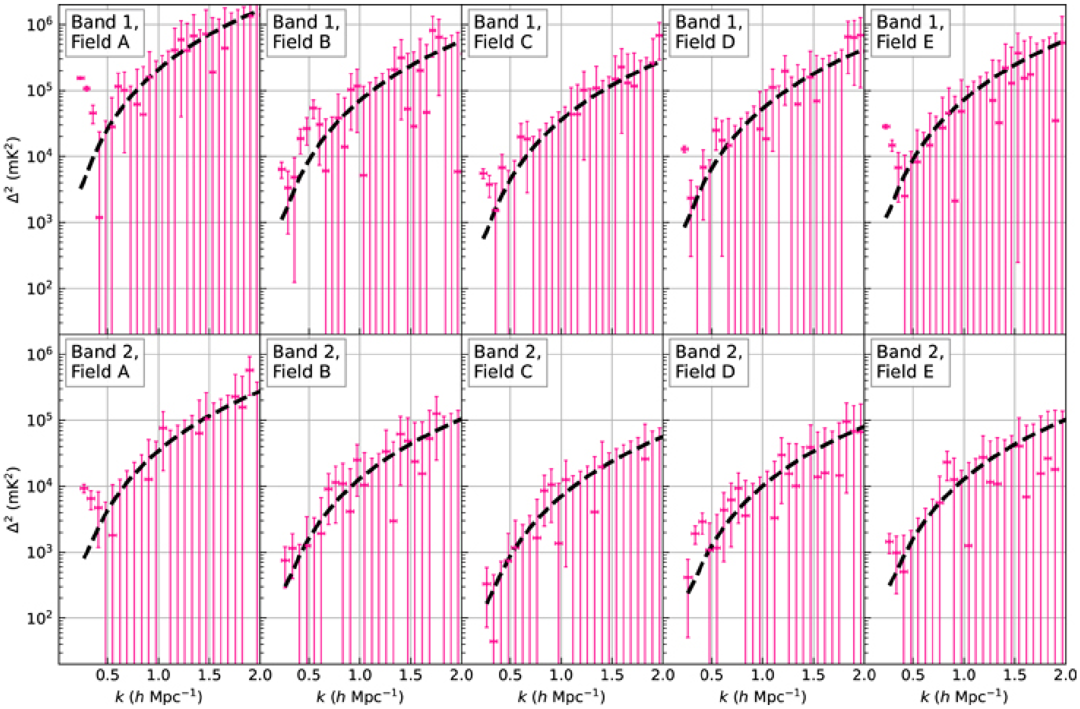

Figure 2.6: Latest upper limits on the 21-cm power spectrum during the EoR from HERA observations. This figure is adapted from [7].

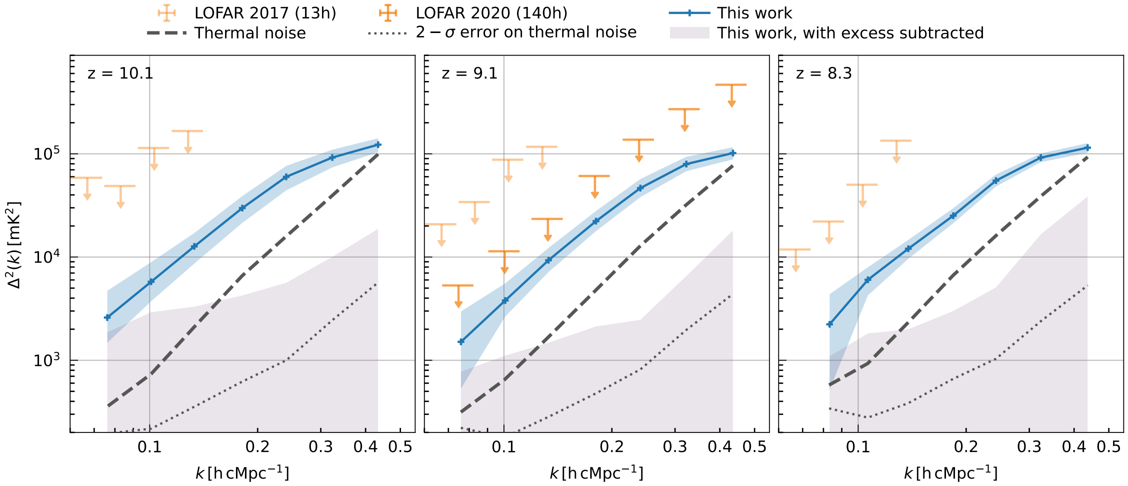

Figure 2.7: Latest upper limits on the 21-cm power spectrum during the EoR from LOFAR observations. This figure is adapted from [8]

(SKA) are expected to push toward the first definitive detection of the 21-cm signal.

2.3.3 Tomographic Imaging with Next-Generation Radio Telescopes

Alongside power spectrum measurements, upcoming highly sensitive radio telescopes such as SKA-Low are expected to enable tomographic imaging of the IGM during the CD and EoR [67]. This technique involves constructing three-dimensional data cubes from redshifted 21-cm maps across multiple frequency channels, allowing for spatial and temporal resolution of the evolving IGM. Tomographic imaging is crucial for visualizing the morphology and topology of ionized regions, connecting them to underlying galaxy populations, and probing the physical conditions and radiation sources driving reionization. Unlike statistical approaches, tomography provides direct insight into the structure and evolution of ionized bubbles, quasar environments, and feedback processes. Once instruments like the SKA become operational, 21-cm tomography will offer a transformative window into the early Universe, complementing statistical constraints such as the power spectrum. Although spatial resolution may be limited, instruments like LOFAR are also projected to produce tomographic maps under specific observational conditions [68].

2.4 Observational Challenges and Current Mitigation Strategies

Detecting the redshifted H I 21-cm signal from the CD and EoR presents a number of formidable observational challenges. Foremost among them is the presence of bright astrophysical foregrounds, primarily Galactic synchrotron emission and extragalactic point sources, which can be 4–5 orders of magnitude brighter than the cosmological 21-cm signal. Accurately modeling and removing these foregrounds without losing the underlying cosmological signal is a major technical hurdle. Additionally, the ionosphere introduces time- and direction-dependent phase and amplitude distortions, especially at low frequencies, further complicating detection. Instrumental systematics, such as chromatic responses of antennas, beam variations, and radio frequency interference (RFI), also degrade sensitivity and must be meticulously mitigated. Achieving the dynamic range and stability required to isolate the faint 21-cm signal demands rigorous calibration techniques, advanced statistical methods, and long integration times. Together, these factors make the detection and interpretation of the H I 21-cm signal one of the most complex tasks in observational cosmology. This section outlines the key observational challenges encountered in 21-cm signal detection experiments. In the subsequent sections, we also provide a brief overview of widely adopted techniques for foreground mitigation and methods used for parameter estimation.

2.4.1 Foreground

The detection of the redshifted 21-cm signal from the CD and EoR is severely hindered by astrophysical foregrounds, which are several orders of magnitude brighter than the cosmological signal. These foregrounds primarily include diffuse galactic synchrotron emission (DGSE), free-free emission from both galactic and extragalactic sources, and compact sources such as star-forming galaxies and active galactic nuclei (AGNs) [9] a schematic representation is shown in Fig. 2.8. While these foregrounds are of astrophysical interest in their own right, they act as contaminants in 21-cm cosmology and must be mitigated to uncover the underlying cosmological information. The dominant

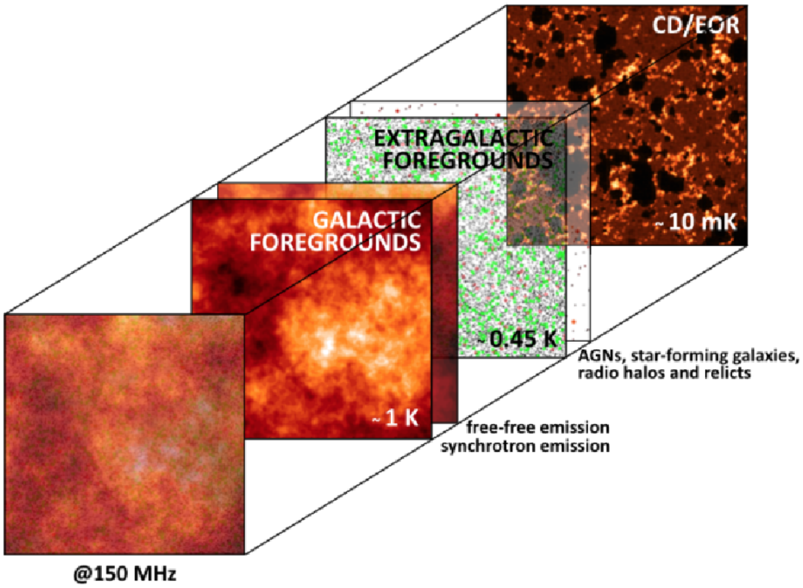

Figure 2.8: An illustration depicting various foreground components relevant to redshifted 21-cm experiments at 150 MHz is shown, figure adapted from [9].

foreground component at frequencies below 150 MHz is DGSE, which originates primarily from our Galaxy. Fig. 2.9 presents a brightness temperature map of the DGSE observed at 408 MHz [10]. It follows a power-law dependence on frequency, $T(\nu) \propto \nu^{-\alpha}$, making its brightness temperature particularly significant at the low frequencies of interest for EoR and CD observations. This emission is especially strong near the Galactic plane but is also observed at high latitudes near the North Celestial and South Galactic Poles [69, 70]. In addition to synchrotron radiation, free-free emission and contributions from radio haloes and relics add to the diffuse galactic foreground.

Extragalactic foregrounds comprise mainly compact radio sources such as AGNs and star-forming galaxies. Although considerable progress has been made in constraining the number counts and luminosity functions of these populations, uncertainties remain, particularly at the faint end of the flux density distribution. Their spatial clustering introduces additional challenges, with studies

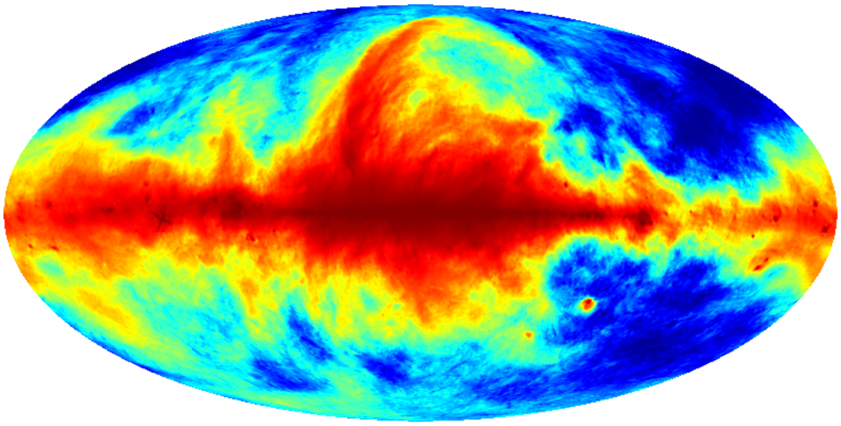

Figure 2.9: All-sky map of Galactic synchrotron emission, showing bright foregrounds along the Galactic plane and fainter regions at high latitudes, figure adapted from [10].

showing that source clustering dominates the angular power spectrum at scales larger than about one arcminute for flux densities above ~ 0.1 mJy at 150 MHz.

The spectral smoothness of foregrounds, particularly synchrotron radiation, is a key feature leveraged by foreground mitigation strategies. Since the 21-cm cosmological signal is expected to fluctuate rapidly with frequency, foreground separation methods exploit this contrast. Techniques such as Principal Component Analysis (PCA), Generalized Morphological Component Analysis (GMCA), Independent Component Analysis (ICA), and Gaussian Process Regression (GPR) are commonly employed. However, these approaches assume perfect spectral smoothness, and their efficacy is reduced in the presence of non-smooth spectral features or instrumental chromaticity, which can introduce mode-mixing and complicate signal recovery. In global 21-cm signal experiments and radio interferometric observations alike, careful foreground modeling, instrumental calibration, and algorithmic sophistication are essential to isolate the cosmological 21-cm signal from these dominant foreground contaminants.

The foreground challenges differ significantly between global 21-cm experiments and radio interferometric (power spectrum) experiments due to their distinct observational strategies. In global experiments, which aim to detect the sky-averaged 21-cm signal, the primary difficulty lies in the need to separate a faint, frequency-dependent signal from extremely bright foregrounds (e.g., galactic synchrotron emission) that are also spectrally smooth. This demands exquisite instrumental calibration and beam modeling, as any frequency-dependent systematics (e.g., chromatic beam effects) can mimic or obscure the global signal. Conversely, in radio interferometric observations, which measure spatial fluctuations of the 21-cm signal via the power spectrum, the dominant issue is "mode-mixing," where instrumental chromaticity and calibration errors scatter smooth foreground power into higher Fourier modes, contaminating the 21-cm window. While both types of experiments rely on the spectral smoothness of foregrounds for mitigation, global experiments are more sensitive to spectral calibration and beam chromaticity, whereas interferometers are more vulnerable to baseline-dependent leakage and angular-spectral coupling caused by the instrument and ionosphere.

2.4.2 Mitigation strategies for Foreground

To address foreground contamination, some ground-based experiments employ a 'foreground avoidance' strategy, while others focus on modelling and subtracting the foregrounds. In this section, we provide a brief overview of both approaches.

a) Foreground Avoidance

The foreground avoidance technique is a conservative yet widely utilized strategy in 21cm cosmology for mitigating contamination from bright, spectrally smooth astrophysical foregrounds: primarily Galactic synchrotron emission and extragalactic point sources, which can exceed the cosmological 21cm signal by five to six orders of magnitude. This method operates in Fourier space, particularly within the two-dimensional (2D) cylindrical power spectrum defined by the transverse and line-of-sight wave numbers, $k_\perp$ and $k_\parallel$, respectively. In this representation, foreground contamination is predominantly restricted to a region termed the wedge (see Fig. 2.10), which arises due to the chromatic response of the interferometer and the geometry of its baselines. The horizon delay limit for each baseline bounds the wedge. Foreground avoidance involves discarding data within this contaminated wedge and restricting analysis to the cleaner Epoch of Reionization (EoR) window the region outside the wedge where the 21cm signal is expected to dominate (see Fig. 2.10). The extent of the EoR window is determined by instrumental and observational parameters: the

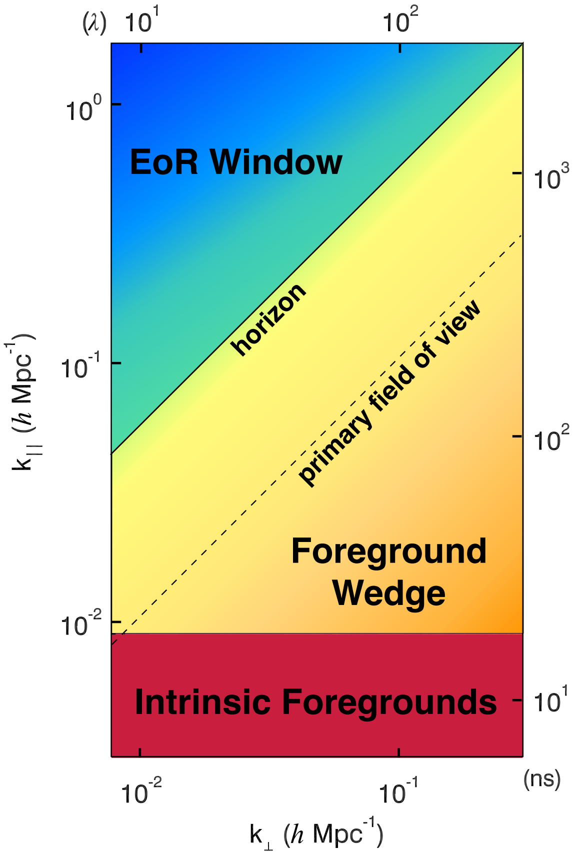

Figure 2.10: A conceptual illustration of the 2D power spectrum highlights how "intrinsic foregrounds" dominate the low $k_{\|}$ modes. Due to the instrument's chromatic response, this contamination spreads into the so-called "foreground wedge," which is bounded by the primary beam and the horizon. The region beyond this wedge, known as the "EoR window," is where the 21-cm signal is least affected by foregrounds, figure adapted from [11].

minimum accessible $k_{\|}$ is set by the total bandwidth, the maximum $k_{\|}$ by the frequency resolution, and the range in $k_{\perp}$ is limited by the array's shortest and longest baselines.

Several studies have characterized the EoR window and its limitations. For instance, [71] focused on bright point sources while neglecting diffuse emission and thermal noise, whereas [72] explored how uv-gridding and the instrument's point spread function contribute to foreground leakage. [73] demonstrated that chromaticity, calibration errors, and model inaccuracies can leak foreground power into high $k_{\|}$ modes. Notably, [74] found that diffuse Galactic synchrotron emission, rather than point sources, constitutes the dominant foreground challenge for signal isolation. Although the foreground avoidance approach sacrifices a significant portion of Fourier modes, thereby reducing sensitivity, it offers a robust and model-independent framework for isolating the cosmological 21cm signal, particularly valuable in the initial detection phase for experiments such as HERA and MWA.

b) Foreground Subtraction

Foreground subtraction is a widely used method in 21cm cosmology that seeks to recover the faint cosmological signal by modeling and removing bright foregrounds from observational data.

Most subtraction techniques rely on the spectrally smooth nature of foregrounds, such as Galactic synchrotron and free–free emission, and employ line-of-sight fitting, typically using low-order polynomials or similar basis functions to capture this smooth component, which is then subtracted from the data [75–78]. However, a major limitation of parametric approaches is that they rely on extrapolations from high-frequency, low-resolution sky maps, while observations at EoR-relevant frequencies and resolutions remain scarce. To overcome these limitations, several non-parametric or 'blind' methods, such as PCA, ICA, or Gaussian Process Regression, Machine learning, are being developed, offering a data-driven alternative that minimizes prior assumptions about foreground structure. A key complication arises from instrumental effects, including beam chromaticity and polarized foreground leakage, which can distort the spectral coherence of foregrounds and introduce artificial structure along the frequency (i.e., line-of-sight) axis [79,80]. This leakage can cause decorrelation and mimic 21cm signal fluctuations, thereby increasing the risk of residual bias. Typically, foreground subtraction assumes a functional form for foregrounds, and the residuals after subtraction include not only the cosmological signal but also fitting errors and thermal noise. Since the 21cm signal is a line emission, redshifted to low radio frequencies, any distortion in its frequency structure could lead to misinterpretation of the spatial distribution of neutral hydrogen. Since thermal noise per resolution element is often much higher than the signal, the central challenge is to design an optimal subtraction algorithm that can minimize foreground contamination without introducing systematic bias or significantly suppressing the cosmological signal.

i) Parametric Method

The parametric method is one of the most commonly employed techniques for subtracting astrophysical foregrounds in 21cm cosmology. It exploits the fact that foregrounds, such as Galactic synchrotron and free–free emission, as well as extragalactic point sources, are typically spectrally smooth, in contrast to the fluctuating nature of the redshifted 21cm signal. This method fits smooth functional forms along each line of sight (LoS), most commonly using low-order polynomials in logarithmic frequency space, to model and subtract the dominant foreground contribution. A classic implementation of this technique was introduced by [75], where the foreground was modeled as the sum of four components, each described by a power-law spectrum with spatially constant spectral indices. The parameters of these power laws were fit simultaneously with frequency correlation parameters to estimate the residual power spectrum. Building on this, [76] proposed a refined model allowing for spatially varying spectral indices, by fitting the logarithm of intensity along each LoS with a second-order polynomial in $\log \nu$, offering greater flexibility to account for spatial foreground variation. This approach has been widely adopted in several other works as well [77,80].

In general, the parametric foreground model can be expressed as:

$$T_{\rm obs}(\nu) = \sum_{n=0}^{N} a_n \log^n(\nu) + T_{21}(\nu) + n(\nu) \tag{2.11}$$

where $T_{\rm obs}$ is the observed brightness temperature, a_n are polynomial coefficients, T_{21} is the cosmological 21cm signal, and n represents thermal noise.

While the method is computationally efficient and straightforward to implement, it does rely on prior assumptions about the spectral form of the foregrounds. It makes it vulnerable to overfitting, leading to signal loss, especially if higher-order polynomials remove both foregrounds and components of the cosmological signal. Moreover, instrumental effects, such as beam chromaticity and polarized foreground leakage, can disrupt the spectral smoothness of the foregrounds, making them harder to model accurately with simple functions. Nevertheless, parametric methods remain a valuable starting point in many global signal and interferometric experiments (e.g., EDGES, SARAS), often serving as a benchmark against which more sophisticated blind or semi-blind approaches, such as PCA, ICA, or Gaussian Process Regression, are tested.

ii) Non-Parametric Foreground Removal Methods

Unlike parametric techniques, which assume a specific functional form for foregrounds, non-parametric or blind methods make minimal or no assumptions about the spectral structure of the data. These approaches aim to isolate and subtract foregrounds by statistically identifying their dominant modes directly from the observed data, primarily relying on foregrounds' spectral smoothness and statistical redundancy in contrast to the rapidly fluctuating cosmological 21-cm signal.

Popular non-parametric methods include:

- **Wp Smoothing**: Fits a smooth function to the line-of-sight signal using a regularization parameter that allows for controlled spectral flexibility [81]. This enables deviations from ideal smoothness, which helps to model real-world foreground variations and instrumental effects.
- **Fast Independent Component Analysis (FastICA)**: Assumes that the foreground components are statistically independent and separates them using blind source separation techniques [82]. FastICA allows the data to determine the shape of the foregrounds without assuming a polynomial or analytic form, and has been successfully applied to CMB and 21 cm datasets.
- **Generalized Morphological Component Analysis (GMCA)**: An ICA-based technique that incorporates sparsity and morphological diversity, often using wavelet transforms to isolate signal components more effectively in frequency and angular space [83].
- **Gaussian Process Regression (GPR)**: Uses Gaussian processes with specific covariance structures to model the foregrounds, noise, and the cosmological signal [84]. GPR provides a flexible Bayesian framework that can preserve the 21 cm signal while fitting and subtracting smooth foregrounds.
- **HIEMICA (HI Expectation-Maximization ICA)**: A semi-blind Bayesian approach that jointly estimates the 3D 21 cm power spectrum and foreground parameters without strong prior assumptions [85]. It uses the Expectation-Maximization (EM) algorithm and has been shown to outperform PCA in multiple regimes.
- **Deep Learning-Based Methods**: Recent progress in deep learning has enabled data-driven techniques for modeling and mitigating foregrounds in 21-cm cosmology. For instance, [13,86] developed an artificial neural network (ANN) for extracting astrophysical parameters from mock global 21-cm data, incorporating instrumental effects and foregrounds, and later extended it to interferometric power spectrum foreground mitigation [87]. [88] introduced a convolutional denoising autoencoder (CDAE), trained on SKA simulations, achieving high-accuracy signal recovery. Further developments include U-Net architectures applied to post-reionization foreground removal [89], frequency-differenced maps for dynamic range compression [90], and VAE-assisted Gaussian Process Regression for power spectrum reconstruction from mock LOFAR data [91]. In this thesis, we extend such frameworks to both global and interferometric 21-cm pipelines.

Non-parametric methods are particularly useful when accurate foreground models are unavailable or when instrumental effects (e.g., beam chromaticity, polarization leakage) distort the ideal spectral smoothness of foregrounds. These techniques have been applied in both global signal experiments and interferometric studies (e.g., LOFAR, HERA, SKA-Low).

However, blind methods must be applied with care. Aggressive mode subtraction or component filtering may lead to substantial signal loss. To mitigate this, many pipelines incorporate signal injection tests to evaluate how much of the cosmological signal is preserved after foreground removal.

2.4.3 Ionospheric effects

The Earth's ionosphere presents significant challenges for both global 21-cm signal experiments and radio interferometers, especially at low radio frequencies. The ionosphere introduces frequency-dependent (chromatic) effects such as refraction, absorption, and thermal emission, primarily from its F and D-layers. A schematic depiction of these ionospheric effects is shown in Fig. 2.11. These effects can distort the shape and reduce the amplitude of the faint cosmological 21-cm signal, sometimes to a degree greater than the signal itself, making detection and calibration extremely difficult [12, 50, 92–94]. Moreover, ionospheric conditions vary with time, direction, and location, leading to complex, direction-dependent phase errors for radio interferometers. This variability complicates calibration, as standard methods may not fully correct for spatial and temporal fluctuations in electron density, especially during periods of severe ionospheric activity [95, 96]. For global 21-cm experiments, the ionospheric effects do not average out over time and must be accounted for at each timestep, further increasing the complexity of foreground calibration and signal extraction. Advanced techniques, such as direction-dependent calibration and machine learning approaches, are being developed to mitigate these challenges, but the ionosphere remains a fundamental obstacle for precise low-frequency radio astronomy.

To mitigate these challenges, several approaches have been developed. For interferometric experiments, direction-dependent calibration methods, such as facet-based calibration and peeling, are widely employed to model and correct for spatially varying ionospheric phase errors [95, 96]. More recently, machine learning (ML) techniques, including deep learning models, have been explored to predict and correct ionospheric distortions by learning from both observational and simulated data sets. These methods aim to model complex, non-linear ionospheric behavior in real time, improving calibration accuracy. In the context of global 21-cm signal experiments, mitigation strategies include ionospheric absorption and refraction modeling based on real-time GPS-derived total electron content (TEC) measurements and ray-tracing simulations. Parametric modeling techniques are used to fit and subtract ionospheric effects alongside foreground and instrumental systematics in the data analysis pipeline. AI/ML frameworks such as artificial neural networks have been employed to model the ionospheric effects and foregrounds, enabling more robust extraction of the global 21-cm signal [50]. These data-driven methods show promise in dealing with the' complex, time-variable nature of ionospheric distortions. However, their integration into large-scale observational campaigns like those planned for the SKA remains an ongoing research effort.

2.4.4 Radio Frequency Interference

Terrestrial radio interferometers are particularly vulnerable to radio frequency interference (RFI) originating from various human-made sources such as telecommunications infrastructure, FM radio broadcasts, aircraft communication, wind turbines, and satellite transits through the telescope beam [97, 98]. These RFI signals are generally localized in both time and frequency, enabling their identification and excision through high time and frequency resolution in interferometric data. However, this flagging process disrupts the smoothness of the instrumental bandpass response, introducing irregularities into the measured visibilities. In power spectrum (PS) estimation, which involves Fourier transforming the visibilities along the frequency axis to delay space, these irregu-

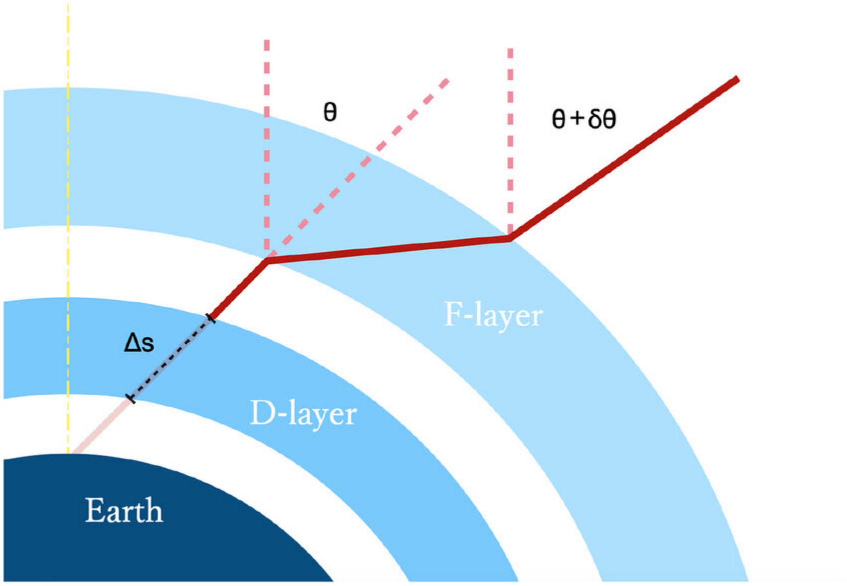

Figure 2.11: Schematic illustration of ionospheric refraction and absorption by uniform ionospheric layers (not to scale), figure adapted from [12].

larities translate into rapid fluctuations across the delay domain. Consequently, spurious structures appear in the line-of-sight Fourier modes, potentially mimicking or obscuring the cosmological 21-cm signal. For instruments such as the MWA and LOFAR, around 1 to 3% of data channels may be excised due to RFI [99, 100]. If uncorrected during calibration, imaging, and foreground subtraction, the resulting excess power does not average down with integration time and can dominate the true 21-cm signal by one to two orders of magnitude [97]. To mitigate these effects, spectral techniques such as CLEAN and least squares spectral analysis (LSSA) have been employed, with LSSA showing consistent efficacy across various RFI flagging patterns [101]. However, ongoing investigation of alternative mitigation strategies is critical to optimize signal recovery.

2.5 Observational Approaches

To observe the redshifted 21-cm signal from the CD and the EoR, several ongoing experiments employ different observational strategies. Based on their working principles, these efforts can be broadly categorized into two classes: (i) radiometer-based experiments, which measure the sky-averaged brightness temperature (known as the global 21-cm signal), and (ii) interferometric techniques, which utilize arrays of radio antennas to detect spatial fluctuations in the signal. These methods are described in detail below.

2.5.1 Single Radiometer Measurement Approach

Global 21-cm signal experiments use single radiometer systems designed to measure the sky-averaged brightness temperature as a function of frequency, aiming to detect the faint, global signature of the redshifted 21-cm line from neutral hydrogen across cosmic time, particularly during the CD and the EoR. These systems typically consist of a wide-beam antenna (e.g., dipole, fat-dipole-like monopole antenna, blade or conical log-spiral) coupled with a calibrated receiver that measures total power over a frequency range of 40–200 MHz, corresponding to redshifts $z \sim 6$–35 [39, 40, 102]. The observed antenna temperature $T_{\text{ant}}(\nu)$ is modeled as a combination of sky temperature, instrumental systematics, and noise, expressed as:

$$T_{\text{ant}}(\nu) = \frac{\int B(\hat{n},\nu)\, T_{\text{sky}}(\hat{n},\nu)\, d\Omega}{\int B(\hat{n},\nu)\, d\Omega} + T_{\text{sys}}(\nu), \tag{2.12}$$

where $B(\hat{n},\nu)$ is the frequency-dependent antenna beam response, $T_{\text{sky}}(\hat{n},\nu)$ is the sky brightness temperature distribution dominated by Galactic synchrotron emission, and $T_{\text{sys}}(\nu)$ represents receiver system temperature including electronic noise [103]. The cosmological 21-cm signal, expected at the level of $\sim$ 10–200 mK, is superimposed on foregrounds that can reach $\sim 10^4$–10^5 K. Foreground separation is performed using smooth spectral models, such as maximally smooth functions or polynomial fitting, exploiting the fact that the cosmological signal has a non-smooth spectral shape due to astrophysical processes like Lyman-α coupling and X-ray heating [104, 105]. The radiometer equation governs the thermal noise level for such measurements:

$$\Delta T = \frac{T_{\text{sys}}}{\sqrt{B\, t_{\text{int}}}}, \tag{2.13}$$

where B is the bandwidth and t_{int} is the integration time, typically several hundred to thousands of hours to achieve the required sensitivity [56]. Mitigating systematic errors due to beam chromaticity, ground reflections, cable reflections, ionospheric effects, and radio frequency interference (RFI) is critical; therefore, experiments are conducted in radio-quiet zones with carefully engineered instrument designs and calibration strategies. Notable single-radiometer experiments employing this methodology include EDGES, SARAS, LEDA, and REACH, all aiming to constrain astrophysical parameters and the timing of key phases in the early Universe [39–41].

2.5.2 Interferometric Measurement Approach

A radio interferometer records spatial Fourier components of the sky's brightness distribution under the far-field approximation. The reconstruction of the sky image is achieved via inverse Fourier transformation of these measurements. This process, known as aperture synthesis, involves an array of spatially separated antennas that collectively emulate a large, synthetic aperture. The maximum baseline between any two antennas defines the effective resolution of the array. Since the aperture is sampled at discrete positions, it is inherently incomplete. Each pair of antennas samples a specific spatial frequency, determined by their separation in units of the observing wavelength. By correlating the signals from each antenna pair, one obtains complex visibilities containing both amplitude and phase information, which together map the Fourier plane of the sky brightness distribution. The fundamental principle underlying the imaging of distant radio sources using an interferometer is described by the van Cittert–Zernike theorem, which relates the spatial coherence of radiation to the intensity distribution of a distant, spatially incoherent source. According to this theorem, the mutual coherence function of the electric fields received at two points on the aperture plane is proportional to the spatial Fourier transform of the sky brightness distribution. Mathematically, this can be expressed as:

$$\langle E_\nu(\mathbf{r}_1) E^*_\nu(\mathbf{r}_2)\rangle \propto \int I_\nu(\hat{s})\, e^{2\pi i \nu \tau_{12}}\, d\Omega \equiv V(\mathbf{r}_1 - \mathbf{r}_2, \nu), \tag{2.14}$$

where $E_\nu(\mathbf{r}_1)$ and $E_\nu(\mathbf{r}_2)$ are the electric fields at positions $\mathbf{r}_1$ and $\mathbf{r}_2$ on the aperture plane, $I_\nu(\hat{s})$ is the sky intensity in the direction $\hat{s}$, and $d\Omega$ is the solid angle element. The quantity $V(\mathbf{r}_1 - \mathbf{r}_2, \nu)$

is the visibility function, a complex quantity dependent on the baseline vector $\mathbf{r}_1 - \mathbf{r}_2$ and the observing frequency ν. A radio interferometer effectively samples this visibility function, providing a measure of the spatial coherence of the incoming wavefronts.

In radio interferometry, the visibilities measured by a network of telescopes must be expressed within a coordinate system that effectively connects the sky brightness distribution to the physical configuration of the array elements. Consider an interferometer directed toward a unit vector $\vec{s}_0$, which defines the phase center. The sky brightness distribution is denoted as $I(l, m, n) = I(\vec{s})$, where l, m, and n are the direction cosines corresponding to the unit vector $\vec{s}$. The reference direction $\vec{s}_0$ corresponds to $(l = 0, m = 0, n = 1)$, and any deviation from this direction is represented as $\vec{s} = \vec{s}_0 + \vec{\sigma}$. The visibility measurements are naturally represented on the so-called uv-plane, which is the tangent plane to the celestial sphere at $\vec{s}_0$ and serves as the projection surface for synthesizing the two-dimensional sky image. This uv-plane is perpendicular to the baseline vectors between antenna elements and defines the spatial frequency coordinates used in aperture synthesis imaging. The transformation between the celestial and instrumental coordinate systems is given by:

The transformation between the Earth-based Cartesian coordinates (x, y, z) and the interferometric coordinate system (u, v, w) is given by:

$$\begin{bmatrix} u \\ v \\ w \end{bmatrix} = \frac{1}{\lambda} \begin{bmatrix} \sin(H) & \cos(H) & 0 \\ -\sin(\delta_0)\cos(H) & \sin(\delta_0)\sin(H) & \cos(\delta_0) \\ -\cos(\delta_0)\cos(H) & -\cos(\delta_0)\sin(H) & \sin(\delta_0) \end{bmatrix} \begin{bmatrix} x \\ y \\ z \end{bmatrix} \tag{2.15}$$

Here, H is the hour angle and δ_0 is the declination of the phase center (pointing direction of the array). The coordinates (u, v, w) are expressed in units of wavelength λ, and define the projected baseline components in the coordinate frame centered on the pointing direction. The w-axis points toward the phase center, while the u and v axes span the plane perpendicular to the line of sight.

In the Earth-based Cartesian coordinate system, the physical positions of antennas are described by (x, y, z) in meters, while in the interferometric coordinate system, these are represented as (u, v, w) and expressed in units of the observing wavelength λ. The position vectors $\vec{r}_1$ and $\vec{r}_2$ from Equation 2.15 can be written in the UVW coordinate system as $\vec{r}_1(u_1, v_1, w_1)$ and $\vec{r}_2(u_2, v_2, w_2)$. The baseline vector $\vec{b}$ between the two antennas is then defined as:

$$\vec{b}(u, v, w) = \vec{r}_1 - \vec{r}_2,$$

with components $u = u_1 - u_2$, $v = v_1 - v_2$, and $w = w_1 - w_2$. Note that the vectors $\vec{r}_1$ and $\vec{r}_2$ are not generally coplanar with the aperture plane; that is, their projections along the pointing direction $\hat{s}_0$ yield nonzero w components ($\vec{r}_1 \cdot \hat{s}_0 = w_1 \neq 0$ and $\vec{r}_2 \cdot \hat{s}_0 = w_2 \neq 0$). As a result, signals arriving from a distant source will reach the two antennas at different times, introducing a geometric delay given by:

$$\tau = \frac{\vec{b} \cdot \hat{s}_0}{\nu} = \frac{w_2 - w_1}{\nu},$$

where ν is the observing frequency. This delay must be corrected before cross-correlating the signals from each antenna pair.

Equation 2.14 can be reformulated in the UVW coordinate system as:

$$V(u, v, w) = \iint I(l, m, n)\, e^{-2\pi i\left(ul + vm + w\sqrt{1-l^2-m^2}\right)} \frac{dldm}{\sqrt{1 - l^2 - m^2}}, \tag{2.16}$$

where $d\Omega = \frac{dldm}{n} = \frac{dldm}{\sqrt{1-l^2-m^2}}$, and (l, m) are the direction cosines on the tangent plane to the celestial sphere at the phase center $\vec{s}_0$. Since the measured visibilities are sampled in the (u, v, w) domain, one can, in principle, recover the sky intensity distribution through the inverse Fourier transform of Equation 2.16.

If the field of view is sufficiently small (i.e., close to the phase center), the curvature of the sky can be neglected and the w-term can be approximated as zero ($w = 0$). Under this small-angle approximation, Equation 2.16 simplifies to a two-dimensional Fourier transform:

$$V(u, v) = \iint I(l, m)\, e^{-2\pi i(ul+vm)}\, dldm, \tag{2.17}$$

which directly relates the measured visibility function $V(u, v)$ to the sky brightness distribution $I(l, m)$ via a 2D spatial Fourier transform.

The observed source brightness distribution is related to the measured visibilities through the van Cittert–Zernike theorem (see Equation 2.14). Each interferometric baseline samples the complex visibility function at a specific point in the uv plane. Since the array consists of a finite number of antenna pairs, the coverage of the uv plane is inherently discrete and incomplete, leading to gaps in the sampling. As a result, the inverse Fourier transform of Equation 2.17 is performed as a discrete summation over the available uv points. To enhance this sampling, the technique of Earth rotation aperture synthesis is employed. As the Earth rotates, the projection of each baseline changes with time, enabling the interferometer to sample additional regions of the uv plane. This improves the uv coverage and thus the fidelity of the reconstructed image by effectively increasing the number of independent measurements of the visibility function.

2.5.3 Calibration and Imaging of Interferometric Data

As indicated by Equation 2.14, raw interferometric data consists of electric field correlations measured across antenna pairs, which in themselves do not directly convey astrophysical information. To extract scientifically meaningful results, the data must undergo a series of post-processing steps, beginning with calibration to correct for instrumental and systematic effects, followed by imaging techniques to reconstruct the sky brightness distribution and deconvolve the instrument's response.

a) Direction-Independent Calibration

The visibilities recorded by an interferometer are affected by instrumental responses, particularly complex, frequency-dependent gain factors introduced by the receiver electronics. These gains alter the measured signal multiplicatively. The observed visibility between a pair of antennas i and j is given by:

$$V_{ij}^{\text{obs}} = g_i g_j^* V_{ij}^{\text{true}} + n_{ij}, \tag{2.18}$$

where V_{ij}^{obs} is the measured visibility, V_{ij}^{true} is the true sky visibility, g_i and g_j are the complex gain terms for antennas i and j respectively, and n_{ij} denotes the noise contribution on the baseline. Each component in Equation 2.18 is typically a function of frequency and time. Accurate calibration of these gains is essential to recover the true sky signal and ensure reliable imaging outcomes.

Antenna-based complex gain solutions are estimated and applied to the observed visibilities in order to correct for instrumental effects. It is typically achieved by observing standard calibration sources, called calibrators, whose intrinsic visibilities are well-characterized. These calibrator observations, conducted periodically during the observation session, are used to solve for the complex gains. The derived gain solutions are then interpolated and applied to the target field visibilities. However, this approach assumes temporal stability of the instrumental gains; any fluctuations occurring during the target observations remain uncorrected.

To address this limitation, a technique known as **self-calibration** is employed. In this method, a sky model of the target field itself is iteratively used to refine the gain solutions over the actual observation time. Self-calibration involves repeated cycles of imaging and calibration to converge on both accurate gain solutions and an improved sky model [106]. The methodology described above operates under the assumption that the gain errors are constant across the entire field of view. In other words, the gain terms g_i in Equation 2.18 are considered to be direction-independent, thereby characterizing a “direction-independent” calibration regime.

b) Direction-Dependent Calibration

At low radio frequencies (typically in the range of a few hundred MHz), the instrumental response becomes increasingly direction-dependent due to several factors. The primary beam pattern of the antennas varies significantly across the wide field of view, and this response evolves with both frequency and time. Moreover, the Earth’s ionosphere introduces additional time- and direction-dependent distortions such as refractive shifts and phase delays [107]. These spatially varying effects necessitate the use of direction-dependent calibration (DDC).

The core principle behind DDC involves solving for antenna or station gains in multiple directions across the field of view, particularly in the directions of bright off-axis sources. These corrections are essential at low frequencies, where ionospheric disturbances are more pronounced and the field of view is inherently larger.

c) Imaging

Following calibration, the measured visibilities are transformed into sky images to recover the intensity distribution of celestial sources. Since the visibility data are obtained at discrete locations in the uv plane, they can be described by a sampling function $S(u, v)$, which is mathematically expressed as a sum of Kronecker delta functions:

$$S(u, v) = \sum_{k} \delta(u - u_k)\delta(v - v_k) \tag{2.19}$$

where the index k corresponds to a specific baseline measurement.

The observed sky image is obtained via a Fourier inversion of the sampled visibility function:

$$I_{\text{obs}}(l, m) = \iint S(u, v)V(u, v)e^{2\pi i(ul+vm)}\, dudv \tag{2.20}$$

This reconstructed image, $I_{\text{obs}}(l, m)$, is referred to as the *dirty image*. It represents the convolution of the true sky brightness distribution with the instrument’s point spread function (PSF). To recover the intrinsic sky signal, a deconvolution algorithm is applied to the dirty image, effectively mitigating the distortions introduced by the incomplete sampling in the uv plane.

2.6 21-cm Parameter Extraction and Inference

The redshifted 21-cm signal offers a unique probe into the astrophysics of the early Universe, particularly during the CD and EoR. Extracting the underlying physical parameters from this signal requires sophisticated inference techniques that can disentangle the weak cosmological signal from bright astrophysical foregrounds and instrumental systematics.

The primary goal of 21-cm parameter inference is to constrain astrophysical parameters such as:

- the ionizing efficiency of galaxies (ζ),
- the minimum virial temperature or halo mass of star-forming galaxies (T_{vir}),
- the X-ray luminosity per star formation rate ($L_{\mathrm{X}}/\mathrm{SFR}$),
- the mean free path of ionizing photons (R_{mfp}),
- and the spin temperature evolution (T_{s}).

These parameters govern the timing and morphology of reionization and heating and are typically inferred by comparing simulations of the 21-cm signal to observational data. Various methods have been developed to extract these parameters and interpret the 21-cm signal within this context, as detailed below.

2.6.1 Bayesian Inference Methods

Bayesian inference provides a principled probabilistic framework for estimating astrophysical parameters from 21-cm observations, where the data are often noisy and contaminated by foregrounds. The core of Bayesian analysis is Bayes' theorem:

$$P(\theta|D) = \frac{P(D|\theta)P(\theta)}{P(D)}, \tag{2.21}$$

where $P(\theta|D)$ is the posterior probability of the model parameters θ given the data D, $P(D|\theta)$ is the likelihood, $P(\theta)$ is the prior distribution, and $P(D)$ is the evidence.

Bayesian frameworks such as `21CMMC` [108] wrap around fast semi-numerical simulations like `21cmFAST` [5] to infer parameters like the ionizing efficiency ζ, X-ray luminosity, and minimum virial mass. For global signal experiments, Bayesian inference tools such as MCMC and MultiNest are commonly used for parameter estimation. Signal reconstruction techniques often rely on simulation frameworks like `ARES` [109], `21cmFAST` [5], and `SCRIPT` [110] to model and fit the sky-averaged brightness temperature spectrum. For modeling foregrounds, a log-log polynomial function is typically employed due to its flexibility in capturing the smooth spectral behavior of foreground emission. These techniques provide full posterior distributions, allowing for robust uncertainty quantification and model comparison. However, they are computationally intensive due to the requirement of evaluating many simulations.

2.6.2 Hybrid Inference Methods

Hybrid methods combine the efficiency of machine learning (ML) with the statistical rigor of Bayesian inference, offering a powerful framework for parameter estimation in 21-cm cosmology. These approaches typically involve training machine learning models, such as Gaussian Processes or neural networks, to emulate computationally expensive forward simulations or likelihood functions. Once trained, these surrogate models are integrated into Bayesian frameworks (e.g., MCMC or nested sampling) for efficient posterior sampling [111–113].

Traditional parameter estimation techniques (e.g., [114]) often rely on strong assumptions about the form of prior distributions and are typically validated under idealized scenarios. While useful, these methods may not account for real-world complexities like instrumental systematics and non-Gaussian noise. Later efforts (e.g., [115, 116]) adopted broader, less informative priors to recover the global 21-cm signal from synthetic data, still assuming simplified instruments and foregrounds. To address more realistic scenarios, [117] introduced a method using Singular Value Decomposition (SVD) to construct basis functions that model systematics specific to each global signal experiment. These basis vectors allow for better separation of the foregrounds and instrumental modes from the cosmological signal. Similarly, HIBAYES [115] offers a fully Bayesian framework that models the signal as a Gaussian process and foregrounds as a high-order polynomial, enabling joint inference while accounting for model uncertainty.

Recent hybrid methods go a step further by using machine learning to accelerate the inference pipeline. For instance, Bayesian Neural Networks (BNNs) can learn posterior distributions directly from data, enabling rapid inference with uncertainty quantification. These models are especially advantageous in high-dimensional parameter spaces where traditional MCMC methods are computationally prohibitive. Neural networks and GPs have already been applied to 21-cm power spectrum analyses for efficient likelihood evaluations [84, 87, 118, 119]. Complementary to this, Fisher matrix-based forecasting approaches have also been employed to predict constraints on astrophysical parameters, such as the efficiency and spectral properties of high-redshift X-ray sources that heated the IGM [120]. Overall, hybrid inference methods represent a promising and flexible solution to the challenges of parameter estimation in the presence of complex foregrounds, instrumental systematics, and large parameter spaces. By combining the strengths of both simulation-driven statistical modeling and data-driven machine learning, these frameworks are well-suited for next-generation global and interferometric 21-cm experiments.

2.6.3 Machine Learning-Based Inference

Machine learning, particularly deep learning, has become an increasingly powerful tool in 21-cm cosmology for inferring astrophysical parameters directly from observations. These models are capable of learning complex, non-linear relationships and non-Gaussian priors from training data, making them highly effective for many astronomical tasks. Supervised learning techniques, such as regression-based Artificial Neural Networks (ANNs), are useful for predicting specific parameters, while unsupervised approaches can identify anomalies, uncover hidden patterns, or detect outliers in large datasets. These capabilities are particularly valuable in data-driven astronomy, where traditional statistical methods may struggle with scalability or model assumptions. Unlike classical Bayesian techniques such as MCMC, which are computationally intensive and limited by their reliance on specific priors, ML models offer a data-driven alternative. By training on a broad and diverse set of simulated 21-cm data, these models can generalize well to unseen data, allowing for fast and efficient parameter inference across large parameter spaces. Once trained, such models can infer key astrophysical quantities almost instantaneously.

In recent years, Artificial Neural Networks (ANNs) have been effectively employed to extract global 21-cm signal parameters from mock observational datasets, accounting for foreground contamination, instrumental effects under simplified assumptions, and thermal noise [13, 86, 87, 118]. Building on this foundation, the present thesis advances a more robust ANN-based framework that accounts for additional observational complexities, including ionospheric distortions, realistic foregrounds, and thermal noise. Furthermore, we develop an ANN-based emulator to replicate simulated observed power spectra for the SKA-Low AA* telescope layout. This emulator is employed to investigate the impact of gain calibration errors and sky model position uncertainties on the recovery of astrophysical parameters, thereby enabling us to determine acceptable thresholds for these systematics.

Chapter 3

Machine learning Methods

In this chapter, we provide an overview of machine learning approaches, including training strategies and optimization algorithms, which are applied extensively throughout this thesis. The content related to artificial neural networks (ANN) is adapted from the paper "Extracting the Global 21-cm Signal from Cosmic Dawn and Epoch of Reionization in the Presence of Foreground and Ionosphere" [50].

In recent years, diverse strategies have been explored for estimating astrophysical and cosmological parameters from observational data affected by strong foreground contamination. Traditional approaches have often relied on Bayesian inference frameworks, where the effectiveness of parameter recovery depends heavily on the choice and quality of statistical priors, as illustrated by [114]. Progressively, incorporating broader and more informative priors has improved these methods. However, with the increasing complexity and volume of astronomical datasets, machine learning (ML) techniques have emerged as a highly effective alternative due to their flexibility and computational speed. Notably, [118] highlighted the potential of ML models in extracting parameters directly from noisy 21-cm spectra. Building on such developments, the present work utilizes artificial neural networks (ANNs) as described by [86].

In essence, supervised machine learning operates through two core steps: first, the model is trained using input–output pairs from a labeled dataset; second, its predictive ability is assessed by applying it to unseen data, comparing predicted values with true outcomes. Machine learning techniques are now deeply embedded in astrophysical research, supporting applications such as galaxy morphology classification, photometric redshift estimation, pulsar candidate identification, radio interferometric calibration, cosmological parameter inference, and automated data quality assessment in large-scale sky surveys. As next-generation surveys promise to deliver exponentially larger and deeper datasets, machine learning is expected to play a central role in future data analysis pipelines. One particularly valuable application is in direct parameter inference from observational data, offering a more computationally efficient pathway than traditional sampling techniques like Markov Chain Monte Carlo (MCMC). The following sections provide a focused discussion on the structure and implementation of ANNs for this purpose, detailing their suitability for parameter estimation tasks in the context of global 21-cm signal analysis.

3.1 Artificial Neural Network (ANN)

Artificial Neural Networks (ANNs) are computational models inspired by biological neural systems' structural and functional principles. A standard feed-forward ANN architecture comprises three main layers: an input layer, one or more hidden layers, and an output layer. The depth of the network corresponds to the number of hidden layers, while the width is determined by the number of neurons within each layer. In a feed-forward configuration, information flows in a single direction, from the input to the output, without forming cycles. Each neuron in one layer is typically connected to every neuron in the subsequent layer, and these connections are characterized by adjustable weights and biases that are optimized during the training process [121]. A schematic diagram illustrating the feed-forward ANN architecture is presented in Fig. 3.1.

Following the structure outlined in [86, 118], let us consider an input dataset with n features: $x_1, x_2, \ldots, x_n$. Each input feature x_j is passed to the corresponding input neuron, which is connected to the hidden layer neurons with weights $w_{ij}^{(1)}$ and biases b_j^1. The pre-activation input z_i to the i-th hidden neuron is calculated as:

$$z_i = \sum_{j=1}^{n} w_{ij}^{(1)} x_j + b_j^1 \tag{3.1}$$

The output y_i of the hidden neuron is obtained by applying a non-linear activation function $h(\cdot)$ to z_i:

$$y_i = h(z_i) \tag{3.2}$$

The final network output Y_i' is computed as a linear combination of the activated outputs from the hidden layer, with weights $w_{ij}^{(2)}$ and biases b_j^2:

$$Y_i' = \sum_{j=1}^{n} w_{ij}^{(2)} y_j + b_j^2 \tag{3.3}$$

The performance of the network is evaluated by a loss function. For regression tasks, we employ the Mean Squared Error (MSE) as the cost function E, defined over N_t training epochs and N output targets as:

$$E = \frac{1}{N_t} \sum_{n=1}^{N_t} E_n(w, b) = \frac{1}{N_t} \sum_{n=1}^{N_t} \left[\frac{1}{N} \sum_{i=1}^{N} \left(Y_{i,n}' - Y_{i,n} \right)^2 \right] \tag{3.4}$$

Here, $Y_{i,n}'$ denotes the network prediction and $Y_{i,n}$ is the true value for the i-th output of the n-th training sample.

3.1.1 Training Method

The ANN is trained using the backpropagation algorithm in conjunction with gradient descent optimization. Gradient descent is an iterative procedure that aims to minimize the loss function by adjusting the model parameters (weights and biases) in the direction of the negative gradient of the loss. After each forward pass, gradients of the loss function with respect to weights and biases

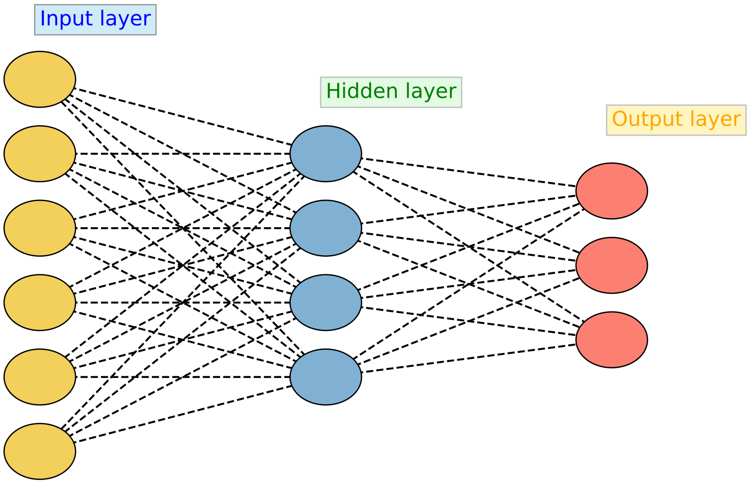

Figure 3.1: Schematic representation of a fully connected feedforward neural network consisting of an input layer (yellow), a hidden layer (blue), and an output layer (red). Each neuron in one layer is connected to every neuron in the subsequent layer, enabling complex function approximation and learning representations.

are computed and used to update the parameters. A schematic illustration of the backpropagation process is shown in Fig. 3.2, and the corresponding mathematical update rules are given below:

$$\Delta w_{ij}^{(l)} = -\eta \frac{\partial E}{\partial w_{ij}^{(l)}} = w_{ij}^{(l)} - \eta \sum_{n=1}^{N_t} \frac{\partial E_n}{\partial w_{ij}^{(l)}} \tag{3.5}$$

$$\Delta b_{ij}^{(l)} = -\eta \frac{\partial E}{\partial b_{ij}^{(l)}} = b_{ij}^{(l)} - \eta \sum_{n=1}^{N_t} \frac{\partial E_n}{\partial b_{ij}^{(l)}} \tag{3.6}$$

Here, $w_{ij}^{(l)}$ and $b_{ij}^{(l)}$ denote the weights and biases at layer l, E_n is the error for the n-th training sample, N_t is the total number of training samples in a batch, and η is the `learning rate`, a hyperparameter that controls the step size at each iteration during the optimization process of a neural network. It governs how significantly the model's weights are updated in response to the computed gradient of the loss function. A high learning rate may lead to faster convergence but carries the risk of overshooting the minimum of the loss surface. In contrast, a low learning rate ensures more stable convergence but can result in slower training or entrapment in local minima. Choosing an appropriate learning rate is crucial for achieving both efficient and effective model training.

Prediction and Validation

Once the ANN model is trained, it can be used to make predictions on previously unseen input data. For each input vector $\mathbf{x} = [x_1, x_2, \ldots, x_n]$, the network computes the forward pass using the trained weights and biases to generate the predicted output $\mathbf{Y}'$. The prediction is computed using the same forward propagation described in Equations 3.1–3.3.

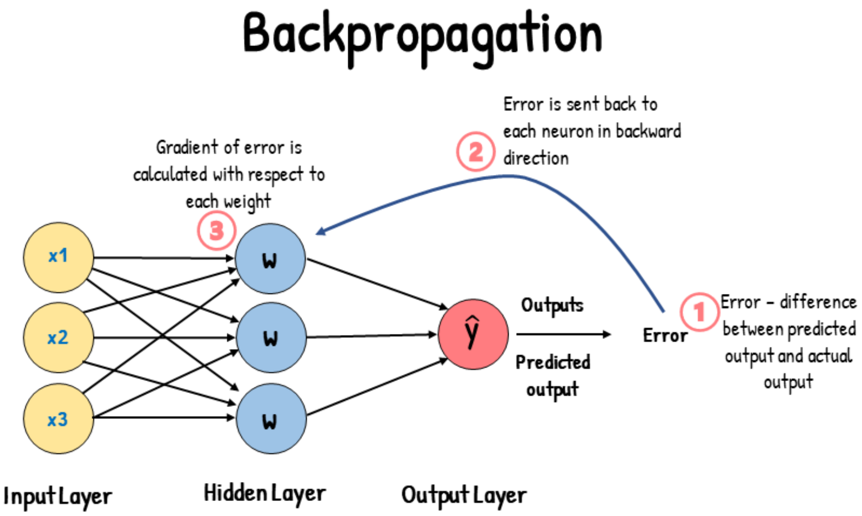

Figure 3.2: Illustration of the backpropagation algorithm in a neural network. The process begins by computing the error between the predicted and actual outputs (Step 1). This error is propagated backward through the network (Step 2), and the gradient of the error is calculated with respect to each weight (Step 3). These gradients are used to update the weights and minimize the overall prediction error during training. This figure is adapted from https://www.analyticsvidhya.com/blog/2023/01/gradient-descent-vs-backpropagation-whats-the-difference/.

To evaluate the generalization ability of the trained model, we validate it on a separate validation dataset that was not used during training. The same cost function, such as Mean Squared Error (MSE), is computed on the validation set:

$$\mathrm{MSE}_{\mathrm{val}} = \frac{1}{N_v} \sum_{n=1}^{N_v} \left[\frac{1}{N} \sum_{i=1}^{N} \left(Y'_{i,n} - Y_{i,n} \right)^2 \right] \tag{3.7}$$

where N_v is the number of validation samples. A low validation error indicates good generalization, whereas a significantly higher validation error compared to the training error may suggest overfitting.

To further assess the performance, additional metrics such as the coefficient of determination (R^2 score), root mean squared error (RMSE), and mean absolute error (MAE) may also be used depending on the specific requirements of the regression task.

3.1.2 Implementation Details

The Artificial Neural Network (ANN) model utilized in this study was implemented in `Python`, leveraging the `Sequential` API provided by the `Keras` library, with `TensorFlow` [1] serving as the computational backend. Additionally, the `scikit-learn` [2] library [122] was employed for data preprocessing, normalization, and model evaluation procedures. The architecture of the ANN, including the number of hidden layers and neurons per layer, was determined empirically through

---

[1] https://www.tensorflow.org/

[2] https://scikit-learn.org/stable/

performance validation on the training and validation datasets. The output layer was configured to have as many neurons as the number of target parameters to be predicted. The selection of activation function, network width, and depth in an ANN can be determined through trial-and-error methods or by utilizing optimization techniques such as `Keras Tuner` [3], `RandomizedSearchCV`, `GridSearchCV`, or `Optuna`. Activation functions introduce non-linearity into neural networks, enabling them to learn complex patterns and approximate non-linear mappings between inputs and outputs. Without activation functions, a neural network composed solely of linear transformations would be limited to modeling only linear relationships, regardless of its depth. By applying non-linear activation functions, such as ReLU (Rectified Linear Unit), sigmoid, ELU (Exponential Linear Unit), or tanh, after each layer, the network gains the capacity to capture intricate features in the data, making them essential for tasks such as classification, regression, and function approximation. A linear activation function is used in the output layer, as is standard practice for regression tasks.

The training of the ANN was performed using the Adam optimizer, which combines the benefits of Adaptive Gradient Algorithm (AdaGrad) and Root Mean Square Propagation (RMSProp) for faster and more stable convergence. The optimizer plays a central role in adjusting the network's weights and biases by minimizing the loss function through gradient-based updates. It directly influences the convergence speed, stability, and generalization capability of the model. Learning rate and other optimizer-specific hyperparameters were carefully tuned to achieve optimal performance. The choice of optimizer can significantly affect the efficiency and accuracy of the training process. A comprehensive description of the final ANN architecture, including the choice of activation functions, number of neurons, hidden layers, training configuration, and selected hyperparameters, is provided in the following chapters.

3.2 Data Preparation and Preprocessing

Adequate data preparation and preprocessing are fundamental to constructing robust, high-performing machine learning (ML) models. Any ML framework's predictive success and generalizability are intrinsically linked to the quality, structure, and scale of the input data. These preparatory steps are designed to ensure that the dataset is cleansed of inconsistencies, properly scaled, and structured in a manner that facilitates efficient learning and improved generalization to unseen data. The preprocessing workflow begins with data cleaning, which involves detecting and addressing missing values, eliminating outliers, and removing redundant or non-informative features. These actions reduce noise and potential biases, enabling the learning algorithm to focus on meaningful patterns within the data.

In this study, we utilize supervised machine learning models, which require the availability of well-labeled training and validation datasets. These datasets are constructed to represent a comprehensive and diverse range of possible 21cm global signal, foregrounds, ionospheric effects, and instrumental systematics. To enable an efficient and representative exploration of the underlying parameter space, we employ three sampling techniques: Random Sampling, Latin Hypercube Sampling [123], and Hammersley Sequence Sampling [124]. A detailed discussion of these methods and their implementation is presented in Chapter 5. Once the dataset is constructed, it is partitioned into **training**, **validation**, and **testing** subsets. Before training, the input features are subjected to preprocessing to enhance the model's ability to learn relevant features and improve convergence. The most widely adopted techniques include Min-Max normalization and standardization, both implemented using Scikit-learn.

---

[3] `https://www.tensorflow.org/`

- **Min-Max normalization** (via `MinMaxScaler`) rescales the data to a fixed range, typically [0, 1], by subtracting the minimum value and dividing by the range of the variable. This method is particularly advantageous when dealing with features expressed in different units or spanning different dynamic ranges.
- **Standardization** (via `StandardScaler`) transforms the input data such that each feature has zero mean and unit variance. This is especially beneficial for algorithms that usually assume distributed input features or are sensitive to the relative magnitudes of feature values.

Throughout this work, the preprocessing pipeline has been refined iteratively. Initially, we employed basic 'MinMaxScaler' and 'StandardScaler' to scale the datasets. Subsequently, a logarithmic transformation was applied to enhance model robustness and better capture subtle signal variations, followed by normalization and standardization. Additionally, the label values were normalized using Min-Max scaling to maintain consistency across all input–output mappings. The data under consideration poses substantial challenges: the cosmological 21-cm signal is exceedingly weak, while foreground emissions are 5 to 6 orders of magnitude stronger. Ionospheric effects further complicate the extraction of the signal by introducing direction-dependent spectral distortions, primarily due to the chromatic response of the instrument's beam. These challenges necessitate careful preprocessing to ensure that the machine learning models can distinguish between the subtle cosmological signal and the dominant foreground and instrumental systematics.

3.3 Evaluation Metrics

To assess the performance of the machine learning models in recovering the global 21-cm signal or its power spectrum, we employ two standard regression metrics: the Root Mean Squared Error (RMSE) and the Coefficient of Determination R^2 score.

3.3.0.1 Root Mean Squared Error (RMSE):

The RMSE measures the average magnitude of the prediction errors. It is defined as:

$$\mathrm{RMSE} = \sqrt{\frac{1}{N}\sum_{i=1}^{N}(Y_i - \hat{Y}_i)^2} \tag{3.8}$$

where Y_i is the true value, $\hat{Y}_i$ is the predicted value, and N is the total number of data points. RMSE is expressed in the same units as the target variable and is sensitive to large deviations.

3.3.0.2 Coefficient of Determination (R^2 Score):

The R^2 score indicates the proportion of variance in the target variable that is explained by the model. It is calculated as:

$$R^2 = 1 - \frac{\sum_{i=1}^{N}(Y_i - \hat{Y}_i)^2}{\sum_{i=1}^{N}(Y_i - \bar{Y})^2} \tag{3.9}$$

where $\bar{Y}$ is the mean of the true values. An R^2 score of 1 signifies an ideal fit between the predicted and actual values, whereas a score of 0 indicates that the model's predictions are no better than simply using the mean of the target data.

These metrics together provide a comprehensive assessment of the regression model's predictive accuracy and generalization capability.

Chapter 4

Extracting the Global 21-cm signal from Cosmic Dawn and Epoch of Reionization in the presence of Foreground and Ionosphere

Adapted from: ***Anshuman Tripahi***, *Abhirup Datta, Madhurima Choudhury, Suman Majumdar “Extracting the Global 21-cm signal from Cosmic Dawn and Epoch of Reionization in the presence of Foreground and Ionosphere, Volume 528, Issue 2, 2024, Pages 1945-1964, 10.1093/mnras/stae078*

Detection of redshifted H I 21-cm emission is a potential probe for investigating the Universe’s first billion years. However, given the significantly brighter foreground, detecting 21-cm is observationally difficult. The Earth’s ionosphere considerably distorts the signal at low frequencies by introducing directional-dependent effects. Here, for the first time, we report the use of Artificial Neural Networks (ANNs) to extract the global 21-cm signal characteristics from the composite all-sky averaged signal, including foreground and ionospheric effects such as refraction, absorption, and thermal emission from the ionosphere’s F and D-layers. We assume a ’perfect’ instrument and neglect instrumental calibration and beam effects. To model the ionospheric effect, we considered the static and time-varying ionospheric conditions for the mid-latitude region where LOFAR is situated. In this work, we trained the ANN model for various situations using a synthetic set of the global 21-cm signals created by altering its parameter space based on the ”tanh” parametrized model and the Accelerated Reionization Era Simulations (ARES) algorithm. The obtained result shows that the ANN model can extract the global signal parameters with an accuracy of $\geq 96\%$ in the final study when we include foreground and ionospheric effects. On the other hand, a similar ANN model can extract the signal parameters from the final prediction data set with an accuracy ranging from 97% to 98% when considering more realistic sets of the global 21-cm signals based on physical models.

4.1 Introduction

The period from the beginning of star and galaxy formation [Cosmic Dawn (CD)] till the change of the state of the Universe from an absolutely neutral to a fully ionized state, i.e., the Epoch of

Reionization (EoR), is still observationally unexplored to astronomers. Detection of the redshifted H I 21-cm line is noticed as one of the most promising future probes of the Universe at these redshifts (z$\approx 7-30$) [125, 126]. The redshifted H I 21-cm lines are formed due to hyperfine splitting of the 1S ground state. Studying these epochs can answer many essential cosmological queries, such as the features of the early galaxies, the physics of mini-quasars, the development of very metal-poor stars, and other major research topics on the origin and evolution of the Universe. The primary science goal of upcoming radio telescopes like the SKA is to study these three extended epochs of the universe's structure formation history. In past decades, significant progress has been made in the theoretical modelling of the expected redshifted 21-cm signal. There are two different experimental techniques for observing these signals in the observational field. [126–128]:
(a) using several dishes and huge interferometric arrays at very low radio frequencies to obtain statistical power spectra of the H I 21-cm variations, for example, Giant Meterwave Radio Telescope (GMRT [44]), Hydrogen Epoch of Reionization Array (HERA [47]), Low Frequency Array (LOFAR[63]), Murchison Wide-field Array (MWA [46]), Square Kilometer Array(SKA [64]), etc.
(b) using a single radiometer to observe the sky-averaged signature of the redshifted H I 21-cm line, for example, Broadband Instrument for global Hydrogen Reionization Signal (BIGHORN [129]), Large-Aperture Experiment to Detect the Dark Ages (LEDA [43]), Experiment to Detect the global EoR Signature (EDGES [61]), Shaped Antenna measurement of the background Radio Spectrum (SARAS [116, 130]),etc.

Recently, the EDGES team announced a probable discovery of the Cosmic Dawn's sky-averaged H I 21-cm global signal. They observed that the measured signal had an absorption trough double the magnitude expected by the standard cosmological model [61]. However, this supposed detection has been challenged by another independent experiment SARAS [62]. This contradiction in independent detection of the global 21-cm signal from ground-based observation further highlights its challenges. One of the reason why this signal is very difficult to detect is because it is very faint. The signal is embedded behind a sea of dazzling galactic as well as extragalactic foregrounds. The magnitude of the foregrounds is several orders brighter than the signal, approximately 10^4 to 10^6 order brighter than the signal. Furthermore, human-made radio frequency interference (RFI), mainly by the FM band and Earth's ionosphere, will also affect ground-based observation. The ionosphere distorts the lower frequency signal significantly when it passes through the ionosphere.

The ionosphere is the uppermost layer of the atmosphere, extending from ~ 50 to ~ 600 km above the Earth's surface. The impacts of solar activity significantly affect the electron density in the ionosphere. The ionospheric existence causes three significant effects in detecting the redshifted global 21-cm signal from the ground-based antenna. All radio waves, including galactic and extragalactic foregrounds, are refracted by the ionosphere, which also attenuates any trans-ionospheric signal and emits thermal radiation [131, 132]. Further, due to solar activation of the ionosphere, these effects are fundamentally time variable [133, 134]. These ionospheric effects scale as ν^{-2}, where ν represents the frequency of observations. Hence, as the observing frequencies get lower, the effect of the ionosphere increases more. It demonstrates that when detecting the signal from the Cosmic Dawn and the Dark Ages ($z \geq 15$), ionospheric effects will have a stronger influence on global signals than when detecting the signal from the Epoch of Reionization ($15 \geq z \geq 6$) [92].

The effects of static ionosphere refraction and absorption for ground-based observation between 30 and 100 MHz were previously examined by [93]. In [92], they presented the dynamic ionosphere effects like refraction, absorption, and thermal emission. They also demonstrated how these combined effects affect the global 21-cm signal from Epoch Reionization and Cosmic Dawn when we are observing from the ground. [12, 94] recently investigated the chromatic ionospheric effects on global 21-cm data by modelling the two principal ionospheric layers, the F and D layers, with a reduced spatial model with temporal variance. The investigation focuses on the chromatic distortions induced by the ionosphere.

Several studies have been done in recent years based on machine learning (ML) techniques to perform signal parameter estimation or signal modelling. [118] and [135] have employed machine learning techniques to predict 21-cm power spectrum parameters. Similarly, [136] extends the ANN to extract the 21-cm PS and corresponding EoR parameters from synthetic observations for different telescope models. [111] used Artificial Neural Network (ANN) to emulate the 21-cm power spectrum for a wide range of parameters. Similarly, [113] have developed an ANN-based emulator for the signal bispectrum, which they have further used to estimate signal parameters via a Bayesian inference pipeline. The global 21-cm signal from Cosmic Dawn and EoR has also been emulated using ANN by [137–139]. Convolutional Neural Networks (CNN) have been utilized to identify reionization sources from 21-cm maps [140]. [141] and [142] have used deep learning models to emulate 21-cm maps from the dark matter distribution directly. [143] used deep learning with CNN to predict astrophysical parameters directly from 21-cm maps. [144] used CNN to estimate parameters and infer posteriors on 3D-tomographic 21-cm images. An ANN model that can extract astrophysical parameters of 21 cm from mock observation data sets, including the effects of foregrounds, instruments, and noise, has been successfully developed and presented by [13,86]. The relevance of non-parametric techniques for this purpose has already been demonstrated in several previous studies [81, 117]. These studies have shown that using a simple parametric technique for signal and foreground subtraction can result in over-subtraction, leading to the loss of the signal.

In this paper, we use ANNs to extract the global 21-cm signal parameters along with foreground and ionospheric parameters from the composite all-sky averaged signal, containing foreground and ionospheric effects. This study considers perfect instrument conditions, representing an ideal scenario in which the instrument is assumed not to modify the signal. In the first case of study, we follow the tanh parametrized model and Accelerated Reionization Era Simulations (ARES) code [145] to construct the cosmological signal. We use the $\log(\mathrm{T}) - \log(\nu)$ polynomial model to map the bright, dominant foregrounds. According to [146], a 3rd or 4th-order polynomial is sufficient to map the sky's spectrum. In contrast, [147] demonstrated that when adding the antenna's principal chromatic beam, a 7th-order polynomial is required. We followed [92] to add the ionospheric effect into the simulated signal and foreground. In this, we consider mainly three effects induced as a resultant: refraction, absorption, and thermal emission, and all these are directly proportional to the electron density (TEC) and temperature of the electrons at various layers of the Ionosphere ($\mathrm{T_e}$). These ionospheric effects introduce two more parameters into our training data sets. To check and validate the robustness and reliability of the developed model, we have considered a minute variation to the parameters TEC and $\mathrm{T_e}$ to generate our final training data set. To further check and validate the ANN model's robustness, we use a more realistic set of global 21-cm signals presented in [13] instead of parametrized global 21-cm signals. This global 21-cm signal data has different parameters than the tanh parametrized global signal. In section 4.2 of this paper, we briefly review about 21-cm signal. Section 4.3 mentions the details about the foreground model that we used to map the galactic and extragalactic sources. Section 4.4 discusses the ionospheric effects and their impacts on the global 21-cm signal observation. We briefly discuss the ANN overview and matrices we used to evaluate the performance of our ANN model in section 4.5. Section 4.6 describes the methodology and procedures to simulate the global 21-cm signal, foreground, and ionospheric effects for training and testing the ANN model. We present the results obtained by our model for all the cases in section 4.7. In the last section, we summarize our work and discuss the implications of our predictions.

4.2 global 21-cm Signal

The 21-cm line of the neutral hydrogen is formed as a result of the hyperfine splitting of the 1S ground state caused by the interchange of the magnetic moments of the proton and electron. The quantity we can measure is known as "differential brightness temperature", $\delta \mathrm{T_b}$. We measure this quantity relative to Cosmic Microwave Background (CMB) followed by [56]:

$$\delta T_b \equiv T_b - T_\gamma \tag{4.1}$$

$$\begin{aligned}\delta T_b =& \frac{T_S - T_R}{1+z}(1-e^{-\tau_\nu}) \\ &\approx 27 x_{H\,i}(1+\delta_b)\left(\frac{\Omega_b h^2}{0.023}\right)\left(\frac{0.15}{\Omega_{m,0}h^2}\frac{1+z}{10}\right)^{\frac{1}{2}} \\ &\left(1-\frac{T_\gamma(z)}{T_s}\right)\left[\frac{\partial_r \nu_r}{(1+z)H(z)}\right]^{-1} mK,\end{aligned} \tag{4.2}$$

where $\mathrm{x_{H\,i}}$ is the hydrogen neutral fraction, δ_b represents the fractional over-density in baryons, Ω_m and Ω_b signify total matter density and baryon density, respectively, H(z) is the Hubble parameter, $\mathrm{T_\gamma}$(z) denotes CMB temperature at redshift z, and $\mathrm{T_s}$ is spin temperature, and $\partial_r \nu_r$ is the velocity gradient along the line of sight.

The 21-cm global signal is a sky averaged signal that offers information on global cosmic occurrences. It can tell us about the story of the thermal history of ionizing radiation like UV radiation which interrupts neutral hydrogen, X-rays that heat the gas and elevate $\mathrm{T_k}$, and Ly_α, which is accountable for the Wouthuysen-Field coupling [148]. In the study, the peculiar velocity and density fluctuation components in the global signal (Eqn. 4.2) are neglected since they average out to a linear order and amount to a minor correction. As a result, the density, neutral fraction, and spin temperature all affect the form of the global signal [149].

$$\delta T_b \approx 27(1-x_i)\left(\frac{\Omega_b h^2}{0.023}\right)\left(\frac{0.15}{\Omega_{m,0}h^2}\frac{1+z}{10}\right)^{\frac{1}{2}}\left(1-\frac{T_\gamma(z)}{T_s}\right) \tag{4.3}$$

To construct the global signal, we primarily use this equation (4.3).

The spin temperature influences the detectability of the 21-cm signal. Three main quantities determine spin temperature: (i) absorption/emission of 21-cm photons by CMB radiation; (ii) collisions with other hydrogen atoms, free electrons, and protons; (iii) scattering of $\mathrm{L_y}\alpha$ photons that cause a spin-flip through intermediate excitation. In this given limit, the spin temperature sky-average defined as [53]:

$$T_s = \frac{T_\gamma + y_\alpha T_\alpha + y_c T_K}{1 + y_\alpha + y_c}, \tag{4.4}$$

where $\mathrm{T_\gamma}$ is the temperature of radio background, primarily CMB, $\mathrm{T_\alpha}$ is the color temperature of ambient Lyman-alpha photons, and $\mathrm{T_K}$ is kinetic gas temperature. $\mathrm{y_\alpha}$, $\mathrm{y_k}$ represents the coupling coefficient, which arises due to atomic collision and Lyman-alpha scattering.

4.3 Foreground

The bright foregrounds, mostly caused by galactic and extragalactic sources, are the greatest observational obstacle in observing the global 21-cm signal for studying the CD-EoR. The radio emission from galactic and extragalactic sources is substantially brighter than the global 21-cm signal. We used a very basic model termed log polynomial ($\log(\mathrm{T}) - \log(\nu)$) to map the foreground, which is based on [126, 147]. In our study, we constrain our foreground model to a 3rd order polynomial in $\log(\mathrm{T}) - \log(\nu)$, followed by [86, 146] which depicts diffuse foregrounds:

$$\ln T_{FG} = \sum_{i=0}^{n=3} a_i \left[\ln(\nu/\nu_0)\right]^i, \tag{4.5}$$

where $\mathrm{a_0, a_1, a_2, ..., a_n}$ denote foreground model parameters and ν_0 is arbitrary reference frequency. In this study, the derived value of the foreground parameters $(\mathrm{a_0, a_1, a_2, a_3}) =$ (3.3094, -2.42096, -0.08062, 0.02898) are taken from [150, 151] and reference frequency taken around $\nu_0 = 80$ MHz followed by [86]. We varied these foreground parameters to construct the different realization of foregrounds (see in the Tab (4.3)).

4.4 Ionospheric Effects

The ionosphere is a region of the Earth's atmosphere that has a high concentration of electrically charged atoms and molecules. The Sun is one of the most powerful energy sources in the Solar System. Its intense Ultraviolet (UV) and X-ray radiation interact with the Earth's atmosphere to create the ionosphere through photo-ionization. The electron density and temperature change significantly depending on the type of solar fluctuations. Any electromagnetic signal travelling through an optically thin medium, such as the ionosphere, obeys the radiative transfer equation. To understand these effects, the ionosphere is divided into various layers, such as D-layers ($60 - 90$ km), E-layers, and a composite F-layer ($160 - 600$ km) [92].

4.4.1 F-layer refraction

The F-layer of the ionosphere, located between ~ 200 to ~ 400 km above the Earth's surface, accounts for most of the ionospheric electron column density. Outside of this layer, the electron density is very low compared to the inside. Although the electron density varies within the F-layer, we consider it a homogenous shell 200 to 400 km in height and assuming a constant electron density of $\sim 5 \times 10^{11}$ electrons/m^3 which resulting column density of 10 TEC units [92, 93]. Due to density differences between the layers, any incoming beam experiences Snell's refraction at the boundaries of the F-layer. The ionosphere's refraction acts like a spherical lens, deflecting incoming light towards the zenith [92, 93]. As a result of this refraction, any radio antenna located on the ground captures the signal from a wider area of the sky, resulting in a higher antenna temperature.

The angular deviation experienced by any incoming ray with angle θ to the horizon in the parabolic layer, which is surrounded by free space with refractive index $\eta = 1$, can be calculated as follows [92, 93, 152] :

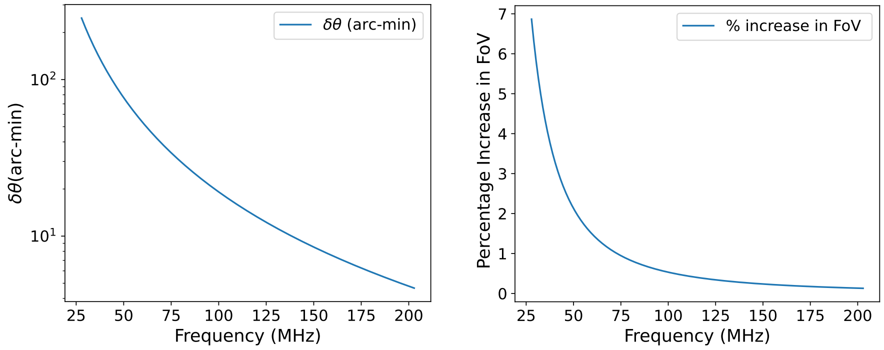

(a) (b)

Figure 4.1: (a) The deviation angle $\delta\theta$ is plotted as a function of frequency for a typical mid-latitude daytime TEC value (TEC = 10 TECU). (b) The percentage increase in the field of view as a function of frequency for the same TEC value.

$$\begin{aligned}\delta\theta(\nu,t)= &\frac{2d}{3R_E}\left(\frac{\nu_p(t)}{\nu}\right)^2\left(1+\frac{h_m}{R_E}\right)\\ &\times\left(sin^2\theta+\frac{2h_m}{R_E}\right)^{-3/2}cos\theta,\end{aligned} \tag{4.6}$$

where $\mathrm{R_E}$ = 6378 km is the Earth's radius, h represents the altitude, $\mathrm{h_m}$ represents the altitude where the electron density is maximum in the F-layer, which is $\mathrm{h_m}$ = 300 km, and d represents the change in altitude with respect to $\mathrm{h_m}$ where the electron density is zero, which is 200 km in our simulation and ν_p is the plasma frequency [153].

As seen from equation (4.6), the ionospheric refraction is proportional to ν^2, with the greatest deviation happening for the horizon ray, which has an incidence angle of 0. As a result of this ionospheric refraction, the field of view at a particular observation frequency will be larger than the primary beam of the antenna. The ionospheric refraction's impact on the angular deviation, as shown in Fig. (4.1a) and increase in the field of view (FoV) is calculated and plotted across the frequency (ν), as shown in Fig. (4.1b). The resultant antenna temperature, which includes ionospheric refraction, as described by [93].

$$\begin{aligned}T^{iono}_{sky}(\nu,TEC(t),\Theta_0,\Phi_0)= &\int_0^{2\pi}d\Phi\\ &\times\int_0^{\pi/2}d\Theta B'(\nu,t;\Theta-\Theta_0-\delta\theta(t),\Phi)\\ &\times T_{sky}(\nu,t;\Theta_0,\Phi_0)sin\Theta,\end{aligned} \tag{4.7}$$

where $\mathrm{T^{iono}_{sky}}$ refers to the antenna temperature that considers ionospheric refraction, (Θ_0, Φ_0) is the pointing centre. $\mathrm{B'(\nu,t;\Theta-\Theta_0-\delta\theta(t),\Phi)}$ describes a modified field of view caused by the ionosphere's refractive effect, and $\mathrm{T_{sky}(\nu,\Theta,\Phi)}$ denotes actual sky temperature which includes signal and foreground.

4.4.2 D-layer absorption and thermal emission

The D-layer is the lowest layer of the ionosphere, extending from ~ 60 to ~ 90 km above the Earth's surface [93]. Due to solar insolation, high electron concentrations in the D-layer are projected to last only during the daytime. At night-time, residual electron concentrations are mostly found of the order of $\sim 10^8$ electron/m^3.

The high concentration of atmospheric gas in the D-layer at these heights results in significant electron collision frequencies, which cause radio wave attenuation ([133]; [134]). The absorption by the D-layer can be expressed follows [92, 133]:

$$L_{dB}(\nu, TEC_D) = 10 * log_{10}\left(1 + \tau(\nu, TEC_D)\right) \tag{4.8}$$

where $\mathrm{TEC_D}$ signifies the D-electron layer's column density and τ indicates the optical depth.

The D-layer is also responsible for thermal emission [92, 131, 132, 154], which is included as a $\tau(\nu, \mathrm{TEC(t)}) < \mathrm{T_e} >$ into the final term [see in Eq. (4.9)]. The terms $\tau(\nu, TEC(t))$ represents optical depth for the corresponding ionosphere, and $<\mathrm{Te}>$ is average electron temperature, which causes thermal radiation. In our simulations, we consider mid-latitude ionosphere, and we take D-layer electron temperature $\mathrm{T_e} = 800$ K [155]. We have calculated the attenuation factor and thermal emission for the corresponding mid-latitude ionosphere and plotted them against the frequency (ν), shown in Fig.(4.2a) and Fig.(4.2b). In the plot, we see that as we go lower in frequency (ν), this attenuation factor and thermal emission increase compared to the higher frequency (ν).

Finally, the brightness temperature of the radio signal recorded by the ground-based radio antenna in the presence of all three ionospheric effects is defined as [92]:

$$\begin{aligned} T^{iono}_{Ant}(\nu, TEC(t), \Theta_0, \Phi_0) = {} & T^{iono}_{sky}(\nu, t; \Theta_0, \Phi_0) \\ & \times (1 - \tau(\nu, TEC(t)) \\ & + \tau(\nu, TEC(t)) * < T_e >, \end{aligned} \tag{4.9}$$

where $\mathrm{T^{iono}_{Ant}}$ is the effective brightness temperature captured by any ground-based antenna, $\mathrm{T^{iono}_{sky}}$ denotes the changed sky brightness temperature as a result of ionospheric refraction, and (Θ_0, Φ_0) are pointing center.

4.5 Basic Overview of Artificial Neural Network

An ANN is a computational algorithm inspired by human biological neural networks. A basic architectural neural network is made up of three primary layers: an input layer, a hidden layer, and an output layer. The number of hidden layers defining its depth and the number of neurons in those layers determines the network width. In a feed-forward network, each neuron in a layer is coupled to every neuron in the next layer, and the information flow is unidirectional. The connections between neurons are associated with weights and biases [121].

To describe the detailed structure of the ANN architecture, we followed [86, 118]. We considered that there is an n input training data set $(\mathrm{x_1, x_2 ....., x_n})$. Each input data set is fed by particular neurons in the input layer. For example, the input data $\mathrm{x_j}$ is provided to the jth neurons in the input layer, which is further connected to the next layer neurons (hidden layer) with associated a

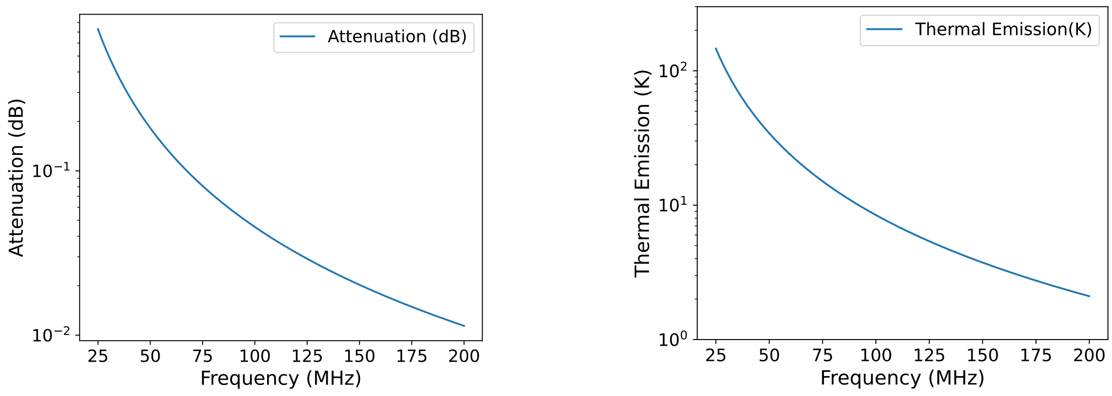

(a) (b)

Figure 4.2: (a) For the TEC value (TEC= 10 TECU), attenuation is plotted as a function of frequency in the solid line. (b) The variation in thermal emission from the ionosphere is also depicted in the solid line.

weight $\mathrm{w}_{\mathrm{ij}}^{(1)}$ and a bias $\mathrm{b}_{\mathrm{j}}^{1}$. In general, this can be described as:

$$z_i = \sum_{j=1}^{n} w_{ij}^{(1)} x_j + b_j^1 \tag{4.10}$$

In the hidden layer, the output from Eqn. (4.10) is further activated by a non-linear activation function h, such that $\mathrm{y_i} = \mathrm{h(z_i)}$. The final output $\mathrm{Y}_{\mathrm{i}}^{'}$ which is the linear combinations of the activated outputs of the neurons in the hidden layer with weights $\mathrm{w}_{\mathrm{ij}}^{(2)}$ and biases $\mathrm{b}_{\mathrm{j}}^{2}$ can be described as [118]:

$$Y_i^{'} = \sum_{j=1}^{n} w_{ij}^{(2)} y_j + b_j^2 \tag{4.11}$$

After each forward pass, a cost or error function is computed at the output layer. This cost function is optimized during training by back-propagating errors iteratively. We can define the total loss (cost) function of the network as follows:

$$\begin{aligned} E =& \frac{1}{N_t}\sum_{n=1}^{N_t} E_n(w,b) \\ =& \frac{1}{N_t}\sum_{n=1}^{N_t}\left[\frac{1}{N}\sum_{n=1}^{N}\left(Y_{(i,n)}^{'} - Y_{(i,n)}\right)^2\right], \end{aligned} \tag{4.12}$$

where $\mathrm{N_t}$ represents the number of training epochs, N represents the number of output data elements, $\mathrm{Y}^{'}$ denotes prediction by the ANN, and Y denotes the actual output feature. These weights (w) and the biases (b) are updated at the end of each training epoch by using methods called gradient descent in the following manners described below:

$$\begin{aligned}\Delta w_{ij}^{l} &= w_{0ij}^{l} - \eta\frac{\partial E}{\partial w_{ij}^{l}} = w_{0ij}^{l} - \eta\sum_{n=1}^{N_{train}}\frac{\partial E_n}{\partial w_{(ij)}^{l}} \\ \Delta b_{ij}^{l} &= b_{0ij}^{l} - \eta\frac{\partial E}{\partial b_{ij}^{l}} = b_{0ij}^{l} - \eta\sum_{n=1}^{N_{train}}\frac{\partial E_n}{\partial b_{(ij)}^{l}},\end{aligned} \tag{4.13}$$

where w_{0ij}^{l} and b_{0ij}^{l} represent the initial weights and bias, respectively, and η is the learning rate. We employed Python and the Sequential Model from the Keras API in our feed-forward network. To develop our network, we utilized standard sci-kit learn [122] and Keras modules. We pick the number of hidden layers and number of neurons such that we can get optimum network performance. The number of neurons in the output layer is the same as the number of output parameters we want to predict. The ANNs architecture employed in our study is discussed in detail in the following sections.

4.5.1 R^2 and RMSE Scores

We choose R^2 and root mean square error (RMSE) scores as a metric to evaluate network performance. The coefficient of R^2 and RMSE is obtained for each parameter from the test set of the predictions. The R^2 scores is defined as:

$$R^2 = \frac{\sum(y_{pred} - \bar{y}_{orig})^2}{\sum(y_{orig} - \bar{y}_{orig})^2} = 1 - \frac{\sum(y_{pred} - y_{orig})^2}{\sum(y_{orig} - \bar{y}_{orig})^2}, \tag{4.14}$$

where $\bar{y}_{orig}$ is the average of the original parameter, the sum is that the score $\mathrm{R}^2 = 1$ denotes a flawless inference of the parameters across the whole test set, whereas R^2 might range between 0 and 1.

We have followed [118] to calculate the normalized RMSE score for prediction :

$$RMSE = \sqrt{\frac{1}{N_{pred}}\sum_{i=1}^{N_{pred}}\left(\frac{y_{orig} - y_{pred}}{y_{orig}}\right)^2}, \tag{4.15}$$

where $\mathrm{N}_{\mathrm{pred}}$ represents the total number of samples in prediction data sets, a lower RMSE value suggests that the parameter prediction is more accurate.

4.6 Building Of Training and Test Data Sets

We follow the steps below to construct the data sets for all the different realizations to combine them to build the final training data sets. We created 360 sets of data sets for all the different realizations for both types of signals, parametrized and physical. These data sets are created using each parameter value sampled randomly and uniformly from the given parameter range by the following Tab.(4.1), Tab.(4.2) and Tab.(4.3). We further split these constructed data sets into three chunks for training, validation and testing of the model. In the test set, we add additional thermal noise for the corresponding observational hour by following the radiometer equation details described in the section (4.6.4).

4.6.1 Simulation methods for the global 21-cm signal

Case 1: parametrized model

In the first case study, we used the tanh parameterization model to replicate the global 21-cm signal across the redshift range $6 < z < 40$ suggested by [109]. This approach utilizes rudimentary tanh functions to describe the Lyα background, IGM temperature (T), and ionization percentage ($\bar{\mathrm{X}}$) , where Lyα background defines the amount of the Wouthuysen-Field coupling [146]. Each quantity is allowed to grow as a tanh function [109] by following given Eq.(4.16):

$$P(z) = \frac{P_{ref}}{2}\left(1 + tanh\frac{(z_0 - z)}{\Delta z}\right), \tag{4.16}$$

where P(z) denotes the tanh model's primary parameter. $\mathrm{P_{ref}}$ is step height, $\mathrm{z_0}$ is pivot redshift, and Δz indicates duration. These are free parameters, and their characteristics are directly linked to IGM features but not to source attributes. That is why this model behaves like an intermediate model, which lies between the physical models and phenomenological models like cubic spline [102] or Gaussian [115,147] models. Now we evolve the model parameters J_α(z) (Lyα background), T(z) (IGM temperature), and $\bar{\mathrm{X}}_\mathrm{i}$ (ionization fraction) as tanh function by plugging these parameters into Eqn.(4.16), the details are shown below:

$$\begin{aligned} J_\alpha(z) &= \frac{J_{ref}}{2}\left(1 + tanh\frac{(J_{z0} - z)}{J_{dz}}\right)\\ \bar{X}_i(z) &= \frac{X_{ref}}{2}\left(1 + tanh\frac{(X_{z0} - z)}{X_{dz}}\right)\\ T(z) &= \frac{T_{ref}}{2}\left(1 + tanh\frac{(T_{z0} - z)}{T_{dz}}\right), \end{aligned} \tag{4.17}$$

where $\mathrm{J_{ref}}$ represents Lyα flux (in order of 10^{-21} erg $\mathrm{s^{-1}}$ $\mathrm{cm^{-2}Hz^{-1}sr^{-1}}$), $\mathrm{J_{dz}}$ and $\mathrm{J_{z0}}$ both represents Lyα background for corresponding redshift interval Δz and for the central redshift $\mathrm{z_0}$ respectively, $\mathrm{T_{dz}}$ and $\mathrm{T_{z0}}$ are X-ray heating term for the interval Δz and for the central redshift $\mathrm{z_0}$ respectively, and $\mathrm{T_{ref}}$ denote step height corresponding T(z) parameter, which is fixed at 1000 K. The exact height of the step is not essential because the signal is saturated with low redshifts. $\mathrm{X_{ref}}$ represents the step height corresponding to the ionization percentage, and Δz and $\mathrm{z_0}$ are represented by $\mathrm{X_{dz}}$ and $\mathrm{X_{z0}}$. Finally, we have seven signal parameters along with two fixed parameters ($\mathrm{X_{ref}} = 1.0$, $\mathrm{T_{ref}} = 1000$ K) to simulate the global 21-cm signal using the tanh parametrization [86]. To generate a simulated 21-cm global signal, we use ARES to determine the coupling coefficient and enter the parameter values into Eq.(4.2). We named this simulated signal as a parametrized global 21-cm signal. The derived value of the parameters is taken from [146] : $\mathrm{J_{ref}} = 11.69$, $\mathrm{J_{dz}} = 3.31$, $\mathrm{J_{z0}} = 18.54$, $\mathrm{X_{z0}} = 8.68$, $\mathrm{X_{dz}} = 2.83$, $\mathrm{T_{z0}} = 9.77$, $\mathrm{T_{dz}} = 2.82$. To produce our training sets, we modified these values by 50% [see Tab. 4.1]. The number of parameters explored is sufficient to cover a wide spectrum of signal morphologies. Figure (4.3a) depicts a typical collection of created signals that we will employ. The idea behind the chosen tanh model was that it can very well mimic the shape of the Global 21-cm signal and is very well tied to the physical characteristics of the IGM. The tanh parameters are closely related to the IGM characteristics, although they do not provide knowledge about the source properties. As a result, it lies between the phenomenological turning point model and other fully physical theories.

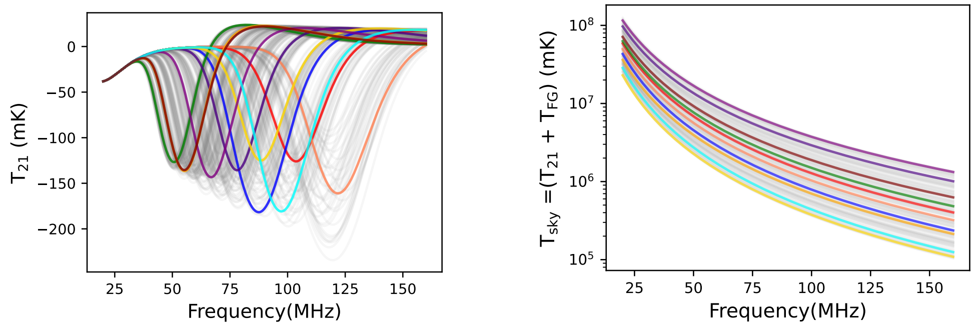

(a) Global 21cm Signals.

(b) Global 21cm signals with added foreground.

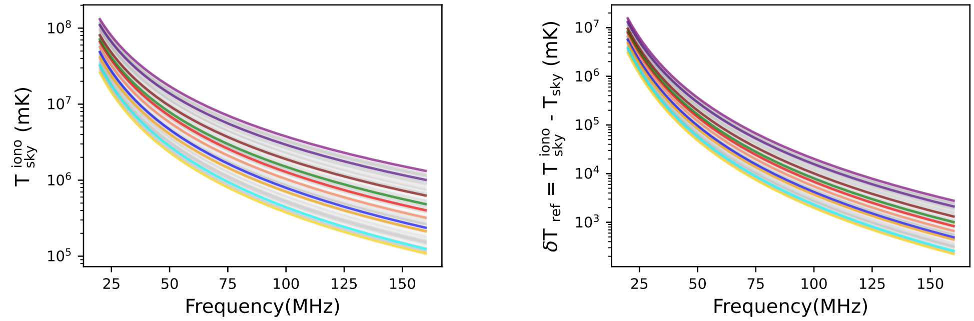

(c) Global 21cm signals and foreground with ionospheric refraction.

(d) Excess temperature cause by ionospheric refraction.

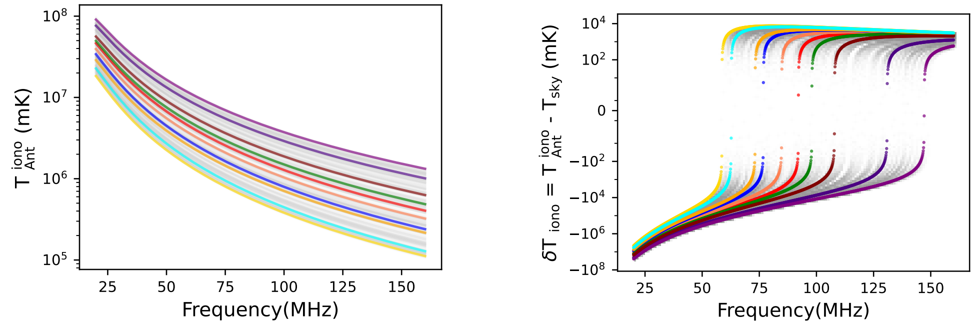

(e) Global 21cm signals and foreground with all three ionospheric effects.

(f) Contribution of all three ionospheric effects.

Figure 4.3: (a) Simulated global 21-cm training data generated by varying signal parameters. (b) Foregrounds added, showing their dominance over the signal. (c) Inclusion of ionospheric refraction for fixed TEC = 10 TECU. (d) Excess antenna temperature due to refraction. (e) Combined ionospheric effects, refraction, absorption, and thermal emission, for varying TEC and T_e. (f) Total ionospheric contribution. Colored curves represent sample training sets; light gray shows the full distribution.

Case 1 (Parametrized)	
Parameter	**Range**
Lyα flux ($\mathrm{J_{ref}}$)	5.85–17.54
Lyα background at z_0 ($\mathrm{J_{z0}}$)	9.27–27.81
Ionization step at z_0 ($\mathrm{X_{z0}}$)	4.34–13.02
X-ray heating term at z_0 ($\mathrm{T_{z0}}$)	4.89–14.65
Lyα background at Δz ($\mathrm{J_{dz}}$)	1.65–4.96
X-ray heating at Δz ($\mathrm{T_{dz}}$)	1.41–4.23
Ionization step at Δz ($\mathrm{X_{dz}}$)	1.42–4.25

Table 4.1: Parameter ranges used to build the training dataset for the parametrized case of global 21-cm signals.

Case 2: Physical Model

In the second case study, we used the similar data set as a training data set for the signal that was earlier used in [13] to construct the training data set for the global 21-cm signals. They used different physical models based on a semi-numerical algorithm to produce various realizations of the global 21-cm signals across the redshift range $6 < z < 50$. The calculation that had been used in the signal construction closely follows [156] and [126], and the parameters given as input to the model are the following astrophysical parameters:

- ionizing photons escape fraction $\mathrm{f_{esc}}$,
- X-ray heating efficiency $\mathrm{f_{xh}}$,
- star formation efficiency $\mathrm{f_\star}$,
- radio background efficiency parameter, $\mathrm{f_R}$,
- number of Lyman-alpha photons produced per baryon in the interested frequency range, $\mathrm{N_\alpha}$,

They vary these astrophysical parameters in the given range, shown in Tab. (4.2), to construct the training data set for global 21-cm shown in figure(4.4 a), the detailed calculation and process described in [13, 157]. [13] mentioned that the parameters $\mathrm{f_x}$ and $\mathrm{f_{xh}}$ are highly correlated, so in our case study, we combine these two parameters and take them as a single parameter so that we can improve network performance. In their study, they used two different kinds of global signals the first one when there is no excess radio background $\mathrm{f_R} = 0$ traditional set of signals, and another case when the excess background is present $\mathrm{f_R}$ non zero, exotic set of signals. For this study, we have considered the traditional set of the global 21-cm signals for constructing the training data sets.

4.6.2 Simulation of foreground

To add foreground into the global 21-cm signal in both cases parametrized and physical, we follow the $\log(\mathrm{T}) - \log(\nu)$ polynomial model described in Section 4.3. We simulated foreground by varying its parameters $(\mathrm{a_0, a_1, a_2, a_3})$ with $(\pm 15\%, \pm 10\%, \pm 1\%, \pm 1\%)$ respectively from its original given value to build the training data for all the scenarios, for more details [see Tab. 4.3]. Each sample in the training data set (see Fig.4.3b) is given by :

Case 2 (Physical)	
Parameter	**Range**
Normalization factor ($\mathrm{f_x}$) · X-ray heating efficiency ($\mathrm{f_{xh}}$)	0.0255–7.9800
Radio background efficiency ($\mathrm{f_R}$), Traditional	0
Radio background efficiency ($\mathrm{f_R}$), Exotic	1800–2000
Star formation efficiency ($\mathrm{f_{star}}$)	0.0030–0.0099
Ionizing photon escape fraction ($\mathrm{f_{esc}}$)	0.06–0.19
Lyman-alpha photon number (N_α)	9000–800000

Table 4.2: Parameter ranges used to construct the training dataset of global 21-cm signals for the physical case [13].

$$T_{sky}(\nu) = T_{21,parametrized}(\nu) + T_{FG}(\nu), \tag{4.18}$$

where $\mathrm{T_{sky}}(\nu)$ is the total sky temperature without including ionospheric effects, $\mathrm{T_{21,parametrized}}(\nu)$ is the global 21-cm signal temperature constructed using the parametrized model, $\mathrm{T_{FG}}(\nu)$ foreground temperature constructed using the log-log polynomial model. For the second case, each sample in the training data set (see Fig.4.4b) can be defined as:

$$T_{sky}(\nu) = T_{21,Physical}(\nu) + T_{FG}(\nu), \tag{4.19}$$

where $\mathrm{T_{21,Physical}}(\nu)$ represents the global 21-cm signal temperature constructed using a semi-numerical physical model.

4.6.3 Simulation of ionospheric effects

To simulate the ionospheric effect, we chose two different scenarios. In the first scenario, we have added only the ionospheric refraction effect for the corresponding fixed TEC value, which is 10 TECU, into the foreground added signal to construct the training data sets shown in Fig.(4.3c) and Fig.(4.4c). Each sample of the training data set is constructed by the following equation (4.7). In the second case study, we have added ionospheric effects, mainly refraction, absorption, and thermal emission, while building the final training data sets shown in Fig.(4.3e) and Fig.(4.4e). In the final training data set, all the samples are constructed by the following equation (4.9).

These ionospheric effects introduce two more parameters in the parameter set: TEC (Total electron content) and $\mathrm{T_e}$, representing the thermal temperature of the electron of the D-layer. In our simulation, we have used an F-layer total electron content of TEC 10 TECU and a D-layer electron temperature of $\mathrm{T_e} = 800$ K for the mid-latitude ionosphere. We used the International Reference Ionospheric (IRI) model to obtain the TEC value for the D-layer [158]. According to this model, the usual ratio of electron column densities in the D-layer and F-layer is 8.0×10^{-4} [92].

For both sets of signals, the parametrized and the physical, to build the final training data sets. We have varied ionospheric parameters by (TEC, $\mathrm{T_e}$) ($\pm1\%, \pm1\%$), respectively from their original defined values. The detailed variation that has been used in our simulation to construct the training data set for each case study in this paper is summarized in Tab.4.3.

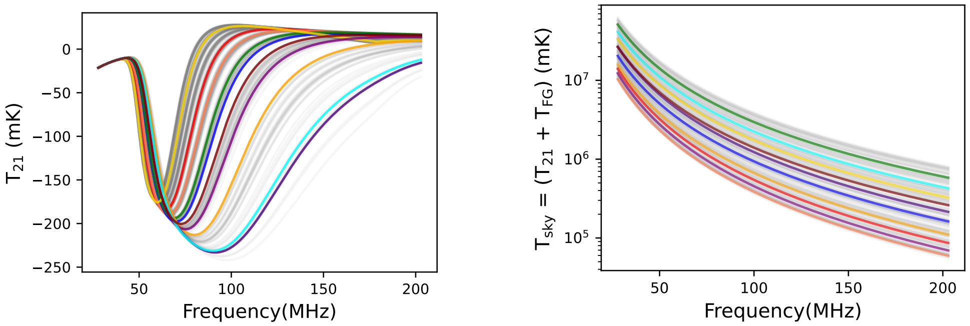

(a) Global 21cm signals.

(b) Foreground added global 21cm signals.

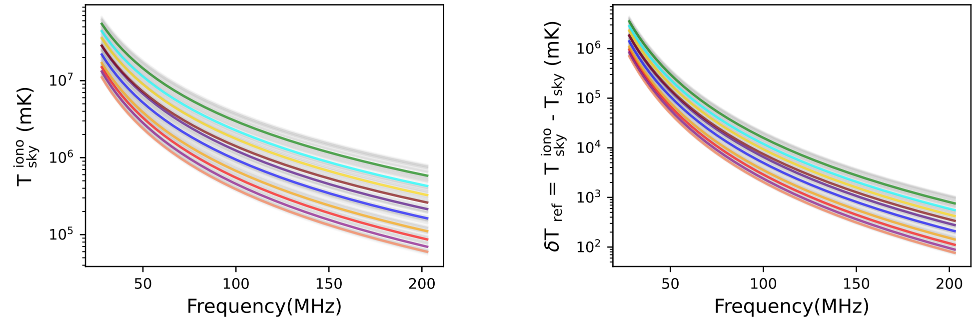

(c) Global 21cm signals and foreground with ionospheric refraction.

(d) Excess temperature due to ionospheric refraction.

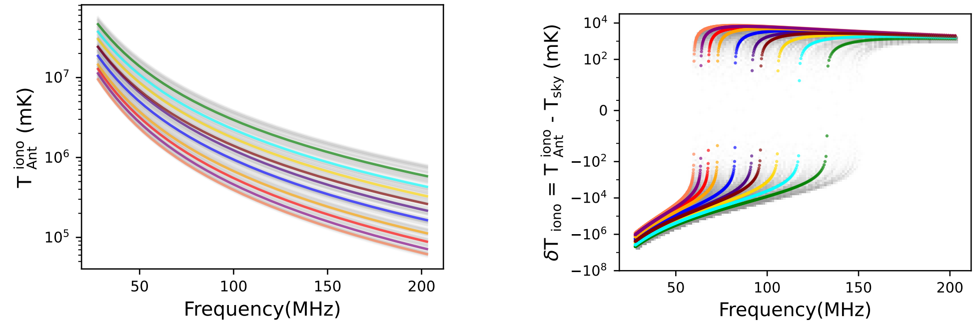

(e) Global 21cm signals and foreground with all three ionospheric effects.

(f) Contribution due to all the ionospheric effects

Figure 4.4: (a) The training data set of the global 21-cm signal was generated using physical model (semi numerical approach). (b) The training data set after we add foreground into the signal. (c) The training data set was constructed by including the ionospheric refraction effect into the signal and foreground for the corresponding fixed TEC value 10 TECU. (d) The excess temperature caused by ionospheric refraction as recorded by the antenna in the training data sets. (e) The samples of the training data set were constructed by adding all three ionospheric effects-refraction, absorption, and thermal emission into the signal and foreground for variable TEC and T_e values. (f) Contribution of all ionospheric effects to the training data sets. In each subplot, a subset of the training data sets is shown in color, while the remaining training data sets are plotted in the background using light gray color.

Parameters	**Case b**	**Case c**	**Case d**
Zeroth order foreground coefficient (a_0)	±15%	±15%	±15%
First order foreground coefficient (a_1)	±10%	±10%	±10%
Second order foreground coefficient (a_2)	±1%	±1%	±1%
Third order foreground coefficient (a_3)	±1%	±1%	±1%
Total electron content (TEC)		Fixed	±1%
Thermal electron temperature (T_e)			±1%

Table 4.3: The percentage variation of each parameter of the foreground and ionosphere from its actual value to create upper and lower boundaries and construct the training data set for each scenario for the Case 1 study when we took the parametrized model and case 2 when we consider physical model.

4.6.4 Thermal Noise

The thermal noise, $n(\nu)$, in the measured spectrum may be represented as follows using the ideal radiometer equation:

$$n(\nu) \approx \frac{T_{sys}(\nu)}{\sqrt{\delta\nu \cdot \tau}}, \tag{4.20}$$

where, $T_{sys}(\nu)$ is system temperature, $\delta\nu$ is the observational bandwidth and τ is the observation time. We are working with simulated observations, which are created using a set of assumptions about signal, foreground, and ionosphere effects. In the future, a similar network will be used to anticipate the redshifted global 21-cm signal based on actual measurements. Actual data from simple observations will replace the with the test data sets.

4.7 Results

In this section, we will discuss results from simulations representing different signal extraction scenarios: signal only, signal with foreground, signal and foreground with ionospheric refraction corresponding to a fixed TEC value, and signal and foreground with all three ionospheric effects with variable TEC and T_e values. We constructed 360 samples of the data sets for training, validation, and testing of the ANN model for the each following cases. We use 240 (67%) samples of the data sets for the training and validation, and the rest of the 120 (33%) data sets we used to test the trained ANN model. The validation mainly guides us in tuning the model's hyperparameters, for example, the number of the hidden layer, the number of neurons in the hidden layer, the activation function, the learning rate, etc. It also assists us in identifying overfitting and underfitting by comparing the model loss of the training and validation. In the test set, we add additional thermal noise, $n(\nu)$, corresponding to 1000 hours of observation by following the radiometer equation (4.20) to construct the final test data set for the each cases of studies.

4.7.1 Case 1a: Signal only (parametrized model)

In the first case, to train our model, we choose the parametrized global 21-cm signals as training data sets, shown in figure (4.3a). The model we use for training is constructed with Keras' Sequential API and comprises 1024 input neurons matching with 1024 frequency channels and two hidden layers with 16 and 11 neurons, respectively, each activated by the 'elu' activation function.

The output layer has 7 neurons to predict the global 21-cm signal parameters. The input training data sets are normalized using the' StandardScaler' function, and corresponding parameters are normalized using 'MinMaxScaler' available in sklearn. We tested our saved model with a test data set and calculated the R^2-score and RMSE score for each parameter from the predictions of test sets to figure out how well the network predicts the parameters. The result of R^2-score is listed in Tab. (4.4) and RMSE scores are listed in Tab. (4.5), and the plots of the original versus predicted values of the parameters for the test data set are shown in Fig. (4.5). The R^2 scores for the predicted signal parameters range from 0.98 to 0.99, which shows the network predicted signal parameter is very accurate. To check the overfitting for all the cases, we have plotted training loss and validation loss as a function of the number of epochs [see Fig. 4.6]. In Fig. (4.6), we can see that training loss and validation loss closely flow, and both got converse after 20 epochs for all the cases.

4.7.2 Case 1b: Signal with foreground

Foregrounds would dominate during the observations of the 21-cm signal for all ground-based experiments. In this case, we train our ANN model with training data constructed by adding foreground to the parametrized global 21-cm signals, shown in Fig. (4.3b). In [86] has already shown a similar implementation. It is a proof-of-concept to see how effectively our model extracts parameters when adding the foreground. The model architecture we used is different from the first case. The model we have used has 4 layers made using sequential API from Keras. The input layer has 1024 neurons that correspond to the 1024 frequency channel, while the hidden layers have 32 and 16 neurons that are activated by the 'sigmoid' activation function. The output layer has 11 output neurons to predict the global 21-cm signal and foreground parameter. We will use the same model architecture, optimizer, and normalization method for the other cases. The only difference is the number of neurons in the output layer, depending on the number of output parameters. We calculate the R^2-scores and RMSE for each parameter from the test set predictions to determine how well the network predicts the parameters. The plots of the original versus the predicted values of the parameters for the test data set are shown in Fig. (4.7), and R^2 score and RMSE score for corresponding parameters are listed in Tab. 4.4 and Tab. 4.5. The R^2 score for this case ranges from 0.97 to 0.98 for predicted signal parameters, which are significantly lower than the previous case (Case 1a). In the predicted foreground parameters, a_0 has the highest R^2 score of 0.99.

4.7.3 Case 1c: Signal and foreground with ionospheric refraction

The ionosphere of the Earth severely distorts low-frequency radio measurements in ground-based observations. We add the ionospheric refraction effects into the signal and foreground while constructing data sets to check this effect, shown in Fig. (4.3c). We followed the same ANN model structure that was used in Case 1b and trained the ANN model using training data sets constructed by adding the effects of ionospheric refraction. We tested the trained model with test data sets and calculated the R^2 score and RMSE score corresponding parameters to evaluate our model performance; the detailed result is listed in Tab. (4.4) and Tab. (4.5). The predicted values of the parameters by the network are plotted in Fig. (4.8). In this case, the obtained R^2 score for the signal parameters ranges from 0.94 to 0.96.

Parameter	**Case 1a**	**Case 1b**	**Case 1c**	**Case 1d**
J_{ref}	0.9809	0.9778	0.9553	0.9614
J_{z0}	0.9957	0.9780	0.9442	0.9738
X_{z0}	0.9865	0.9760	0.9534	0.9713
T_{z0}	0.9911	0.9746	0.9534	0.9668
J_{dz}	0.9826	0.9735	0.9482	0.9634
X_{dz}	0.9830	0.9848	0.9487	0.9578
T_{dz}	0.9874	0.9781	0.9574	0.9595
a_0		0.9936	0.9757	0.9810
a_1		0.9738	0.9494	0.9655
a_2		0.9773	0.9534	0.9586
a_3		0.9774	0.9568	0.9610
TEC				0.9658
T_e				0.9728

Table 4.4: The computed R^2-scores for all signal, foreground, and ionosphere parameters for each case studied are listed here. We used the parametrized model to construct the global 21-cm signal.

4.7.4 Case 1d: Signal and foreground with all three ionospheric effects- refraction, absorption and thermal Emission

In this case, we add other ionospheric effects like absorption and thermal emission and construct the training data set, which we name the ”final training data set”, shown in Fig. (4.3e). We utilized the same architecture as in previous cases (Cases 1b and 1c) to build an ANN model; the only difference here is that the output layer of the model has 13 output neurons corresponding to the 7 signal parameters, 4 foreground parameters, and 2 ionospheric parameters. We test this model with test data and calculate the R^2 score and RMSE score corresponding parameters to evaluate our model performance. The R^2 and RMSE scores for each parameter are listed in Tab. 4.4 and Tab. 4.5, and predicted values of the parameters by the network are plotted in Fig. (4.9). From Table 4.4, and 4.5, we can see that R^2 values slightly decrease, and the RMSE value slightly increases when we introduce foreground and ionospheric effects into the signals compared to Case 1a when we take signal only. When we add more complexity to the training data set, we have to train our network sufficiently well to maintain high accuracy levels.

4.7.5 Case 2a : Signal only (physical model)

To check the robustness and reliability of the network, we trained the ANN model for all the scenarios that we have studied previously with an entirely new set of the global 21-cm signal, taken from [13]. They constructed the global 21-cm signals by using semi-numerical code followed by [157]. It contains a more realistic and diverse group of the 21-cm signal than the parametrized model signals. The signal parameters are also different than the parametrized model; here we use astrophysical parameters ($f_{xh} * f_x$, f_{star},f_{esc}, N_α). In the first case of the study, we take global 21-cm signals as a training, validation, and testing of the ANN model, shown in Fig. (4.4a). The training

Parameter	Case 1a	Case 1b	Case 1c	Case 1d
J_{ref}	0.0337	0.0440	0.0608	0.0628
J_{z0}	0.0175	0.0438	0.0675	0.0605
X_{z0}	0.0329	0.0453	0.0621	0.0616
T_{z0}	0.0253	0.0470	0.0645	0.0577
J_{dz}	0.0353	0.0482	0.0650	0.0608
X_{dz}	0.0370	0.0467	0.0584	0.0658
T_{dz}	0.0312	0.0434	0.0642	0.0636
a_0		0.0232	0.0449	0.0439
a_1		0.0477	0.0639	0.0590
a_2		0.0443	0.0621	0.0642
a_3		0.0445	0.0599	0.0625
TEC				0.0578
T_e				0.0588

Table 4.5: The calculated RMSE values for all the signal, foreground, and ionospheric parameters are listed here for each case studied.

model consists of a four-layer structure built with Keras' sequential API, with 1024 input neurons matching 1024 frequency channels and two hidden layers with 12 and 11 neurons activated by the 'elu' activation function. The output layer contains four output neurons that predict astrophysical parameters of the global 21-cm signal ($f_{xh} * f_x$, f_{star}, f_{esc}, N_α). We used the StandardScaler function, which is available in 'sklearn' to preprocess input signals. At the same time, we use MinMaxScaler to scale the signal parameters before passing them to the model. We use 'adam' as the optimizer and' mean squared error' as the loss function. Once the network is trained and validated, we save the model. We used the same optimizer and normalization method for the other cases.

We test the model using a test data set and obtain the R^2 scores and RMSE for each parameter from the test set predictions to see how well the network predicts the parameters. The predicted parameters are plotted in Fig. (4.10) and the corresponding R^2 score and RMSE score for each parameter are listed in Tab.4.6 and Tab. 4.7. From the Tab.4.6, we can see that the parameter N_α has the highest R^2 scores of 0.99 and parameters f_{esc} has the lowest R^2 score of 0.98. To check the overfitting for all the cases, we have plotted training loss and validation loss, similar to the parametrized case [see Fig. (4.11)]. In Fig. (4.11), we can see that training loss and validation loss closely flow, and both got converse after 20 epochs for all the cases.

4.7.6 Case 2b : Signal with foreground

In this case, we train our model with a training data set, which is constructed by the combination of the foreground with different realizations of the global 21-cm signal, shown in Fig. (4.4b). We employed a 5-layer model architecture for training, with 1024 input neurons matching the 1024 frequency channels and three hidden layers with 32, 16 and 16 neurons activated by the 'elu' activation function. The output layer of the model has 8 output neurons corresponding to 4 astrophysical parameters of the global 21-cm signal and 4 foreground parameters. We test our trained model with the test data set and calculate the R^2 and RMSE scores for the corresponding parameters shown in Tab. 4.6 and Tab. 4.7, and plot of predicted values of the parameters against the original values is shown in Fig. (4.12). From Tab. 4.6, we can see that the foreground parameters' R^2 score is much higher than the signal parameters; this means the network predicts the foreground parameter more accurately than the signal parameters. In the signal, the parameter $\mathrm{f}_{\mathrm{x,h}} * \mathrm{f}_{\mathrm{x}}$ has the highest R^2 scores of 0.98, and N_α has the lowest R^2 scores of 0.96.

follow

4.7.7 Case 2c : Signal and foreground with ionospheric refraction

In the third case, we added foreground and ionospheric refraction effects for corresponding fixed TEC value into the global 21-cm signal to build the training data set, shown in Fig. (4.4c), and randomly divide these samples into the same ratio as in Case 2(b) to train and test the ANN model. We follow the same model architecture that we used previously for the signal in the foreground case to build the model for this case. Now we train this model and save it for further validation and testing. We test the saved model with test data sets, and we calculate the R^2 score and RMSE score for the corresponding parameter. Details of the result are listed in Tab. 4.6 and Tab. 4.7, and a plot of predicted values of the parameters against the original values is shown in Fig. (4.13). The R^2 score for the foreground parameters has been improved from the previous case, but the signal parameter R^2 score decreases in comparison; this means adding more complexity to the training data making signal extraction more difficult. We obtained the R^2 score for the signal parameters around 0.96 to 0.98 [see Tab. 4.6].

4.7.8 Case 2d : Signal and foreground with all three ionospheric effects- refraction, absorption, and thermal emission

In the last case, we have constructed training data sets by the combination of the global 21-cm signal, foreground, and ionospheric effects (refraction, absorption, and thermal emission), shown in Fig. (4.4e). To build the model for this case, we use the same architecture that we used in previous models except for the outer layer. Here, the output layer of the model has 10 output neurons corresponding to the 4 signal parameters, 4 foregrounds, and 2 ionospheric parameters. Once the models were trained and validated, we saved them for further testing. We tested the saved train model with the test data set and calculated the R^2 score and RMSE score for the corresponding parameters to check the network performance. The values of R^2 score and RMSE score of each parameter are tabulated in Tab. (4.6) and Tab. (4.7). The plots of the actual versus predicted values of the parameters for the test data set are shown in Fig. (4.14). The R^2 score for the foreground and ionospheric parameters is much higher than the signal parameters R^2 score. The reason is simple: foreground and ionospheric effects dominated the final training data sets signal that we are giving to the network as fed compared to the signals. The R^2 score we obtained for the signal parameters is around 0.96 to 0.98 [see Tab. 4.6].

Parameter	**Case 2a**	**Case 2b**	**Case 2c**	**Case 2d**
$\mathrm{f_{xh}} * \mathrm{f_x}$	0.9906	0.9813	0.9839	0.9804
$\mathrm{f_{star}}$	0.9893	0.9731	0.9675	0.9704
$\mathrm{f_{esc}}$	0.9863	0.9772	0.9756	0.9751
N_α	0.9952	0.9607	0.9579	0.9620
$\mathrm{a_0}$		0.9752	0.9812	0.9981
$\mathrm{a_1}$		0.9964	0.9957	0.9990
$\mathrm{a_2}$		0.9739	0.9773	0.9793
$\mathrm{a_3}$		0.9736	0.9743	0.9773
TEC				0.9733
$\mathrm{T_e}$				0.9742

Table 4.6: The computed R^2-scores for all signal, foreground, and ionosphere parameters for each case studied are listed here. We used physical model (semi numerical model) to construct the global 21-cm signal.

4.7.9 Time varying ionospheric effects- refraction, absorption and thermal emission

We conducted further assessments to evaluate the robustness of the ANN model. We used a dynamic ionospheric model with temporal variations. This model assumes random fluctuations in Total Electron Content (TEC) and electron temperature (Te) throughout the observation period. We integrated the F-layer TEC and Te values at 15-minute intervals over a span of 1000 hours to create an observational data set, see Fig. (4.15) and Fig. (4.16). We calculated the average antenna temperatures measured by the radiometer for each integration over the entire 1000-hour observation period to create the final observation data set that accounts for the time-varying ionospheric effects. Additionally, we have included the thermal noise associated with the 1000-hour observation in this recorded data set. We feed this noise-added final observation data set to the trained ANN model and extract the parameters. The ANN model demonstrated commendable performance for both parametrized and physically-based signal scenarios. Even in time-varying conditions, the ANN model exhibited accurate predictions. The predicted mean values by the ANN are closely aligned with the actual mean values of TEC and Te, see Fig. (4.17, 4.18, 4.19 and 4.20) and rest other parameters like signal and foreground are also consistent with the actual one [see Tab. 4.8, 4.9] . This is clearly indicating the ANN model's accuracy and ability to capture complex temporal variations in ionospheric phenomena.

4.8 Summary and Discussions

In this study, we presented an ANN model to extract the 21-cm global signal by estimating their parameters from a combined spectrum that included signal, foreground, ionospheric effects, and thermal noise. We trained our ANN model with four different scenarios described in detail in Section 4.7. To check the robustness of the ANN, we also used two different ways of modelling the global 21-cm signal; one is based on the functional parametrized [109, 145] and the other one is a physically motivated approach [13, 157]. The parameter space in both cases is entirely different; parametrized model parameters are more directly related to IGM properties; however, the physical

Parameter	**Case 2a**	**Case 2b**	**Case 2c**	**Case 2d**
$\mathrm{f_{xh} \cdot f_x}$	0.0174	0.0428	0.0395	0.0411
$\mathrm{f_{star}}$	0.0287	0.0476	0.0540	0.0488
$\mathrm{f_{esc}}$	0.0334	0.0453	0.0507	0.0475
N_α	0.0176	0.0562	0.0567	0.0508
$\mathrm{a_0}$		0.0473	0.0410	0.0442
$\mathrm{a_1}$		0.0107	0.0276	0.0094
$\mathrm{a_2}$		0.0433	0.0503	0.0420
$\mathrm{a_3}$		0.0481	0.0533	0.0445
TEC				0.0480
$\mathrm{T_e}$				0.0473

Table 4.7: Root Mean Square Error (RMSE) values for signal, foreground, and ionospheric parameters in each of the studied cases. Missing values indicate parameters not included in the respective case.

model includes both IGM and source properties. In the physical model, the parameter $\mathrm{f_R}$ played the most crucial role in defining the form of the reconstructed signal in the semi-numerical code [13]. A high $\mathrm{f_R}$ value implies a strong radio background, resulting in a substantial absorption trough signal. In contrast, $\mathrm{f_R} = 0$ suggests that the excess radio background is turned off, resulting in a conventional signal. In our study, We have taken the traditional data set of the global 21-cm signals from [13].

For both parametrized and physical models, in the final case studies, Case 1d and Case 2d, the trained ANN model predicted the signal parameters from the test data set with an accuracy of $\geq 96\%$. This clearly demonstrates how a basic ANN model can easily manage up to 13 parameters (7 signal parameters, 4 foreground parameters, and 2 ionospheric parameters. We have estimated the uncertainty of the parameter by calculating the RMSE score of the individual parameters for all the cases [See Tab. 4.5, 4.7]. We found the error in the parameter estimation increase when we increase the number of training parameters, e.g., in the first case of the study, when we used signal only (Case 1a), the ANN estimated the parameter with a maximum error of $\approx 4\%$, but in the final case (Case 1d), the maximum error was $\approx 6\%$. Similarly, in the second case of the study for Case 2a, the maximum error was $\approx 3\%$, but in the final case- Case 2d, the maximum error was $\approx 5\%$. This clearly indicates that when complexity increased in the training data set, the prediction accuracy slightly decreased with the reference lower complexity training data set [see Tab. 4.4, 4.5, 4.6, and 4.7]. It means adding complexity to the training data set, making signal extraction more challenging for the network. The accuracy levels will remain high if the network has been trained well enough. We also demonstrated that for the dynamic ionospheric model where TEC and Te are varying randomly, ANN prediction accuracy is still consistent [see Tab. 4.8, 4.9].

To further emphasise the utility of the ANN method, we conducted an analysis attempting to fit the signal, foreground, and ionospheric effects using a simple analytical approach. This method failed to extract the signal parameters from both scenarios. Conversely, our trained ANN model demonstrated remarkable accuracy in predicting parameters for the same data set, as elaborated in Appendix A. Additionally, we evaluated the ANN's performance in terms of accuracy by comparing it with existing prior signal extraction methods. To assess this, we compared the predictions of these prior models with the true parameters, calculating the Mean Absolute Percentage Error (MAPE), as detailed in Appendix B. Our findings revealed that the predicted parameters by the

Parameter	**Actual Value**	**Predicted by ANN**	**Percentage Error (%)**
$\mathrm{J_{ref}}$	11.690	11.823	1.138
$\mathrm{J_{z0}}$	18.540	18.693	0.825
$\mathrm{X_{z0}}$	8.680	8.627	0.610
$\mathrm{T_{z0}}$	9.770	10.144	3.828
$\mathrm{J_{dz}}$	3.310	3.407	2.930
$\mathrm{X_{dz}}$	2.820	2.901	2.872
$\mathrm{T_{dz}}$	2.830	2.853	0.813
$\mathrm{a_0}$	3.323	3.336	0.391
$\mathrm{a_1}$	-2.354	-2.416	2.638
$\mathrm{a_2}$	-0.0805	-0.0806	0.124
$\mathrm{a_3}$	0.0290	0.0290	0.000
$\langle \mathrm{TEC} \rangle$	10.0	10.001	0.010
$\langle \mathrm{T_e} \rangle$	800.00	799.73	0.033

Table 4.8: Comparison of actual and ANN-predicted parameter values for the time-varying ionospheric model. Percentage errors are computed for each parameter.

ANN model are significantly more accurate than these traditional methods.

The other benefit of using ANN is that it can efficiently extract the observed sky signal's characteristics without modelling and eliminating foreground and ionospheric effects. Compared to the other existing parameter estimation techniques, ANN can extract features from data by building functions that connect the input and output parameters. The ANN model, unlike Bayesian approaches, does not require a defined prior; instead, we must provide training data sets, which may be seen as playing a similar role as the prior in Bayesian techniques. We may avoid computing the likelihood function a large number of times by using ANN to arrive at inferred parameter values. As a result, even when dealing with a larger dimensional parameter space, ANN is computationally faster and more efficient.

In this work, the ANN model on a limited set of scenarios involving the signal, foregrounds, and both static and time-varying ionospheric conditions, which is very robust and sensitive for all the given input parameters with their defined parameter ranges used in the preparation of the data sets. By incorporating problems like beam chromaticity, and other systematic effects, we hope to create a more reliable ANN model in the future. Depending on telescope design and their geomagnetic, various systematics corrupt observations, such as standing waves from cable lengths internal to the system, chromaticity caused by environmental factors like antenna ground planes [159, 160], ionosphere and RFI. These non-astronomical signal need to be modelled for accurate signal extraction. We plan to include these effects in our future study.

In this chapter, the ANN model is trained and tested on a limited set of scenarios involving the signal, foregrounds, and ionospheric effects. These experiments demonstrate good prediction accuracy within the restricted parameter space. However, to make the approach more practical, the ANN must be trained on the full range of possible signal and foreground scenarios, especially since we lack prior observational constraints. In the next chapter, we expand the parameter space

Parameter	**Actual Value**	**Predicted by ANN**	**Percentage Error (%)**
$\mathrm{f_{xh}f_x}$	2.815	2.257	19.822
$\mathrm{f_{star}}$	-2.162	-2.194	1.480
$\mathrm{f_{esc}}$	0.133	0.127	4.511
N_α	4.719	4.643	1.611
$\mathrm{a_0}$	3.384	3.323	1.803
$\mathrm{a_1}$	-2.354	-2.406	2.209
$\mathrm{a_2}$	-0.0805	-0.0806	0.124
$\mathrm{a_3}$	0.0290	0.0289	0.345
$\langle \mathrm{TEC} \rangle$	10.000	10.001	0.010
$\langle \mathrm{T_e} \rangle$	800.00	800.44	0.055

Table 4.9: Comparison of actual and ANN-predicted parameter values for the physical model with time-varying ionosphere. Includes percentage errors for each parameter.

to more comprehensively cover all relevant scenarios. The ANN is trained on this broader dataset, and the details of this extended framework are discussed there.

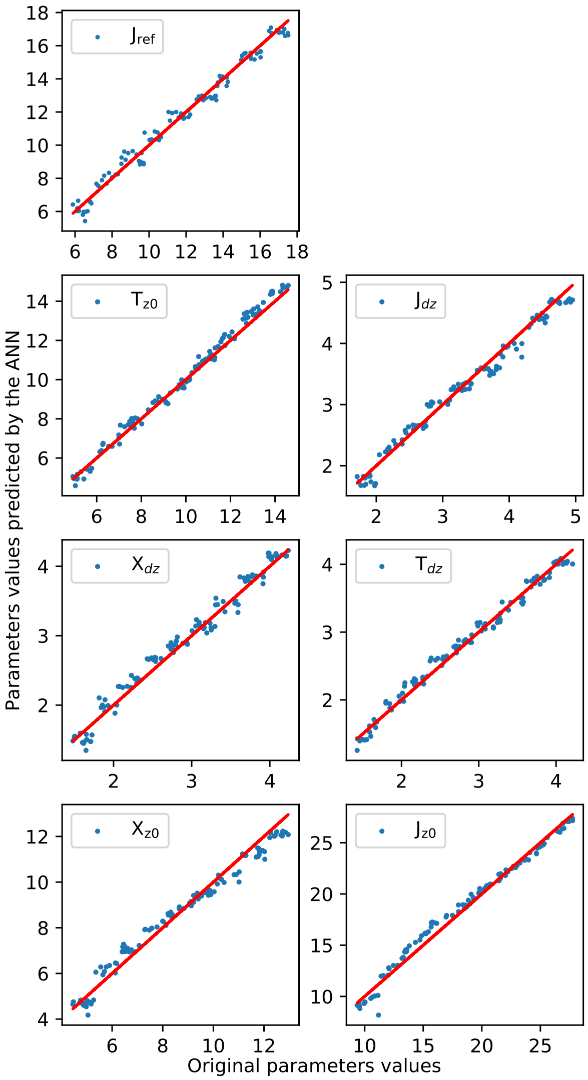

Figure 4.5: Case 1a: Parmeterized global 21-cm signals. The original values of the parameters are shown by the solid straight line in each plot, while the dots indicate the predicted values by ANN.

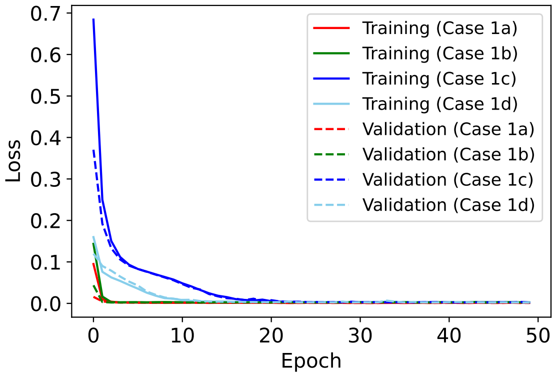

Figure 4.6: This graph depicts the evolution of the network's loss function when parametrized signals were incorporated. For all situations, the training loss is represented as a solid line, and the validation loss is plotted as a dashed line as a function of epochs. We can see that the test loss function closely follows the training loss function.

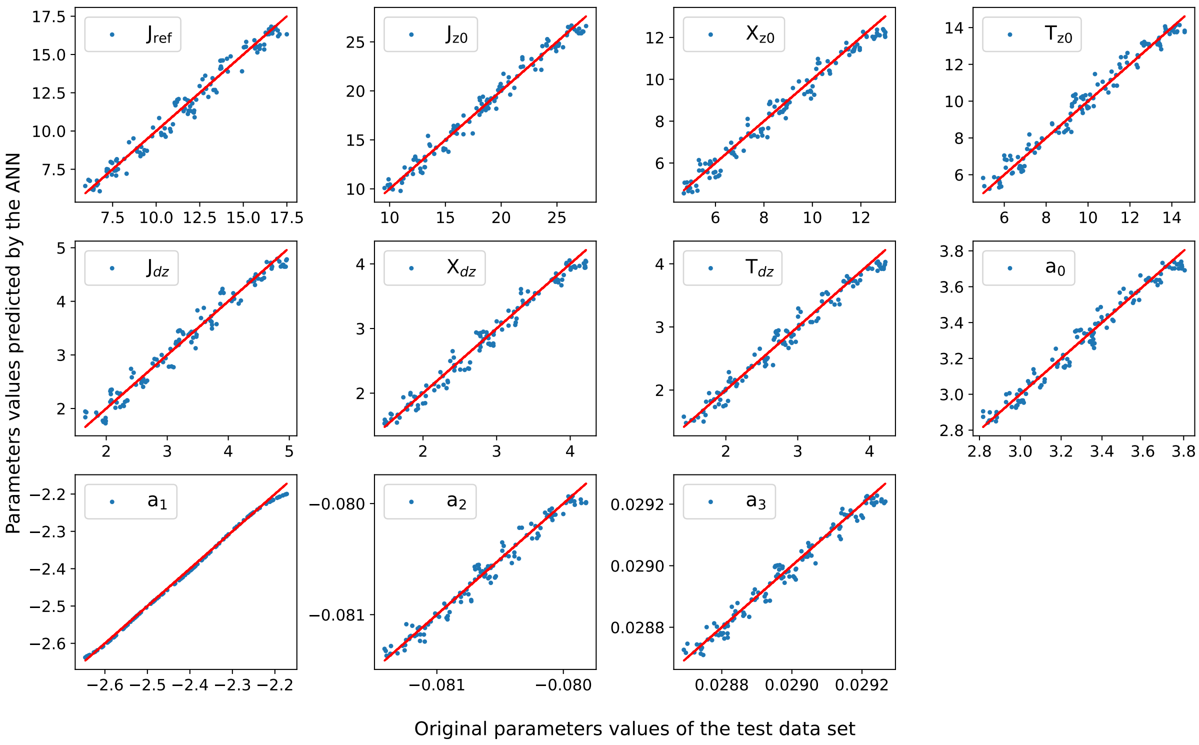

Figure 4.7: Case1b: parametrized global 21-cm signal with foreground. The original values of the parameters are shown by the solid straight line in each plot, while the dots indicate the predicted values by ANN.

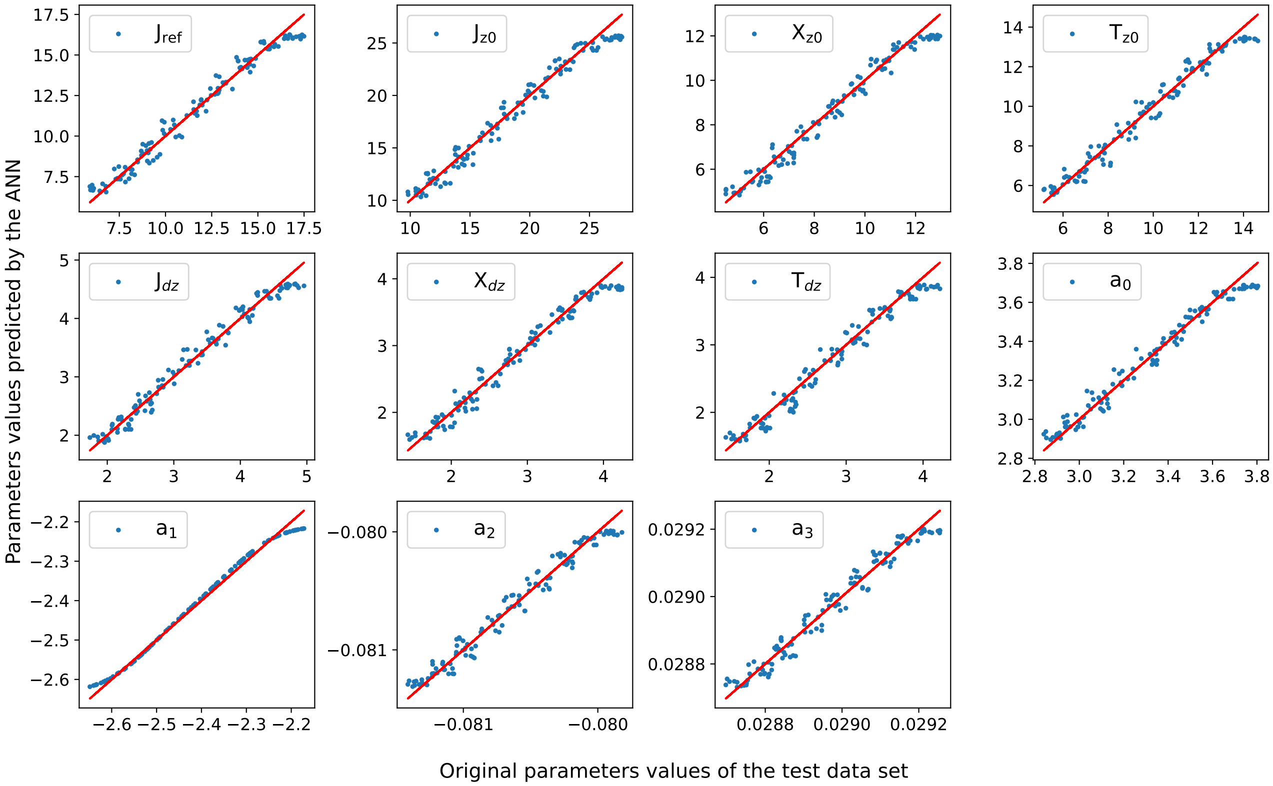

Figure 4.8: Case 1c: parametrized global 21cm signal and foreground with ionospheric refraction for fixed TEC value. The original values of the parameters are shown by the solid straight line in each plot, while the dots indicate the predicted values by ANN.

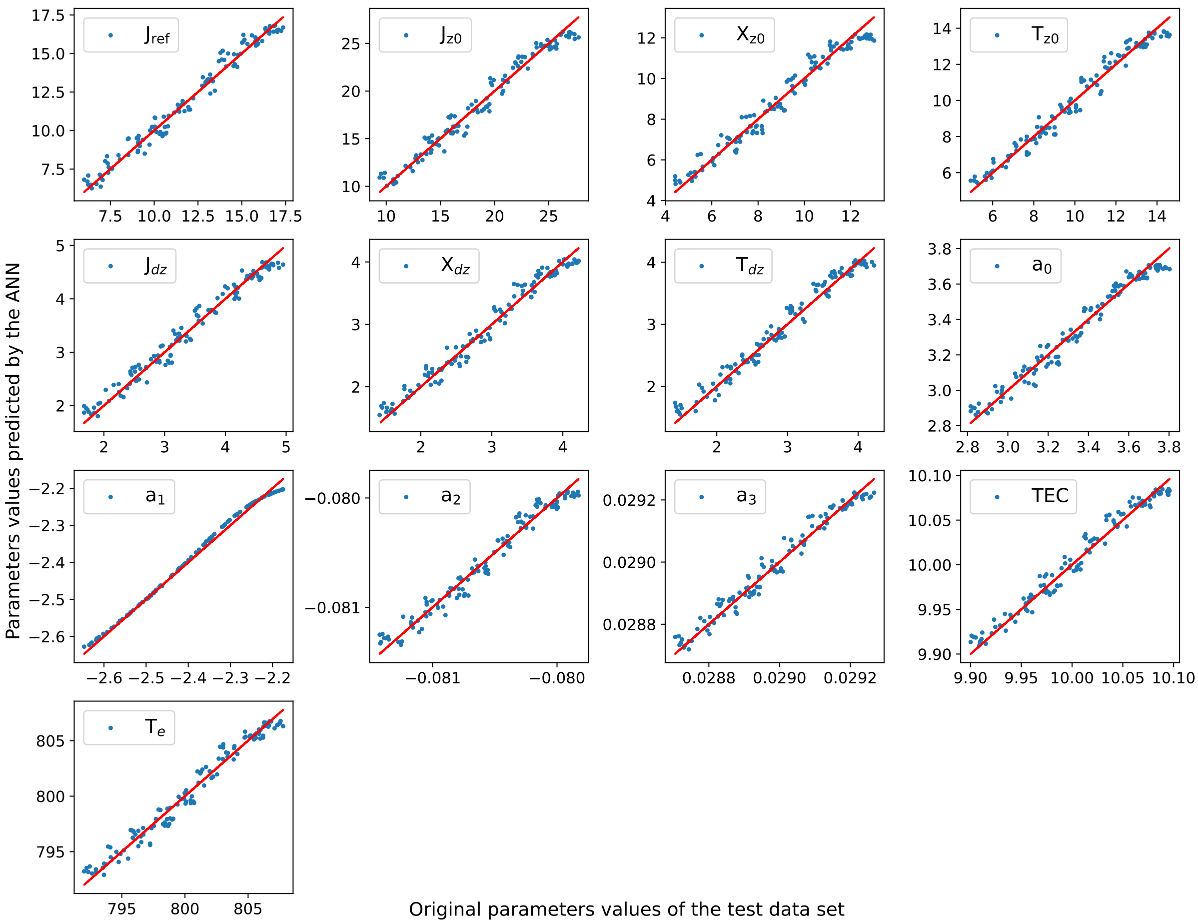

Figure 4.9: Case 1d: parametrized global 21-cm signal and foreground with all three ionospheric effects- refraction, absorption, and thermal emission. The original values of the parameters are shown by the solid straight line in each plot, while the dots indicate the predicted values by ANN.

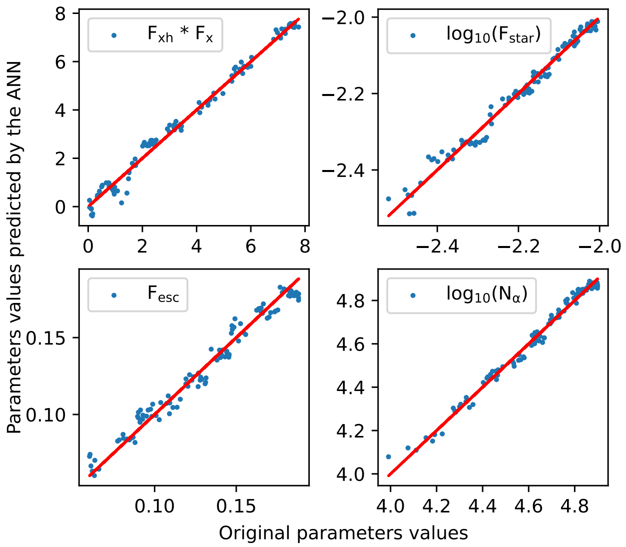

Figure 4.10: Case 2a: Global 21-cm signal constructed using physical model. The original values of the parameters are shown by the solid straight line in each plot, while the dots indicate the predicted values by ANN. However, F_{star} and N_α are plotted in logarithmic scale.

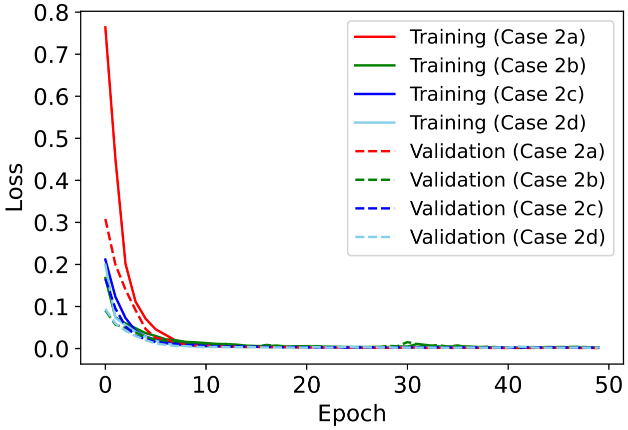

Figure 4.11: This graph shows the evolution of the network's loss function when we used a signal generated by a physical model. In all cases, the training loss is depicted as a solid line as a function of epochs, whereas the validation loss is plotted as a dashed line. The test loss function closely matches the training loss function in this case.

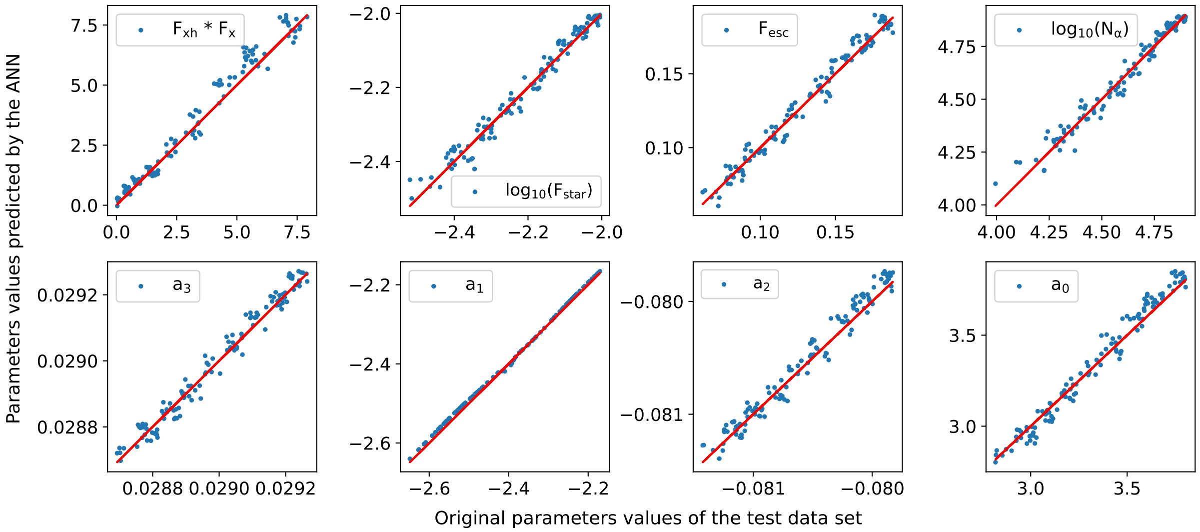

Figure 4.12: Case 2b: Signals with foreground. In the each plots the original values of the parameters are shown by the solid straight line, while the dots indicate the predicted values by ANN. However, F_{star} and N_α are plotted in logarithmic scale.

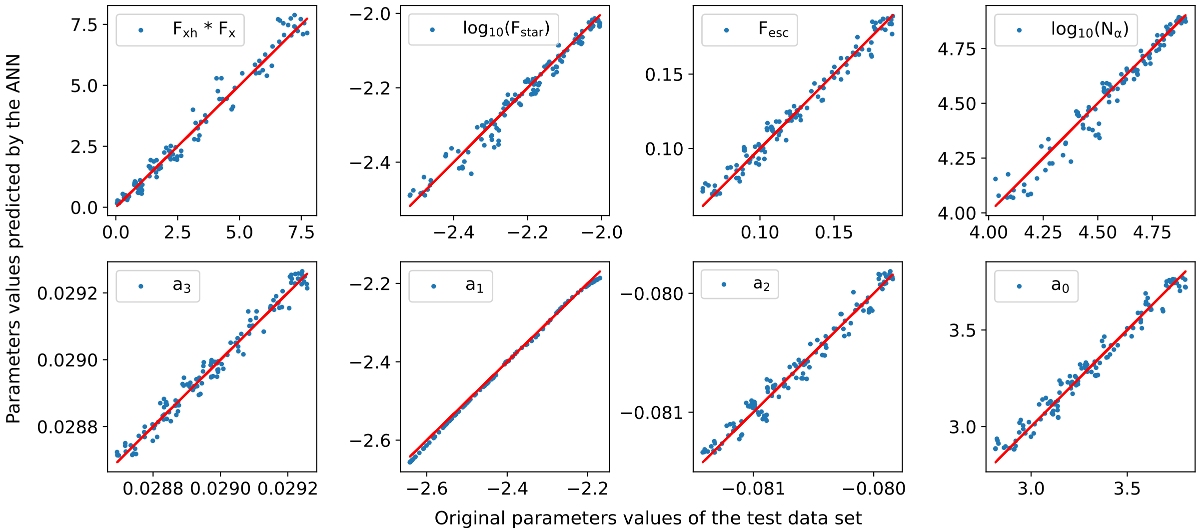

Figure 4.13: Case 2c: Signal and foreground with ionospheric refraction for fixed TEC value. In the each plots, the original values of the parameters are shown by the solid straight line, while the dots indicate the predicted values by ANN. However, F_{star} and N_α are plotted in logarithmic scale.

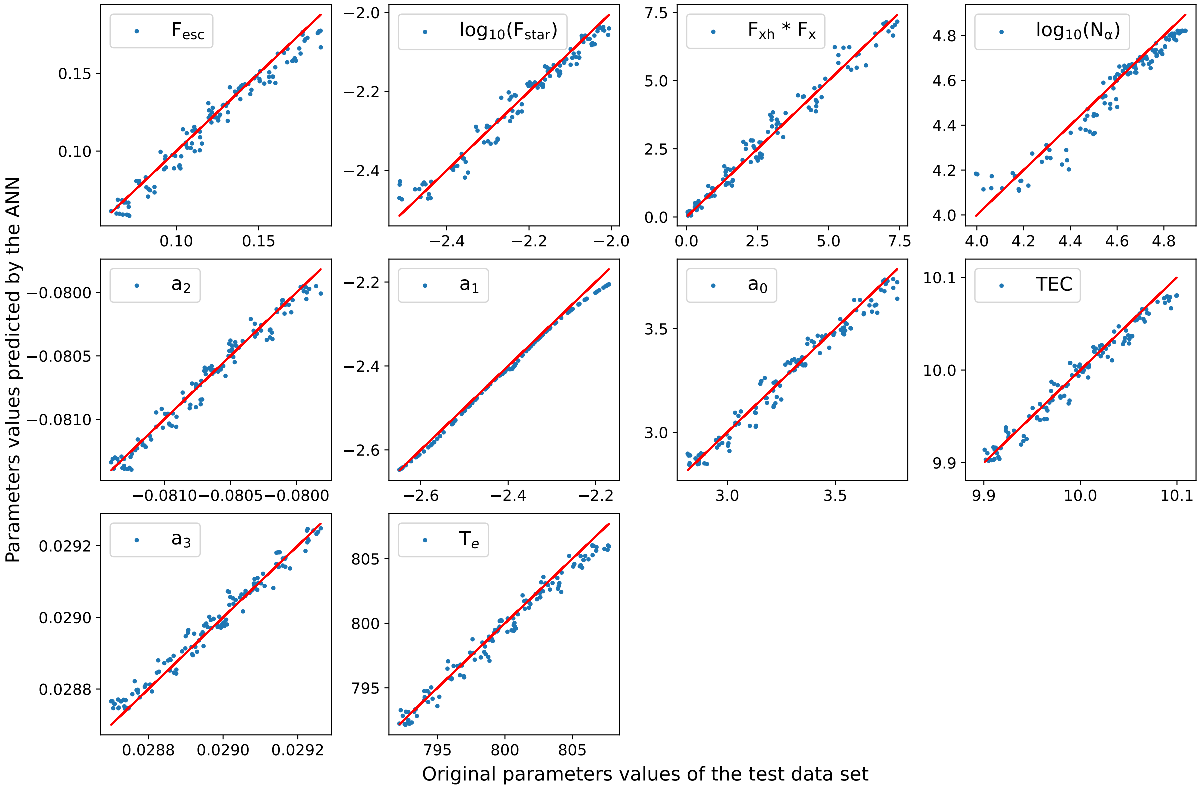

Figure 4.14: Case 2d: Signal and foreground with all three ionospheric effects-Refraction, Absorption, and Thermal Emission. In the each plots the original values of the parameters are shown by the solid straight line, while the dots indicate the predicted values by ANN. However, F_{star} and N_α are plotted in logarithmic scale.

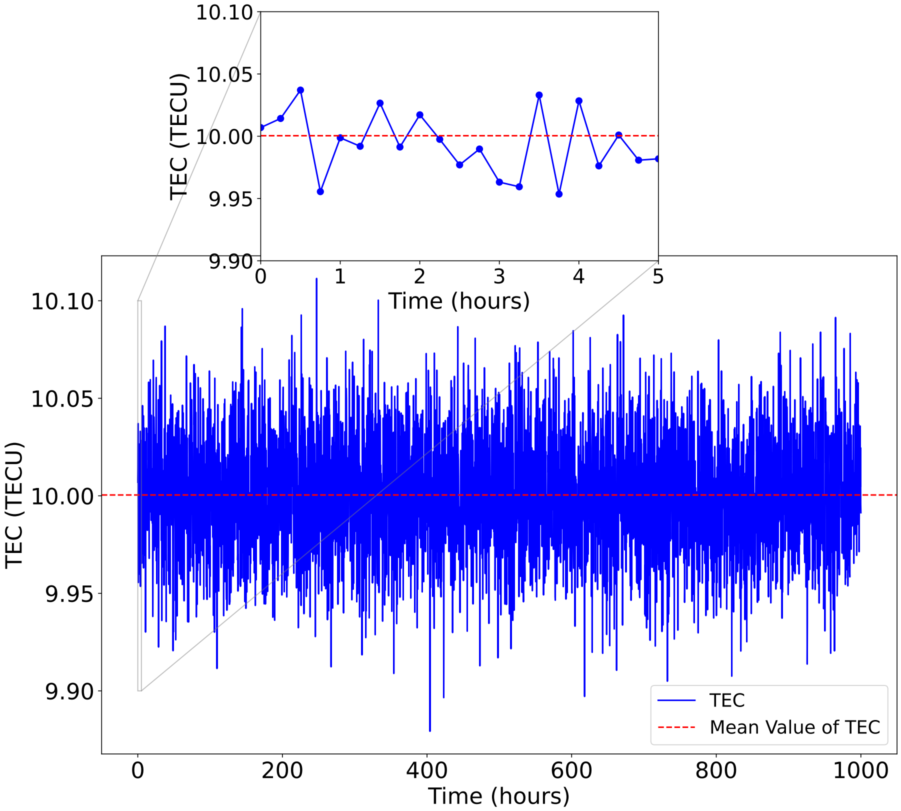

Figure 4.15: The blue lines in this graph depict the F-layer Total Electron Content (TEC) variation across a 1000-hour observation period. The red dashed line represents the calculated mean TEC value derived from these fluctuations.

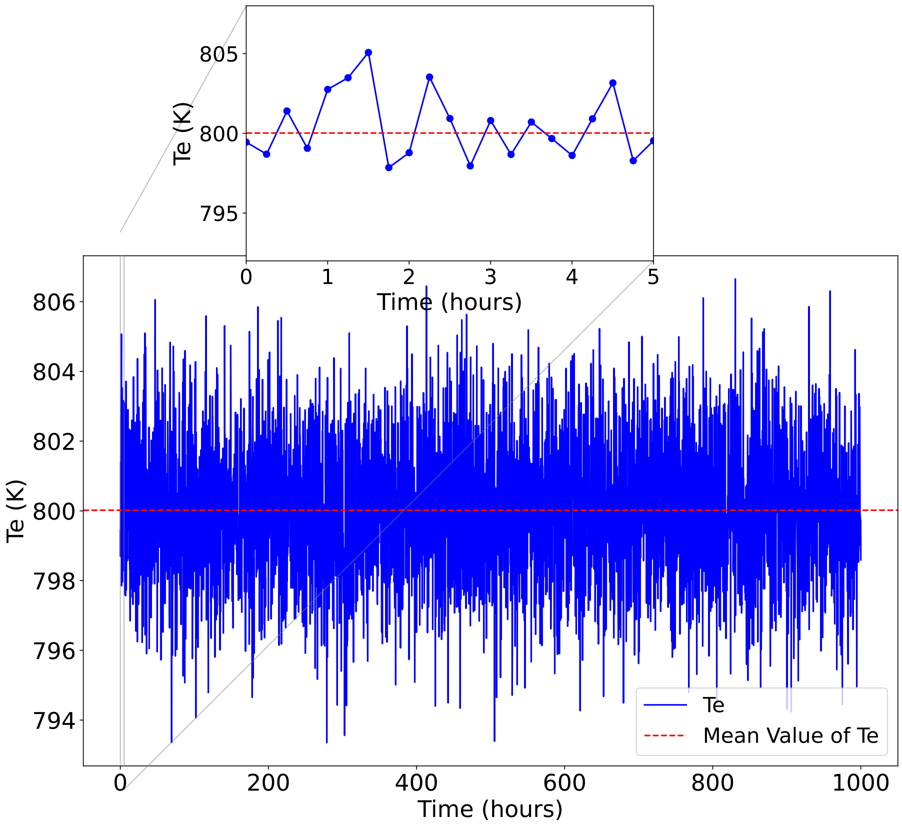

Figure 4.16: The blue lines in this graph depict the variation of the D-layer electron temperature (Te) across a 1000-hour observation period. The red dashed line represents the calculated mean Te value derived from these fluctuations.

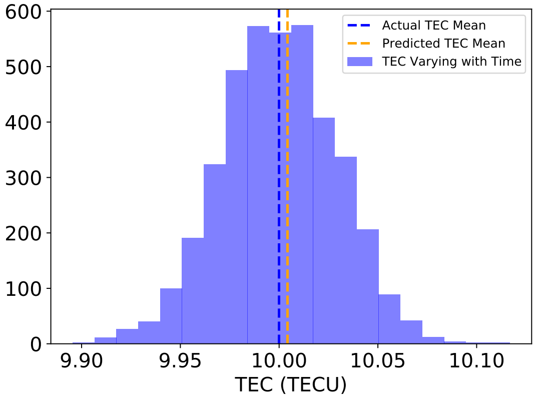

Figure 4.17: This histogram presents the distribution of TEC values containing the entire observation duration in the context of the parametrized signal scenario. The blue dashed line denotes the average value of the actual TEC, while the orange dashed line corresponds to the mean of the predicted TEC values by the ANN model.

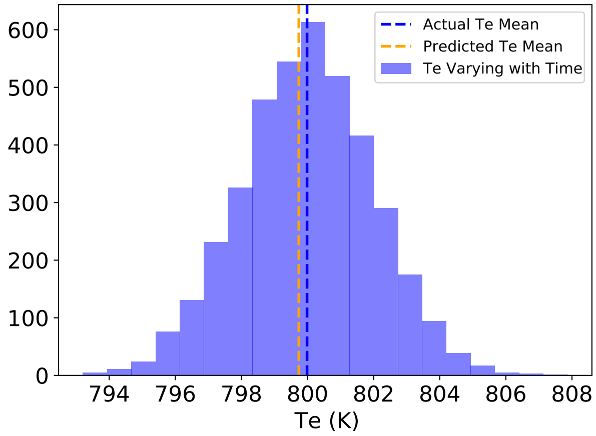

Figure 4.18: This histogram presents the distribution of Te values containing the entire observation duration in the context of the parametrized signal scenario. The blue dashed line denotes the average value of the actual Te, while the orange dashed line corresponds to the mean of the predicted Te values by the ANN model.

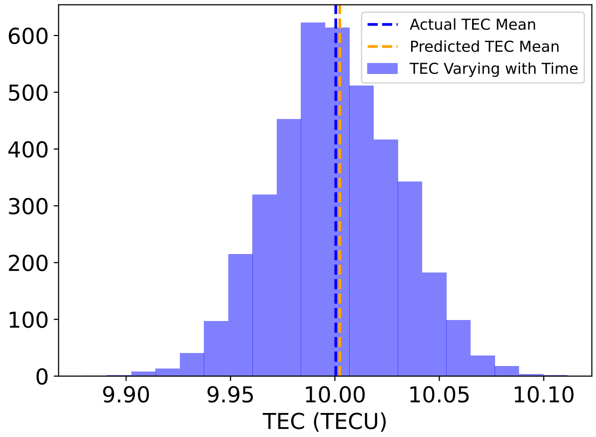

Figure 4.19: This histogram presents the distribution of TEC values containing the entire observation duration in the context of the Physical signal scenario. The blue dashed line denotes the average value of the actual TEC, while the orange dashed line corresponds to the mean of the predicted TEC values by the ANN model.

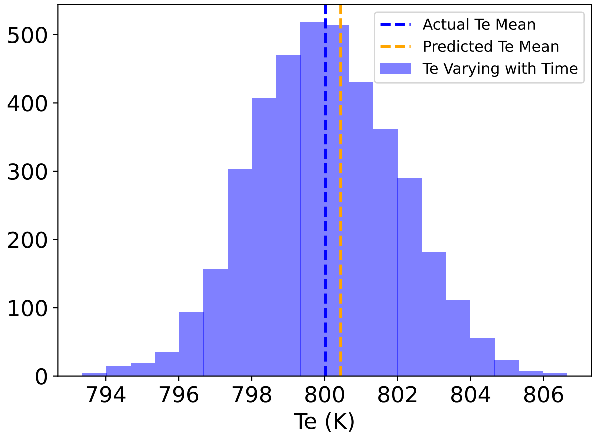

Figure 4.20: This histogram presents the distribution of Te values containing the entire observation duration in the context of the Physical signal scenario. The blue dashed line denotes the average value of the actual Te, while the orange dashed line corresponds to the mean of the predicted Te values by the ANN model.

Appendix A: Extraction of Signal, Foreground and Ionospheric effect Parameters using Analytical Method

We attempted to analytically fit two scenarios: one with signal and foreground and another with signal, foreground, and ionospheric effects using Least Square Fit from Scipy libraries in Python. For the first scenario, input data sets are simulated based on equation 4.18, and the corresponding true input parameters are listed in Tab. 4.10. Similarly, for the second scenario, the simulation relied on equation 4.9, with the true input parameters listed in Tab. 4.11. We follow two approaches to fit the signal and foreground. In the first approach, We attempted to fit both the signal and foreground simultaneously for the given sky signal simulated using equation 4.18, but encountered significant instability in the fit. The residual left after the best-fit signal and foreground is shown in Fig. 4.21, and best-fit parameters are listed in the table Tab. 4.10. In the second approach, we attempted individual fitting of the foreground and signal from the sky signal, initially fitting the foreground by following equation 4.5 and subtracting its best-fit model from the total observed sky signal. The remaining 21 cm signal was then fitted separately using the signal's parametrized model, described in section 4.6.1. However, the fitting function failed to accurately capture the foreground and global signal parameters. It is evident from the distinct residual signal, noticeably different from the input signal, indicating inaccurate foreground fitting (Fig. 4.21). The small uncertainty in the best-fit foreground parameters indicates under-constraint. The fitting function's performance for signal fitting was notably inadequate. The summarized results are in Tab. 4.10. We attempted to fit the total sky signal, incorporating the global 21 cm signal, foreground, and ionospheric effects similarly to the previous case. However, the fitting function failed to accurately capture the foreground and ionospheric parameters, as indicated by the statistically significant magnitude of the residual (Fig. 4.22). We also applied ANN to fit the same data sets for both scenarios, resulting in ANN-predicted parameters that closely approximated the true values of the parameters, see Tab. (4.10, 4.11) and reconstructed 21-cm signals in Fig. 4.21 and 4.22, accompanied by residuals from the true input signals.

Parameter	**True**	**Analytical** (Simult.)	**Analytical** (Indiv. ± Unc.)	**ANN**
J_{ref}	**11.6900**	-5.64×10^5	$(0.0036 \pm 8.74)\times10^7$	11.5351
J_{z0}	**18.5400**	5.89×10^3	$9.18 \pm 2.75\times10^3$	18.5470
X_{z0}	**8.6800**	7.92×10^5	9.14 ± 0.22	8.5926
T_{z0}	**9.7700**	6.34×10^5	10.50 ± 0.37	9.8942
J_{dz}	**3.3100**	6.39×10^4	2.21 ± 0.21	3.3012
X_{dz}	**2.8200**	-7.91×10^4	2.96 ± 0.44	2.8133
T_{dz}	**2.8300**	6.72×10^2	1.50 ± 0.37	2.8163
a_0	**3.30942**	3.30940	$3.30941 \pm 3.48\times10^{-7}$	3.31261
a_1	**-2.40960**	-2.40963	$-2.40959 \pm 2.57\times10^{-6}$	-2.41448
a_2	**-0.08062**	-0.08059	$-0.08054 \pm 9.02\times10^{-6}$	-0.08063
a_3	**0.02898**	0.02905	$0.02909 \pm 9.53\times10^{-6}$	0.02897

Table 4.10: Comparison of true values, analytical fits (simultaneous and individual), and ANN predictions for signal and foreground parameters.

Parameter	**True Value**	**Analytical** (Simult.)	**Analytical** (Indiv. ± Unc.)	**ANN**
$\mathrm{J_{ref}}$	**11.6900**	-5.98×10^{2}	$10.9367 \pm 9.49\times10^{5}$	11.6877
$\mathrm{J_{z0}}$	**18.5400**	1.08×10^{2}	$12.1768 \pm 1.58\times10^{5}$	18.5304
$\mathrm{X_{z0}}$	**8.6800**	-5.55×10^{6}	$7.1700 \pm 4.91\times10^{5}$	8.6748
$\mathrm{T_{z0}}$	**9.7700**	9.78×10^{4}	$8.0830 \pm 2.82\times10^{4}$	9.7236
$\mathrm{J_{dz}}$	**3.3100**	-4.15	$3.2672 \pm 1.83\times10^{4}$	3.3036
$\mathrm{X_{dz}}$	**2.8200**	2.38×10^{5}	$2.0259 \pm 3.12\times10^{5}$	2.8140
$\mathrm{T_{dz}}$	**2.8300**	4.33×10^{3}	$0.3418 \pm 1.43\times10^{4}$	2.8284
$\mathrm{a_0}$	**3.30942**	3.30932	$3.30930 \pm 5.98\times10^{-6}$	3.30651
$\mathrm{a_1}$	**-2.40960**	-2.40946	$-2.40951 \pm 7.57\times10^{-6}$	-2.40808
$\mathrm{a_2}$	**-0.08062**	-0.08074	$-0.08071 \pm 3.48\times10^{-5}$	0.08063
$\mathrm{a_3}$	**0.02898**	0.03076	$0.03079 \pm 8.36\times10^{-5}$	0.02897
TEC	**10.0000**	1.0299	10.1183 ± 0.0076	9.9998
$\mathrm{T_e}$	**800.0000**	275.6359	813.7119 ± 0.8743	799.8309

Table 4.11: True values, analytical best-fit estimates (simultaneous and individual), and ANN predictions for the signal, foreground, and ionospheric parameters.

Appendix B: Comparison with Other Existing Techniques

We evaluated the accuracy of our ANN predictions in comparison to other methods by calculating the Mean Absolute Percentage Error (MAPE) detailed in Tab. 4.12. Our study demonstrated that while some prior techniques performed well with simpler signal models (those with fewer free parameters), they faltered when dealing with more complex signal models requiring additional parameters. In contrast, the ANN model consistently outperformed these methods. Tab. 4.12 demonstrates that our ANN predictions exhibited less than 5% error across all parameters, regardless of the signal scenarios, including foreground with ionospheric effects. For the physical signals, except for one parameter with more than 10% error, all other parameters are accurately constrained, with most falling below the range of 5% to 1.0% error.

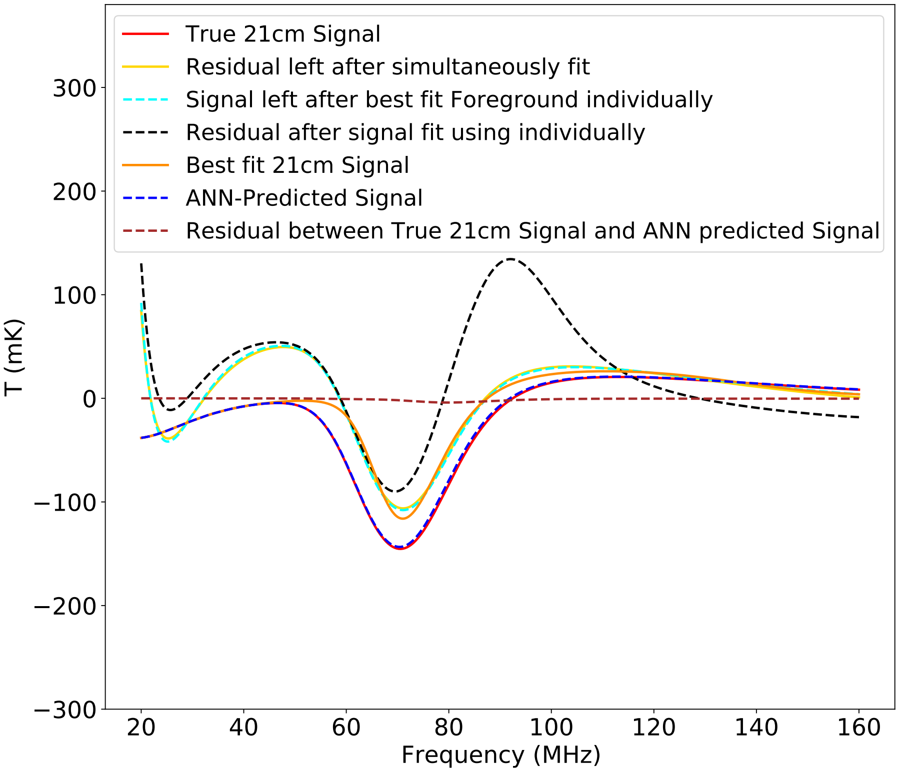

Figure 4.21: In this figure: true 21-cm signal (solid red line); residual after simultaneous fitting of signal and foreground (yellow solid line); residual after fitting foreground individually (cyan dashed line); best-fitted 21-cm signal from foreground residual (orange solid line); ultimate residual after fitting both foreground and signal individually (black dashed line). Signal reconstructed with ANN predicted parameters (blue dashed line) and residual between the true 21-cm signal and ANN reconstructed signal (brown dashed line).

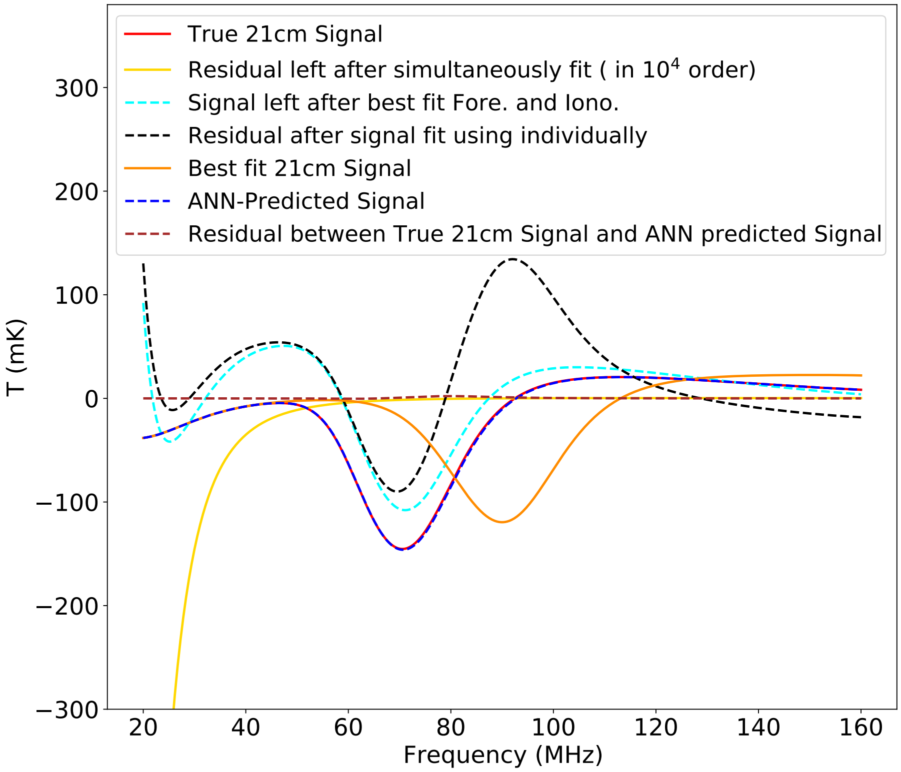

Figure 4.22: In this figure: true 21-cm signal (solid red line); residual after simultaneous fitting of signal, foreground, and ionospheric effects (yellow solid line); residual after fitting foreground and ionospheric effect individually (cyan dashed line); best-fitted 21-cm signal from foreground residual (orange solid line); ultimate residual after fitting both foreground with ionospheric effects and signal individually (black dashed line). Signal reconstructed with ANN predicted parameters (blue dashed line) and residual between the true 21-cm signal and ANN reconstructed signal (brown dashed line).

Method	Data & Parameters	MAPE (Selected Parameters)
MCMC [114]	Signal Only (Turning Point Model): $(\nu_B, T_B, \nu_C, T_C, \nu_D, T_D)$	ν_B: 3.77, $\mathbf{T_B}$: 591.43, ν_C: 0.50, T_C: 12.28, ν_D: 0.22, $\mathbf{T_D}$: 39.15
SVD+MCMC [161]	Flattened Gaussian + TP Model w/ Foreground: (A, ν_0, w, τ) Turning Points: $(\nu_A, T_A, ..., \nu_E)$	FG: A: 0.050, ν_0: 0.003, w: 0.052, τ: 0.683 TP: ν_A: 14.19, $\mathbf{T_A}$: 42.01, ν_E: 1.75
SVD+MCMC [162]	Signal + Foreground + Instrument Effects (Turning Point Model): $(\nu_B, T_B, \nu_C, T_C, \nu_D, T_D)$	ν_B: 0.011, $\mathbf{T_B}$: N.C., ν_C: 0.754, T_C: 1.942, ν_D: 0.278, $\mathbf{T_D}$: N.C.
Scipy Fit [12]	Signal + Foreground + Ionosphere (Gaussian Model): (A, μ, σ)	F-layer: A: 18.87, μ: 0.77, σ: 6.95 D-layer: $\mathbf{A}$: 24.53, μ: 5.69, σ: 66.85
MSF / PSF / Poly [163]	Global 21-cm Signal (Simulated)	TP Count in Residuals: MSF: 56, PSF: 99, Poly($N = 5$): 100
This Work (ANN)	Signal + Foreground + Ionosphere 1) Parametric Model: $(J_{\text{ref}}, J_{z0}, ..., \text{TEC}, T_e)$ 2) Physical Model: $(f_{xh}f_x, f_{\text{star}}, f_{\text{esc}}, N_\alpha, a_0, ..., T_e)$	1) MAPE: All $< 5\%$ 2) $f_{xh}f_x$: 13.31, f_{esc}: 4.91, a_1: 0.33, etc.

Table 4.12: Comparison of methods used for global 21-cm signal parameter extraction, with Mean Absolute Percentage Error (MAPE) of key parameters. Bold values indicate MAPE > 20 or unconstrained (N.C.).

Chapter 5

Comparing sampling techniques to chart parameter space of 21 cm Global signal with Artificial Neural Networks

Adapted from: ***Anshuman Tripahi***, *Gursharanjit Kaur, Abhirup Datta, Suman Majumdar "Comparing sampling techniques to chart parameter space of 21 cm Global signal with Artificial Neural Networks, Volume 2024, number 10, Pages 041,* *10.1088/1475-7516/2024/10/041*

Understanding the first billion years of the universe requires studying two critical epochs: the Epoch of Reionization (EoR) and Cosmic Dawn (CD). However, due to limited data, the properties of the Intergalactic Medium (IGM) during these periods remain poorly understood, leading to a vast parameter space for the global 21cm signal. Training an Artificial Neural Network (ANN) with a narrowly defined parameter space can result in biased inferences. To mitigate this, the training dataset must be uniformly drawn from the entire parameter space to cover all possible signal realizations. However, drawing all possible realizations is computationally challenging, necessitating the sampling of a representative subset of this space. This study aims to identify optimal sampling techniques for the extensive dimensionality and volume of the 21cm signal parameter space. The optimally sampled training set will be used to train the ANN to infer from the global signal experiment. We investigate three sampling techniques: random, Latin hypercube (stratified), and Hammersley sequence (quasi-Monte Carlo) sampling, and compare their outcomes. Our findings reveal that sufficient samples must be drawn for robust and accurate ANN model training, regardless of the sampling technique employed. The required sample size depends primarily on two factors: the complexity of the data and the number of free parameters. More free parameters necessitate drawing more realizations. Among the sampling techniques utilized, we find that ANN models trained with Hammersley sequence sampling demonstrate greater robustness compared to those trained with Latin hypercube and Random sampling.

5.1 Introduction

The ΛCDM (Lambda Cold Dark Matter) cosmological model asserts that the initial structures in the universe formed during the Cosmic Dawn as hydrogen gas collapsed under the effect of gravity. The ultraviolet (UV) photons emitted by the first luminous sources initiated the ionization of the surrounding intergalactic medium (IGM), causing the last transition phase in the universe's evolution. This phase transition period is called the Epoch of Reionization (EoR) [18,126,156,164]. Due to the lack of observational data at these high redshifts, the characteristics and timeline of the EoR remain poorly constrained. The HI 21cm signal stands out as a promising probe for exploring these uncharted redshift ranges. This signal originates from the hyperfine splitting of the ground state of the hydrogen atom, which arises from the spin alignments of the proton and electron [38, 55, 165]. The "spin-flip" transition responsible for the signal is inherently forbidden. Nevertheless, an abundance of hydrogen in the universe makes it an important astrophysical probe [166].

However, there are several challenges in observing the signal. The 21 cm signal is overshadowed by the foregrounds, 10^4 times brighter than the signal in the redshifted frequency range. The foregrounds are predominantly due to galactic synchrotron emission. These foregrounds, along with the ionospheric effects and the instrument response to the observation, pose a significant challenge to the detectability. Two distinct experimental techniques are used for observing these faint cosmological signals. One approach involves single-radiometer, as seen in experiments like Experiment to Detect the Global Epoch of Reionization Signature (EDGES, [167]), Shaped Antenna Measurement of the Background Radio Spectrum (SARAS, [40, 168]), Radio Experiment for the Analysis of Cosmic Hydrogen (REACH, [41]) and Large-Aperture Experiment to Detect the Dark Ages (LEDA, [43]). Alternatively, interferometers such as the Giant Meterwave Radio Telescope (GMRT, [44]), Hydrogen Epoch of Reionization Array (HERA, [47]), Low-Frequency Array (LOFAR [63]), and the upcoming Square Kilometer Array (SKA, [64]) are utilized. Recently, EDGES has reported a possible detection of the sky-averaged global 21 cm signal with an unexpectedly deep absorption trough at 78 MHz [168]. The depth is more than twice what the standard cosmology model predicted. If true, the signal can give new insights into the physics of the reionization era. However, another independent experiment, SARAS, has challenged this detection, suggesting that the anomalous result might be due to uncalibrated systematics [167]. Thus, it emphasizes that correctly modelling and removing the corruption from the signal is essential.

Over recent years, machine learning (ML) algorithms have gained extensive popularity in signal modelling and parameter estimation. For signal modelling, approaches such as those by [111,113,135,137–139] leverage Artificial Neural Networks (ANN) to model the 21cm signal across various aspects. Simultaneously, [13, 50, 86, 87, 169] employ ANN algorithms to extract parameters linked to the signal. Additionally, simulation-based inference (SBI) techniques, leveraging deep learning, are increasingly preferred for astrophysical inference from cosmic 21 cm signals, particularly for retrieving posteriors of astrophysical parameters via likelihood-free Bayesian inference directly from power spectrum and light-cone image analysis [170–174]. [175] introduced the Solid Harmonic Wavelet Scattering Transform (WST) and "3D ScatterNet" to enhance the inference of astrophysical parameters. Apart from the ML algorithm, several traditional methods are used to remove the signal and associated parameters [114,161–163]. Currently, due to limited observational constraints on intergalactic medium (IGM) properties, there is no singular and firmly established set of quantities to parameterize the underlying astrophysical processes shaping the signal. Several potential parameters have been suggested in various proposed models of the signal[108, 176–178].

Previously, [13, 50, 86] successfully developed and presented an ANN model capable of extracting astrophysical parameters of the 21 cm signal from mock observation data sets. These models considered limited sets of possible signal combinations, incorporating the effects of foregrounds, ionosphere, instruments, and noise. To develop a robust ANN model for foreground removal, it is crucial to consider all possible varieties of signals in the training set [177]. However, considering all the possible signal combinations will be computationally expensive. To address this issue, in this study, we create a sub-sample from the entire signal parameter space, ensuring it represents the overall parameter space using various sampling methods. Nonetheless, there are no straightforward rules to determine the optimal sampling technique and identify the minimum number of samples required for training the ANN model in a robust and accurate manner, which poses uncertainties. Addressing these questions requires a more in-depth exploration.

To address these questions, this study explores three distinct sampling methods—Random (Rand) sampling, Latin hypercube sampling (LHS), and Hammersley sequence sampling (HSS)—to comprehensively map the parameter space and generate various global 21cm signal types. We also analyzed the minimum number of samples required to train the ANN effectively, ensuring its robustness across different signal types. Furthermore, our investigation aims to understand the efficiency of these sampling algorithms and determine the minimum training data size needed to achieve consistent accuracy as the parameter space dimensionality and dataset complexity increase, particularly with the addition of foreground and thermal noise to the global 21cm signal. Additionally, we conducted generalizability tests by generating multiple training datasets through repeated parameter space sampling. The ANN was trained multiple times with these datasets and subsequently tested with unknown datasets generated using various sampling methods. This approach allows us to examine the consistency of the sampling algorithms in effectively covering the parameter space and to understand the clustering issues associated with these sampling methods by examining the consistency of the ANN's predictions.

This paper is structured as follows: Section 5.2 outlines the observable aspects of the HI 21cm Signal. Section 5.3 delves into the observational challenges, while Section 5.4 describes the methods for simulating the global 21cm signal. Section 5.5 covers sampling techniques, and Section 5.6 provides a basic overview of ANN. Section 5.7 discusses the training and test datasets for the ANN, and Section 5.8 outlines the results, including a discussion of the ANN predictions. The final section, Section 5.9, comprises the summary and overall discussions.

5.2 HI 21cm Signal

The 21cm signal arises because of hyperfine splitting of 1S ground level of hydrogen atom due to the interaction of magnetic moments of electrons and protons. Commonly, this transition is known as the spin-flip transition, where the spin transition from parallel to anti-parallel takes place. This transition results in the spontaneous emission of 21cm photon.

A single dish experiment measures the brightness temperature of the signal T_b in contrast to the background temperature of Cosmic Microwave Background (CMB), T_{CMB}; this is called the differential brightness temperature:

$$\delta T_b \approx 27(1 - x_{HI}) \left(\frac{\Omega_b h^2}{0.023} \right) \left(\frac{0.15}{\Omega_{m,0}} \frac{1+z}{10} \right)^{1/2} \left(1 - \frac{T_{CMB}(z)}{T_s} \right) \tag{5.1}$$

where x_{HI} is the neutral fraction of hydrogen, Ω_b and Ω_m are the baryon and total matter density, respectively, in units of the critical density, $H(z)$ is the Hubble parameter at redshift z and, T_s is the spin temperature of neutral hydrogen.

The spin temperature, which is the relative populations of hydrogen atoms in the two spin states, is decided by competition between 3 processes and their corresponding physical quantities: (1) absorption of CMB photons and stimulated emission; T_{CMB}, the temperature of CMB, (2) collisions with other hydrogen atoms (H-H), free electrons (H-e), free hydrogen nuclei (H-p); T_k, Kinetic gas temperature of IGM, and (3) scattering of Lyman- α photons, T_α, colour temperature for Wouthuysen–Field effect. The spin temperature, T_s is calculated as [55][179]:

$$T_s^{-1} = \frac{T_{CMB}^{-1} + x_k T_k^{-1} + x_\alpha T_\alpha^{-1}}{1 + x_k + x_\alpha} \tag{5.2}$$

Here, x_k, x_α are collisional and Lyman- α coupling coefficients. Thus, the global signal evolves over the redshift range as a function of the properties of IGM.

5.3 Observational Challenges

Observing the redshifted 21cm signal poses challenges due to various observational obstacles, including bright foregrounds, ionospheric effects, beam chromaticity, thermal noise, and radio frequency interference (RFI). In this study, our primary focus is on addressing two specific challenges: the impact of foreground and thermal noise, while simulating observations to construct the training datasets.

5.3.1 Foregrounds

About 70% of the foregrounds obscuring the 21 cm signal come from galactic synchrotron sources, and the rest are free-free emissions and thermal dust emissions. Extragalactic foregrounds are primarily caused by radio emission from star-forming galaxies. There are two ways to deal with the foreground: avoiding and removing it. The former can be applied for interferometric observations but not for the global 21cm signal. For global 21cm experiments, the foregrounds must be modelled and removed. The foregrounds are spectrally smooth compared to the global 21cm signal. The high coherence of the diffuse galactic foregrounds across frequency compared to the signal can be used for foreground subtraction [78]. Due to their spectral smoothness, the foregrounds can be modelled as a low-order polynomial [126]. In this study, we simulated the diffuse foreground using a third-order polynomial in $log(\nu) - log(T)$, as previously described by [86, 150].

$$\log(T_{FG}) = \sum_{i=0}^{n} a_i \left(\log\left(\frac{\nu}{\nu_0}\right)\right) \tag{5.3}$$

where $\nu_0 = 80$ MHz. The four foreground parameters, constants of the $log(\nu) - log(T)$ polynomial, are varied around their inferred value by [150], $a_0 = \log(T_0) = 3.30955$; $a_1 = -2.42096$; $a_2 = -0.08062$; $a_3 = 0.02898$.

5.3.2 Thermal Noise

The thermal noise, denoted as $n(\nu)$, in the observed spectrum can be expressed using the ideal radiometer equation in the following manner:

$$n(\nu) \approx \frac{T_{sys}(\nu)}{\sqrt{\delta\nu \cdot \tau}}, \tag{5.4}$$

In this context, $\mathrm{T_{sys}}(\nu)$ represents the system temperature, $\delta\nu$ is the observational bandwidth, and τ denotes the observation time.

5.4 Models for the Global 21cm Signal

To simulate the global 21cm signal, we employed two distinct models. The first model is based on a parametrized model, while the other utilizes a semi-numerical astrophysical approach. Further details are provided below:

5.4.1 *tanh* Parametrization Model

We have used the tanh model to simulate the global 21 cm signal during the cosmic dawn (CD) and the EoR using ARES [180]. The model uses simple parametric forms for the Lyman α background, IGM temperature, and re-ionization histories [181]. This method models the signal using IGM properties like the strength of Lyman α coupling, $J_\alpha(z)$; the temperature of the IGM, $T(z)$; and ionization fraction, $\overline{X}_i$, but does not take into account the source properties. Each of these quantities is evolved as:

$$A(z) = \frac{A_{ref}}{2}\left(1 + tanh\left(\frac{z_0 - z}{\Delta z}\right)\right) \tag{5.5}$$

Here A_{ref} is the step height, z_0 is the pivot redshift, and Δz is the width. The quantities become zero at high redshift, turn on for a redshift interval Δz around a z_0, the central redshift, and achieve maximum A_{ref} saturation at low redshift.

The step height, A_{ref}, in units of 10^{-21} $\text{ergs}^{-1}\text{cm}^{-2}\text{Hz}^{-1}\text{sr}^{-1}$ corresponding to the Lyman α ($Ly\alpha$) background is J_{ref}. It saturates at low redshift, with a value of 11.69, as determined by [181] using MCMC parameter estimation. In our study, we treat it as a constant, as done in our work. The redshift interval and pivot redshift for $Ly\alpha$ background tanh parametrization are J_{dz} and J_{z0} respectively. Similarly, for X-ray heating, the temperature of IGM, $T(z)$, T_{dz} and T_{z0} denotes redshift interval and central redshift in units of Kelvin. The amplitude, A_{ref}, corresponding to IGM temperature, represented by T_{ref}, saturates at around 1000K. For the ionization fraction, $\overline{X}_i$, the natural value for step height is unity. The redshift interval Δz and the pivot redshift z_0 over which ionization takes place are given by X_{dz} and X_{z0}, respectively. The values for these parameters inferred by [181] are: $J_{dz} = 3.31$, $J_{z0} = 18.54$, $T_{dz} = 2.82$, $T_{z0} = 9.77$, $X_{dz} = 2.83$, $X_{z0} = 8.68$.

5.4.2 Astrophysical Model

We used a semi-numerical model which simulates the global signal based on the evolution of the properties of the IGM during the EoR, described in [182]. The astrophysical input parameters to simulate the global 21 cm signal from the Cosmic Dawn are the following:

1. Star formation efficiency, f_*: A high value of star-forming efficiency implies earlier cosmic heating and a shallower absorption feature;
2. The escape fraction of the ionizing photons into the IGM, f_{esc}: The number of ionizing photons able to reach the IGM decides the duration of the reionization;
3. X-ray heating efficiency, f_X: The efficiency of X-ray sources to heat the IGM decides the depth of the absorption trough. For high values of f_X, the shallower absorption feature is shifted to higher redshifts;
4. Number of Ly α photons produced per baryon, N_α: The Lyman α background emission depends upon the metallicity of the stars;

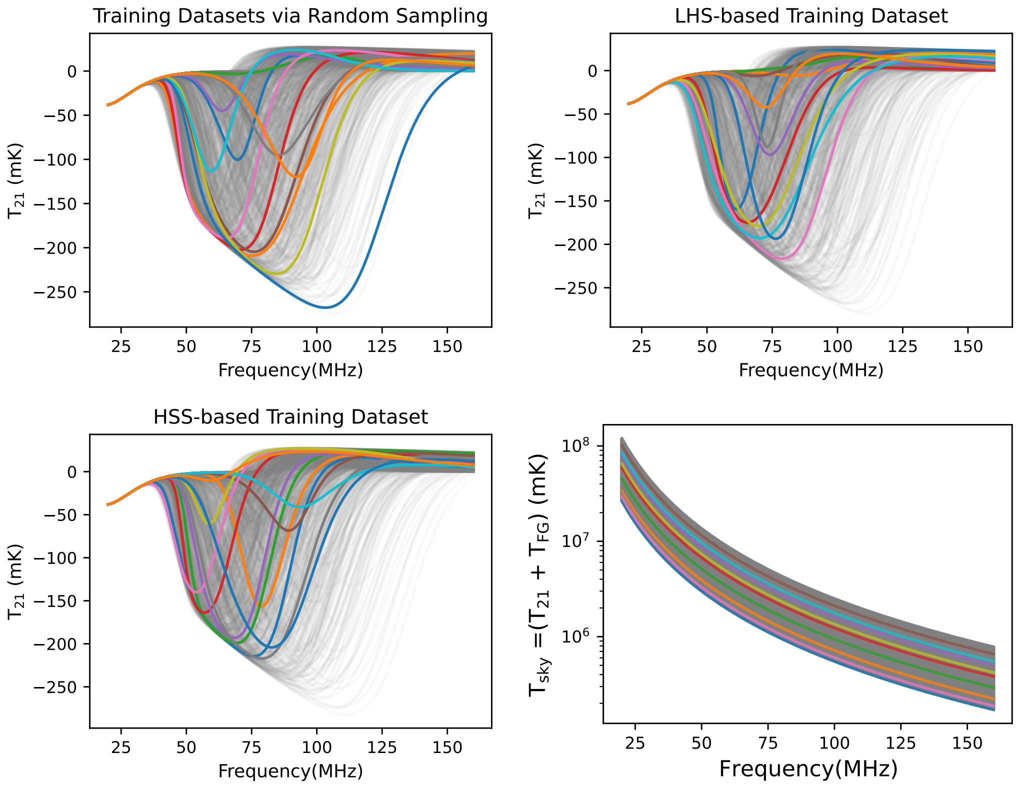

Training Datasets via Random Sampling

LHS-based Training Dataset

HSS-based Training Dataset

Figure 5.1: Each subplot illustrates training datasets for the global 21cm signal, constructed using Random, Latin hypercube, and Hammersley sequence sampling methods, respectively, for the parametrized signal. The final subplot depicts training datasets with added foreground and thermal noise. Signal subsets are highlighted in color, while the remaining sets are displayed in gray as the background.

The parameters are described in detail in [13, 182]. Due to the limited observation for detecting the 21 cm signal from the Cosmic Dawn, the astrophysical parameters and the IGM properties still need to be determined. Some of the astrophysical parameters are poorly constrained, like the optical depth of the CMB by Planck data [183]. Thus, the astrophysical parameters can have any value within an extensive range. For this work, we have assumed the following ranges for the parameters to simulate the different realization of the global 21cm as tabulated in Tab. 5.1.

5.5 Sampling the parameter space

To train artificial neural networks (ANNs) or any machine learning model for parameter extraction from the 21 cm signal, a comprehensive training set is required, ideally covering all possible signal templates. As described earlier, the challenge is the computational power required to construct such a gallery, given that the parameters governing the signal theoretically span large ranges. The problem can be tackled by considering a sub-sample of the parameter space that optimally covers the range of all parameters. For instance, Cohen 2017 [177] computed 193 signal realizations for different sets of astrophysical parameters. For this work, we consider and compare three different sampling techniques to optimally sample the parameter space of the global 21 cm signal:

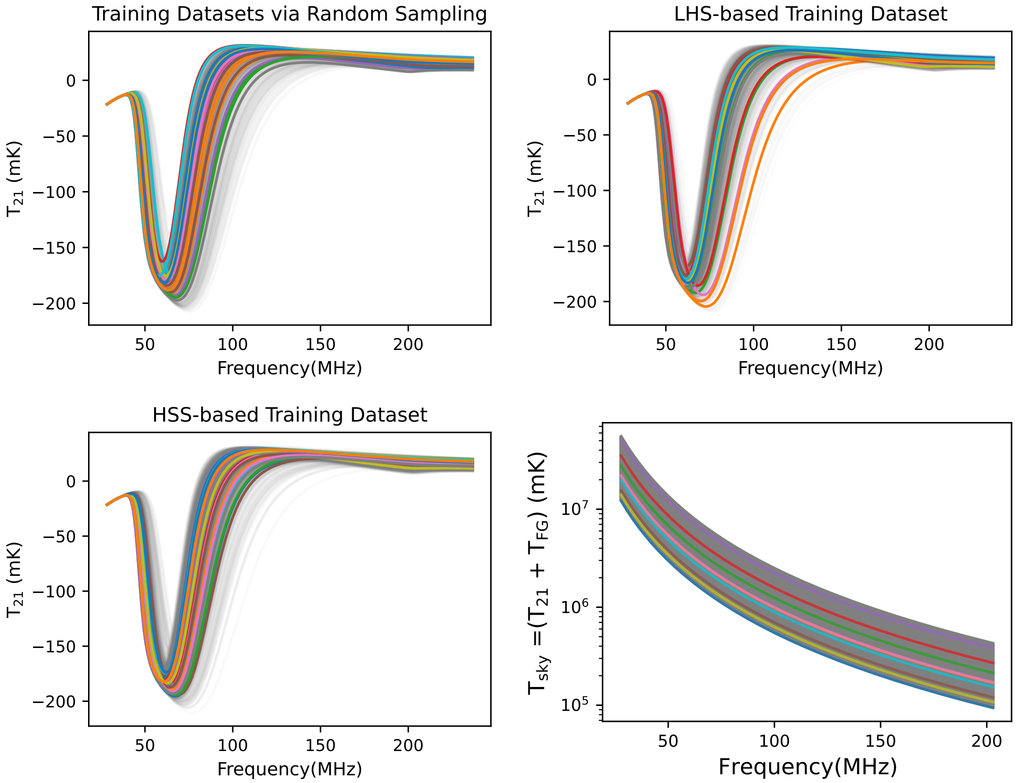

Figure 5.2: Each subplot illustrates training datasets for the global 21cm signal, constructed using Random, Latin hypercube, and Hammersley sequence sampling methods, respectively, for the physical signal. The final subplot depicts training datasets with added foreground and thermal noise. Signal subsets are highlighted in color, while the remaining sets are displayed in gray as the background.

5.5.1 Random sampling

Random sampling is the commonly used sampling to ensure an unbiased selection of points in the parameter space. Each parameter is assumed to have a uniform probability distribution. This implies that each possible value within the parameter space has an equal likelihood of being selected during the sampling process.

5.5.2 Latin hypercube sampling

Latin hypercube sampling (LHS) is a type of stratified sampling [123]. In LHS, the range of each input parameter is divided into N intervals having equal marginal probability $\frac{1}{N}$. The key idea is to ensure an even and representative sampling of the entire parameter space. For each parameter, N samples are drawn at random from each interval. In the case of a Latin square with only two parameters x and y, the x_i, y_i, for $i = 1, 2, ..., N$ are sampled independently. The samples taken from each parameter are matched at random as (x_i, y_j) for $i, j = 1, 2, ..., N$. A Latin hypercube extends this concept to higher-dimensional spaces. Simple Latin hypercube design and its variant have been commonly used in computer experiments designed for their space-filling properties. In cosmology, the use of LH algorithms has been explored for the construction of training sets for emulators [111, 113, 135, 184].

LHS has certain merits over random sampling. Random sampling could lead to the clustering of points in specific regions of the parameter space, thereby creating an uneven representation across different regions. LHS ensures an even coverage of the whole parameter space by spreading the sample points over the entire range of each parameter. Furthermore, LHS can achieve this goal with a relatively small number of samples compared to random sampling.

5.5.3 Hammersley sequence sampling

Hammersley sequence sampling (HSS) is a sampling method developed by Kalagnanam and Diwekar [124] to address certain limitations associated with other sampling methods, particularly in the context of quasi-monte carlo methods and numerical integration. Low discrepancy sequences (LDS) like Hammersley sequences are one of the solutions to achieve a distribution of points with low discrepancy, where discrepancy is a metric for the deviation from a uniform distribution. The low discrepancy sequences have a deterministic structure as opposed to the stochastic nature of the random sampling, meaning that the sequence of points is fully determined by the number of points and the dimensionality of the space. Notably, in scenarios involving large-dimensional parameter spaces, the HSS demonstrates good uniformity over the Latin hypercube sampling [185].

To construct a Hammersley sequence sample, n relatively prime numbers (integers that have no common divisors other than 1) are chosen: $p_1, p_2, .., p_n$. Each non-negative integer k can be expressed with a prime base p

$$k = a_0 + a_1 p + a_2 p^2 + a_3 p^3 + ... \tag{5.6}$$

where, a_i is an integer in [0, p − 1]. Subsequently, the following expression is computed for each prime p:

$$\phi_p(k) = \frac{a_0}{p} + \frac{a_1}{p^2} + \frac{a_2}{p^3} + ... \tag{5.7}$$

For d dimensions, the k^{th} d-dimensional Hammersley's point is $(\frac{k}{n}, \phi_{p_1}(k), \phi_{p_2}(k), ..., \phi_{p_{d-1}}(k))$ for $k = 0, 1, 2, ..., n1$,where n is the total number of Hammersley's points and $p_1 < p_2 < ... < p_{d1}$. HSS finds its main applications in computer graphics and design optimization. This work is the first to employ this sampling method in the context of cosmology.

5.6 Artificial Neural Networks

Artificial neural networks (ANNs) are widely used supervised machine learning algorithms, with applications increasingly found in cosmology as well. Mathematically, for a given set of $[x_i, y_i]$, ANNs try to find a function, f(x), such that $y_i = f(x_i)$ through a series of weighted summations. This operation occurs in a series of layers. The neurons are the building blocks of the ANN. The ANN contains n number of layers, with one input layer, one output layer, and n-2 hidden layers. The input values x_i with D dimensions are given to the first layer with D nodes. The output from one layer a_i goes to the next layer's j^{th} neuron as input a_j. The computation for the activation of the $j^t h$ neuron in layer $l + 1$ is given by:

$$a_j^{l+1} = h\left(\sum_{i=1}^{D} w_{ji} a_i^l + w_{j0}\right) \tag{5.8}$$

Here, h represents the activation function, l denotes the layer index, and a refers to the inputs for the corresponding layer. For l= 0, $a_i^0 = x_i$ which represents the input values for the first layer. The terms w_{ji} and w_{j0} are weights and biases associated with the neuron set, respectively. There is no activation function used in the output layer.

The aim is to train the model to minimize the loss function, i.e., finding the weight values that mimic the function. It involves updating the weights with an optimizer using back-propagation to reduce the loss at a rate called the learning rate. The default loss function in the training of ANNs, including in this work, is the Mean Squared Error (MSE), given by:

$$\mathrm{MSE} = \frac{1}{n}\sum_{i=1}^{n}(y_i - \hat{y}_i)^2 \tag{5.9}$$

Here, n is number of samples, y_i is the true output label and $\hat{y}_i$ is the prediction after updating the weights, w_{ji}, and biases, w_{j0}, with every iterations of the ANNs. The prediction $\hat{y}_j$ for the j^{th} neuron in the output layer is calculated as:

$$\hat{y}_j = \sum_{i=1}^{D} w_{ji} \cdot a_i^{L-1} + w_{j0} \tag{5.10}$$

Here, L is the index of the final layer. Most optimizers are based on the gradient descent method of loss optimization.

The number of layers, number of neurons in each layer, learning rate, and activation function are to predecided. These parameters are known as hyperparameters. We can search over a range of hyperparameters and use the ones giving minimum loss and maximum accuracy. In this work, Scikit-learn [1] and Keras[2] are used for building an ANN. We optimized hyperparameters using trial and error to determine the best architecture for the ANNs. Details of the final architecture are provided in the following section.

5.6.1 Metric of accuracy

For testing and validating the data set, RMSE and R-squared value is used as a measure to see the difference between predictions of input parameters made by the model for testing data and the actual value.

If N samples are there for testing, and $\mathrm{y_{true}}, \mathrm{y_{pred}}$ are the actual and predicted value of the parameter, $\bar{\mathrm{y}}_{\mathrm{true}}$, mean of all actual values of the parameter. Then,

$$\mathrm{RMSE}(y_{true}, y_{pred}) = \sqrt{\frac{1}{N}\sum(y_{true} - y_{pred})^2} \tag{5.11}$$

$$R^2(y_{true}, y_{pred}) = 1 - \frac{\sum_{i=1}^{N}(y_{true} - y_{pred})^2}{\sum_{i=1}^{N}(\bar{y}_{true} - y_{true})^2} \tag{5.12}$$

5.7 Training and testing data set

In this work, we systematically explored parameter space using diverse sampling techniques to ensure comprehensive coverage. We generated a comprehensive array of global 21cm signals to

---

[1] https://scikit-learn.org/stable/

[2] https://keras.io/

	Parametrized		Physical	
	Parameters	Ranges	Parameters	Ranges
Signal	J_{z0}	9.27, 27.81	$f_x * f_{xh}$	0.0255, 7.9800
	X_{z0}	4.34, 13.02	f_{star}	0.0030, 0.0099
	T_{z0}	4.89, 14.65	f_{esc}	0.06, 0.19
	J_{dz}	1.65, 4.96	N_{α}	9000-800000
	T_{dz}	1.41, 4.23		
	X_{dz}	1.42, 4.25		
Foreground	a_0	2.97, 3.64	a_0	2.97, 3.64
	a_1	-2.45, -2.37	a_1	-2.45, -2.37
	a_2	-0.082, -0.079	a_2	-0.082, -0.079
	a_3	0.027, 0.030	a_3	0.027, 0.030

Table 5.1: The range of parameters used to build the training dataset for the Parametrized and Non-parametrized (Physical) cases of global 21cm signals and foregrounds.

enhance the robustness of our ANN model training. Additionally, we drew datasets of various sizes for each sampling method to determine the minimum sample size requirement for training the ANN more robustly and accurately. Our objective extended to evaluating the efficacy of various sampling methods in ANN training, described in section 5.5. Furthermore, we also check the robustness of these trained ANN models, which are trained with the different sampled datasets by testing them with test datasets sampled with other sampling methods, to understand whether the prediction accuracy of the final trained ANN model is consistent with any random sets of the datasets or not.

To perform the above operation, we used two different types of signal models, one parametrized and the other non-parametrized, based on the semi-numerical model, details described in section 5.4. In the parametrized model, we used 6 parameters to simulate the global 21cm signal, and for the non-parametrized model, we used 3 parameters to simulate the global 21cm signal. Incorporating these two distinct models not only introduced diversity in the signal parameters but also enabled the exploration of different dimensions within these parameters. Similarly, integrating foreground and noise into the dataset added complexity and increased the dimensionality of free parameters. We employed the same sampling methods used for the signal case to chart both signal and foreground parameters simultaneously.

5.7.1 Signal only

For this scenario, we simulated the training and testing datasets by sampling the parameter space of the global 21 cm signal, defined within a specific range of parameter values, using three distinct sampling methods. The signal simulated utilizing the physical model and tanh parametrization illustrated in Fig. 5.1 and 5.2, respectively.

We generated three datasets of varying sizes - 1000, 5000, and 10,000 samples - using given sampling methods. Subsequently, we utilized these datasets to train ANN models, aiming to analyze how the performance of the ANNs varies across these different dataset sizes. For the training of the ANN, we split these sampled datasets into a 7:3 ratio, allocating 70 % for training and reserving the remaining 30 % for network testing.

5.7.2 Foreground and thermal noise corrupted signal

In this scenario, our training dataset is created by exploring the parameter space of both the signal and foreground using the three given sampling methods. These sampled parameters are then utilized to construct the signal and foreground components. We utilized two different models to simulate the signal: the parametrized and physical models. We have simulated the foreground using a log-log polynomial model, as detailed in section 3. To simulate a realistic observational scenario spanning 1000 hours, we have added the thermal noise into the simulated signal and foreground datasets using the radiometer equation, resulting in the generation of our final training datasets. We generated three different dataset sizes: 10,000, 50,000, and 200,000 samples by drawing parameters from the specified ranges for the parametrized signal case. We created dataset sizes of 10,000, 50,000, and 100,000 samples for the physical case. Given the comparatively larger size of the datasets compared to scenarios where only the signal is considered, adhering to the common thumb rule, we have partitioned the datasets in a 9:1 ratio. Here, 90 % is designated for training the ANN model, while 10% is set aside for evaluating its performance, which should be sufficient. This split ensures an adequate representation of the variety of signals in the dataset, enhancing the accuracy and robustness of the model's predictions.

5.8 Results

In this study, we trained the ANN model under two scenarios: one with the signal alone and another that included the signal, foreground, and thermal noise. These datasets were generated using three unique sampling methods: Random sampling, Latin hypercube sampling, and Hammersley sequence sampling. To ensure accurate and robust training, we employed varying dataset sizes, as elaborated below. We also employed two distinct types of global signals generated by two different models: one based on parametrized modelling and the other referred to as non-parametrized to showcase ANNs generalizability. The detailed result for the non-parametric signal is showcased in Appendix 5.9.

5.8.1 Signal only

The model we use for training is constructed with Keras' Sequential API and comprises 1024 input neurons matching with 1024 frequency channels and three hidden layers with 64, 27 and 18 neurons, respectively; these hidden layers are activated by ReLU (Rectified Linear Unit) and 'tanh' activation function. The output layer has 6 neurons to predict the parametrized global 21cm signal parameters. The input training data sets are normalized and standardized with the 'MinMaxScaler' and 'StandardScaler' functions, and corresponding parameters are normalized using 'MinMaxScaler', available in Scikit-learn. We evaluated the performance of the trained ANN using a test dataset and assessed its prediction accuracy by calculating the R^2 and the RMSE.

The ANN trained with 1000 datasets achieved the overall R^2 score of 0.6744 for datasets sampled using HSS. For LHS, the overall R^2 score obtained is 0.6594, while for Random sampling, the R^2 score is obtained at 0.6367. Similarly, with 5000 datasets, the overall R^2 score of 0.9059 was achieved for datasets sampled using HSS. For LHS, the overall R^2 score obtained was 0.8937, while the overall R^2 score of 0.8837 was obtained for the dataset sampled using Random sampling. With 10,000 datasets, the overall R^2 score of 0.9259 was obtained for datasets sampled using HSS. For Random sampling, the overall R^2 score obtained was 0.9187, while the overall R^2 score of 0.9210 was obtained for the dataset sampled using LHS. The detailed results for each sampling method with the various dataset sizes, the R^2 and RMSE score for the individual parameters are listed

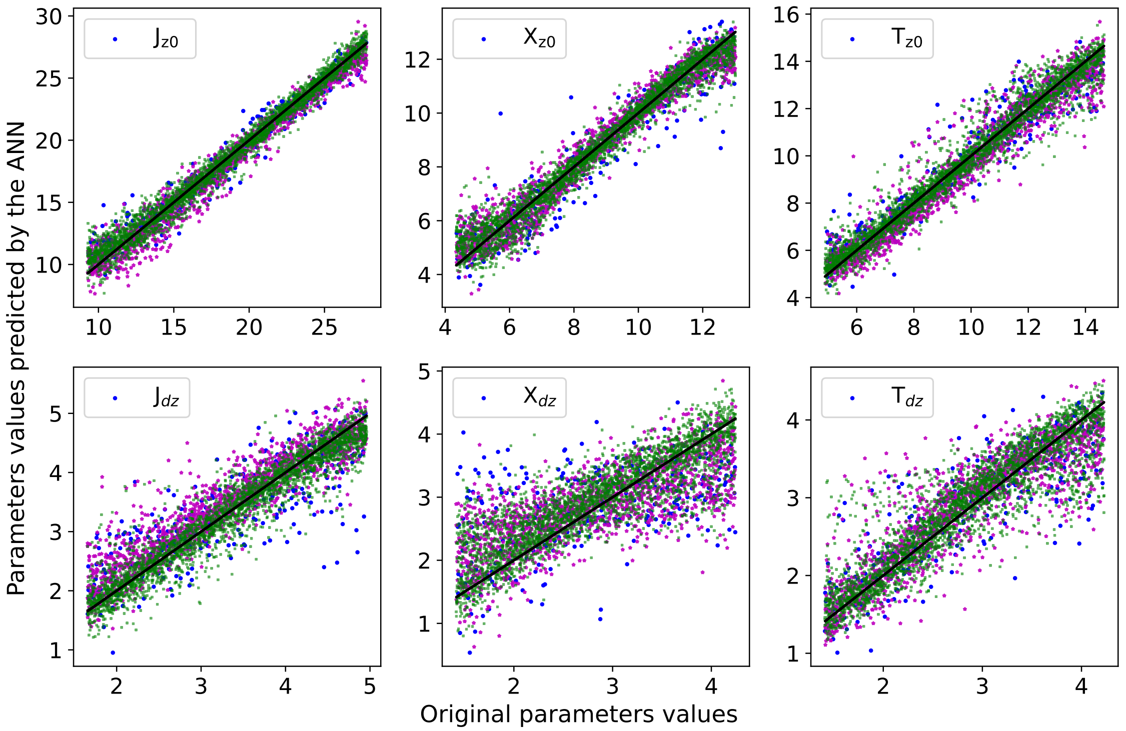

Figure 5.3: The scatter plots above show predicted signal parameter values obtained through an ANN model trained on the global 21cm signal. The signal data sets are generated by sampling the parameter space using Hammersley sequence sampling in three sizes: 1000, 5000, and 10,000 samples. Blue points in each scatter plot denote predictions made by the ANN trained with 1000 samples, while magenta and green points indicate predictions from ANN models trained with 5000 and 10000 samples, respectively. The true value of the parameters are plotted in solid black line in the each plot.

in Tab. 5.2 and Tab. 5.3. We also individually show the predicted parameter values against the original values for each sampling method across different dataset sizes. These visualizations are presented in Fig. 5.3 for HSS, Fig. 5.4 for LHS, and Fig. 5.5 for Random sampling.

Our investigation revealed that, across all three sampling techniques, the accuracy of the ANN improved with an increase in the number of training datasets. For example, when dealing with datasets consisting of 10,000 samples, all three sampling methods demonstrated significantly higher prediction accuracy compared to situations where the network was trained with 5,000 and 1,000 samples using the same techniques. Further details are provided in Tab. 5.2. Additionally, it was observed that ANN models trained with Hammersley sequence-sampled datasets achieved slightly higher overall R^2 scores for dataset sizes of 1000, 5000, and 10,000 compared to models trained with LHS and Randomly sampled datasets.

5.8.2 Signal and foreground with thermal noise

In this study, we trained an ANN using datasets that included signals corrupted with foreground and thermal noise. The addition of foreground into the global 21cm signal not only increases the complexity of the dataset but also expands the dimensionality of the parameter space. We followed

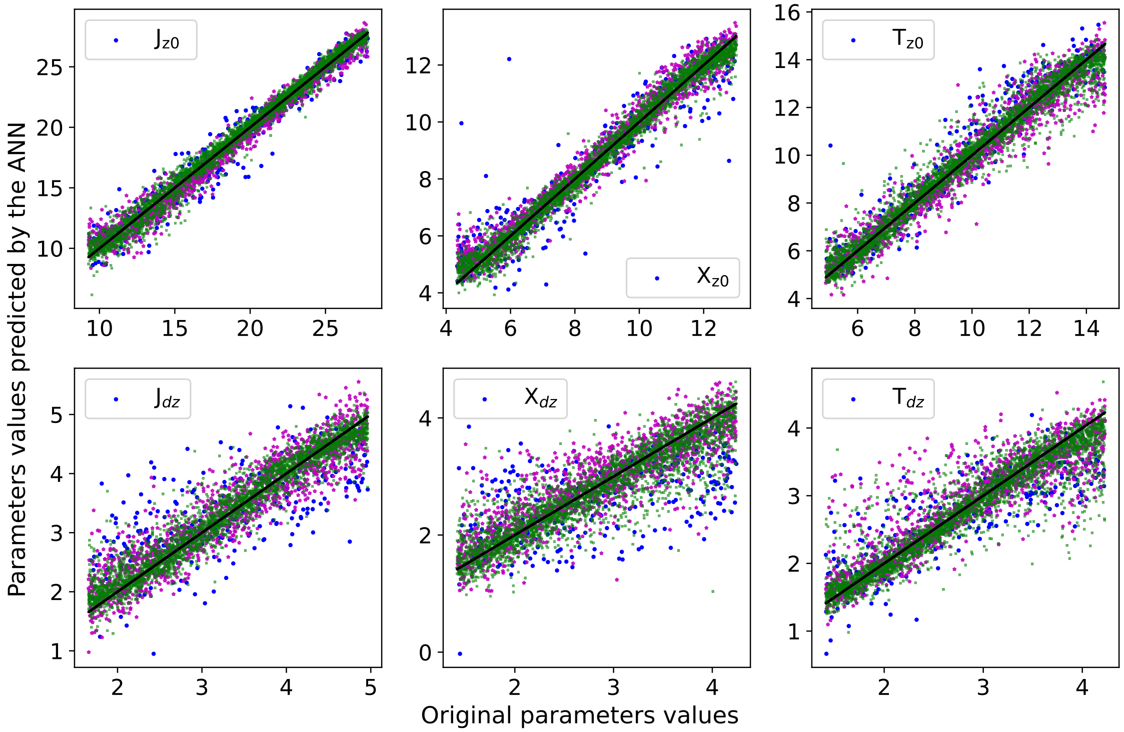

Figure 5.4: The scatter plots above show predicted signal parameter values obtained through an ANN model trained on the parametrized global 21cm signal. The signal datasets are generated by sampling the parameter space using Latin hypercube sampling in three sizes: 1000, 5000, and 10,000 samples. Blue points in each scatter plot denote predictions made by the ANN trained with 1000 samples, while magenta and green points indicate predictions from ANN models trained with 5000 and 10000 samples, respectively. The true values of the parameters are plotted in a solid black line in each plot.

Size		1000			5000			10000	
	HSS	LHS	Rand	HSS	LHS	Rand	HSS	LHS	Rand
Avg.	0.6744	0.6594	0.6379	0.9059	0.8937	0.8837	0.9259	0.9187	0.9210
J_{z0}	0.9471	0.9442	0.9389	0.9821	0.9780	0.9770	0.9868	0.9844	0.9859
X_{z0}	0.8797	0.8552	0.8687	0.9716	0.9681	0.9693	0.9751	0.9793	0.9758
T_{z0}	0.8589	0.8899	0.8908	0.9449	0.9431	0.9410	0.9686	0.9583	0.9615
J_{dz}	0.5514	0.4943	0.4107	0.9094	0.8790	0.8978	0.9323	0.9294	0.9258
X_{dz}	0.1942	0.1372	0.0807	0.7982	0.7759	0.7200	0.8395	0.8075	0.8161
T_{dz}	0.6151	0.6377	0.6377	0.8289	0.8180	0.7973	0.8450	0.8534	0.8607

Table 5.2: The computed R^2-scores for all signal parameters for predicted each case studied are listed here. We used the parametrized model to construct the global 21cm signal.

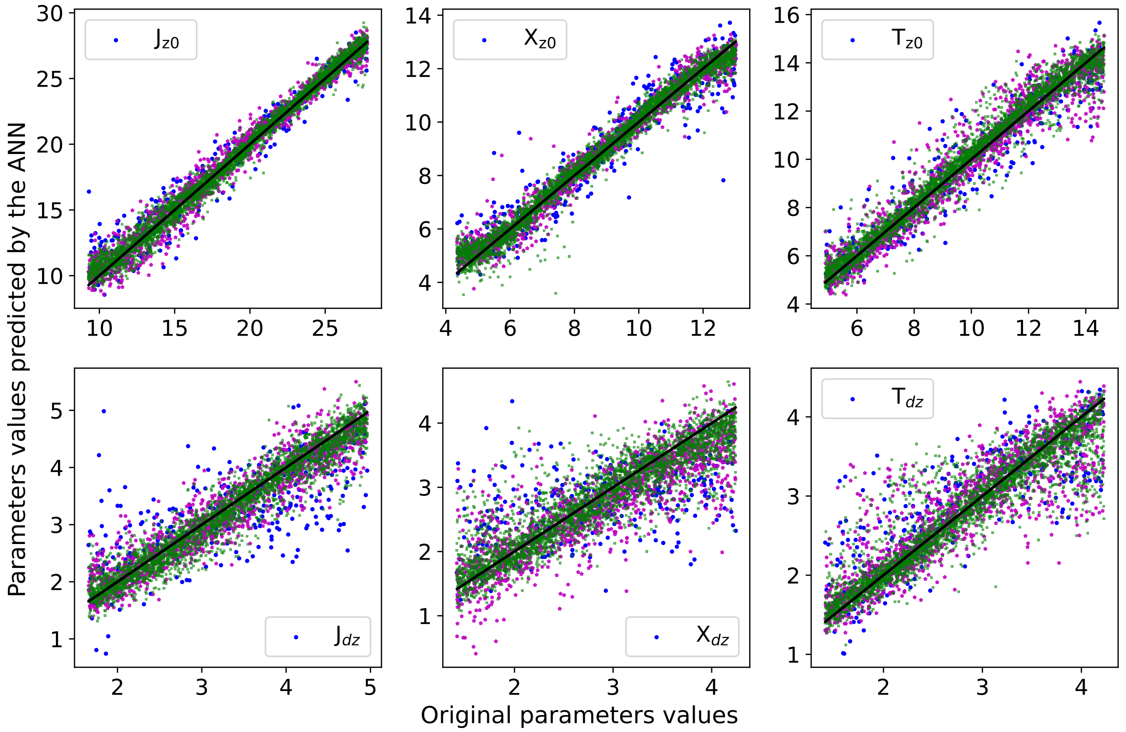

Figure 5.5: The scatter plots above show predicted signal parameter values obtained through an ANN model trained on parametrized the global 21cm signal. The signal data sets are generated by sampling the parameter space using Random sampling in three sizes: 1000, 5000, and 10,000 samples. Blue points in each scatter plot denote predictions made by the ANN trained with 1000 samples, while magenta and green points indicate predictions from ANN models trained with 5000 and 10000 samples, respectively. The true values of the parameters are plotted in a solid black line in each plot.

Size		1000			5000			10000	
	HSS	LHS	Rand	HSS	LHS	Rand	HSS	LHS	Rand
J_{z0}	0.0661	0.0679	0.0720	0.0392	0.0429	0.0447	0.0354	0.0356	0.0346
X_{z0}	0.1044	0.1137	0.1035	0.0502	0.0513	0.0508	0.0460	0.0420	0.0452
T_{z0}	0.1077	0.0944	0.0980	0.0680	0.0678	0.0716	0.0586	0.0588	0.0572
J_{dz}	0.1905	0.1997	0.2211	0.0876	0.1018	0.0920	0.0754	0.0772	0.0788
X_{dz}	0.2661	0.2740	0.2657	0.1303	0.1347	0.1527	0.1153	0.1265	0.1238
T_{dz}	0.1805	0.1710	0.1754	0.1186	0.1242	0.1294	0.1118	0.1118	0.1060

Table 5.3: The computed RMSE scores for all signal parameters for predicted each case studied are listed here. We used the parametrized model to construct the global 21cm signal.

a methodology similar to that used for signal data to construct our training datasets. We charted the parameter space for both the signal and foreground components using three different sampling methods. We generated three distinct dataset sizes for the parametrized signal: 10,000, 50,000, and 200,000 samples to explore the minimum sample size required to train the ANN for improved accuracy and robustness effectively. We pursued two distinct approaches to train the ANN with a signal corrupted by foreground and thermal noise. In the first method, we normalized and standardized with 'MinMaxScaler' and 'StandardScaler'; in the second method, we logarithmically scaled the training dataset. Subsequently, we normalized and standardized the datasets further. In the first case, we achieved better accuracy in recovering only two foreground parameters, a_1 and a_2, while the rest of the parameters are recovered poorly. In the second case, we successfully recovered all parameters with reasonable accuracy, except for the two foreground parameters a_1 and a_2, where the accuracy ranged from 50 % to 60 % in the best-case scenario. Based on these experiences, we decided to train two separate ANN models for both parametrized and physical cases. The first ANN model focused on the recovery of the two foreground parameters (a_1, a_2) without the use of logarithmically scaled datasets. For the remaining parameters, the second ANN model utilized logarithmically scaled datasets. A detailed description of the architectures of these ANN models is described below.

The first ANN model's architecture featured an input layer with 1024 neurons, aligning with the data's 1024 frequency channels. This was followed by two hidden layers with 64 and 16 neurons, respectively, and the output layer with 2 neurons to predict the two foreground parameters (a_1, a_2). In the case of the second ANN model, the input layer mirrored the first model with 1024 neurons. Following this, four hidden layers were introduced, consisting of 256, 64, 32, and 16 neurons. The output layer of the second ANN model comprised 8 neurons, each representing 6 signal parameters and 2 foreground parameters (a_0, a_3). In both models, each hidden layer utilized the Exponential Linear Unit (ELU) activation function. To mitigate overfitting, both ANN models employed the 'normal' kernel initializer and implemented L2 kernel regularization. Before training the ANN models in both scenarios, we normalized the parameters using the 'MinMaxScaler' scaling.

The ANN trained with 10,000 datasets achieved the overall R^2 score of 0.7534 for datasets sampled using LHS. For Random, the overall R^2 score obtained was 0.7307, while the R^2 score of 0.7307 was obtained for the dataset sampled using HSS. Similarly, with 50,000 datasets, the overall R^2 score of 0.8738 was achieved for datasets sampled using Random sampling. For LHS, the overall R^2 score obtained was 0.8679, while the overall R^2 score of 0.8673 was obtained for the sampled dataset using HSS. With 200,000 datasets, the overall R^2 score of 0.9296 was attained for datasets sampled using LHS. For HSS, the overall R^2 score obtained was 0.9139, while the R^2 score of 0.9016 was obtained for the sampled dataset using Random sampling. The detailed results for each sampling method with the various dataset sizes, the R^2 and RMSE score for individual parameters are listed in Tab. 5.4 and Tab. 5.5. We also individually showed the predicted parameter values against the original values for each sampling method across different dataset sizes. These visualizations are presented in Fig. 5.6 for HSS, Figure 5.7 for LHS, and Fig. 5.8 for Random sampling.

We noticed that as we increased the complexity and dimensionality of the problem, achieving an optimal solution with the ANN required drawing more sample sets to cover the entire parameter space. In contrast to the scenario where only the signal was considered, where optimal ANN prediction was achieved with 10,000 datasets, here, with the same number of datasets, we only achieved an accuracy of around $\sim 75\%$, regardless of the sampling method. For this particular case, to attain a similar level of accuracy in prediction, we found that drawing approximately 200,000 samples was necessary.

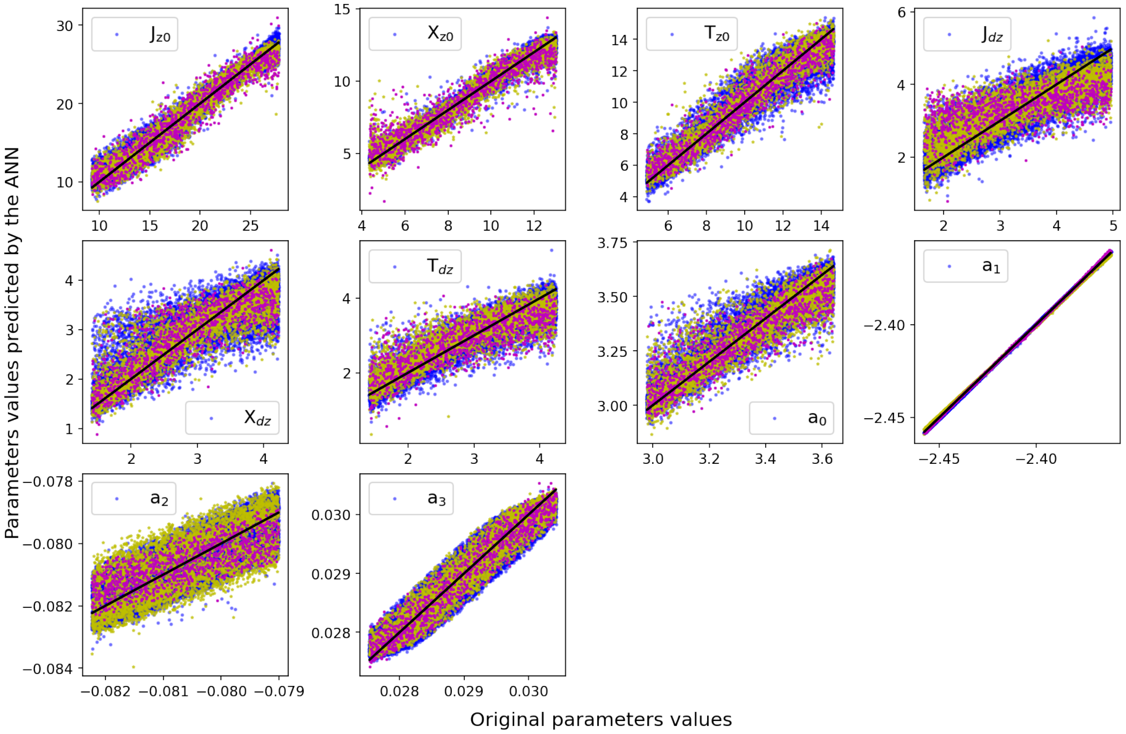

Figure 5.6: The scatter plots above show predicted signal and foreground parameter values obtained through an ANN model trained on a parametrized global 21cm signal. The signal and foreground data sets are generated by sampling the parameter space using Hammersley sequence sampling in three sizes: 10,000, 50,000, and 200,000 samples. Magenta scatter points in each scatter plot denote predictions made by the ANN trained with 10,000 samples, while yellow and blue scatter points indicate predictions from ANN models trained with 50,000 and 200,000 samples, respectively. The actual values of the parameters are plotted in a solid black line in each plot.

Size		10000			50000			200000	
	HSS	LHS	Rand	HSS	LHS	Rand	HSS	LHS	Rand
Total	0.7252	0.7534	0.7307	0.8673	0.8679	0.8738	0.9139	0.9296	0.9016
J$_{z0}$	0.8993	0.9020	0.9109	0.9573	0.9659	0.9626	0.9753	0.9798	0.9784
X$_{z0}$	0.8297	0.8962	0.8414	0.9447	0.9408	0.9447	0.9798	0.9796	0.9461
T$_{z0}$	0.8875	0.8689	0.8634	0.9315	0.9336	0.9396	0.9483	0.9554	0.9434
J$_{dz}$	0.2186	0.2677	0.2813	0.6651	0.7356	0.7244	0.8246	0.8603	0.8328
X$_{dz}$	0.6568	0.6968	0.6595	0.7838	0.7934	0.8025	0.8248	0.8458	0.8361
T$_{dz}$	0.4979	0.5837	0.5005	0.7953	0.7472	0.7875	0.8896	0.9083	0.7240
a$_0$	0.7229	0.7452	0.7292	0.8375	0.8672	0.8773	0.9086	0.9214	0.8889
a$_1$	0.9994	0.9997	0.9996	0.9989	0.9997	0.9999	0.9994	0.9999	0.9994
a$_2$	0.6095	0.6460	0.5964	0.8274	0.7659	0.7684	0.8606	0.9152	0.9363
a$_3$	0.9298	0.9281	0.9248	0.9319	0.9296	0.9311	0.9277	0.9302	0.9304

Table 5.4: The computed R^2-scores for all signal and foreground parameters for each case studied are listed here. We used the parametrized model to construct the global 21cm signal and the log-log polynomial to construct the foreground.

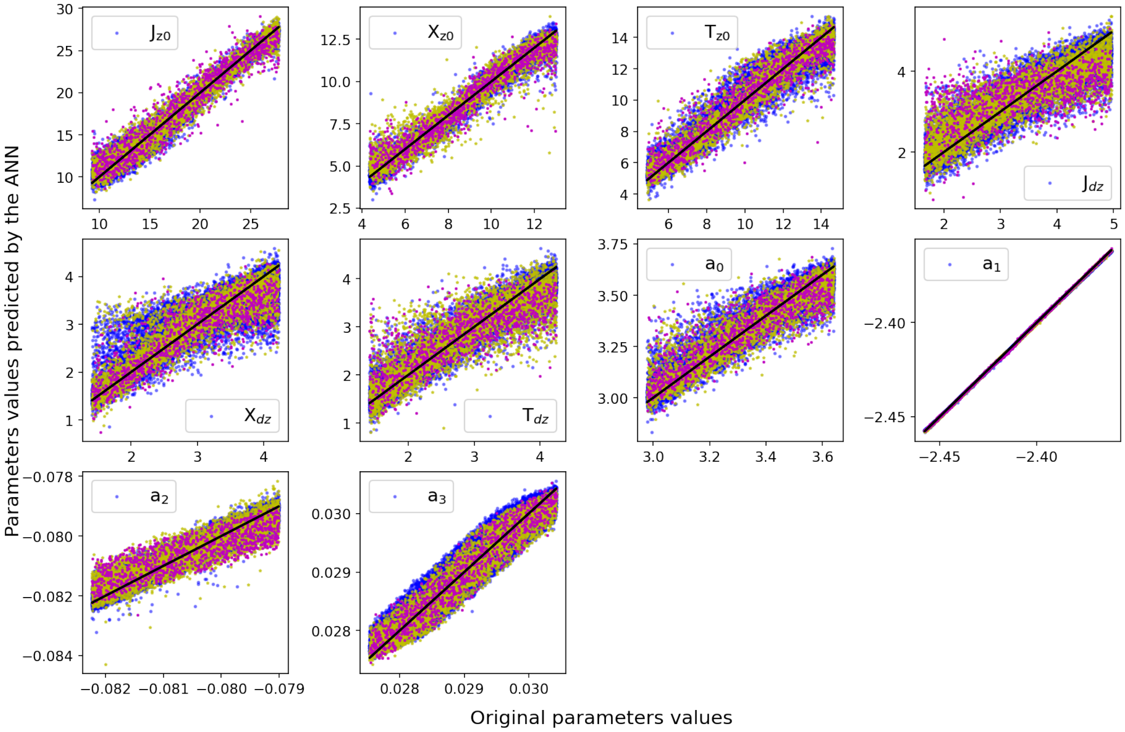

Figure 5.7: The scatter plots above show predicted signal and foreground parameter values obtained through an ANN model trained on a parametrized global 21cm signal. The signal and foreground data sets are generated by sampling the parameter space using Latin hypercube sampling in three sizes: 10,000, 50,000, and 200,000 samples. Magenta scatter points in each scatter plot denote predictions made by the ANN trained with 10,000 samples, while yellow and blue scatter points indicate predictions from ANN models trained with 50,000 and 200,000 samples, respectively. The actual values of the parameters are plotted in a solid black line in each plot.

Size		10000			50000			200000	
	HSS	LHS	Rand	HSS	LHS	Rand	HSS	LHS	Rand
J_{z0}	0.0917	0.0914	0.0861	0.0593	0.0532	0.0556	0.0456	0.0408	0.0423
X_{z0}	0.1180	0.0904	0.1139	0.0679	0.0709	0.0673	0.0409	0.0412	0.0670
T_{z0}	0.0980	0.1049	0.1063	0.0750	0.0737	0.0705	0.0659	0.0610	0.0683
J_{dz}	0.2567	0.2426	0.2442	0.1655	0.1494	0.1513	0.1211	0.1082	0.1185
X_{dz}	0.1651	0.1580	0.1666	0.1332	0.1307	0.1281	0.1210	0.1133	0.1166
T_{dz}	0.2019	0.1828	0.2016	0.1310	0.1453	0.1336	0.0961	0.0874	0.1508
a_0	0.1480	0.1464	0.1500	0.1170	0.1051	0.1008	0.0870	0.0808	0.0964
a_1	0.0068	0.0048	0.0053	0.0092	0.0043	0.0028	0.0066	0.0021	0.0065
a_2	0.1803	0.1750	0.1833	0.1189	0.1400	0.1394	0.1073	0.0840	0.0728
a_3	0.0758	0.0769	0.0778	0.0750	0.0762	0.0759	0.0077	0.0760	0.0759

Table 5.5: The computed RMSE-scores for all signal and foreground parameters for each case studied are listed here. We used the parametrized model to construct the global 21cm signal and the log-log polynomial to construct the foreground.

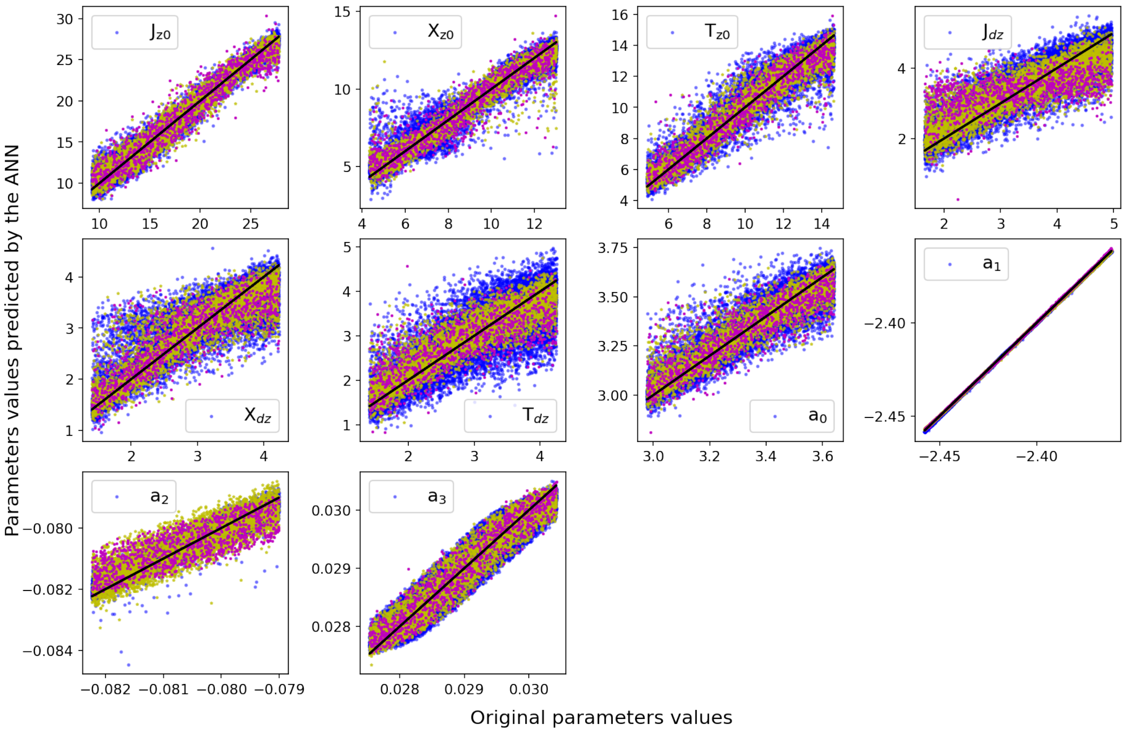

Figure 5.8: The scatter plots above show predicted signal and foreground parameter values obtained through an ANN model trained on a parametrized global 21cm signal. The signal and foreground data sets are generated by sampling the parameter space using Random sampling in three sizes: 10,000, 50,000, and 200,000 samples. Magenta scatter points in each scatter plot denote predictions made by the ANN trained with 10,000 samples, while yellow and blue scatter points indicate predictions from ANN models trained with 50,000 and 200,000 samples, respectively. The actual values of the parameters are plotted in a solid black line in each plot.

5.8.3 Generalizability test of the ANN models

To assess the robustness and generalizability of our trained ANN models, we conducted tests using separate unknown test datasets generated via three distinct sampling techniques. This comprehensive analysis aims to identify the most robustly trained ANN model among those trained with differently sampled datasets. Throughout the training process, we identified the likelihood of bias when drawing conclusions based on a single instance of training the ANN model. This recognition stemmed from factors including variations in initial sample seeds, clustering issues, dataset partitioning, and the inherent variability in training the ANN itself. To mitigate this bias and ensure the consistency of our results across multiple trials, we repeated the entire training and sampling procedure 11 times and saved these individual ANN models for further testing with unknown test datasets drawn via these three distinct sampling techniques: HSS, LHS and Random.

We computed the mean prediction accuracy in terms of R^2 and found that ANNs trained on Hammersley-sampled datasets exhibited lower fluctuations from the mean R^2 value across test datasets, compared to those trained on LHS and Random datasets. For instance, the ANN trained on HSS-sampled datasets achieved a mean R^2 score of 0.9309, with a range of 0.9255 to 0.9373. Similarly, for LHS-sampled test datasets, the mean R^2 score was 0.9285 (range: 0.9213 to 0.9348), and for Random-sampled test datasets, it was 0.9290 (range: 0.9221 to 0.9348). In contrast, ANNs trained on LHS-sampled datasets had a mean R^2 score of 0.9204 on HSS-sampled test datasets (range: 0.9093 to 0.9308), 0.9219 on LHS-sampled test datasets (range: 0.9100 to 0.9347), and 0.9209 on Random-sampled test datasets (range: 0.9089 to 0.9347). For ANNs trained on Random-sampled datasets, the mean R^2 scores were 0.9195 on HSS-sampled test datasets (range: 0.8911 to 0.9296), 0.9205 on LHS-sampled test datasets (range: 0.8924 to 0.9315), and 0.9194 on Random-sampled test datasets (range: 0.8940 to 0.9313). For a detailed visual representation of these results, refer to Fig. 5.9, depicted in the first row. The histogram plots are color-coded: blue represents the prediction accuracy, in terms of R^2 score, of HSS-trained ANN models; orange represents ANN models trained with LHS-sampled datasets, and green represents the R^2 score histogram for ANN models trained with Random-sampled datasets.

Similarly, for the parametrized signal and foreground case, ANN models trained with Hammersley sampled datasets consistently exhibited high prediction accuracy across all test datasets, with the highest R^2 score approximately around 0.92 and the lowest around 0.88, with a mean of approximately 0.91 for each case. Detailed results are depicted in Fig. 5.9 in the second row. Conversely, ANN models trained with Latin hypercube and Random sampled datasets showed inconsistent prediction accuracy for both cases. For test datasets generated with HSS, the lowest R^2 score was less than 0.70, approximately 19-20 % lower than the mean R^2 score, approximately 0.90. Similar fluctuations were observed for test datasets constructed using Latin hypercube and Random sampling methods; detailed results are presented in Fig. 5.9, with the colour scheme remaining consistent across all subplots. Similarly, for the non-parametrized signal case, we observed consistent behaviour, with ANN models trained on Hammersley sampled datasets exhibiting less deviation from the mean R^2 score compared to models trained on LHS and Random datasets, the detailed result present in **Appendix** of this chapter.

5.9 Summary and discussions

In this study, our objective was to systematically explore the vast parameter space encompassing the 21cm global signal and foreground. Our goal was to simulate all possible variations using these parameters and then utilize the generated datasets to enhance the resilience of our trained ANN model. Recognizing the computational challenges posed by considering every possible parameter combination, we tested diverse sampling techniques to map the parameter space efficiently. Determining the ideal number of training datasets necessary for robust ANN model training is not straightforward due to the complexity of the model and the multitude of free parameters involved. Therefore, our research delved into a detailed analysis to establish the minimum dataset requirement. This exploration was essential in understanding how the number of datasets correlates with the model's complexity and the number of free parameters, ensuring comprehensive coverage of the parameter space and enabling the robust training of the ANN model. In our study, we explored various aspects by mapping the parameter space using three distinct sampling methods: Random, Latin hypercube, and Hammersley sequence sampling. Additionally, we investigated different sample sizes within specified boundary conditions to determine the minimum number of samples required to train the ANN effectively. To evaluate the performance of these sampling methods, we calculated metrics such as the R^2 score and Root Mean Square Error (RMSE) using the ANN model. Additionally, we test the ANN's performance across different dataset sizes generated through these sampling techniques. These are some key findings noted from this study:

- Regardless of the sampling method, the ANN's performance improved when trained with larger, well-sampled datasets. For instance, in parametrized signal scenarios, training with 1000 samples yielded an R^2 score of 0.6744, while 5000 samples improved the score to

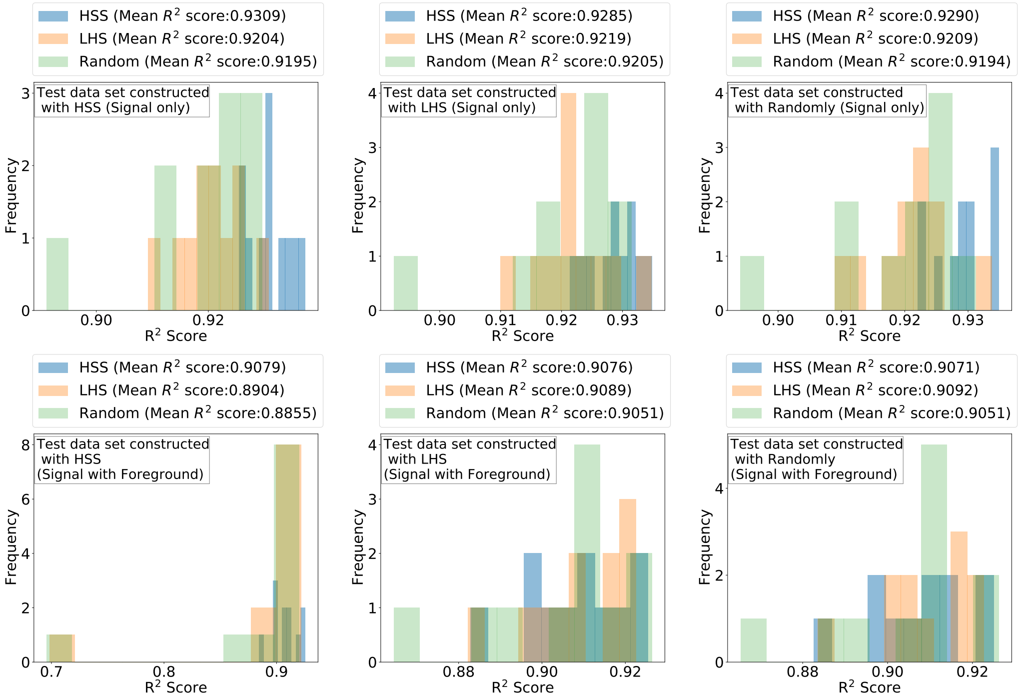

Figure 5.9: The figure illustrates ANN model predictions for various trials trained on datasets sampled using HSS, LHS, and Random methods with optimal sample sizes. Histograms depict ANN prediction accuracy measured by R^2 scores. Panels in the figure's rows correspond to different signal scenarios: the top three panels in the first row show predictions for the Parameterized signal, followed by predictions for the Parameterized signal with foreground and thermal noise in the second row. Histograms are colour-coded: blue represents HSS-trained ANN models, orange represents LHS-trained ANN models, and green represents the Random-trained ANN model's prediction accuracy.

0.9059. Increasing the sample size to 10,000 resulted in a marginal improvement to 0.9226, indicating diminishing returns relative to the computational cost.

- The number of free parameters played a critical role; fewer parameters required fewer samples for optimal results, while more parameters necessitated larger sample sizes. For example, in the case of parametric signals with 6 free parameters, 10,000 datasets were sufficient for optimal results. However, for foreground-corrupted signals with 10 free parameters, 200,000 datasets were needed to achieve the same level of accuracy. This trend persisted when introducing different signal models as well.
- Models trained with datasets from HSS showed consistent performance across various unknown test datasets, regardless of the sampling method used. Conversely, models trained with LHS and Random methods exhibited inconsistent prediction accuracy, indicating less robustness.
- In lower dimensions (< 10), the ANN trained with HSS sampled datasets demonstrated slightly higher accuracy than those trained with LHS and Random methods. However, in higher-dimensional parameter spaces (≥ 10), HSS performance declined due to clustering issues. For instance, when dealing with signal, foreground, and noise in parametric signal cases, HSS performance was slightly lower than the other sampling methods.

- We also obtained consistent results when using a non-parametric signal model instead of a parametric one. The primary difference observed was that, since the non-parametric model only had three free parameters for signal modeling, optimal ANN performance was achieved with a smaller dataset size. This finding suggests that the efficacy of sampling methods is influenced more by the dimensionality of the parameter space associated with the signal rather than by the specific signal model employed.

To address the high-dimensionality limitations of Hammersley sequence sampling, future research will explore alternative sampling methods that may offer viable solutions. Additionally, we plan to consider the ionospheric effect and beam chromaticity effect, investigating how these parameters impact the parameter space when combined with signal and foreground parameters. This investigation will help us to determine the minimum number of samples required for robust training of the ANN model, enabling accurate parameter inference from real observational datasets. In this study, we have compared these sampling methods solely within an ANN-based framework. In future research, we plan to incorporate other machine learning regression models to evaluate and compare their performance.

Appendix: Non parametric model

We have conducted similar analyses across different signal model to demonstrate their generalizability. The comprehensive results are discussed below.

Signal only

To ensure consistency and generalizability of the sampling techniques, we employ a different signal model, a non-parametrized signal model. This allows us to highlight any biases of the sampling techniques over the signal model, and assess performance in lower dimensions due to fewer free parameters. In contrast to the parametric model, the architecture of the ANN for this case is different. The input layer consisted of 1024 neurons, corresponding to the 1024 frequency channels. There were two hidden layers with 64 and 16 neurons, respectively, and these layers were activated using the 'sigmoid' and 'relu' activation functions. To prevent overfitting, we also applied L2 kernel regularization. The output layer has 3 neurons, each representing different signal parameters. We have used Adam optimizer with a learning rate of 10^{-4}.

Similar to the parametric context, a consistent trend is observed in the non-parametric signal scenario: the ANN model trained with 1000 datasets achieves an overall R^2 score of around 0.92, which increases to approximately 0.93 with 5000 datasets, and around 0.94 with 10,000 datasets. Detailed results for each sampling method and dataset size, including R^2 and RMSE scores, are provided in Tab. 5.6 and Tab. 5.7. Visualizations comparing predicted parameter values against original values for each sampling method are displayed in Fig. 5.10 (HSS), Fig. 5.11 (LHS), and Fig. 5.12 (Random sampling). Notably, model performance improves with larger sample sizes, with all methods achieving comparable accuracy levels for substantial datasets. The lower dimensionality of the problem compared to the parametric case allows for higher prediction accuracy with fewer sampled datasets.

Size		1000			5000			10000	
	HSS	LHS	Rand	HSS	LHS	Rand	HSS	LHS	Rand
Avg.	0.9155	0.9252	0.9214	0.9392	0.9367	0.9346	0.9447	0.9446	0.9418
$f_*.f_{esc}$	0.9936	0.9922	0.9893	0.9945	0.9957	0.9940	0.9974	0.9970	0.9944
$f_{X,h}.f_X$	0.8255	0.8373	0.8408	0.8785	0.8682	0.8642	0.8837	0.8737	0.8783
N_α	0.9275	0.9454	0.9341	0.9531	0.9539	0.9555	0.9531	0.9532	0.9527

Table 5.6: The computed R^2-scores for all signal parameters for each case studied are listed here. We used the physical model to construct the global 21cm signal.

Size		1000			5000			10000	
	HSS	LHS	Rand	HSS	LHS	Rand	HSS	LHS	Rand
$f_*.f_{esc}$	0.0230	0.0253	0.0281	0.0149	0.0162	0.0162	0.0130	0.0135	0.0150
$f_{X,h}.f_X$	0.1154	0.1000	0.1130	0.1022	0.1064	0.1043	0.0875	0.0851	0.0800
N_α	0.0554	0.0482	0.0530	0.0447	0.0421	0.0421	0.0408	0.0392	0.0390

Table 5.7: The computed RMSE scores for all signal parameters for each case studied are listed here. We used the physical model to construct the global 21cm signal.

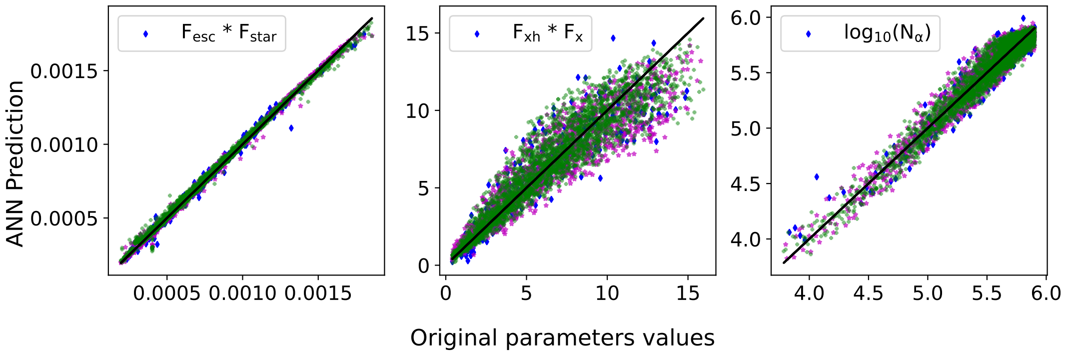

Figure 5.10: The scatter plots above show predicted signal parameter values obtained through an ANN model trained on a physical global 21cm signal. The signal data sets are generated by sampling the parameter space using Hammersley sequence sampling in three sizes: 1000, 5000, and 10,000 samples. Blue points in each scatter plot denote predictions made by the ANN trained with 1000 samples, while magenta and green points indicate predictions from ANN models trained with 5000 and 10000 samples, respectively. The actual value of the parameters is plotted in a solid black line in each plot.

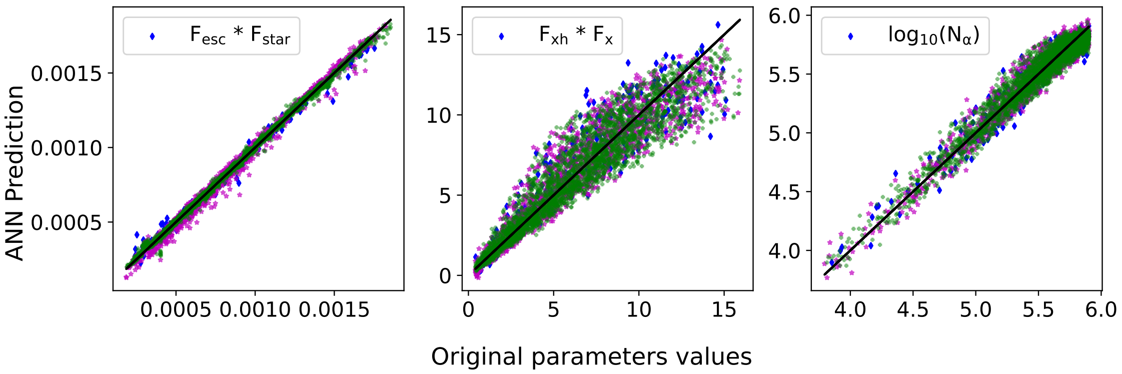

Figure 5.11: The scatter plots above show predicted signal parameter values obtained through an ANN model trained on a physical global 21cm signal. The signal data sets are generated by sampling the parameter space using Latin hypercube sampling in three sizes: 1000, 5000, and 10,000 samples. Blue points in each scatter plot denote predictions made by the ANN trained with 1000 samples, while magenta and green points indicate predictions from ANN models trained with 5000 and 10000 samples, respectively. The actual values of the parameters are plotted in a solid black line in each plot.

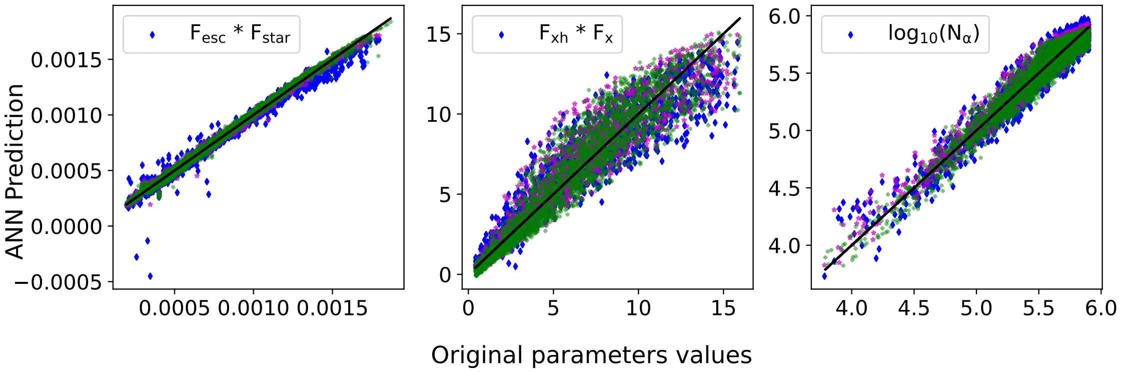

Figure 5.12: The scatter plots above show predicted signal parameter values obtained through an ANN model trained on a physical global 21cm signal. The signal data sets are generated by sampling the parameter space using Random sampling in three sizes: 1000, 5000, and 10,000 samples. Blue points in each scatter plot denote predictions made by the ANN trained with 1000 samples, while magenta and green points indicate predictions from ANN models trained with 5000 and 10000 samples, respectively. The actual value of the parameters is plotted in a solid black line in each plot.

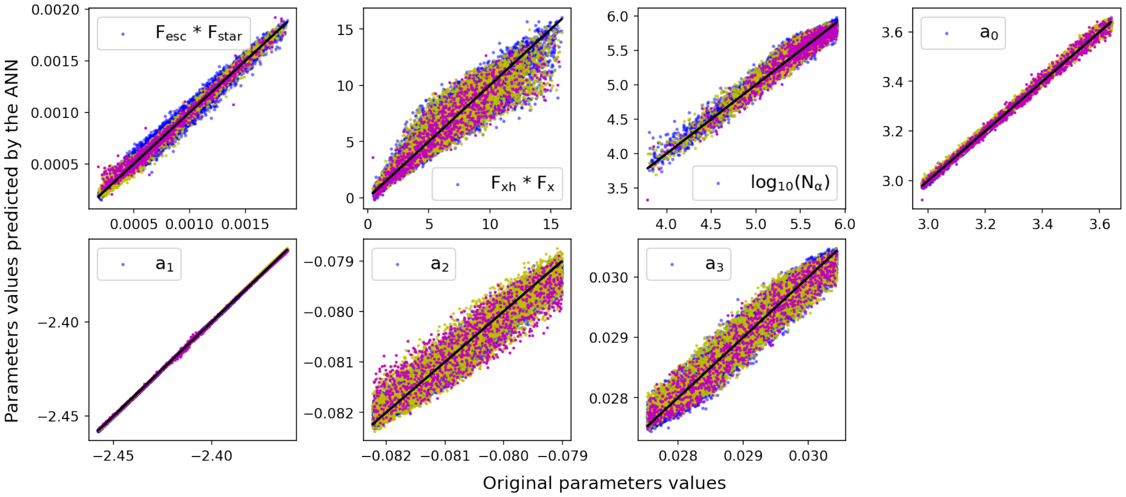

Figure 5.13: The scatter plots above show predicted signal and foreground parameter values obtained through an ANN model trained on a physical global 21cm signal. The signal and foreground data sets are generated by sampling the parameter space using Hammersley sequence sampling in three sizes: 10,000, 50,000, and 100,000 samples. Magenta scatter points in each scatter plot denote predictions made by the ANN trained with 10,000 samples, while yellow and blue scatter points indicate predictions from ANN models trained with 50,000 and 100,000 samples, respectively. The actual values of the parameters are plotted in a solid black line in each plot.

Signal with foreground and thermal noise

Similar to the parametrized case, we introduced the effects of foreground and thermal noise in the non-parametric signal. Given fewer free parameters than the parametric case, we generated datasets in three sizes: 10,000, 50,000, and 100,000 samples. The architecture of the ANN model closely resembles that of the parametrized case, with the primary difference being the output layer of the second ANN model, which comprises 5 neurons. Each neuron represents 3 signal parameters and 2 foreground parameters (a_0, a_3). Here, we observe a consistent trend similar to parametric scenarios: the ANN model trained with 10000 datasets achieves an overall R^2 score of around 0.92, which increases to approximately 0.94 with 50000 datasets, and around 0.96 with 10,0000 datasets. The detailed results for each sampling method with the various dataset sizes, the R^2 and RMSE score for individual parameters, are listed in Tab. 5.8 and Tab. 5.9. We also individually visualized the predicted parameter values against the original values for each sampling method across different dataset sizes. These visualizations are presented in Fig. 5.13 for HSS, Fig. 5.14 for LHS, and Fig. 5.15 for Random sampling.

In our study, we observed that for optimal performance of the ANN model with any sampling method, training with a sufficient number of datasets is essential. For example, training the ANN model with 100,000 datasets resulted in precise prediction of signal parameters, with R^2 scores ranging from 0.92 to 0.98 and root mean square error (RMSE) values between 0.021 and 0.066. Additionally, the ANN effectively predicted foreground parameters, yielding R^2 scores ranging from 0.95 to 0.99 and RMSE values between 0.008 and 0.064, showcasing significantly improved accuracy compared to the model trained with 10,000 datasets. Detailed results are provided in Tab.5.8 and Tab.5.9.

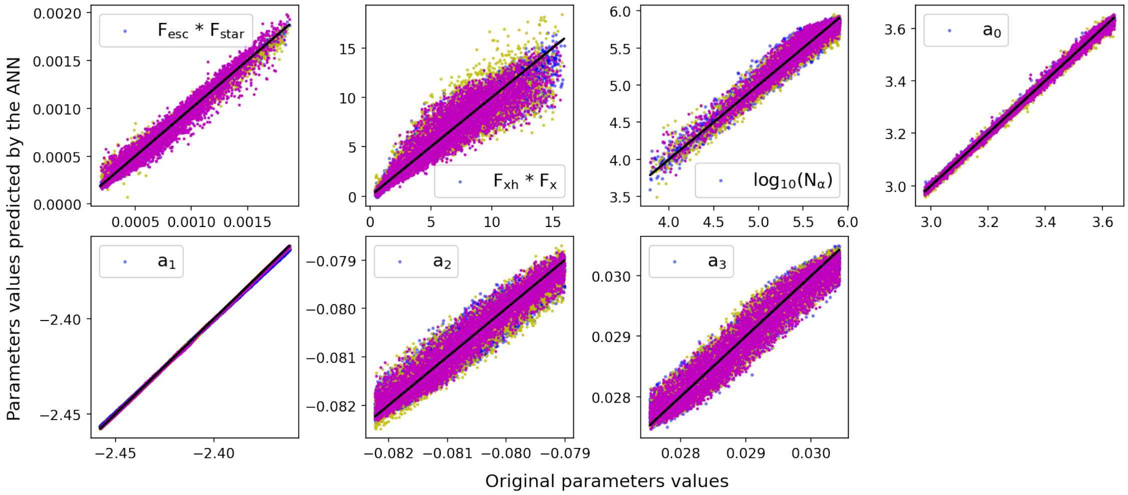

Figure 5.14: The scatter plots above show predicted signal and foreground parameter values obtained through an ANN model trained on a physical global 21cm signal. The signal and foreground data sets are generated by sampling the parameter space using Latin hypercube sampling in three sizes: 10,000, 50,000, and 200,000 samples. Magenta scatter points in each scatter plot denote predictions made by the ANN trained with 10,000 samples, while yellow and blue scatter points indicate predictions from ANN models trained with 50,000 and 100,000 samples, respectively. The actual values of the parameters are plotted in a solid black line in each plot.

Size		10000			50000			100000	
	HSS	LHS	Rand	HSS	LHS	Rand	HSS	LHS	Rand
Avg.	0.9277	0.9187	0.9018	0.9505	0.9448	0.9429	0.9670	0.9647	0.9608
$f_*.f_{esc}$	0.9813	0.9532	0.9776	0.9890	0.9510	0.9634	0.9843	0.9903	0.9860
$f_{X,h}.f_X$	0.8574	0.8727	0.8272	0.8807	0.8502	0.8570	0.9139	0.9168	0.9142
N_α	0.9395	0.9398	0.8502	0.9512	0.9454	0.9405	0.9620	0.9563	0.9629
a_0	0.9925	0.9978	0.9960	0.9968	0.9959	0.9969	0.9988	0.9986	0.9973
a_1	0.9996	0.9969	0.9974	0.9993	0.9982	0.9998	0.9999	0.9991	0.9998
a_2	0.7921	0.7281	0.7291	0.9080	0.9386	0.9084	0.9590	0.9415	0.9242
a_3	0.9317	0.9427	0.9353	0.9340	0.9327	0.9337	0.9505	0.9504	0.9400

Table 5.8: The computed R^2-scores for all signal and foreground parameters for each case studied are listed here. We used the physical model to construct the global 21cm signal and the log-log polynomial to construct the foreground.

Size		10000			50000			100000	
	HSS	LHS	Rand	HSS	LHS	Rand	HSS	LHS	Rand
$f_{*}{\cdot}f_{esc}$	0.0303	0.0457	0.0319	0.0219	0.0460	0.0403	0.0265	0.0205	0.0246
$f_{X,h}{\cdot}f_{X}$	0.0886	0.0819	0.0945	0.0770	0.0885	0.0853	0.0670	0.0661	0.0675
N_{α}	0.0457	0.0433	0.0715	0.0424	0.0432	0.0456	0.0363	0.0386	0.0361
a_0	0.0248	0.0137	0.0179	0.0113	0.0184	0.0151	0.0098	0.0107	0.0149
a_1	0.0054	0.0159	0.0145	0.0075	0.0037	0.0036	0.0023	0.0085	0.0035
a_2	0.1279	0.1497	0.1465	0.0880	0.0714	0.0878	0.0581	0.0695	0.0763
a_3	0.0757	0.0708	0.0739	0.0741	0.0749	0.0740	0.0644	0.0643	0.0711

Table 5.9: The computed RMSE-scores for all signal and foreground parameters for each case studied are listed here. We used the physical model to construct the global 21cm signal and the log-log polynomial to construct the foreground.

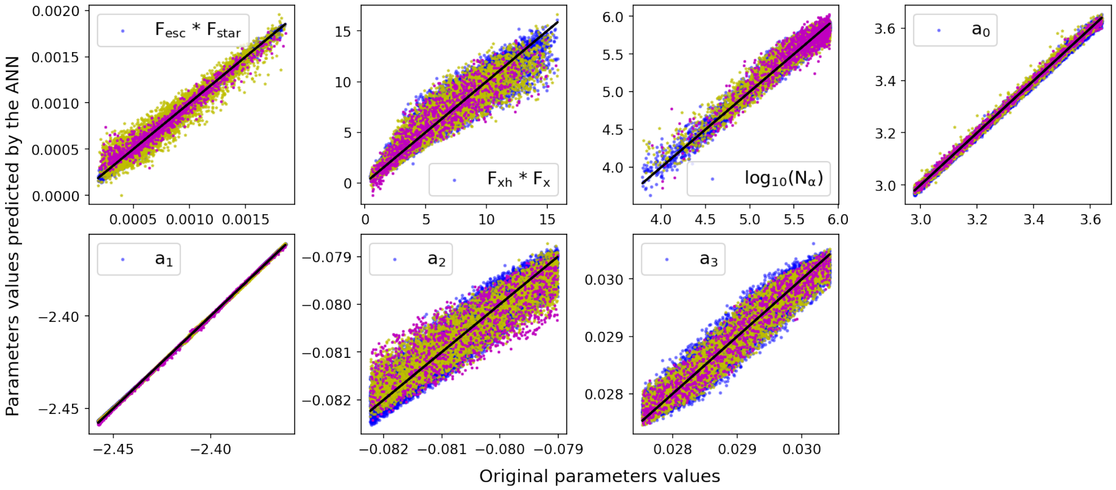

Figure 5.15: The scatter plots above show predicted signal and foreground parameter values obtained through an ANN model trained on a physical global 21cm signal. The signal and foreground data sets are generated by sampling the parameter space using Random sampling in three sizes: 10,000, 50,000, and 100,000 samples. Magenta scatter points in each scatter plot denote predictions made by the ANN trained with 10,000 samples, while yellow and blue scatter points indicate predictions from ANN models trained with 50,000 and 100,000 samples, respectively. The actual values of the parameters are plotted in a solid black line in each plot.

Generalizability test

We have conducted a generalizability test to demonstrate the robustness of the ANN model for non-parametrized scenarios. The detailed results are plotted below in the histogram, see Fig. 5.16.

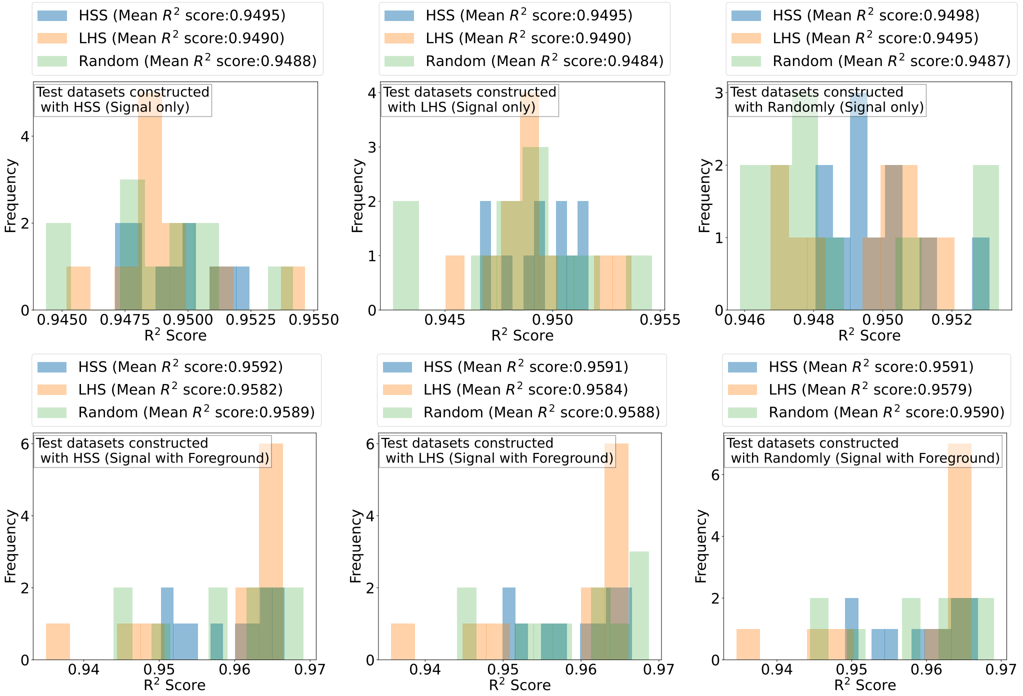

Figure 5.16: The figure illustrates ANN model predictions for various trials trained on datasets sampled using HSS, LHS, and Random methods with optimal sample sizes. Histograms depict ANN prediction accuracy measured by R^2 scores. Panels in the figure's rows correspond to different scenarios: the top three panels in the first row show predictions for the Non-parametrized signal, followed by predictions for the Non-parametrized signal with foreground and thermal noise in the second row. Histograms are colour-coded: blue represents HSS-trained ANN models, orange represents LHS-trained ANN models, and green represents the Random-trained ANN model's prediction accuracy.

Training loss and validation loss of the ANN models

We have plotted the training and validation loss of the ANN models for various scenarios; see Fig.5.17 and Fig.5.18.

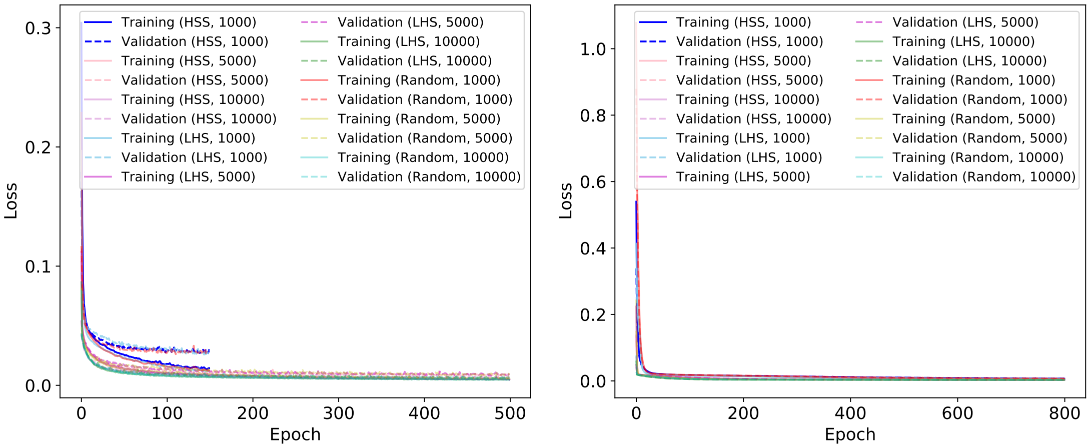

Figure 5.17: The figure illustrates the evolution of the network's loss function across various scenarios. The training loss is denoted by a solid line, and the validation loss is indicated by a dashed line over epochs. Notably, the test loss closely follows the training loss in this visualization. training loss for parametrized signal (**left**) and non-parametrized signal (**right**).

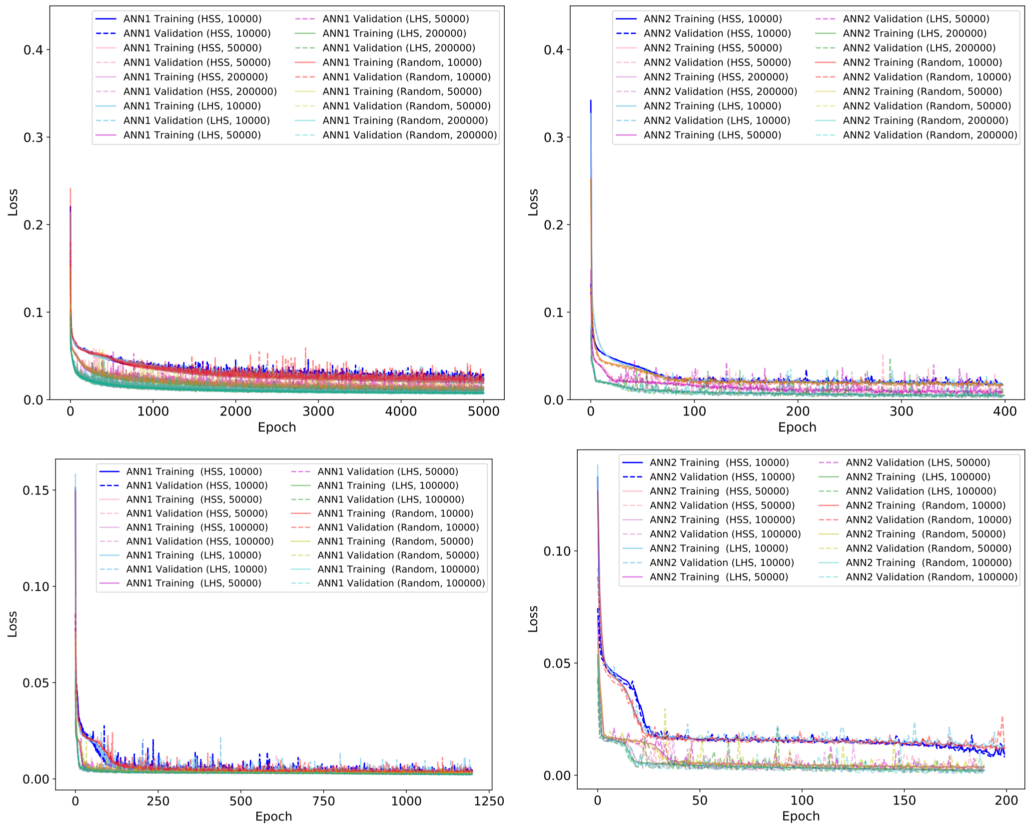

Figure 5.18: The figure illustrates the evolution of the network's loss function across various scenarios. The training loss is denoted by a solid line, and the validation loss is indicated by a dashed line over epochs. Notably, the test loss closely follows the training loss in this visualization. **Top row:** training and validation loss for parametrized signals with foreground. **Bottom row**: training and validation loss for foreground-added non-parametrized signals.

Chapter 6

Impact of Calibration and Position Errors on Astrophysical Parameters of the H I 21cm Signal

Adapted from: ***Anshuman Tripathi***, *Abhirup Datta, Aishrila Mazumder, Suman Majumdar “Impact of Calibration and Position Errors on Astrophysical Parameters of the H I 21cm Signal”, Journal of Cosmology and Astroparticle Physics, Volume 2025, number 10, Pages 035, 10.1088/1475-7516/2025/10/035*

The Epoch of Reionization (EoR) and Cosmic Dawn (CD) are pivotal stages during the first billion years of the universe, exerting a significant influence on the development of cosmic structure. The detection of the redshifted 21-cm signal from these epochs is challenging due to the dominance of significantly stronger astrophysical foregrounds and the presence of systematics. This work used the 21cm E2E (end to end) pipeline, followed by simulation methodology described [186] to conduct synthetic observations of a simulated sky model that includes both the redshifted 21-cm signal and foregrounds. A framework was constructed using Artificial Neural Networks (ANN) and Bayesian techniques to directly deduce astrophysical parameters from the measured power spectrum. This approach eliminates the need for explicit telescope layout effects correction in interferometric arrays such as SKA-Low. The present work investigates the impact of gain calibration errors and sky model position errors on the recovery of the redshifted 21-cm power spectrum for the SKA-Low AA* array configuration. We assessed the effects of these inaccuracies on the deduced astrophysical parameters and established acceptable tolerance levels. Based on our results, the gain calibration error tolerance for ideal signal detection is 0.001 %. However, if the sky model position errors exceed 0.048 arcseconds, the remaining foregrounds would obscure the target signal.

6.1 Introduction

The redshifted 21cm line is a potential probe of the early Universe [38, 55, 165], mainly from the era post recombination until the universe became fully ionized. Based on the theoretical model, in the first billion years of the Universe, Cosmic Dawn (CD) is when the first star or galaxy will be formed ($30 > z > 12$). These stars and galaxies are formed due to gravitational instability, which causes small-scale fluctuation in the matter density. The UV photons produced by these objects ionized the neutral hydrogen (H I) in the intergalactic medium (IGM). This transition period is known as Epoch of Reionization (EoR) [4, 54, 57, 164, 187]. Based on various indirect observations such as quasar absorption [18] at high redshifts, Thompson scattering optical depth [26] suggest that the reionization extended the process and lasted at least til the redshift $z \sim 6$.

The observation of H I 21cm power spectrum using large interferometric arrays currently holds the most significant potential to observe the redshifted H I 21cm line [65, 188–190]. The 21cm signal inherently encodes information about the underlying dark matter distribution and the properties of the ionizing sources. As a result, it has the potential to trace the history of reionization, reflecting the evolution of the average ionization state of the intergalactic medium (IGM) with redshift during the EoR. Detection of the redshifted H I signal is the key science goal of several ongoing and future experiments. Recently, the detection of a global 21cm signal reported by the Experiment to Detect Global Epoch of Reionization Signature (EDGES) team [167]. However, the detection has been challenged by another independent experiment, SARAS [40, 168]. Besides EDGES and SARAS, there are other independent single radiometer experiments like BIGHORNS [60], SCI-HI [59], and LEDA [43] are also aiming to detect the global signal but have not yet to report any detection. Conversely, interferometers focusing on statistical fluctuations have yielded significant upper limits on the EoR power spectrum (PS) amplitude. The most sensitive operational interferometers, such as the GMRT, MWA, LOFAR, and HERA, have all established upper limits on the power spectrum amplitude of the signal [6, 7, 91, 191, 192], but there has been no confirmed detection of the cosmological H I 21cm signal.

However, observing the 21cm signal is highly challenging due to bright astrophysical foregrounds primarily Galactic synchrotron emission and extragalactic point sources that are several orders of magnitude brighter than the signal of interest [193–199]. Additionally, other sources of contamination, such as the Earth's ionosphere and instrument systematics, make detection even more difficult. The observation of the 21cm signal heavily relies on the accuracy of foreground removal and the use of instruments with high sensitivity and controlled systematics. Over the past decade, several novel methods have been proposed to quantify and mitigate each type of contamination for foreground avoidance and removal [71,72,74,84,200–203] , model the systematics of the instruments [204–207] , address calibration effects [100, 112, 208–213], and account for the impact of the Earth's ionosphere [214–216]. These advancements are paving the way for highly sensitive next-generation interferometers, such as the Hydrogen Epoch of Reionization Array (HERA, [217]) and the Square Kilometer Array (SKA-Low, [49]), to detect the 21-cm signal and characterize the multi-redshift power spectrum (PS). This will result in tighter constraints on astrophysical parameters in the early universe. The forthcoming SKA-Low is specifically designed to have the sensitivity needed to detect the PS precisely and is anticipated to generate tomographic images of the HII regions [67].

The EoR signal can be distinguished from foreground contamination because the EoR signal exhibits a spectral structure and is inherently uniform in spatial wavenumber (k) space, whereas foregrounds are spectrally smooth [218]. The foregrounds' smooth spectral nature, along with the inherent chromaticity of the instruments, limit the contamination to the 'wedge' in cylindrical Fourier space (i.e., the 2D power spectrum) [71, 72, 74]. The area outside this wedge, where the foregrounds are less prominent than the EoR signal, is referred to as the 'EoR window' [73]. However, the interaction between astrophysical foregrounds and the instrument results in the leakage of wedge power into the clean modes of the window, a phenomenon known as 'mode mixing' [73]. This mode mixing impacts the "EoR window," the region outside the wedge, complicating the detection process. One major recurring challenge in detecting cosmic signals is improper calibration. In radio astronomy sky-based calibration is commonly used, but CD/EoR observations often produce inaccurate models due to low angular resolutions and noise confusion, resulting in residual errors and hindering target cosmological signal detection [11, 71, 210, 219]. The redundant calibration method, investigated by observatories such as HERA, addresses this by repeatedly measuring the redundant baselines of interferometers to correct for the incoming sky signal and instrumental parameters [220]. However, as demonstrated by [221], redundant calibration remains susceptible to errors introduced during the absolute calibration step, which necessarily depends on a sky model. Even in the case of a perfectly redundant array with identical antenna beams, incompleteness in the sky model leads to frequency-dependent calibration errors that can contaminate the 21cm power spectrum. To mitigate these limitations, [222] introduced a unified Bayesian calibration framework that integrates both sky-based and redundant approaches. This framework explicitly accounts for instrumental systematics, such as antenna position offsets, beam non-uniformities, and incomplete sky models, thereby improving the robustness and accuracy of 21cm power spectrum estimation.

The signal-to-noise ratio (SNR) is a critical factor in the detection of faint cosmic signals, such as the redshifted 21-cm line from the epoch of reionization. [**71**] demonstrated that even minor calibration errors can significantly reduce the dynamic range, thereby obscuring the cosmological signal. Building on this, [186], through an analysis of the one-dimensional power spectrum (1D PS), determined that the optimal calibration error tolerance for reliable signal detection is approximately 0.01%. Consistently, [11] showed that calibration errors must be limited to below approximately 10^{-5} or 0.001 % in amplitude in order to prevent contamination of the EoR window in power spectrum measurements. Despite these insights, further investigation is needed to determine the precise tolerance limits for various instrumental imperfections that could hinder weak signal detection. This study aims to quantify the tolerance levels required for the successful detection of the redshifted 21-cm signal and the recovery of astrophysical parameters from the epoch of reionization using the SKA-Low telescope. To achieve this, we utilize a hybrid machine learning (ML) approach that integrates artificial neural networks (ANN) with Bayesian methods to analyze the effects of imperfections on observational data and their direct impact on the associated astrophysical parameters.

Over the past few years, machine learning (ML) techniques have seen extensive application in various areas of cosmology and astrophysics, particularly in imaging, statistics and inference. Among these ML techniques, artificial neural networks (ANNs) are commonly used in 21cm cosmology for signal modelling, in both kinds, the global signal [137–139] and the power spectrum [223, 224]. ANNs are also employed to infer parameters linked to the signal directly, bypassing traditional Bayesian approaches in both the global 21cm signal [13, 50, 51, 86] and power spectrum [87, 118]. Besides ANNs, other ML algorithms are also widely used in various applications of 21cm cosmology. For example, [140] utilized Convolutional Neural Networks (CNNs) to detect reionization sources in 21-cm maps. In [141], deep learning models were employed to replicate the entire time-evolving 21-cm brightness temperature maps from the reionization epoch. The authors validated their predicted 21-cm maps against brightness temperature maps generated by radiative transfer simulations. [143] employed deep learning with CNNs to directly extract astrophysical parameters from 21-cm images. [135] conducted a comparative analysis of machine learning techniques for predicting the 21-cm power spectrum from reionization simulations. [225] proposes a Convolutional Denoising Autoencoder (CDAE) to recover the Epoch of Reionization (EoR) signal by training on SKA images simulated with realistic beam effects.

In this work, we have developed an emulator using an artificial neural network (ANN) framework. This trained ANN emulator was employed as model statistics to constrain EoR astrophysical parameters from the total observed sky power spectrum, which includes the H I signal and systematic effects, via a Bayesian inference process. The motivation for building ANN emulators arises from the computational challenges in EoR 21cm cosmology. Generating numerous observable model signals for multi-dimensional parameter space to perform Bayesian inference using semi-numerical or radiative transfer methods is computationally intensive. Additionally, incorporating telescope layout effects through simulated observations further increases the computational expense. To address these challenges, we adopted a formalism already utilized by several groups [223, 224], using emulators for EoR signal modeling instead of actual simulations. To construct the training datasets for the emulators, we performed simulated radio interferometric observations using a 21cm E2E pipeline for SKA-Low core array configurations. This allowed us to calculate the total observed sky power spectrum with telescope layout effect. We also studied the systematic biases introduced in the observed power spectrum by comparing it with the true power spectrum. Furthermore, we examined how these biases influence parameter extraction and quantified the tolerance levels for calibration and position errors necessary for the successful detection of the H I 21cm signal from the EoR using this sensitive telescope through Bayesian inferences. This is followup work by [186], which quantified the tolerance for calibration and position errors in detecting the H I 21cm signal using various interferometers by analyzing variations in RMS in the image plane and visually examining the 2D and 1D power spectra. Our research investigates the effects of gain calibration and position errors on astrophysical parameters, quantifying the tolerance levels needed to obtain inferred parameters that closely match the true values. Specifically, this work highlights the impact of these errors on the 21cm signal's astrophysical parameters when no mitigation techniques are applied to the residual foreground contamination caused by them. Furthermore, we are developing a mitigation pipeline, as outlined by [226], to effectively correct these errors, enabling the accurate inference of the true power spectrum and astrophysical parameters.

The structure of this paper is organized as follows: Section 6.2 outlines the simulation methodology for the H I signal and provides a description of the foreground models used. Section 6.3 provides the input parameters and telescope array information for performing synthetic observations. Section 6.4 discusses the Power Spectrum (PS) estimation. Section 6.5 covers the emulation details of the PS. Section 6.6 presents the formulation of Bayesian Inference for EoR parameter estimation. Section 6.7 outlines the method for calculating error covariances of the PS. Finally, Section 6.8 presents the results.

6.2 Astrophysical Components in the Simulation

To perform the synthetic observation using the 21cm E2E pipeline, the sky model provided to the pipeline includes the simulated redshifted 21cm signal along with the point source astrophysical foreground model, as detailed below.

6.2.1 H I 21cm Maps

To generate 21cm maps for our simulated observation, we use a semi-numerical simulation 21cmFAST [5, 227]. 21cmFAST generates H I 21cm maps by first constructing a matter density field and applying the Zeldovich approximation. It employs the guided excursion set formalism to convert the matter density field at a given redshift into an ionization field, which is subsequently used to derive 21-cm brightness temperature fluctuations. In contrast to a detailed radiative transfer approach, this method employs perturbation theory, excursion set formalism, and analytical prescriptions to generate evolved fields for density, ionization, peculiar velocity, and spin temperature. These fields are subsequently integrated to determine the 21-cm brightness temperature. Instead of relying on a halo finder, the code directly processes the evolved density field, enhancing computational efficiency and minimizing memory consumption. This enables the production of numerous realizations of 21-cm maps, power spectra of brightness temperature, matter density, velocity, spin temperature, and ionization fraction at specific redshifts, all at a very low computational cost.

We simulated lightcones in a 500 Mpc^3 comoving box with 232^3 of grid cells for a range for redshift extent of $8.73 \leq z \leq 9.29$. The constructed lightcone volume is saved on a grid of size $232 \times 232 \times 64$ and projected on a World Coordinate System (WCS) to generate an input signal for simulating observations. For this study, we simulate different lightcones to probe different realizations of reionization history using varying EoR parameters. To simulate these lightcones, we use three key EoR parameters R_{mfp}, T_{vir}, and ζ which can be tweaked to create different reionization histories. These parameters are commonly used to characterize the EoR, as they effectively capture the timing, source population, and morphology of reionization while remaining physically interpretable and computationally efficient [108]. We describe these in detail below following [108, 118]:

- R_{mfp}, Mean Free path of ionizing photon: The ionizing photons travel through the ionized IGM strongly depends on the presence of absorption systems and the sizes of ionized regions [228]. Distance travel by a photon from its source of origin to its sink within ionized regions is called the mean free path of ionizing photon [229,]. In the semi-numerical model, R_{mfp} specifies the maximum scale over which ionizing photons can propagate; it does not directly determine the sizes of the ionized regions but limits their growth only once they approach this maximum scale, typically toward the later stages of reionization.
- $\mathrm{T}_{\mathrm{vir}}$, Minimum virial temperature of haloes producing ionizing photons: This represents the minimum mass of haloes producing ionizing photons during the EoR. Usually, $\mathrm{T}_{\mathrm{vir}}$ is chosen to be larger than 10^4K such that atomic cooling become effective [230, 231].
- ζ, Ionizing efficiency: Ionizing efficiency refers to the ability of sources, such as stars or galaxies, to convert their energy into ionizing photons that can ionize hydrogen in the intergalactic medium. This is a combination of several degenerate astrophysical parameters and is defined as $\zeta = f_{\mathrm{esc}} f_\star \, N_\gamma/(1 + n_{\mathrm{rec}})$ [232, 233]. Here, $\mathrm{f}_{\mathrm{esc}}$ is the fraction of ionizing photons escaping from galaxies into the IGM, $\mathrm{f}_\star$ is the fraction of baryons locked into stars and N_γ is the number of ionizing photons produced per baryon in stars and $\mathrm{n}_{\mathrm{rec}}$ is the mean recombination rate per baryon.

6.2.2 Foreground Models

The foreground component employed in this study includes compact sources based on the Tiered Radio Extragalactic Continuum Simulation (T-RECS, [234]). T-RECS simulates the continuum radio sky from 150 MHz to 20 GHz, modeling Active Galactic Nuclei (AGNs) and Star-Forming Galaxies (SFGs), incorporating observational constraints for realistic cosmological evolution. For this study, a subset covering approximately 4 deg^2 was extracted from the full 25 deg^2 T-RECS catalogue, with a flux cut-off applied between 0.6 Jy to 3.1 mJy at 150 MHz. Flux densities originally specified at 150 MHz were extrapolated to 142 MHz using a spectral index $\alpha = -0.8$, yielding a total of 2522 compact sources within the chosen field of view. To maintain simplicity, the current analysis focuses solely on compact sources and excludes both diffuse foreground emission and complex sources with extended morphology or non-power-law spectral characteristics. Future studies will incorporate these additional components to evaluate their influence on signal recovery.

6.3 Synthetic Observations

To conduct synthetic observations, we utilized a 21cm end-to-end (E2E) pipeline [186]. This pipeline employs the OSKAR software package [235] for simulating SKA-Low configurations, the Common Astronomy Software Applications (CASA) package [236] for further reading and process-

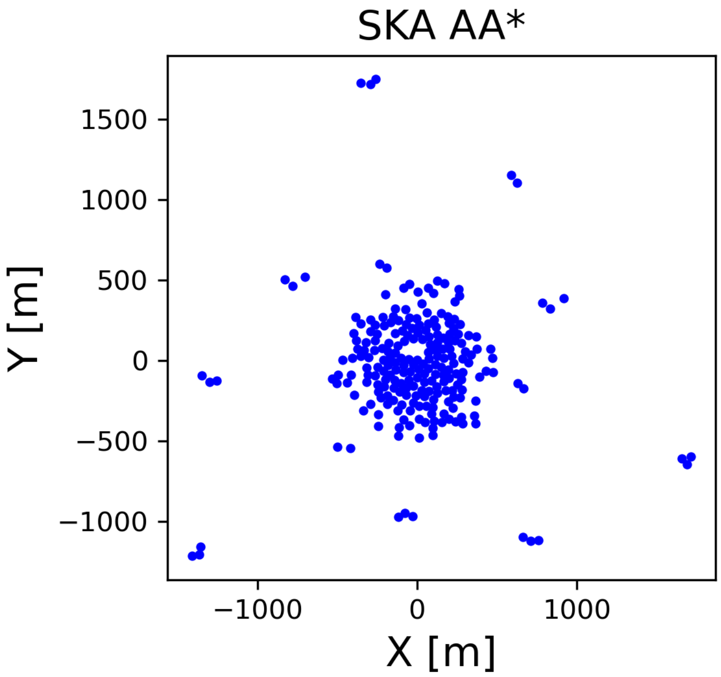

Figure 6.1: Telescope configuration utilized in the simulation: SKA-Low AA* (with a 2 km central core).

ing of the visibility data. In this simulated observation, the sky was observed with a phase center at $\alpha = 15^{\mathrm{h}}00^{\mathrm{m}}00^{\mathrm{s}}$ and $\delta = -30°$ for a duration of 4 hours (±2 hours hour angle). The observing bandwidth of the lightcone spans 8 MHz with a channel separation of 125 kHz. For additional details, refer to Tab. 6.1.

6.3.1 Telescope Model

In this work, we focus primarily on the upcoming SKA-Low telescope. The Square Kilometre Array (SKA)[1] is a next-generation, highly sensitive radio telescope designed to detect low-frequency radio signals, such as the 21-cm signal, making it a powerful tool for probing the Epoch of Reionization (EoR) [49]. The SKA-Low array design includes 512 stations (referred to as AA4), each with a 35-meter diameter, comprising 256 antennas per station. Approximately 50 % of these stations will be concentrated within a 1 km diameter central core, while the remaining stations are distributed along three spiral arms, arranged in clusters of 6 stations with logarithmic spacing. The configuration allows for a maximum baseline of about 73.4 km. In this study, we focus on the AA* SKA-Low layout, which consists of 307 stations with a maximum baseline of 73.4 km. From this layout, we selected all stations located within a 2 km radius (equivalent to a maximum baseline of 2000 meters from the central station), resulting in a subset of 231 stations, array shown in Fig. 6.1.

---

[1] https://www.skao.int/en/explore/telescopes/ska-low

Parameters	SKA (AA*)
Central Frequency	142 MHz (z$\sim$9)
Bandwidth	8 MHz
Number of frequency channels	64
Image Field of view	4°
Number of array elements (N_{a})	231
Maximum baseline (m)	$\sim$2000
Effective collective area (A_{eff})	$\sim 962\ m^2$
Core area of an array (A_{core})	$\sim 12.57\ km^2$

Table 6.1: Parameter values used to conduct these synthetic simulations.

6.4 Power Spectrum

A key scientific objective of both ongoing and upcoming radio interferometric arrays is to detect and characterize fluctuations in the brightness temperature of the redshifted 21cm signal from the EoR. Various statistical tools are available in interferometric experiments to estimate the 21-cm brightness temperature fluctuations through the power spectrum (PS), either directly from the measured visibilities using the delay spectrum technique [**237**, **238**], or via image-based methods that involve gridding, calibration, and deconvolution to reconstruct the full 2D or 3D power spectrum [45, 211]. In this study, we compute the theoretical power spectrum (PS) from the image plane and the observed PS from simulated visibility data using the SKA-Low layout, as illustrated in Fig. 6.2.

6.4.1 Theoretical Power Spectrum

The fluctuation of the brightness temperature $\delta \mathrm{T_b}$ for the 21 cm signal can be defined as [239]:

$$\delta T_b(\nu) \sim 27 x_{HI}(1+\delta_m)\left(\frac{H}{\frac{dv_r}{dr}+H}\right)\left(1-\frac{T_\gamma}{T_S}\right)\times\left(\frac{1+z}{10}\frac{0.15}{\Omega_m h^2}\right)^{1/2}\left(\frac{\Omega_m h^2}{0.023}\right)\left(\frac{\Omega_b h}{0.031}\right)[\mathrm{mK}] \quad (6.1)$$

where, x_{HI} denotes the neutral hydrogen fraction, Ω_{m} represents the matter overdensity, and H refers to the Hubble parameter. Additionally, $\mathrm{dv_r/dr}$ signifies the local gradient of gas velocity along the line of sight, while T_{S} and T_γ correspond to the spin temperature of the intergalactic medium (IGM) and the temperature of the cosmic microwave background (CMB), respectively.

We can define the dimensionless 21cm power spectrum as :

$$\Delta^2(k) = \frac{k^3}{2\pi^2}P(\mathbf{k}) \quad (6.2)$$

$P(\mathbf{k})$ can define as

$$< \delta \mathrm{T_b(k)} \delta \mathrm{T_b(k')} >= (2\pi)^3 \delta(\mathrm{k}+\mathrm{k'})\mathrm{P}(\mathbf{k}) \quad (6.3)$$

where $\delta T_{\mathrm{b}}(k)$ is Fourier conjugate of $\delta T_{\mathrm{b}}(\nu)$.

6.4.2 Observational Power Spectrum

The interferometric visibility is defined as the correlation between the signals received by a pair of antennas, which is given by [106, 201] :

$$V(\mathbf{U},\nu) = \iint A(\hat{\mathbf{s}},\nu)B(\nu)I(\hat{\mathbf{s}},\nu)e^{-i2\pi\nu\mathbf{U}.\hat{\mathbf{s}}}d\Omega, \tag{6.4}$$

Here, $\mathbf{U}$ represents the baseline vector, while $I(\hat{\mathbf{s}},\nu)$ and $A(\hat{\mathbf{s}},\nu)$ correspond to the specific intensity and the antenna beam pattern, respectively, both as functions of frequency (ν). The term $B(\nu)$ represents the instrumental bandpass response. For this simulated observation, we assume an isotropic, frequency-independent antenna beam pattern, resulting in a flat bandpass response with $B(\nu) = 1$. The unit vector is defined as $\hat{\mathbf{s}} \equiv (l, m, n)$, where l, m, and n are the direction cosines pointing towards the east, north, and zenith, respectively, with $n = \sqrt{1 - l^2 - m^2}$. The solid angle element is given by $d\Omega = \frac{dldm}{\sqrt{1-l^2-m^2}}$. In this study, $A(\hat{\mathbf{s}},\nu)$ is assumed to be 1, meaning the primary beam effect is not taken into account.

The inverse Fourier transform of $V(\mathbf{U},\nu)$ along the frequency axis converts the visibility into the delay domain, denoted as τ, resulting in $V(\mathbf{U},\tau)$. Based on this approach, the cylindrical power spectrum, as described in [201], is expressed as follows:

$$P(\mathbf{k}_\perp, k_\parallel) = \left(\frac{\lambda^2}{2k_B}\right)^2 \left(\frac{X^2Y}{\Omega B}\right)|V(\mathbf{U},\tau)|^2, \tag{6.5}$$

where λ represents the wavelength corresponding to the central frequency, k_B is the Boltzmann constant, Ω denotes the primary beam response, and B is the bandwidth. The factors X and Y convert angular and frequency measurements into the transverse co-moving distance $D(z)$ and the co-moving depth along the line of sight, respectively [201]. The term $\mathbf{k}\perp$ corresponds to the Fourier modes perpendicular to the line of sight, while $k\|$ represents the modes along the line of sight, defined as follows:

$$\mathbf{k}_\perp = \frac{2\pi|\mathbf{U}|}{D(z)} \qquad \& \qquad k_\parallel \approx \frac{2\pi\tau\nu_{21}H_0E(z)}{c(1+z)^2}$$

Here, ν_{21} represents the rest-frame frequency of the 21 cm spin-flip transition of H I, while z denotes the redshift corresponding to the observing frequency. The Hubble parameter is given by H_0, and $E(z) \equiv [\Omega_\mathrm{M}(1+z)^3 + \Omega_\Lambda]^{1/2}$. The parameters Ω_M and Ω_Λ correspond to the matter and dark energy densities, respectively [240].

The 1D power spectrum is derived from the 2D power spectrum by performing a spherical average of $P(\mathbf{k}\perp, k\|)$ and is given by:

$$\Delta^2(k) = \frac{k^3}{2\pi^2} < P(\mathbf{k}) >_k \tag{6.6}$$

where, $k = \sqrt{k_\perp^2 + k_\parallel^2}$.

6.5 Emulating H I 21cm Power Spectrum

The objective of developing ANN-based emulators for this work is to study the power spectrum, as these emulators can generate efficient and reliable EoR models. ANNs are a class of machine learning models inspired by the neural architecture of the human brain. They consist of multiple

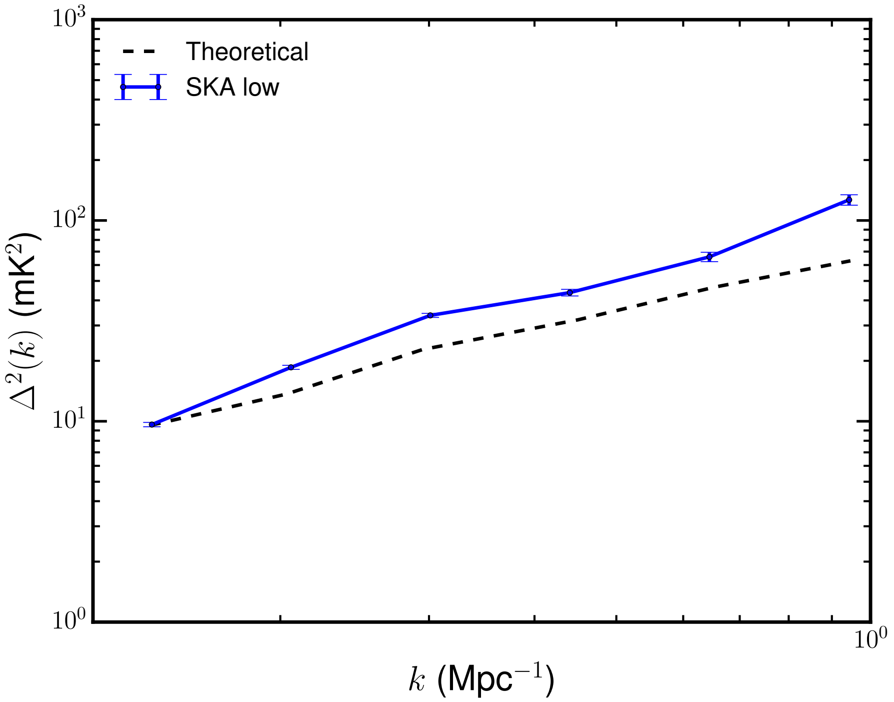

Figure 6.2: Shows a comparison between the theoretical spherical power spectrum (PS) and the simulated observed PS for the same sky model. The theoretical PS for the signal models is represented by a black dashed line, while the simulated observed PS for the SKA-Low array configurations is shown as solid blue lines.

layers of interconnected computational units, referred to as neurons, which process and propagate information through the network. Each neuron applies a transformation to its input via a mathematical function known as an activation function, and passes the result to subsequent layers. Hidden layers those situated between the input and output layers facilitate the learning of complex and non-linear relationships within the data. Commonly used activation functions such as the Rectified Linear Unit (ReLU) and the Exponential Linear Unit (ELU) introduce the necessary non-linearity for the network to approximate highly intricate mappings between inputs and outputs.

These models can then be utilized as substitutes for computationally intensive simulations in Bayesian parameter inference. In addition to this, a non-parametric feature of ANN emulators is the ability to replicate various signal features without relying on their specific parametric characteristics, as they are solely dependent on the training data sets. This capability allows us to utilize the features directly without the need to remove or apply any cleaning algorithms, thereby enabling the inference of associated label parameters. In this study, we are developing an emulator by training it on a set of mock observed power spectra generated from simulated observations with the SKA-Low interferometric array. We also train the emulator on the theoretical power spectrum, that is, in the absence of both instrumental effects and array configuration influences. We use the ANN model to build these emulators. To develop ANN architecture, we are using the Python-based deep learning Keras API, and standard sci-kit learn [241]. To achieve significant accurate PS from the emulator for test set of EoR parameter we have to train the emulator with the sufficient number of the training datasets. To construct an optimal training data set, we sample the parameter space with Latin Hypercube Sampling. Latin Hypercube sampling method samples

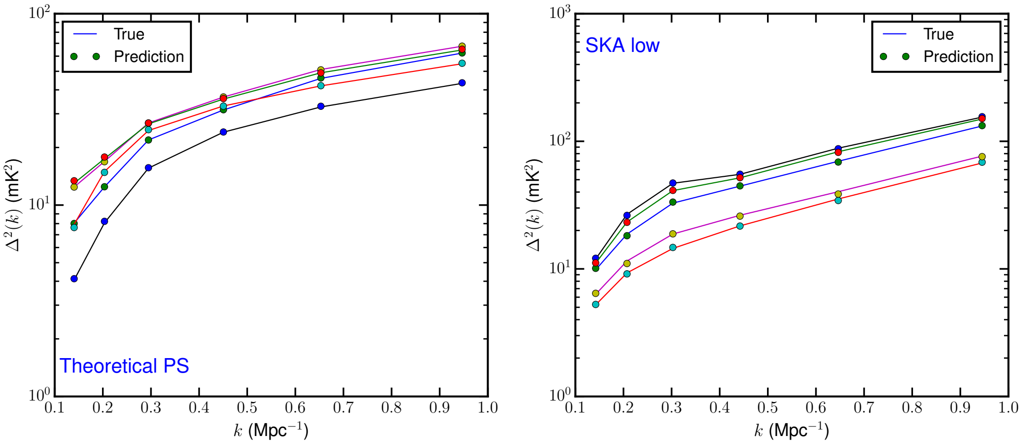

Figure 6.3: The figure shows a comparison between the simulated true power spectrum (solid lines) and the emulated power spectrum by the ANN (dots). The **left panel** shows emulator predictions trained on theoretical power spectra, while the **right panel** presents predictions based on observed power spectra from SKA-Low.

the multi-dimensional parameter space such that no two parameters share the same value in the parameter space, providing an all-unique set of parameters. We generated 300 unique combinations of astrophysical parameters using Latin Hypercube Sampling from the defined parameter ranges to construct the training and test datasets. These sampled parameter sets were used to simulate lightcones, as detailed in Section 6.2.1, and subsequently to compute the observed power spectra using the 21cm end-to-end (E2E) pipeline. To develop construct training and test datasets for the theoretical PS, we use 21cmFast. The parameters range we follow to construct the training datasets are $R_{\rm mfp} = (10\ {\rm Mpc}, 60\ {\rm Mpc}\ )$, $log(T_{\rm vir}) = (4.5\ {\rm K}, 6.0\ {\rm K}\ )$, and $\zeta = (10, 60)$. We construct training and test data sets of observed/theoretical power spectrum ($\Delta^2(k)$) by following these sample parameters for 6 different k modes. We use 270 PS data sets to train and validate the ANN model and 30 data sets to test the ANN emulator. We constructed the network architecture by following Python-based Keras' Sequential API. The network consists of an input layer consisting 3 neurons matching with the training 3 EoR key parameter ($R_{\rm mfp}$, $\log(T_{\rm vir})$, ζ) and two hidden layers with 28 and 14 neurons, respectively, each activated by the 'elu' activation function. The number of neurons in the hidden layers is determined empirically through trial and error, based on the configuration that yields the best performance in terms of accuracy and robustness. The output layer has 6 neurons to predict the observed PS. To ensure effective model training and convergence, the input PS values are standardized using the `StandardScaler` function, which removes the mean and scales the features to unit variance. The corresponding EoR parameters are normalized to the [0, 1] range using `MinMaxScaler`. Both scalers are implemented using the `sklearn` library. This preprocessing step is essential for bringing all input features to a comparable scale, thereby enhancing training stability and learning efficiency. We trained this ANN model using different PS observed by SKA-Low interferometric arrays, to create emulator. Fig. 6.3 presents a comparison between the true test set 21-cm PS, shown as solid lines, and the emulated PS by the ANN, represented by dots. For this comparison, we randomly selected five test sets of power spectra and compared them with the predicted PS from the emulators in each case.

6.6 Bayesian Inference of EoR Parameters

To constrain the EoR parameters and associated errors in the inferred parameter values, the Bayesian approach is one of the most popular methods. In the Bayesian approach, the posterior distribution of the parameters can be defined using Bayes' theorem:

$$p(\theta|D, M) = \frac{p(D|\theta, M)\Pi(\theta|M)}{p(D|M)} \tag{6.7}$$

where θ represents the parameters, D is data, and M represents a model. The evidence $p(D|M)$ serves as a constant normalization factor for a given model. The posterior distribution is determined solely by the product of the likelihood function $L = p(D|\theta, M)$ and the prior distribution of the parameters θ, denoted as $\Pi(\theta|M)$. For this study, we considered a multivariate Gaussian likelihood which can expressed as:

$$lnL = -\frac{1}{2}[\vec{d}_{ref} - \mu]^T[\sigma^2]^{-1}[\vec{d}_{ref} - \mu] - \frac{1}{2}ln(2\pi \ \det\{\sigma^2\}) \tag{6.8}$$

where $\vec{d}_{\mathrm{ref}}$ represents reference data, μ represents the model observable corresponding to the observable parameters and σ^2 is the error covariance associated with $\vec{d}_{\mathrm{ref}}$.

We design our pipeline to extract the most likely EoR parameter values using MCMC for the given log-likelihood. We used the CosmoHammer [242] Python package, utilizing an affine-invariant [243] Markov Chain Monte Carlo (MCMC) ensemble sampler, to conduct model parameter estimation. We have tested the performance of the pipeline using both the theoretical power spectrum and the simulated observed power spectrum. Further details are discussed in Section 6.8.

6.7 Error Covariances of Power Spectrum

The error estimate in the observables is essential to predict the posterior of the parameters. The EoR 21cm signal has varoius contamination from the foreground, systematics, noise, calibration errors etc. To estimate the error covariance of the power spectrum (PS), we assume that the foregrounds have been perfectly modeled and entirely removed from the observed signal. This perfect modelling assume of the sky and instrument to establish a baseline for evaluating performance under idealized conditions. This allows us to isolate the intrinsic capabilities and limitations of the methodology without complications from model inaccuracies. In the following section, we introduce modelling imperfections such as gain calibration and sky position errors to assess the robustness of the method and quantify their impact on power spectrum estimation. This comparison highlights the potential biases that arise when instrumental and modelling errors are neglected, motivating future work on mitigation strategies. Under the perfect modelling assumption, the remaining observed signal consists of the EoR 21cm signal and Gaussian thermal noise. Hence, in this analysis, the total covariance (σ_{t}^2) is defined as the sum of the sample variance (σ_{SV}^2) and the thermal noise variance (σ_{N}^2).

$$\sigma_t^2(i) = \sigma_{SV}^2(i) + \sigma_N^2(i) \tag{6.9}$$

In this analysis, we assume that the measurements at any two bins are mutually uncorrelated which simplifies the error computation. In this study we use variance instead of covariance to calculate error σ^2. We estimated the sample variance for the bin average power spectrum $P(k_{\mathrm{i}})$ by following equation

$$\sigma_{SV}^2(P_i) = [\Delta^2(k_i)]^2/N_{k_i} \tag{6.10}$$

where $N_{\mathrm{k_i}}$ denotes the number of measurement at each k-mode. The thermal noise for given radio interferometric array can be estimated using the following equation [77, 244]:

$$\sigma_N(P_i) = \frac{k^3}{2\pi^2\sqrt{N_{k_i}}}\left(\frac{2T_{sky}^2}{Bt_{obs}}\frac{D^2(z)\Delta D\Omega_{FoV}}{n_p}\left(\frac{A_{eff}A_{core}}{A_{coll}^2}\right)\right) \tag{6.11}$$

where $\mathrm{A_{eff}}$, $\mathrm{A_{coll}}$, and $\mathrm{A_{core}}$ denote the effective area, collecting area, and core area, respectively, of the specified radio interferometric array. The symbol $\mathrm{t_{obs}}$ signifies the total observation time in hours. Additionally, D and ΔD denote the comoving distance to the redshifts where the center is located and the comoving distance corresponding to a bandwidth B at that comoving distance. $\mathrm{T_{sky}}$ denotes the sky temperature calculated using $\mathrm{T_{sky}} \sim 180\left(\frac{\nu}{180\mathrm{MHz}}\right)^{-2.6}$ K [57], symbol Ω_{FoV} denotes field of view symbol, n_{p} represents the number of polarization and $N_{\mathrm{k_i}}$ denotes the number of measurement at each k-mode.

6.8 Result

This section presents the simulation results and discusses their implications for real observations. Detailed outcomes for each case are provided in the following subsections.

6.8.1 Perfect Observing Condition

In this study, we infer astrophysical parameters from the power spectra (PS) obtained using the SKA-Low interferometric array. We assumed that foregrounds were perfectly removed from the observed PS and that there were no calibration or positional errors, as shown in Fig. 6.2. To achieve this, we simulated observations using the 21cm E2E pipeline with only input H I lightcone maps and calculated the PS from the resulting observed H I visibility. To derive the astrophysical parameters, we employed an emulator-based Markov Chain Monte Carlo (MCMC) pipeline. The advantage of employing this emulator-based MCMC pipeline lies in its ability to reduce computational time significantly. Furthermore, since the emulators are trained on observed power spectra that inherently incorporate the effects of the telescope layout, they enable direct parameter inference without requiring separate corrections for these effects. The astrophysical parameters inferred using the SKA-Low interferometric array are presented in Fig. 6.4. In this case, we found that the two parameters, ζ and T_{vir}, closely matched the actual values. However, the third parameter, R_{mfp}, was not correctly constrained. To investigate this issue, we examined whether the lack of constraint could be due to the effects introduced by the telescope layout. Additionally, we compared this result with the inferred astrophysical parameters derived from theoretical power spectra. A similar trend was observed in this case as well. Specifically, ζ and T_{vir} closely matched the actual values, as shown in Fig. 6.4. However, R_{mfp} remained unconstrained, which may be attributed to the degeneracy of the R_{mfp} parameter. To further assess the robustness of this pipeline, we inferred parameters for two additional power spectra generated using astrophysical parameters near the boundary values of those used in the training dataset. The inferred parameters for these power spectra are presented in Fig. 6.7, with set 2 on the left and set 3 on the right, as detailed in Appendix 6.9. Similar to the initial case, the astrophysical parameters ζ and $\mathrm{T_{vir}}$ were well-constrained and closely aligned with the true values in most instances, as depicted in Fig. 6.7.

However, the parameter R_{mfp} remained poorly constrained across both sets. A possible reason is that variations in R_{mfp} within the explored range do not lead to sufficiently distinct signatures in the 21-cm power spectrum for the models considered. In other words, the power spectrum is comparatively insensitive to this parameter, especially when contrasted with $T_{\mathrm{vir}}^{\mathrm{min}}$ and ζ, which more directly regulate the abundance and brightness of the galaxy population and therefore imprint more strongly on the signal. Consequently, the inferred constraints on R_{mfp} are dominated by degeneracies rather than by any clear physical imprint.

As discussed in [111], one manifestation of this degeneracy occurs around redshift $z \simeq 9.0$, where a population of low-mass galaxies with relatively bright stellar populations can reproduce the same observational signatures as the fiducial model. Such galaxies tend to ionize the IGM earlier, effectively masking the influence of R_{mfp} on the morphology of ionized regions. A natural way to mitigate this issue is to exploit the redshift evolution of reionization: combining observations across multiple redshifts provides additional temporal information that can help disentangle early ionizing efficiency from the mean free path of ionizing photons. In future work, a detailed investigation is needed to fully understand this behaviour. We also plan to test it explicitly by incorporating multi-redshift observations to assess whether they can improve constraints on R_{mfp}.

We also noticed that the power spectrum from set 1, whose astrophysical parameters are around the centre of the boundaries, generated more accurate conclusions. By contrast, the power spectra generated in close proximity to the boundary values of the astrophysical parameters yielded an inferred parameter mean that slightly differed from the actual value. For example, in Set 3, the true value of ζ is 57.42, while the inferred mean using the theoretical power spectrum is 50.8. Using the SKA power spectrum, the inferred mean is 59.8. Although these values differ from the true mean, they still lie within 1σ of the inferred uncertainty range (see Table 6.2). This mismatch could be due to the ANN emulator being trained on less training datasets. Potential future development of a more precise emulation could involve training it with a more extensive dataset that cover the parameter space in the effective manner.

6.8.2 Imperfect Observing Conditions

Sensitive radio observations targeting the H I signal from the CD and EoR are highly susceptible to contamination from various sources. Small errors in early data processing steps, such as calibration, can propagate into the final power spectrum (PS) estimates, potentially leading to misinterpretation of the results. In [186], the authors investigated the effects of gain calibration errors and sky model position errors on the recovery of the 21-cm power spectrum. In this study, we build upon that work by examining how such errors impact the recovery of astrophysical parameters. [186] previously conducted a visual comparison of the power spectrum, analyzing both 2D and 1D residual PS in the presence of gain calibration and sky position errors. They also evaluated how the root mean square (RMS) of the residual image varies with different levels of gain calibration and position errors, comparing these values against the signal and thermal noise levels. Their findings showed that a gain calibration error as small as 0.01% could result in a high image RMS in SKA-Low observations, potentially causing confusion or even masking faint cosmological signals. Likewise, a sky model position error exceeding 0.48 arcseconds was found to significantly elevate the image RMS, leading to similar challenges in signal detection. In our analysis, we extend this investigation by comparing the corrupted 1D power spectrum with the original and estimating the astrophysical parameters from the corrupted spectra in two scenarios: one with gain calibration errors and another with sky model position errors.

6.8.2.1 Gain Calibration Errors

Gain calibration errors were incorporated by applying complex gain perturbations to each antenna individually, as expressed in Equation 6.12, following the methodology of [186]. These per-antenna errors propagate through the visibilities since each visibility is formed from a pair of antennas and thus impact the entire k space range. The visibility measured between a pair of antennas i and j, denoted as $V_{\mathrm{ij}}^{m}(t)$, is given by:

$$V_{ij}^{m}(t) = g_i(t)\, g_j^{*}(t)\, V_{ij}^{t}(t) \tag{6.12}$$

Here, $V_{\mathrm{ij}}^{t}(t)$ is the true visibility from the sky, while $g_{\mathrm{i}}(t)$and $g_{\mathrm{j}}(t)$ are the complex gains of antennas i and j, respectively. Although gain calibration attempts to estimate and correct for these instrumental effects, it is typically imperfect, leaving behind residual errors that can propagate through the analysis and bias the recovered signal.

The complex gain for each antenna can be modeled as:

$$g_i = (a_i + \delta a_i)\ \exp[-i(\phi_i + \delta\phi_i)] \tag{6.13}$$

where a_{i} is the nominal amplitude and ϕ_{i} the phase (in radians), with δa_{i} and $\delta\phi_{\mathrm{i}}$ representing the residual errors in amplitude and phase, respectively. In an ideal scenario, $a_{\mathrm{i}} = 1$ and $\phi_{\mathrm{i}} = 0$, yielding a perfect gain of 1. However, with calibration imperfections, the gain simplifies to:

$$g_i = (1 + \delta a_i)\ \exp[-i\,\delta\phi_i] \tag{6.14}$$

To assess the influence of gain calibration errors on the observed power spectrum (PS) and their subsequent impact on associated astrophysical parameters for SKA-Low, we introduced various gain calibration errors as detailed in [186]. The resulting residual PS was visually compared with the actual PS, depicted in the left panel of Fig. 6.5. The parameter obtained from the PS analysis with SKA-Low, incorporating actual signal and PS for gain error residuals, is depicted in the right panel of Fig. 6.5. Upon examining the plotted residual PS spectrum, we observed that for gain calibration error of 0.001 %, the residual PS overlaps with the true PS. For residual PS with a gain calibration error of 0.01%, we observe overlapping at lower k modes but with minor deviation at higher k modes. However, when deriving astrophysical parameters from the residual power spectrum, we found that for a gain calibration error of 0.001%, the derived parameters match those derived from the true PS. In contrast, for PS with the gain calibration error of 0.01%, the derived parameters exhibit significant differences from the actual values. This indicates that astrophysical parameters are highly sensitive to gain calibration errors, and even minor deviations in the PS due to gain calibration errors can severely impact the estimation of parameters, introducing bias. The sensitivity of derived parameters to gain calibration errors clearly suggests that the gain calibration error threshold should be much lower than 0.01%, ideally closer to 0.001%. If the gain calibration error exceeds 0.001%, it is advisable to model them to prevent bias in the derived parameter values.

6.8.2.2 Sky Model Position Error

To evaluate the impact of sky model position errors in the sky model, simulations were conducted using inaccurate sky models as described in [186]. Sky model position errors were modeled with zero-mean Gaussian distributions and varying standard deviations (up to 0.048”, 0.48”, and 4.8”) and applied to the right ascension (RA) of sources, resulting in a new catalog with positional inaccuracies. Residuals were then obtained following equation 4 from [186], by subtracting the corrupted sky from the true sky, and these residuals were used to analyze the effects on the PS. Unlike gain calibration errors which arise from instrumental calibration inaccuracies sky model position errors are rooted in prior assumptions about the sky and do not depend on the calibration solution itself. However, they can still introduce significant foreground residuals that mimic spectral structure, making them especially relevant for 21cm cosmology. This distinction is important, as position errors affect subtraction fidelity rather than the correction of instrumental response, and thus represent a separate and critical source of systematic error.

Similar to gain calibration errors, we evaluated the impact of sky model position errors on the observed power spectrum (PS) and their effect on the inferred astrophysical parameters for SKA-Low. Different sky model position errors, as described above, were introduced, and the resulting residual PS was compared with the true PS, as shown in the left panel of Fig. 6.6. The parameters obtained from the PS, which incorporates actual signals and position error residuals, are depicted in the right panel of Fig. 6.6. Upon examining the plotted residual PS spectrum, we found that for a sky model position error of 0.048", the residual PS overlaps with the true PS. At lower k modes, the residual PS with this position error overlaps well with the true PS, but at higher k modes, there is a minor deviation. This occurs because real-space scales are more affected by arcsecond-level errors at higher k values. However, since we used the entire k range to derive astrophysical parameters from the residual power spectrum, we observed that for a position error of 0.048", the derived parameters closely match those obtained from the true PS. Similarly, for a sky model position error of 0.48", the derived parameters exhibit substantial deviations from the true values. This indicates that astrophysical parameters are highly sensitive to sky model position errors, and even small deviations in the PS due to these errors can severely impact parameter estimation, introducing bias. The sensitivity of derived parameters to sky model position errors, similar to gain calibration errors, suggests that the acceptable sky model position error threshold should be much lower than 0.48", ideally around 0.048". If the sky model position error exceeds 0.048", modeling the errors becomes crucial to prevent bias in the derived parameter values.

6.9 Summary and Discussion

This study presents the development of an ANN and Bayesian-based framework for inferring astrophysical parameters from observed H I power spectra (PS). We used the 21cm E2E pipeline to generate the mock observed power spectrum (PS) for SKA-Low core array configurations. However, generating a large number of modeled observable signals across a multi-dimensional parameter space for Bayesian inference is computationally expensive, particularly when using simulated observations. To address this, we adopted a formalism utilized by several groups, employing emulators for modelling the EoR signal instead of actual simulations.

For constructing the training datasets of observed PS, EoR 21cm signals were generated using the semi-numerical simulation 21cmFAST, with key EoR parameters ($\mathrm{R}_{\mathrm{mfp}}$, T_{vir}, and ζ) described in section 6.2.1. These signals served as sky signals for mock observations using the 21cm E2E pipeline with interferometric arrays like SKA Low, allowing us to construct sets of PS under different astrophysical conditions. These simulated observed PS were then used to train emulator, facilitating Bayesian inference of the corresponding astrophysical parameters. A key advantage of our ANN-based emulators, beyond conserving computational resources, is their ability to perform direct parameter inference using observed power spectrum (PS) data while inherently accounting for telescope layout effects. In radio interferometric observations, limited and uneven uv-coverage introduces deviations from the theoretical PS through sampling artifacts, resolution loss, and convolution with the uv-sampling window. Traditionally, inferring astrophysical parameters from the observed PS requires applying separate corrections to account for these instrumental and sampling effects before comparing with theoretical models. In our approach, however, the ANN models are trained directly on observed-like PS data that already include all such instrumental and sampling-induced distortions. As a result, the emulator learns to incorporate these effects during training, allowing for parameter inference directly from the observed PS without requiring additional correction steps. This contrasts with methods relying on theoretical PS models, where observed data must first be adjusted to match idealized conditions to enable accurate parameter estimation.

In the first case of the study, we perform the inference using the developed ANN and Bayesian-based pipeline assuming perfect observing conditions where we assume the foreground had been perfectly removing only signal and layout effect is there in the observed PS. We infer the astrophysical EoR parameters for the three sets for the signals constructed using the true astrophysical parameters, as listed in Tab.6.2. Both sample variance and thermal noise (calculated for 1000 hours of observation with the given interferometer at redshift z=9) are incorporated in the inference. The detailed results are listed in Tab.6.2. Additionally, we have inferred astrophysical parameters from theoretical power spectra (PS) and compared these findings with parameters inferred from observed PS. In all three cases, the inferred mean values of the parameters $\mathrm{T_{vir}}$ and ζ showed excellent agreement with the true input values, with the true values consistently falling within the 1σ confidence intervals of the inferred posteriors (see Tab. 6.2). However, the parameter $\mathrm{R_{mfp}}$ was often poorly constrained, indicating a high level of degeneracy. In the second case of the study, we assumed that the foregrounds were not perfectly removed, leaving some residual foreground due to gain calibration or sky model position errors. This study aimed to determine the threshold level of gain calibration or sky model position error for SKA-Low. In a previous study by [186], 2D and 1D power spectra with gain and position errors were visually examined. They also calculated the root mean square (RMS) in the residual image across different percentage errors in gain calibration and sky model position, comparing it with signal levels and thermal noise. They found the gain calibration error threshold to be 0.01 % and the sky model position error threshold to be 0.48”.

In this study, we delve deeper and systematically analyze these effects by performing inference on the observed power spectra upcoming SKA-Low. This allows us to understand the impact of various gain calibration and sky model position errors on astrophysical parameters. The key findings noted from this study:

- Our analysis showed that the calibration error threshold for SKA-Low is 0.001%. Exceeding this threshold results in significant deviations in the inferred astrophysical parameters from their actual values, severely affecting the astrophysical processes. An equivalent calibration threshold was identified by [11].
- The position error threshold for SKA-Low is found to be < 0.48”, as displacements $>$ 0.048” cause significant deviations between the inferred astrophysical parameters and their actual values. This suggests that sky model position errors can bias the inference of the astrophysical parameters.
- We also observed that, among all three parameters, ζ is the most sensitive to the power spectrum (PS). Even small variations in the PS, caused by calibration gain or position errors, have a significant impact on the ionization efficiency parameter, ζ.

Thus, we conclude that for the upcoming SKA Low interferometer, the gain calibration error should be nearly 0.001%, and the sky model position error should be less than 0.48” to avoid biasing the inference. Beyond these thresholds, these errors start to affect the results. To reduce their impact, calibration must be performed with the same level of accuracy, or we need to develop modeling or mitigation techniques to eliminate the residual foregrounds arising from calibration or sky model inaccuracies, ensuring minimal influence on the inference. It is important to note that the simulations presented in this study rely on several simplifying assumptions regarding foregrounds and instrumental effects. This underscores the need for more realistic and detailed simulations, including factors such as primary beam chromaticity and other instrumental systematics, to more accurately assess the robustness of parameter inference and to inform optimal array design. These complexities will be addressed in future work for a more comprehensive understanding.

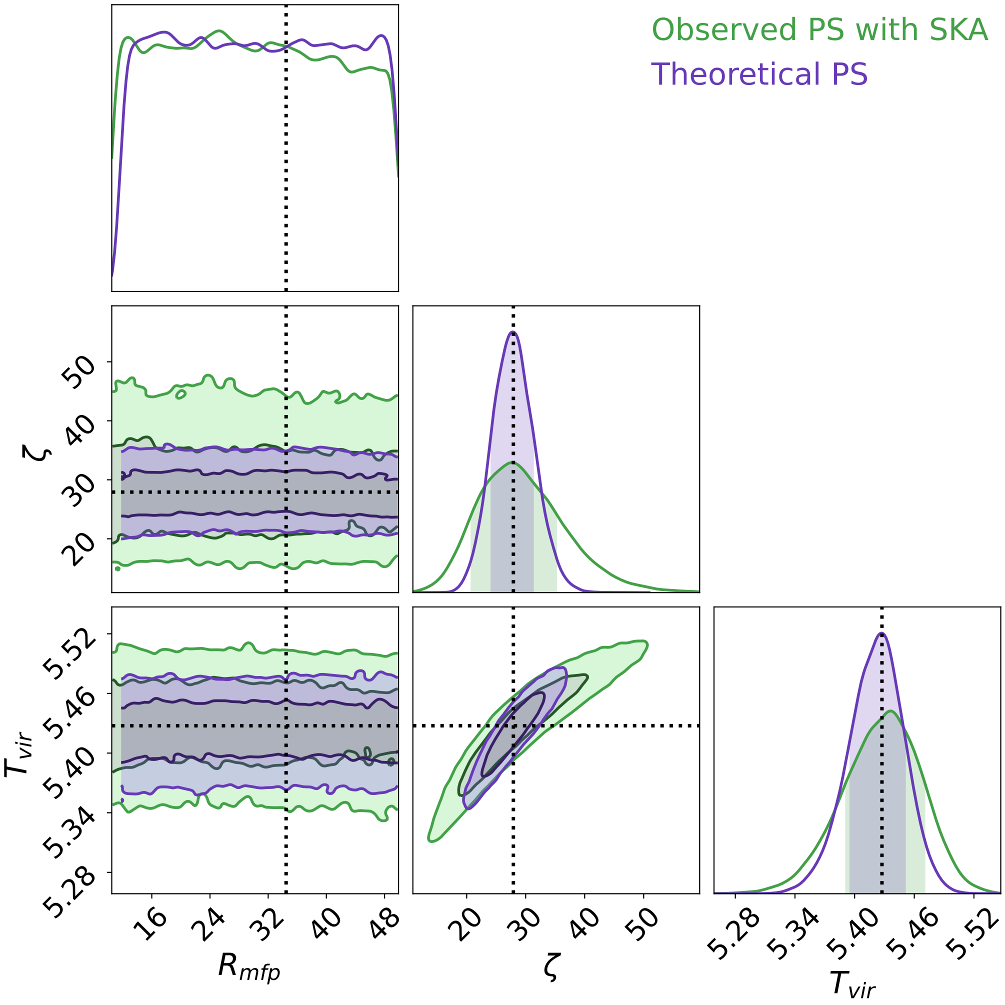

Figure 6.4: Depicts the posterior distribution of model parameters obtained through power spectrum analysis, comparing the theoretical power spectrum with the observed power spectrum from SKA-Low. The enclosed areas between the inner and outer contours signify the 1σ and 2σ confidence levels, respectively.

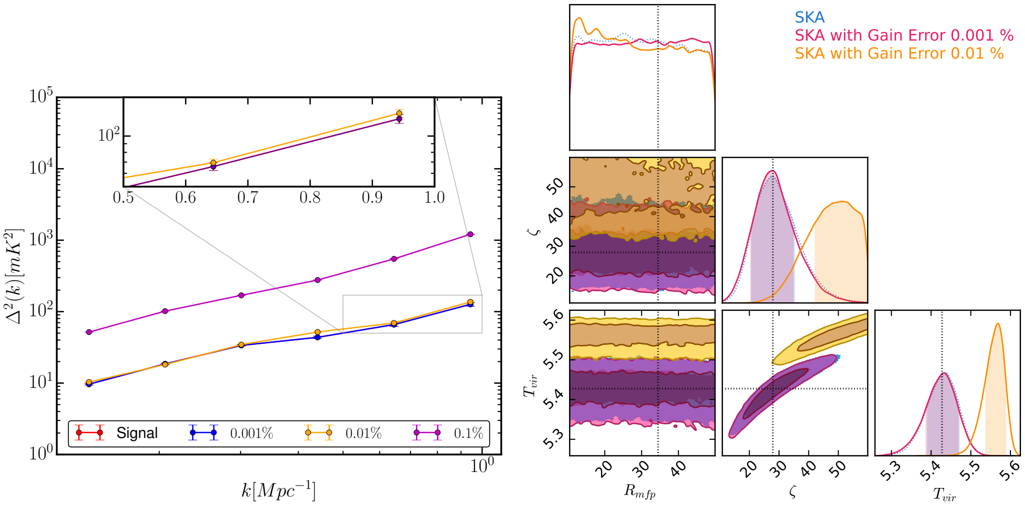

Figure 6.5: **(Left)** Residual power spectra for gain calibration errors (0.001%, 0.01%, and 0.1%) compared to the signal power for SKA-Low array layouts. Error bars represent 1σ uncertainties, including sample variance and thermal noise. **(Right)** Posterior distributions of model parameters from the power spectrum analysis (blue), with gain calibration errors of 0.001% (magenta) and 0.01% (orange) for SKA-Low. The shaded regions represent the 1σ and 2σ confidence intervals.

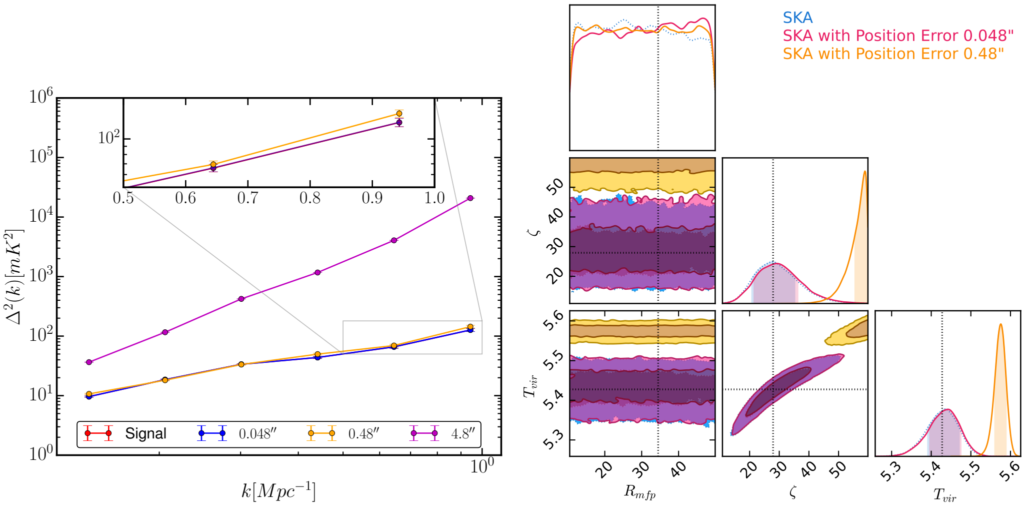

Figure 6.6: **(Left)** Residual power spectra for position errors (0.048”, 0.48”, and 4.8”) for SKA-Low. The error bars are 1σ uncertainties for the k-bins including sample variance and thermal noise. **(Right)** Posterior distributions of model parameters from residual power spectra for position errors of 0.048” (magenta) and 0.48” (orange), with SKA-Low. The shaded regions represent the 1σ and 2σ confidence intervals.

Appendix: Robustness Evaluation of the Emulator-based MCMC Pipeline

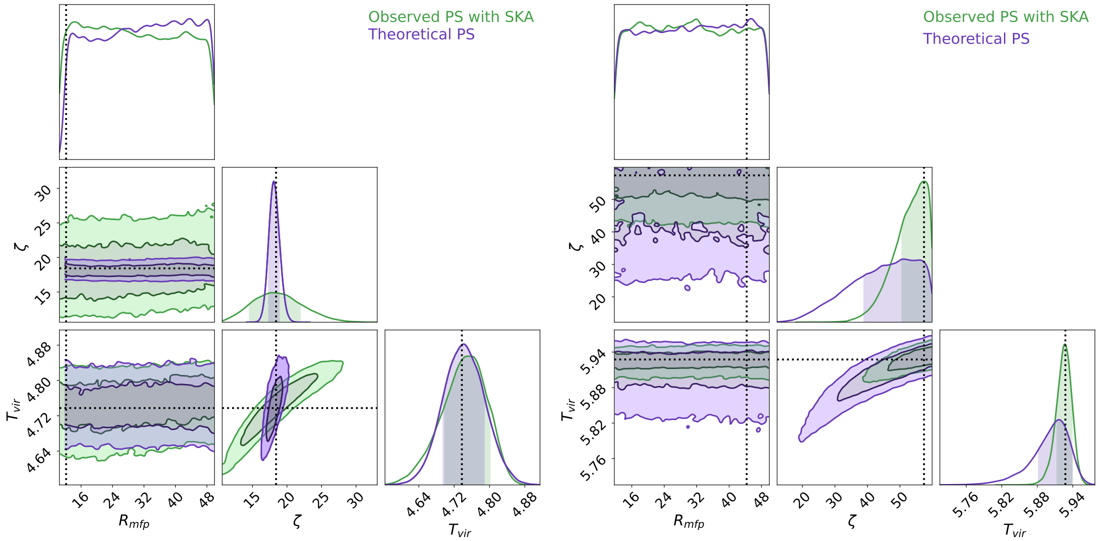

Figure 6.7: Depicts the posterior distribution of model parameters obtained through power spectrum analysis, comparing the theoretical power spectrum with the observed power spectrum from SKA-Low for two different test sets (**left:** Set 2, **right:** Set 3). The enclosed areas between the inner and outer contours signify the 1σ and 2σ confidence levels, respectively.

Set	Parameters & True value	Theoretical PS	Observed PS with SKA-Low
Set 1	R_{mfp}: 34.67	–	–
	ζ: 27.92	$27.5^{+3.7}_{-3.4}$	$27.76^{+7.5}_{-6.9}$
	T_{vir}: 5.428	$5.428^{+0.023}_{-0.032}$	$5.437^{+0.033}_{-0.046}$
Set 2	R_{mfp}: 12.2	50.0^{+0}_{-27}	–
	ζ: 18.42	$18.09^{+0.80}_{-0.75}$	$17.7^{+4.2}_{-3.2}$
	T_{vir}: 4.738	$4.734^{+0.046}_{-0.048}$	$4.761^{+0.041}_{-0.062}$
Set 3	R_{mfp}: 44.33	–	–
	ζ: 57.42	$50.8^{+9.0}_{-11.9}$	$59.8^{+0.0}_{-9.3}$
	T_{vir}: 5.928	$5.917^{+0.022}_{-0.035}$	$5.926^{+0.013}_{-0.013}$

Table 6.2: Inferred EoR model parameters (ζ, T_{vir}, and R_{mfp}) with 1σ uncertainties for different parameter sets. Theoretical power spectrum (PS) estimates are compared with observed PS constraints from SKA-Low.

Chapter 7

Summary and Future scope

In this Chapter, we briefly summarize the work done in the thesis, and highlight the future scope of the work done.

7.1 Summary

This thesis presents a comprehensive machine learning (ML)-based framework developed to extract both the global 21-cm signal and the 21-cm power spectrum from the early Universe, with a particular focus on the Cosmic Dawn (CD) and the Epoch of Reionization (EoR). The 21-cm signal, originating from the hyperfine transition of neutral hydrogen, serves as a powerful probe of the thermal and ionization history of the intergalactic medium (IGM). However, the detection of this faint cosmological signal is extremely challenging due to contamination from bright astrophysical foregrounds, primarily Galactic synchrotron radiation, as well as ionospheric distortions and instrumental systematics, all of which are several orders of magnitude stronger than the signal itself.

To address these challenges, the first part of this thesis is devoted to developing a robust, data-driven pipeline using Artificial Neural Networks (ANNs). The ANN is trained on an extensive library of mock observations that combine theoretical global 21-cm signal models, foregrounds, ionospheric effects, and thermal noise. Two types of signal models are employed: (i) a parameterized tanh-based model implemented through the Accelerated Reionization Era Simulations (ARES), which effectively captures the characteristic features of the global signal and reflects key IGM properties; and (ii) physically motivated models generated by varying source parameters, allowing for a more realistic description of astrophysical scenarios. The tanh-based model, in particular, serves as an intermediate approach between purely phenomenological models (e.g., turning points) and fully physical simulations, it is computationally efficient while maintaining a direct connection to the thermal and ionization state of the IGM. Foregrounds are modeled using a log-log polynomial function, and ionospheric effects are incorporated by modeling frequency-dependent refraction from the F-layer as well as thermal absorption and emission from the D-layer. Instrumental noise is included via the standard radiometer equation. These components are combined to form composite spectra that serve as the input to the ANN, which learns to map from contaminated observations to the underlying astrophysical parameters.

We developed and discuss an ANN-based framework trained on composite sky spectra that incorporated the global 21-cm signal, astrophysical foregrounds, and ionospheric effects. The trained neural network was evaluated on independent test datasets and achieved prediction accuracies ranging from 96% to 97% in scenarios for fixed ionospheric and slowly time varying ionospheric conditions. These results demonstrate the potential of ANNs for accurate parameter inference in the presence of complex observational contaminants. The model's predictive performance was robust across both types of signal models, recovering the global 21-cm signal parameters with consistent accuracy. Furthermore, we compared the ANN's performance against conventional analytical fitting approaches. The ANN consistently outperformed the analytical models, which failed to recover the signal and tended to overfit the foreground component. This highlights the ANN's superior capability to disentangle faint cosmological signals from dominant foreground and ionospheric contributions.

A significant challenge in simulation-based inference frameworks is that they heavily rely on the training dataset. To ensure the robustness of data-driven models, it is essential to construct training sets that adequately sample the full range of the astrophysical parameter space. This requirement becomes particularly demanding in the context of 21-cm cosmology, where direct observational constraints are limited and the underlying parameter space is high-dimensional and complex. In this thesis, we present a systematic evaluation of three widely used sampling strategies, Random Sampling, Latin Hypercube Sampling (LHS), and Hammersley Sampling, to assess their effectiveness in generating representative training datasets for ANN models. Our results demonstrate that Hammersley Sampling offers superior performance in terms of coverage and uniformity in the parameter space, resulting in more accurate and robust ANN predictions. Beyond comparing sampling strategies, we investigate the crucial question of how many training samples are required to reliably train ANNs under varying conditions, including changes in model complexity and parameter dimensionality. We assess model performance across different signal scenarios, including both parametric (tanh-based) and physically motivated global 21-cm signals. The study reveals that the ANN's predictive performance is highly sensitive to the number of training samples, regardless of the sampling method employed. As the dimensionality of the parameter space increases, particularly when foreground contamination and thermal noise are incorporated, the training data required for stable convergence and accurate inference also increases. Notably, the robustness of the ANN framework remains consistent across different signal models, indicating that performance is primarily influenced by the complexity and dimensionality of the input space rather than the specific form of the underlying signal or signal simulation model. These findings emphasize the importance of effective sampling strategies and sufficient data volume in designing reliable machine learning pipelines for global 21-cm signal recovery.

In the final part of this thesis, we extend the machine learning framework to interferometric experiments. Specifically, we develop a hybrid pipeline that combines Artificial Neural Network (ANN) emulators with Bayesian inference techniques to extract astrophysical parameters from the redshifted 21-cm power spectrum (PS) observed by the SKA-Low telescope. The ANN emulator is trained on simulated PS data generated using the SKA-Low AA* array configuration. This approach allows the emulator to learn a direct mapping between the observed PS and the underlying astrophysical parameters—without requiring explicit removal of instrumental effects or sampling artifacts. In interferometric observations, limited and non-uniform uv-coverage introduces complications such as resolution loss, mode mixing, and convolution with the telescope's sampling window, all of which distort the observed PS. Traditional parameter inference pipelines typically apply separate corrections to account for these effects before comparing data with theoretical models. In contrast, our ML-based framework incorporates these observational effects into the training process, enabling end-to-end inference directly from the observed PS. We further apply this pipeline to investigate the impact of two critical systematics: gain calibration errors and source position uncertainties in the input sky model. Our results show that both types of errors can significantly affect the recovery of astrophysical parameters. Specifically, gain calibration errors must be controlled to below 0.001% to prevent distortion of the recovered signal. Likewise, sky model position errors exceeding 0.048 arcseconds lead to residual foreground contamination that overwhelms the 21-cm signal, making reliable inference impossible. These findings highlight the practical utility of our ANN+Bayesian pipeline and underscore the importance of controlling instrumental systematics in upcoming 21-cm cosmology experiments.

7.2 Future Scope

In the next phase of this research, We plan to systematically extend the current 21-cm signal extraction pipeline by incorporating additional real-world observational complexities such as radio frequency interference (RFI), instrumental systematics, real-time ionospheric fluctuations, and realistic antenna beam patterns. These enhancements will make the pipeline directly applicable to data from ongoing global 21-cm experiments, thereby improving its robustness and observational relevance. Building on this, We aim to further expand the scope of the pipeline to target the 21-cm signal from the Dark Ages, an unexplored cosmic epoch preceding the formation of the first luminous sources. During this period, the 21-cm signal serves as a pristine probe of primordial density fluctuations and cosmic evolution. However, detecting this signal is exceptionally challenging due to its extremely low brightness temperature and the need to observe at ultra-low radio frequencies (below 50 MHz), which are inaccessible from Earth due to ionospheric opacity and terrestrial interference.

To address these challenges, We propose developing an advanced machine learning-based framework specifically designed for Dark Ages observations. This framework will incorporate realistic simulations of ultra-low-frequency foregrounds, complex space-based instrumental effects, and novel observational constraints relevant to upcoming lunar or space-based missions such as DARE, LuSEE-Night, and FARSIDE, which plan to operate on the radio-quiet far side of the Moon. These platforms present unique operational challenges, including the absence of ionospheric contamination but the presence of strong cosmic ray and thermal backgrounds, operation with semi-calibrated or uncalibrated instrumentation in harsh space environments, extremely sparse and low signal-to-noise data regimes, and the need for autonomous, real-time processing pipelines suitable for onboard analysis. To effectively address these requirements, the next-generation pipeline will integrate semi-supervised learning, physics-informed neural networks, and Bayesian deep learning techniques. This combination will enable improved generalization from limited labeled data, incorporation of known physical constraints, and robust uncertainty quantification in signal extraction.

In parallel, as instruments like the SKA and JWST come online, they will produce unprecedented volumes of complex astrophysical data. This necessitates the development of scalable and computationally efficient analysis frameworks. Leveraging machine learning's strengths in handling high-dimensional and noisy data, We also plan to explore the synergy between SKA and JWST observations. By jointly constraining astrophysical parameters using combined datasets from both facilities, we can enhance our understanding of cosmic structure formation and evolution.

To support the broader scientific community, We plan to develop a publicly accessible repository of mock observations and simulation outputs generated through this work. This resource will serve as a standardized platform for testing, validating, and benchmarking signal recovery techniques, similar to curated datasets that have accelerated progress in fields like image processing and computer vision. Ultimately, equipping the pipeline to handle increasingly realistic observational conditions and making its outputs openly available will significantly enhance our ability to extract astrophysical information from 21-cm data. It will also help establish a foundation for future data-driven research in radio astronomy and cosmology, where expertise in machine learning, statistical inference, and Big Data handling will be indispensable.

Bibliography

[1] C. L. Reichardt, "Observing the Epoch of Reionization with the Cosmic Microwave Background," in *Understanding the Epoch of Cosmic Reionization: Challenges and Progress* (A. Mesinger, ed.), vol. 423 of *Astrophysics and Space Science Library*, p. 227, Jan. 2016.

[2] B. Greig, A. Mesinger, F. B. Davies, F. Wang, J. Yang, and J. F. Hennawi, "IGM damping wing constraints on reionization from covariance reconstruction of two z $\gtrsim$ 7 QSOs," *Monthly Notices of the Royal Astronomical Society*, vol. 512, pp. 5390–5403, June 2022.

[3] Y. Qin, A. Mesinger, S. E. I. Bosman, and M. Viel, "Reionization and galaxy inference from the high-redshift Ly α forest," *Monthly Notices of the Royal Astronomical Society*, vol. 506, pp. 2390–2407, Sept. 2021.

[4] J. R. Pritchard and A. Loeb, "21 cm cosmology in the 21st century," *Reports on Progress in Physics*, vol. 75, p. 086901, jul 2012.

[5] A. Mesinger, S. Furlanetto, and R. Cen, "21CMFAST: a fast, seminumerical simulation of the high-redshift 21-cm signal," *Monthly Notices of the Royal Astronomical Society*, vol. 411, pp. 955–972, Feb. 2011.

[6] C. M. Trott, C. H. Jordan, S. Midgley, N. Barry, B. Greig, B. Pindor, J. H. Cook, G. Sleap, S. J. Tingay, D. Ung, P. Hancock, A. Williams, J. Bowman, R. Byrne, A. Chokshi, B. J. Hazelton, K. Hasegawa, D. Jacobs, R. C. Joseph, W. Li, J. L. B. Line, C. Lynch, B. McKinley, D. A. Mitchell, M. F. Morales, M. Ouchi, J. C. Pober, M. Rahimi, K. Takahashi, R. B. Wayth, R. L. Webster, M. Wilensky, J. S. B. Wyithe, S. Yoshiura, Z. Zhang, and Q. Zheng, "Deep multiredshift limits on Epoch of Reionization 21 cm power spectra from four seasons of Murchison Widefield Array observations," *Monthly Notices of the Royal Astronomical Society*, vol. 493, pp. 4711–4727, 02 2020.

[7] HERA Collaboration, Z. Abdurashidova, T. Adams, J. E. Aguirre, P. Alexander, Z. S. Ali, R. Baartman, Y. Balfour, R. Barkana, A. P. Beardsley, G. Bernardi, T. S. Billings, J. D. Bowman, R. F. Bradley, D. Breitman, P. Bull, J. Burba, S. Carey, C. L. Carilli, C. Cheng, S. Choudhuri, D. R. DeBoer, E. de Lera Acedo, M. Dexter, J. S. Dillon, J. Ely, A. Ewall-Wice, N. Fagnoni, A. Fialkov, R. Fritz, S. R. Furlanetto, K. Gale-Sides, H. Garsden, B. Glendenning, A. Gorce, D. Gorthi, B. Greig, J. Grobbelaar, Z. Halday, B. J. Hazelton, S. Heimersheim, J. N. Hewitt, J. Hickish, D. C. Jacobs, A. Julius, N. S. Kern, J. Kerrigan, P. Kittiwisit, S. A. Kohn, M. Kolopanis, A. Lanman, P. La Plante, D. Lewis, A. Liu, A. Loots, Y.-Z. Ma, D. H. E. MacMahon, L. Malan, K. Malgas, C. Malgas, M. Maree, B. Marero, Z. E. Martinot, L. McBride, A. Mesinger, J. Mirocha, M. Molewa, M. F. Morales, T. Mosiane, J. B. Muñoz, S. G. Murray, V. Nagpal, A. R. Neben, B. Nikolic, C. D. Nunhokee, H. Nuwegeld, A. R. Parsons, R. Pascua, N. Patra, S. Pieterse, Y. Qin, N. Razavi-Ghods, J. Robnett, K. Rosie, M. G. Santos, P. Sims, S. Singh, C. Smith, H. Swarts, J. Tan, N. Thyagarajan, M. J. Wilensky, P. K. G. Williams, P. van Wyngaarden, and H. Zheng, "Improved Constraints

on the 21 cm EoR Power Spectrum and the X-Ray Heating of the IGM with HERA Phase I Observations," *The Astrophysical Journal*, vol. 945, p. 124, Mar. 2023.

[8] F. G. Mertens, M. Mevius, L. V. E. Koopmans, A. R. Offringa, S. Zaroubi, A. Acharya, S. A. Brackenhoff, E. Ceccotti, E. Chapman, K. Chege, B. Ciardi, R. Ghara, S. Ghosh, S. K. Giri, I. Hothi, C. Höfer, I. T. Iliev, V. Jelić, Q. Ma, G. Mellema, S. Munshi, V. N. Pandey, and S. Yatawatta, "Deeper multi-redshift upper limits on the Epoch of Reionization 21-cm signal power spectrum from LOFAR between z=8.3 and z=10.1," *arXiv e-prints*, p. arXiv:2503.05576, Mar. 2025.

[9] E. Chapman and V. Jelić, "Foregrounds and their mitigation," *arXiv e-prints*, p. arXiv:1909.12369, Sept. 2019.

[10] C. G. T. Haslam, U. Klein, C. J. Salter, H. Stoffel, W. E. Wilson, M. N. Cleary, D. J. Cooke, and P. Thomasson, "A 408 MHz all-sky continuum survey. I - Observations at southern declinations and for the North Polar region.," *Astronomy and Astrophysics*, vol. 100, pp. 209–219, July 1981.

[11] N. Barry, B. Hazelton, I. Sullivan, M. F. Morales, and J. C. Pober, "Calibration requirements for detecting the 21 cm epoch of reionization power spectrum and implications for the SKA," *Monthly Notices of the Royal Astronomical Society*, vol. 461, pp. 3135–3144, Sept. 2016.

[12] E. Shen, D. Anstey, E. de Lera Acedo, A. Fialkov, and W. Handley, "Quantifying ionospheric effects on global 21-cm observations," *Monthly Notices of the Royal Astronomical Society*, vol. 503, pp. 344–353, May 2021.

[13] M. Choudhury, A. Chatterjee, A. Datta, and T. R. Choudhury, "Using artificial neural networks to extract the 21-cm global signal from the EDGES data," *Monthly Notices of the Royal Astronomical Society*, vol. 502, pp. 2815–2825, Apr. 2021.

[14] A. A. Penzias and R. W. Wilson, "A Measurement of Excess Antenna Temperature at 4080 Mc/s.," *The Astrophysical Journal*, vol. 142, pp. 419–421, July 1965.

[15] R. H. Dicke, P. J. E. Peebles, P. G. Roll, and D. T. Wilkinson, "Cosmic Black-Body Radiation.," *The Astrophysical Journal*, vol. 142, pp. 414–419, July 1965.

[16] Planck Collaboration, N. Aghanim, Y. Akrami, F. Arroja, M. Ashdown, J. Aumont, C. Baccigalupi, M. Ballardini, A. J. Banday, R. B. Barreiro, N. Bartolo, S. Basak, R. Battye, K. Benabed, J. P. Bernard, M. Bersanelli, P. Bielewicz, J. J. Bock, J. R. Bond, J. Borrill, F. R. Bouchet, F. Boulanger, M. Bucher, C. Burigana, R. C. Butler, E. Calabrese, J. F. Cardoso, J. Carron, B. Casaponsa, A. Challinor, H. C. Chiang, L. P. L. Colombo, C. Combet, D. Contreras, B. P. Crill, F. Cuttaia, P. de Bernardis, G. de Zotti, J. Delabrouille, J. M. Delouis, F. X. Désert, E. Di Valentino, C. Dickinson, J. M. Diego, S. Donzelli, O. Doré, M. Douspis, A. Ducout, X. Dupac, G. Efstathiou, F. Elsner, T. A. Enßlin, H. K. Eriksen, E. Falgarone, Y. Fantaye, J. Fergusson, R. Fernandez-Cobos, F. Finelli, F. Forastieri, M. Frailis, E. Franceschi, A. Frolov, S. Galeotta, S. Galli, K. Ganga, R. T. Génova-Santos, M. Gerbino, T. Ghosh, J. González-Nuevo, K. M. Górski, S. Gratton, A. Gruppuso, J. E. Gudmundsson, J. Hamann, W. Handley, F. K. Hansen, G. Helou, D. Herranz, S. R. Hildebrandt, E. Hivon, Z. Huang, A. H. Jaffe, W. C. Jones, A. Karakci, E. Keihänen, R. Keskitalo, K. Kiiveri, J. Kim, T. S. Kisner, L. Knox, N. Krachmalnicoff, M. Kunz, H. Kurki-Suonio, G. Lagache, J. M. Lamarre, M. Langer, A. Lasenby, M. Lattanzi, C. R. Lawrence, M. Le Jeune, J. P. Leahy, J. Lesgourgues, F. Levrier, A. Lewis, M. Liguori, P. B. Lilje, M. Lilley, V. Lindholm, M. López-Caniego, P. M. Lubin, Y. Z. Ma, J. F. Macías-Pérez, G. Maggio, D. Maino, N. Mandolesi, A. Mangilli, A. Marcos-Caballero, M. Maris, P. G. Martin,

M. Martinelli, E. Martínez-González, S. Matarrese, N. Mauri, J. D. McEwen, P. D. Meerburg, P. R. Meinhold, A. Melchiorri, A. Mennella, M. Migliaccio, M. Millea, S. Mitra, M. A. Miville-Deschênes, D. Molinari, A. Moneti, L. Montier, G. Morgante, A. Moss, S. Mottet, M. Münchmeyer, P. Natoli, H. U. Nørgaard-Nielsen, C. A. Oxborrow, L. Pagano, D. Paoletti, B. Partridge, G. Patanchon, T. J. Pearson, M. Peel, H. V. Peiris, F. Perrotta, V. Pettorino, F. Piacentini, L. Polastri, G. Polenta, J. L. Puget, J. P. Rachen, M. Reinecke, M. Remazeilles, C. Renault, A. Renzi, G. Rocha, C. Rosset, G. Roudier, J. A. Rubiño-Martín, B. Ruiz-Granados, L. Salvati, M. Sandri, M. Savelainen, D. Scott, E. P. S. Shellard, M. Shiraishi, C. Sirignano, G. Sirri, L. D. Spencer, R. Sunyaev, A. S. Suur-Uski, J. A. Tauber, D. Tavagnacco, M. Tenti, L. Terenzi, L. Toffolatti, M. Tomasi, T. Trombetti, J. Valiviita, B. Van Tent, L. Vibert, P. Vielva, F. Villa, N. Vittorio, B. D. Wandelt, I. K. Wehus, M. White, S. D. M. White, A. Zacchei, and A. Zonca, "Planck 2018 results. I. Overview and the cosmological legacy of Planck," *Astronomy and Astrophysics*, vol. 641, p. A1, Sept. 2020.

[17] P. Dayal and A. Ferrara, "Early galaxy formation and its large-scale effects," *Physics Reports*, vol. 780, pp. 1–64, Dec. 2018.

[18] X. Fan, C. Carilli, and B. Keating, "Observational constraints on cosmic reionization," *Annual Review of Astronomy and Astrophysics*, vol. 44, no. 1, pp. 415–462, 2006.

[19] R. H. Becker, X. Fan, R. L. White, M. A. Strauss, V. K. Narayanan, R. H. Lupton, J. E. Gunn, J. Annis, N. A. Bahcall, J. Brinkmann, A. J. Connolly, I. Csabai, P. C. Czarapata, M. Doi, T. M. Heckman, G. S. Hennessy, Ž. Ivezić, G. R. Knapp, D. Q. Lamb, T. A. McKay, J. A. Munn, T. Nash, R. Nichol, J. R. Pier, G. T. Richards, D. P. Schneider, C. Stoughton, A. S. Szalay, A. R. Thakar, and D. G. York, "Evidence for Reionization at z∼6: Detection of a Gunn-Peterson Trough in a z=6.28 Quasar," *The Astronomical Journal*, vol. 122, pp. 2850–2857, Dec. 2001.

[20] J. X. Prochaska, S. Herbert-Fort, and A. M. Wolfe, "The SDSS Damped Lyα Survey: Data Release 3," *The Astrophysical Journal*, vol. 635, pp. 123–142, Dec. 2005.

[21] R. Adam, N. Aghanim, M. Ashdown, J. Aumont, C. Baccigalupi, M. Ballardini, A. Banday, R. Barreiro, N. Bartolo, S. Basak, *et al.*, "Planck intermediate results-xlvii. planck constraints on reionization history," *Astronomy & Astrophysics*, vol. 596, p. A108, 2016.

[22] M. McQuinn, "The Evolution of the Intergalactic Medium," *Annual Review of Astronomy and Astrophysics*, vol. 54, pp. 313–362, Sept. 2016.

[23] M. J. Rees, "Polarization and Spectrum of the Primeval Radiation in an Anisotropic Universe," *The Astrophysical Journal Letters*, vol. 153, p. L1, July 1968.

[24] W. Hu and M. White, "A CMB polarization primer," *New Astronomy*, vol. 2, pp. 323–344, Oct. 1997.

[25] Planck Collaboration, R. Adam, N. Aghanim, M. Ashdown, J. Aumont, C. Baccigalupi, M. Ballardini, A. J. Banday, R. B. Barreiro, N. Bartolo, S. Basak, R. Battye, K. Benabed, J. P. Bernard, M. Bersanelli, P. Bielewicz, J. J. Bock, A. Bonaldi, L. Bonavera, J. R. Bond, J. Borrill, F. R. Bouchet, F. Boulanger, M. Bucher, C. Burigana, E. Calabrese, J. F. Cardoso, J. Carron, H. C. Chiang, L. P. L. Colombo, C. Combet, B. Comis, F. Couchot, A. Coulais, B. P. Crill, A. Curto, F. Cuttaia, R. J. Davis, P. de Bernardis, A. de Rosa, G. de Zotti, J. Delabrouille, E. Di Valentino, C. Dickinson, J. M. Diego, O. Doré, M. Douspis, A. Ducout, X. Dupac, F. Elsner, T. A. Enßlin, H. K. Eriksen, E. Falgarone, Y. Fantaye, F. Finelli, F. Forastieri, M. Frailis, A. A. Fraisse, E. Franceschi, A. Frolov, S. Galeotta, S. Galli, K. Ganga, R. T. Génova-Santos, M. Gerbino, T. Ghosh, J. González-Nuevo, K. M.

Górski, A. Gruppuso, J. E. Gudmundsson, F. K. Hansen, G. Helou, S. Henrot-Versillé, D. Herranz, E. Hivon, Z. Huang, S. Ilić, A. H. Jaffe, W. C. Jones, E. Keihänen, R. Keskitalo, T. S. Kisner, L. Knox, N. Krachmalnicoff, M. Kunz, H. Kurki-Suonio, G. Lagache, A. Lähteenmäki, J. M. Lamarre, M. Langer, A. Lasenby, M. Lattanzi, C. R. Lawrence, M. Le Jeune, F. Levrier, A. Lewis, M. Liguori, P. B. Lilje, M. López-Caniego, Y. Z. Ma, J. F. Macías-Pérez, G. Maggio, A. Mangilli, M. Maris, P. G. Martin, E. Martínez-González, S. Matarrese, N. Mauri, J. D. McEwen, P. R. Meinhold, A. Melchiorri, A. Mennella, M. Migliaccio, M. A. Miville-Deschênes, D. Molinari, A. Moneti, L. Montier, G. Morgante, A. Moss, P. Naselsky, P. Natoli, C. A. Oxborrow, L. Pagano, D. Paoletti, B. Partridge, G. Patanchon, L. Patrizii, O. Perdereau, L. Perotto, V. Pettorino, F. Piacentini, S. Plaszczynski, L. Polastri, G. Polenta, J. L. Puget, J. P. Rachen, B. Racine, M. Reinecke, M. Remazeilles, A. Renzi, G. Rocha, M. Rossetti, G. Roudier, J. A. Rubiño-Martín, B. Ruiz-Granados, L. Salvati, M. Sandri, M. Savelainen, D. Scott, G. Sirri, R. Sunyaev, A. S. Suur-Uski, J. A. Tauber, M. Tenti, L. Toffolatti, M. Tomasi, M. Tristram, T. Trombetti, J. Valiviita, F. Van Tent, P. Vielva, F. Villa, N. Vittorio, B. D. Wandelt, I. K. Wehus, M. White, A. Zacchei, and A. Zonca, "Planck intermediate results. XLVII. Planck constraints on reionization history," *Astronomy and Astrophysics*, vol. 596, p. A108, Dec. 2016.

[26] Planck Collaboration, Aghanim, N., Akrami, Y., Arroja, F., Ashdown, M., Aumont, J., Baccigalupi, C., Ballardini, M., Banday, A. J., Barreiro, R. B., Bartolo, N., Basak, S., Battye, R., Benabed, K., Bernard, J.-P., Bersanelli, M., Bielewicz, P., Bock, J. J., Bond, J. R., and et al., "Planck 2018 results. i. overview and the cosmological legacy of planck," *A&A*, 2019.

[27] J. E. Gunn and B. A. Peterson, "On the Density of Neutral Hydrogen in Intergalactic Space.," *The Astrophysical Journal*, vol. 142, pp. 1633–1636, Nov. 1965.

[28] R. H. Becker, X. Fan, R. L. White, M. A. Strauss, V. K. Narayanan, R. H. Lupton, J. E. Gunn, J. Annis, N. A. Bahcall, J. Brinkmann, A. J. Connolly, I. Csabai, P. C. Czarapata, M. Doi, T. M. Heckman, G. S. Hennessy, Ž. Ivezić, G. R. Knapp, D. Q. Lamb, T. A. McKay, J. A. Munn, T. Nash, R. Nichol, J. R. Pier, G. T. Richards, D. P. Schneider, C. Stoughton, A. S. Szalay, A. R. Thakar, and D. G. York, "Evidence for Reionization at z∼6: Detection of a Gunn-Peterson Trough in a z=6.28 Quasar," *The Astronomical Journal*, vol. 122, pp. 2850–2857, Dec. 2001.

[29] J. Yang, F. Wang, X. Fan, J. F. Hennawi, F. B. Davies, M. Yue, E. Banados, X.-B. Wu, B. Venemans, A. J. Barth, F. Bian, K. Boutsia, R. Decarli, E. P. Farina, R. Green, L. Jiang, J.-T. Li, C. Mazzucchelli, and F. Walter, "Pōniuā'ena: A Luminous z = 7.5 Quasar Hosting a 1.5 Billion Solar Mass Black Hole," *The Astrophysical Journal Letters*, vol. 897, p. L14, July 2020.

[30] I. D. McGreer, A. Mesinger, and V. D'Odorico, "Model-independent evidence in favour of an end to reionization by $z \approx 6$," *Monthly Notices of the Royal Astronomical Society*, vol. 447, pp. 499–505, Feb. 2015.

[31] I. G. B. Wold, S. Malhotra, J. Rhoads, J. Wang, W. Hu, L. A. Perez, Z.-Y. Zheng, A. A. Khostovan, A. R. Walker, L. F. Barrientos, J. González-López, S. Harish, L. Infante, C. Jiang, J. Pharo, C. Moya-Sierralta, F. E. Bauer, G. Galaz, F. Valdes, and H. Yang, "LAGER Lyα Luminosity Function at z 7: Implications for Reionization," *The Astrophysical Journal*, vol. 927, p. 36, Mar. 2022.

[32] M. Ouchi, K. Shimasaku, H. Furusawa, T. Saito, M. Yoshida, M. Akiyama, Y. Ono, T. Yamada, K. Ota, N. Kashikawa, M. Iye, T. Kodama, S. Okamura, C. Simpson, and M. Yoshida,

"Statistics of 207 Lyα Emitters at a Redshift Near 7: Constraints on Reionization and Galaxy Formation Models," *The Astrophysical Journal*, vol. 723, pp. 869–894, Nov. 2010.

[33] Z.-Y. Zheng, J. Wang, J. Rhoads, L. Infante, S. Malhotra, W. Hu, A. R. Walker, L. Jiang, C. Jiang, P. Hibon, A. Gonzalez, X. Kong, X. Zheng, G. Galaz, and L. F. Barrientos, "First Results from the Lyman Alpha Galaxies in the Epoch of Reionization (LAGER) Survey: Cosmological Reionization at z $\sim$ 7," *The Astrophysical Journal Letters*, vol. 842, p. L22, June 2017.

[34] A. J. Taylor, L. L. Cowie, A. J. Barger, E. M. Hu, and A. Songaila, "The Evolution of the Ultraluminous Lyα Luminosity Function over z = 5.7-6.6," *The Astrophysical Journal*, vol. 914, p. 79, June 2021.

[35] E. Sobacchi and A. Mesinger, "The clustering of Lyman α emitters at z $\approx$ 7: implications for reionization and host halo masses," *Monthly Notices of the Royal Astronomical Society*, vol. 453, pp. 1843–1854, Oct. 2015.

[36] C. A. Mason, T. Treu, M. Dijkstra, A. Mesinger, M. Trenti, L. Pentericci, S. de Barros, and E. Vanzella, "The Universe Is Reionizing at z $\sim$ 7: Bayesian Inference of the IGM Neutral Fraction Using Lyα Emission from Galaxies," *The Astrophysical Journal*, vol. 856, p. 2, Mar. 2018.

[37] A. Hoag, M. Bradač, K. Huang, C. Mason, T. Treu, K. B. Schmidt, M. Trenti, V. Strait, B. C. Lemaux, E. Q. Finney, and M. Paddock, "Constraining the Neutral Fraction of Hydrogen in the IGM at Redshift 7.5," *The Astrophysical Journal*, vol. 878, p. 12, June 2019.

[38] G. B. Field, "Excitation of the hydrogen 21-cm line," *Proceedings of the IRE*, vol. 46, pp. 240–250, Jan 1958.

[39] J. D. Bowman, A. E. E. Rogers, R. A. Monsalve, T. J. Mozdzen, and N. Mahesh, "An absorption profile centred at 78 megahertz in the sky-averaged spectrum," *Nature*, vol. 555, pp. 67–70, Mar. 2018.

[40] S. Singh and R. Subrahmanyan, "The redshifted 21 cm signal in the EDGES low-band spectrum," *The Astrophysical Journal*, vol. 880, p. 26, jul 2019.

[41] E. de Lera Acedo, "Reach: Radio experiment for the analysis of cosmic hydrogen," in *2019 International Conference on Electromagnetics in Advanced Applications (ICEAA)*, pp. 0626–0629, 2019.

[42] L. Philip, Z. Abdurashidova, H. C. Chiang, N. Ghazi, A. Gumba, H. M. Heilgendorff, J. M. Jáuregui-García, K. Malepe, C. D. Nunhokee, J. Peterson, J. L. Sievers, V. Simes, and R. Spann, "Probing Radio Intensity at High-Z from Marion: 2017 Instrument," *Journal of Astronomical Instrumentation*, vol. 8, p. 1950004, Jan. 2019.

[43] L. J. Greenhill and G. Bernardi, "HI Epoch of Reionization Arrays," *arXiv e-prints*, p. arXiv:1201.1700, Jan. 2012.

[44] G. Swarup, S. Ananthakrishnan, V. K. Kapahi, A. P. Rao, C. R. Subrahmanya, and V. K. Kulkarni, "The Giant Metre-Wave Radio Telescope," *Current Science*, vol. 60, p. 95, Jan. 1991.

[45] F. G. Mertens, M. Mevius, L. V. E. Koopmans, A. R. Offringa, G. Mellema, S. Zaroubi, M. A. Brentjens, H. Gan, B. K. Gehlot, V. N. Pandey, A. M. Sardarabadi, H. K. Vedantham, S. Yatawatta, K. M. B. Asad, B. Ciardi, E. Chapman, S. Gazagnes, R. Ghara, A. Ghosh, S. K. Giri, I. T. Iliev, V. Jelić, R. Kooistra, R. Mondal, J. Schaye, and M. B. Silva, "Improved upper limits on the 21cm signal power spectrum of neutral hydrogen at z $\approx$ 9.1 from LOFAR," *Monthly Notices of the Royal Astronomical Society*, vol. 493, pp. 1662–1685, 02 2020.

[46] S. J. Tingay, R. Goeke, J. D. Bowman, D. Emrich, S. M. Ord, D. A. Mitchell, M. F. Morales, T. Booler, B. Crosse, R. B. Wayth, C. J. Lonsdale, S. Tremblay, D. Pallot, T. Colegate, A. Wicenec, N. Kudryavtseva, W. Arcus, D. Barnes, G. Bernardi, F. Briggs, S. Burns, J. D. Bunton, R. J. Cappallo, B. E. Corey, A. Deshpande, L. Desouza, B. M. Gaensler, L. J. Greenhill, P. J. Hall, B. J. Hazelton, D. Herne, J. N. Hewitt, M. Johnston-Hollitt, D. L. Kaplan, J. C. Kasper, B. B. Kincaid, R. Koenig, E. Kratzenberg, M. J. Lynch, B. Mckinley, S. R. Mcwhirter, E. Morgan, D. Oberoi, J. Pathikulangara, T. Prabu, R. A. Remillard, A. E. E. Rogers, A. Roshi, J. E. Salah, R. J. Sault, N. Udaya-Shankar, F. Schlagenhaufer, K. S. Srivani, J. Stevens, R. Subrahmanyan, M. Waterson, R. L. Webster, A. R. Whitney, A. Williams, C. L. Williams, and J. S. B. Wyithe, "The Murchison Widefield Array: The Square Kilometre Array Precursor at Low Radio Frequencies," *Publications of the Astronomical Society of Australia*, vol. 30, p. e007, Jan. 2013.

[47] D. R. DeBoer, A. R. Parsons, J. E. Aguirre, P. Alexander, Z. S. Ali, A. P. Beardsley, G. Bernardi, J. D. Bowman, R. F. Bradley, C. L. Carilli, C. Cheng, E. de Lera Acedo, J. S. Dillon, A. Ewall-Wice, G. Fadana, N. Fagnoni, R. Fritz, S. R. Furlanetto, B. Glendenning, B. Greig, J. Grobbelaar, B. J. Hazelton, J. N. Hewitt, J. Hickish, D. C. Jacobs, A. Julius, M. Kariseb, S. A. Kohn, T. Lekalake, A. Liu, A. Loots, D. MacMahon, L. Malan, C. Malgas, M. Maree, Z. Martinot, N. Mathison, E. Matsetela, A. Mesinger, M. F. Morales, A. R. Neben, N. Patra, S. Pieterse, J. C. Pober, N. Razavi-Ghods, J. Ringuette, J. Robnett, K. Rosie, R. Sell, C. Smith, A. Syce, M. Tegmark, N. Thyagarajan, P. K. G. Williams, and H. Zheng, "Hydrogen Epoch of Reionization Array (HERA)," *Publications of the Astronomical Society of the Pacific*, vol. 129, p. 045001, Apr. 2017.

[48] G. Mellema, L. V. E. Koopmans, F. A. Abdalla, G. Bernardi, B. Ciardi, S. Daiboo, A. G. de Bruyn, K. K. Datta, H. Falcke, A. Ferrara, I. T. Iliev, F. Iocco, V. Jelić, H. Jensen, R. Joseph, P. Labroupoulos, A. Meiksin, A. Mesinger, A. R. Offringa, V. N. Pandey, J. R. Pritchard, M. G. Santos, D. J. Schwarz, B. Semelin, H. Vedantham, S. Yatawatta, and S. Zaroubi, "Reionization and the Cosmic Dawn with the Square Kilometre Array," *Experimental Astronomy*, vol. 36, pp. 235–318, Aug. 2013.

[49] L. Koopmans, J. Pritchard, G. Mellema, J. Aguirre, K. Ahn, R. Barkana, I. van Bemmel, G. Bernardi, A. Bonaldi, F. Briggs, A. G. de Bruyn, T. C. Chang, E. Chapman, X. Chen, B. Ciardi, P. Dayal, A. Ferrara, A. Fialkov, F. Fiore, K. Ichiki, I. T. Illiev, S. Inoue, V. Jelic, M. Jones, J. Lazio, U. Maio, S. Majumdar, K. J. Mack, A. Mesinger, M. F. Morales, A. Parsons, U. L. Pen, M. Santos, R. Schneider, B. Semelin, R. S. de Souza, R. Subrahmanyan, T. Takeuchi, H. Vedantham, J. Wagg, R. Webster, S. Wyithe, K. K. Datta, and C. Trott, "The Cosmic Dawn and Epoch of Reionisation with SKA," in *Advancing Astrophysics with the Square Kilometre Array (AASKA14)*, p. 1, Apr. 2015.

[50] A. Tripathi, A. Datta, M. Choudhury, and S. Majumdar, "Extracting the Global 21-cm signal from Cosmic Dawn and Epoch of Reionization in the presence of Foreground and Ionosphere," *Monthly Notices of the Royal Astronomical Society*, vol. 528, pp. 1945–1964, 01 2024.

[51] A. Tripathi, G. Kaur, A. Datta, and S. Majumdar, "Comparing sampling techniques to chart parameter space of 21 cm global signal with Artificial Neural Networks," *Journal of Cosmology and Astroparticle Physics*, vol. 2024, p. 041, Oct. 2024.

[52] A. Tripathi, A. Datta, A. Mazumder, and S. Majumdar, "Impact of Calibration and Position Errors on Astrophysical Parameters of the HI 21cm Signal," *arXiv e-prints*, p. arXiv:2502.20962, Feb. 2025.

[53] G. B. Field, “The Spin Temperature of Intergalactic Neutral Hydrogen.,” *The Astrophysical Journal*, vol. 129, p. 536, May 1959.

[54] R. Barkana, “The rise of the first stars: Supersonic streaming, radiative feedback, and 21-cm cosmology,” *Physics Reports*, vol. 645, pp. 1–59, 2016. The rise of the first stars: Supersonic streaming, radiative feedback, and 21-cm cosmology.

[55] G. B. Field, “The spin temperature of intergalactic neutral hydrogen.,” *The Astrophysical Journal*, vol. 129, p. 536, May 1959.

[56] S. R. Furlanetto, “The global 21-centimeter background from high redshifts,” *Monthly Notices of the Royal Astronomical Society*, vol. 371, pp. 867–878, Sept. 2006.

[57] S. R. Furlanetto, S. Peng Oh, and F. H. Briggs, “Cosmology at low frequencies: The 21cm transition and the high-redshift universe,” *Physics Reports*, vol. 433, no. 4, pp. 181–301, 2006.

[58] P. Madau, A. Meiksin, and M. J. Rees, “21 centimeter tomography of the intergalactic medium at high redshift,” *The Astrophysical Journal*, vol. 475, pp. 429–444, feb 1997.

[59] T. C. Voytek, A. Natarajan, J. M. J. García, J. B. Peterson, and O. López-Cruz, “PROBING THE DARK AGES AT z $\sim$ 20: THE SCI-HI 21 cm ALL-SKY SPECTRUM EXPERIMENT,” *The Astrophysical Journal*, vol. 782, p. L9, jan 2014.

[60] M. Sokolowski, S. E. Tremblay, R. B. Wayth, S. J. Tingay, N. Clarke, P. Roberts, M. Waterson, R. D. Ekers, P. Hall, M. Lewis, and et al., “Bighorns - broadband instrument for global hydrogen reionisation signal,” *Publications of the Astronomical Society of Australia*, vol. 32, p. e004, 2015.

[61] J. D. Bowman, A. E. E. Rogers, R. A. Monsalve, T. J. Mozdzen, and N. Mahesh, “An absorption profile centred at 78 megahertz in the sky-averaged spectrum,” *Nature*, vol. 555, pp. 67–70, Mar. 2018.

[62] S. Singh, N. T. Jishnu, R. Subrahmanyan, N. Udaya Shankar, B. S. Girish, A. Raghunathan, R. Somashekar, K. S. Srivani, and M. Sathyanarayana Rao, “On the detection of a cosmic dawn signal in the radio background,” *Nature Astronomy*, vol. 6, pp. 607–617, Feb. 2022.

[63] M. P. van Haarlem, M. W. Wise, A. W. Gunst, G. Heald, J. P. McKean, J. W. T. Hessels, A. G. de Bruyn, R. Nijboer, J. Swinbank, R. Fallows, M. Brentjens, A. Nelles, R. Beck, H. Falcke, R. Fender, J. Hörandel, L. V. E. Koopmans, G. Mann, G. Miley, H. Röttgering, B. W. Stappers, R. A. M. J. Wijers, S. Zaroubi, M. van den Akker, A. Alexov, J. Anderson, K. Anderson, A. van Ardenne, M. Arts, A. Asgekar, I. M. Avruch, F. Batejat, L. Bähren, M. E. Bell, M. R. Bell, I. van Bemmel, P. Bennema, M. J. Bentum, G. Bernardi, P. Best, L. Bîrzan, A. Bonafede, A. J. Boonstra, R. Braun, J. Bregman, F. Breitling, R. H. van de Brink, J. Broderick, P. C. Broekema, W. N. Brouw, M. Brüggen, H. R. Butcher, W. van Cappellen, B. Ciardi, T. Coenen, J. Conway, A. Coolen, A. Corstanje, S. Damstra, O. Davies, A. T. Deller, R. J. Dettmar, G. van Diepen, K. Dijkstra, P. Donker, A. Doorduin, J. Dromer, M. Drost, A. van Duin, J. Eislöffel, J. van Enst, C. Ferrari, W. Frieswijk, H. Gankema, M. A. Garrett, F. de Gasperin, M. Gerbers, E. de Geus, J. M. Grießmeier, T. Grit, P. Gruppen, J. P. Hamaker, T. Hassall, M. Hoeft, H. A. Holties, A. Horneffer, A. van der Horst, A. van Houwelingen, A. Huijgen, M. Iacobelli, H. Intema, N. Jackson, V. Jelic, A. de Jong, E. Juette, D. Kant, A. Karastergiou, A. Koers, H. Kollen, V. I. Kondratiev, E. Kooistra, Y. Koopman, A. Koster, M. Kuniyoshi, M. Kramer, G. Kuper, P. Lambropoulos, C. Law, J. van Leeuwen, J. Lemaitre, M. Loose, P. Maat, G. Macario, S. Markoff, J. Masters, R. A. McFadden, D. McKay-Bukowski, H. Meijering, H. Meulman, M. Mevius, E. Middelberg, R. Millenaar,

J. C. A. Miller-Jones, R. N. Mohan, J. D. Mol, J. Morawietz, R. Morganti, D. D. Mulcahy, E. Mulder, H. Munk, L. Nieuwenhuis, R. van Nieuwpoort, J. E. Noordam, M. Norden, A. Noutsos, A. R. Offringa, H. Olofsson, A. Omar, E. Orrú, R. Overeem, H. Paas, M. Pandey-Pommier, V. N. Pandey, R. Pizzo, A. Polatidis, D. Rafferty, S. Rawlings, W. Reich, J. P. de Reijer, J. Reitsma, G. A. Renting, P. Riemers, E. Rol, J. W. Romein, J. Roosjen, M. Ruiter, A. Scaife, K. van der Schaaf, B. Scheers, P. Schellart, A. Schoenmakers, G. Schoonderbeek, M. Serylak, A. Shulevski, J. Sluman, O. Smirnov, C. Sobey, H. Spreeuw, M. Steinmetz, C. G. M. Sterks, H. J. Stiepel, K. Stuurwold, M. Tagger, Y. Tang, C. Tasse, I. Thomas, S. Thoudam, M. C. Toribio, B. van der Tol, O. Usov, M. van Veelen, A. J. van der Veen, S. ter Veen, J. P. W. Verbiest, R. Vermeulen, N. Vermaas, C. Vocks, C. Vogt, M. de Vos, E. van der Wal, R. van Weeren, H. Weggemans, P. Weltevrede, S. White, S. J. Wijnholds, T. Wilhelmsson, O. Wucknitz, S. Yatawatta, P. Zarka, A. Zensus, and J. van Zwieten, “LOFAR: The LOw-Frequency ARray,” *Astronomy and Astrophysics*, vol. 556, p. A2, Aug. 2013.

[64] L. Koopmans, J. Pritchard, G. Mellema, J. Aguirre, K. Ahn, R. Barkana, I. van Bemmel, G. Bernardi, A. Bonaldi, F. Briggs, A. G. de Bruyn, T. C. Chang, E. Chapman, X. Chen, B. Ciardi, P. Dayal, A. Ferrara, A. Fialkov, F. Fiore, K. Ichiki, I. T. Illiev, S. Inoue, V. Jelic, M. Jones, J. Lazio, U. Maio, S. Majumdar, K. J. Mack, A. Mesinger, M. F. Morales, A. Parsons, U. L. Pen, M. Santos, R. Schneider, B. Semelin, R. S. de Souza, R. Subrahmanyan, T. Takeuchi, H. Vedantham, J. Wagg, R. Webster, S. Wyithe, K. K. Datta, and C. Trott, “The Cosmic Dawn and Epoch of Reionisation with SKA,” in *Advancing Astrophysics with the Square Kilometre Array (AASKA14)*, p. 1, Apr. 2015.

[65] S. Bharadwaj and S. S. Ali, “On using visibility correlations to probe the HI distribution from the dark ages to the present epoch - I. Formalism and the expected signal,” *Monthly Notices of the Royal Astronomical Society*, vol. 356, pp. 1519–1528, Feb. 2005.

[66] B. Greig, “Inference from the 21cm signal,” *arXiv e-prints*, p. arXiv:1909.13860, Sept. 2019.

[67] G. Mellema, L. Koopmans, H. Shukla, K. K. Datta, A. Mesinger, and S. Majumdar, “HI tomographic imaging of the Cosmic Dawn and Epoch of Reionization with SKA,” in *Advancing Astrophysics with the Square Kilometre Array (AASKA14)*, PoS, 2014.

[68] S. Zaroubi, A. G. de Bruyn, G. Harker, R. M. Thomas, P. Labropolous, V. Jelić, L. V. E. Koopmans, M. A. Brentjens, G. Bernardi, B. Ciardi, S. Daiboo, S. Kazemi, O. Martinez-Rubi, G. Mellema, A. R. Offringa, V. N. Pandey, J. Schaye, V. Veligatla, H. Vedantham, and S. Yatawatta, “Imaging neutral hydrogen on large scales during the Epoch of Reionization with LOFAR,” *Monthly Notices of the Royal Astronomical Society*, vol. 425, pp. 2964–2973, Oct. 2012.

[69] G. Bernardi, A. G. de Bruyn, G. Harker, M. A. Brentjens, B. Ciardi, V. Jelić, L. V. E. Koopmans, P. Labropoulos, A. Offringa, V. N. Pandey, J. Schaye, R. M. Thomas, S. Yatawatta, and S. Zaroubi, “Foregrounds for observations of the cosmological 21 cm line. II. Westerbork observations of the fields around 3C 196 and the North Celestial Pole,” *Astronomy and Astrophysics*, vol. 522, p. A67, Nov. 2010.

[70] E. Lenc, B. M. Gaensler, X. H. Sun, E. M. Sadler, A. G. Willis, N. Barry, A. P. Beardsley, M. E. Bell, G. Bernardi, J. D. Bowman, F. Briggs, J. R. Callingham, R. J. Cappallo, P. Carroll, B. E. Corey, A. de Oliveira-Costa, A. A. Deshpande, J. S. Dillon, K. S. Dwarkanath, D. Emrich, A. Ewall-Wice, L. Feng, B. Q. For, R. Goeke, L. J. Greenhill, P. Hancock, B. J. Hazelton, J. N. Hewitt, L. Hindson, N. Hurley-Walker, M. Johnston-Hollitt, D. C. Jacobs, A. D. Kapińska, D. L. Kaplan, J. C. Kasper, H. S. Kim, E. Kratzenberg, J. Line, A. Loeb,

C. J. Lonsdale, M. J. Lynch, B. McKinley, S. R. McWhirter, D. A. Mitchell, M. F. Morales, E. Morgan, J. Morgan, T. Murphy, A. R. Neben, D. Oberoi, A. R. Offringa, S. M. Ord, S. Paul, B. Pindor, J. C. Pober, T. Prabu, P. Procopio, J. Riding, A. E. E. Rogers, A. Roshi, N. Udaya Shankar, S. K. Sethi, K. S. Srivani, L. Staveley-Smith, R. Subrahmanyan, I. S. Sullivan, M. Tegmark, N. Thyagarajan, S. J. Tingay, C. Trott, M. Waterson, R. B. Wayth, R. L. Webster, A. R. Whitney, A. Williams, C. L. Williams, C. Wu, J. S. B. Wyithe, and Q. Zheng, "Low-frequency Observations of Linearly Polarized Structures in the Interstellar Medium near the South Galactic Pole," *The Astrophysical Journal*, vol. 830, p. 38, Oct. 2016.

[71] A. Datta, J. D. Bowman, and C. L. Carilli, "BRIGHT SOURCE SUBTRACTION REQUIREMENTS FOR REDSHIFTED 21 cm MEASUREMENTS," *The Astrophysical Journal*, vol. 724, pp. 526–538, nov 2010.

[72] H. Vedantham, N. U. Shankar, and R. Subrahmanyan, "IMAGING THE EPOCH OF REIONIZATION: LIMITATIONS FROM FOREGROUND CONFUSION AND IMAGING ALGORITHMS," *The Astrophysical Journal*, vol. 745, p. 176, jan 2012.

[73] M. F. Morales, B. Hazelton, I. Sullivan, and A. Beardsley, "FOUR FUNDAMENTAL FOREGROUND POWER SPECTRUM SHAPES FOR 21 cm COSMOLOGY OBSERVATIONS," *The Astrophysical Journal*, vol. 752, p. 137, jun 2012.

[74] C. M. Trott, R. B. Wayth, and S. J. Tingay, "THE IMPACT OF POINT-SOURCE SUBTRACTION RESIDUALS ON 21 cm EPOCH OF REIONIZATION ESTIMATION," *The Astrophysical Journal*, vol. 757, p. 101, sep 2012.

[75] M. G. Santos, A. Cooray, and L. Knox, "Multifrequency Analysis of 21 Centimeter Fluctuations from the Era of Reionization," *The Astrophysical Journal*, vol. 625, pp. 575–587, June 2005.

[76] X. Wang, M. Tegmark, M. G. Santos, and L. Knox, "21 cm Tomography with Foregrounds," *The Astrophysical Journal*, vol. 650, pp. 529–537, Oct. 2006.

[77] M. McQuinn, O. Zahn, M. Zaldarriaga, L. Hernquist, and S. R. Furlanetto, "Cosmological Parameter Estimation Using 21 cm Radiation from the Epoch of Reionization," *The Astrophysical Journal*, vol. 653, pp. 815–834, Dec. 2006.

[78] A. Liu, M. Tegmark, J. Bowman, J. Hewitt, and M. Zaldarriaga, "An improved method for 21-cm foreground removal," *Monthly Notices of the Royal Astronomical Society*, vol. 398, no. 1, pp. 401–406, 2009.

[79] V. Jelić, A. G. de Bruyn, M. Mevius, F. B. Abdalla, K. M. B. Asad, G. Bernardi, M. A. Brentjens, S. Bus, E. Chapman, B. Ciardi, S. Daiboo, E. R. Fernandez, A. Ghosh, G. Harker, H. Jensen, S. Kazemi, L. V. E. Koopmans, P. Labropoulos, O. Martinez-Rubi, G. Mellema, A. R. Offringa, V. N. Pandey, A. H. Patil, R. M. Thomas, H. K. Vedantham, V. Veligatla, S. Yatawatta, S. Zaroubi, A. Alexov, J. Anderson, I. M. Avruch, R. Beck, M. E. Bell, M. J. Bentum, P. Best, A. Bonafede, J. Bregman, F. Breitling, J. Broderick, W. N. Brouw, M. Brüggen, H. R. Butcher, J. E. Conway, F. de Gasperin, E. de Geus, A. Deller, R. J. Dettmar, S. Duscha, J. Eislöffel, D. Engels, H. Falcke, R. A. Fallows, R. Fender, C. Ferrari, W. Frieswijk, M. A. Garrett, J. Grießmeier, A. W. Gunst, J. P. Hamaker, T. E. Hassall, M. Haverkorn, G. Heald, J. W. T. Hessels, M. Hoeft, J. Hörandel, A. Horneffer, A. van der Horst, M. Iacobelli, E. Juette, A. Karastergiou, V. I. Kondratiev, M. Kramer, M. Kuniyoshi, G. Kuper, J. van Leeuwen, P. Maat, G. Mann, D. McKay-Bukowski, J. P. McKean, H. Munk, A. Nelles, M. J. Norden, H. Paas, M. Pandey-Pommier, G. Pietka, R. Pizzo, A. G. Polatidis, W. Reich, H. Röttgering, A. Rowlinson, A. M. M. Scaife, D. Schwarz, M. Serylak, O. Smirnov,

M. Steinmetz, A. Stewart, M. Tagger, Y. Tang, C. Tasse, S. ter Veen, S. Thoudam, C. Toribio, R. Vermeulen, C. Vocks, R. J. van Weeren, R. A. M. J. Wijers, S. J. Wijnholds, O. Wucknitz, and P. Zarka, “Initial LOFAR observations of epoch of reionization windows. II. Diffuse polarized emission in the ELAIS-N1 field,” *Astronomy and Astrophysics*, vol. 568, p. A101, Aug. 2014.

[80] M. F. Morales, J. D. Bowman, and J. N. Hewitt, “Improving Foreground Subtraction in EOR Power Spectrum Observations,” in *American Astronomical Society Meeting Abstracts*, vol. 207 of *American Astronomical Society Meeting Abstracts*, p. 33.04, Dec. 2005.

[81] G. Harker, S. Zaroubi, G. Bernardi, M. A. Brentjens, A. G. de Bruyn, B. Ciardi, V. Jelić, L. V. E. Koopmans, P. Labropoulos, G. Mellema, A. Offringa, V. N. Pandey, J. Schaye, R. M. Thomas, and S. Yatawatta, “Non-parametric foreground subtraction for 21-cm epoch of reionization experiments,” *Monthly Notices of the Royal Astronomical Society*, vol. 397, pp. 1138–1152, Aug. 2009.

[82] E. Chapman, F. B. Abdalla, G. Harker, V. Jelić, P. Labropoulos, S. Zaroubi, M. A. Brentjens, A. G. de Bruyn, and L. V. E. Koopmans, “Foreground removal using FASTICA: a showcase of LOFAR-EoR,” *Monthly Notices of the Royal Astronomical Society*, vol. 423, pp. 2518–2532, July 2012.

[83] E. Chapman, F. B. Abdalla, J. Bobin, J. L. Starck, G. Harker, V. Jelić, P. Labropoulos, S. Zaroubi, M. A. Brentjens, A. G. de Bruyn, and L. V. E. Koopmans, “The scale of the problem: recovering images of reionization with Generalized Morphological Component Analysis,” *Monthly Notices of the Royal Astronomical Society*, vol. 429, pp. 165–176, Feb. 2013.

[84] F. G. Mertens, A. Ghosh, and L. V. E. Koopmans, “Statistical 21-cm signal separation via Gaussian Process Regression analysis,” *Monthly Notices of the Royal Astronomical Society*, vol. 478, pp. 3640–3652, 06 2018.

[85] L. Zhang, E. F. Bunn, A. Karakci, A. Korotkov, P. M. Sutter, P. T. Timbie, G. S. Tucker, and B. D. Wandelt, “Bayesian Semi-blind Component Separation for Foreground Removal in Interferometric 21 cm Observations,” *The Astrophysical Journal Supplement Series*, vol. 222, p. 3, Jan. 2016.

[86] M. Choudhury, A. Datta, and A. Chakraborty, “Extracting the 21 cm Global signal using artificial neural networks,” *Monthly Notices of the Royal Astronomical Society*, vol. 491, pp. 4031–4044, Jan. 2020.

[87] M. Choudhury, A. Datta, and S. Majumdar, “Extracting the 21-cm power spectrum and the reionization parameters from mock data sets using artificial neural networks,” *Monthly Notices of the Royal Astronomical Society*, vol. 512, pp. 5010–5022, June 2022.

[88] W. Li, H. Xu, Z. Ma, R. Zhu, D. Hu, Z. Zhu, J. Gu, C. Shan, J. Zhu, and X.-P. Wu, “Separating the EoR signal with a convolutional denoising autoencoder: a deep-learning-based method,” *Monthly Notices of the Royal Astronomical Society*, vol. 485, pp. 2628–2637, May 2019.

[89] T. Chen, M. Bianco, E. Tolley, M. Spinelli, D. Forero-Sanchez, and J. P. Kneib, “The stability of deep learning for 21cm foreground removal across various sky models and frequency-dependent systematics,” *Monthly Notices of the Royal Astronomical Society*, vol. 532, pp. 2615–2634, Aug. 2024.

[90] F. Shi, H. Chang, L. Zhang, H. Shan, J. Zhang, S. Zhou, M. Jiang, and Z. Wang, “21-cm foreground removal using AI and the frequency-difference technique,” *Physical Review D*, vol. 109, p. 063509, Mar. 2024.

[91] A. Acharya, F. Mertens, B. Ciardi, R. Ghara, L. V. E. Koopmans, and S. Zaroubi, “Revised LOFAR upper limits on the 21-cm signal power spectrum at z $\approx$ 9.1 using machine learning and gaussian process regression,” *Monthly Notices of the Royal Astronomical Society*, vol. 534, pp. L30–L34, Oct. 2024.

[92] A. Datta, R. Bradley, J. O. Burns, G. Harker, A. Komjathy, and T. J. W. Lazio, “The Effects of the Ionosphere on Ground-based Detection of the Global 21 cm Signal from the Cosmic Dawn and the Dark Ages,” *The Astrophysical Journal*, vol. 831, p. 6, Nov. 2016.

[93] H. K. Vedantham, L. V. E. Koopmans, A. G. de Bruyn, S. J. Wijnholds, B. Ciardi, and M. A. Brentjens, “Chromatic effects in the 21 cm global signal from the cosmic dawn,” *Monthly Notices of the Royal Astronomical Society*, vol. 437, pp. 1056–1069, Jan. 2014.

[94] E. Shen, D. Anstey, E. de Lera Acedo, and A. Fialkov, “Bayesian data analysis for sky-averaged 21-cm experiments in the presence of ionospheric effects,” *Monthly Notices of the Royal Astronomical Society*, vol. 515, pp. 4565–4573, 07 2022.

[95] H. T. Intema, S. van der Tol, W. D. Cotton, A. S. Cohen, I. M. van Bemmel, and H. J. A. Röttgering, “Ionospheric calibration of low frequency radio interferometric observations using the peeling scheme. I. Method description and first results,” *Astronomy and Astrophysics*, vol. 501, pp. 1185–1205, July 2009.

[96] M. Mevius, S. van der Tol, V. N. Pandey, H. K. Vedantham, M. A. Brentjens, A. G. de Bruyn, F. B. Abdalla, K. M. B. Asad, J. D. Bregman, W. N. Brouw, S. Bus, E. Chapman, B. Ciardi, E. R. Fernandez, A. Ghosh, G. Harker, I. T. Iliev, V. Jelić, S. Kazemi, L. V. E. Koopmans, J. E. Noordam, A. R. Offringa, A. H. Patil, R. J. van Weeren, S. Wijnholds, S. Yatawatta, and S. Zaroubi, “Probing ionospheric structures using the LOFAR radio telescope,” *Radio Science*, vol. 51, pp. 927–941, July 2016.

[97] A. R. Offringa, J. J. van de Gronde, and J. B. T. M. Roerdink, “A morphological algorithm for improving radio-frequency interference detection,” *Astronomy and Astrophysics*, vol. 539, p. A95, Mar. 2012.

[98] J. Prasad and J. Chengalur, “FLAGCAL: a flagging and calibration package for radio interferometric data,” *Experimental Astronomy*, vol. 33, pp. 157–171, Mar. 2012.

[99] A. R. Offringa, F. Mertens, and L. V. E. Koopmans, “The impact of interference excision on 21-cm epoch of reionization power spectrum analyses,” *Monthly Notices of the Royal Astronomical Society*, vol. 484, pp. 2866–2875, Apr. 2019.

[100] A. R. Offringa, R. B. Wayth, N. Hurley-Walker, D. L. Kaplan, N. Barry, A. P. Beardsley, M. E. Bell, G. Bernardi, J. D. Bowman, F. Briggs, and et al., “The low-frequency environment of the murchison widefield array: Radio-frequency interference analysis and mitigation,” *Publications of the Astronomical Society of Australia*, vol. 32, p. e008, 2015.

[101] A. Chakraborty, A. Datta, and A. Mazumder, “A Comparative Analysis to Deal with Missing Spectral Information Caused by RFI in Cosmological H I 21 cm Observations,” *The Astrophysical Journal*, vol. 929, p. 104, Apr. 2022.

[102] J. R. Pritchard and A. Loeb, “Constraining the unexplored period between the dark ages and reionization with observations of the global 21 cm signal,” *Physical Review D*, vol. 82, p. 023006, July 2010.

[103] R. A. Monsalve, A. E. E. Rogers, J. D. Bowman, and T. J. Mozdzen, "Calibration of the EDGES High-band Receiver to Observe the Global 21 cm Signature from the Epoch of Reionization," *The Astrophysical Journal*, vol. 835, p. 49, Jan. 2017.

[104] C. A. Watkinson and J. R. Pritchard, "The impact of spin-temperature fluctuations on the 21-cm moments," *Monthly Notices of the Royal Astronomical Society*, vol. 454, pp. 1416–1431, Dec. 2015.

[105] J. H. Cook, S. Balu, B. Greig, C. M. Trott, J. L. B. Line, Y. Qin, and J. S. B. Wyithe, "The impact of ionization morphology and X-ray heating on the cosmological 21-cm skew spectrum," *Monthly Notices of the Royal Astronomical Society*, vol. 529, pp. 2734–2752, Apr. 2024.

[106] G. B. Taylor, C. L. Carilli, and R. A. Perley, "Synthesis imaging in radio astronomy ii," *Synthesis Imaging in Radio Astronomy II*, vol. 180, Jan 1999.

[107] G. Bernardi, "21 cm observations: calibration, strategies, observables," *arXiv e-prints*, p. arXiv:1909.11938, Sept. 2019.

[108] B. Greig and A. Mesinger, "21CMMC: an MCMC analysis tool enabling astrophysical parameter studies of the cosmic 21 cm signal," *Monthly Notices of the Royal Astronomical Society*, vol. 449, pp. 4246–4263, June 2015.

[109] J. Mirocha, G. J. A. Harker, and J. O. Burns, "Interpreting the Global 21-cm Signal from High Redshifts. II. Parameter Estimation for Models of Galaxy Formation," *The Astrophysical Journal*, vol. 813, p. 11, Nov. 2015.

[110] T. R. Choudhury and A. Paranjape, "SCRIPT: Semi-numerical Code for ReIonization with PhoTon-conservation." Astrophysics Source Code Library, record ascl:2204.013, Apr. 2022.

[111] C. J. Schmit and J. R. Pritchard, "Emulation of reionization simulations for Bayesian inference of astrophysics parameters using neural networks," *Monthly Notices of the Royal Astronomical Society*, vol. 475, pp. 1213–1223, Mar. 2018.

[112] N. S. Kern, A. R. Parsons, J. S. Dillon, A. E. Lanman, N. Fagnoni, and E. de Lera Acedo, "Mitigating internal instrument coupling for 21 cm cosmology. i. temporal and spectral modeling in simulations," *The Astrophysical Journal*, vol. 884, p. 105, oct 2019.

[113] H. Tiwari, A. K. Shaw, S. Majumdar, M. Kamran, and M. Choudhury, "Improving constraints on the reionization parameters using 21-cm bispectrum," *Journal of Cosmology and Astroparticle Physics*, vol. 2022, p. 045, Apr. 2022.

[114] G. J. A. Harker, J. R. Pritchard, J. O. Burns, and J. D. Bowman, "An MCMC approach to extracting the global 21-cm signal during the cosmic dawn from sky-averaged radio observations," *Monthly Notices of the Royal Astronomical Society*, vol. 419, pp. 1070–1084, Jan. 2012.

[115] G. Bernardi, J. T. L. Zwart, D. Price, L. J. Greenhill, A. Mesinger, J. Dowell, T. Eftekhari, S. W. Ellingson, J. Kocz, and F. Schinzel, "Bayesian constraints on the global 21-cm signal from the Cosmic Dawn," *Monthly Notices of the Royal Astronomical Society*, vol. 461, pp. 2847–2855, 06 2016.

[116] S. Singh, R. Subrahmanyan, N. Udaya Shankar, M. Sathyanarayana Rao, A. Fialkov, A. Cohen, R. Barkana, B. S. Girish, A. Raghunathan, R. Somashekar, and K. S. Srivani, "First Results on the Epoch of Reionization from First Light with SARAS 2," *The Astrophysical Journal Letters*, vol. 845, p. L12, Aug. 2017.

[117] K. Tauscher, D. Rapetti, and J. O. Burns, “A new goodness-of-fit statistic and its application to 21-cm cosmology,” *Journal of Cosmology and Astroparticle Physics*, vol. 2018, p. 015, Dec. 2018.

[118] H. Shimabukuro and B. Semelin, “Analysing the 21 cm signal from the epoch of reionization with artificial neural networks,” *Monthly Notices of the Royal Astronomical Society*, vol. 468, pp. 3869–3877, July 2017.

[119] S. Heimersheim, L. Rønneberg, H. Linton, F. Pagani, and A. Fialkov, “FlexKnot and Gaussian Process for 21 cm global signal analysis and foreground separation,” *Monthly Notices of the Royal Astronomical Society*, vol. 527, pp. 11404–11421, Feb. 2024.

[120] A. Ewall-Wice, J. Hewitt, A. Mesinger, J. S. Dillon, A. Liu, and J. Pober, “Constraining high-redshift X-ray sources with next generation 21-cm power spectrum measurements,” *Monthly Notices of the Royal Astronomical Society*, vol. 458, pp. 2710–2724, May 2016.

[121] S. Agatonovic-Kustrin and R. Beresford, “Basic concepts of artificial neural network (ann) modeling and its application in pharmaceutical research,” *Journal of pharmaceutical and biomedical analysis*, vol. 22, no. 5, pp. 717–727, 2000.

[122] F. Pedregosa, G. Varoquaux, A. Gramfort, V. Michel, B. Thirion, O. Grisel, M. Blondel, P. Prettenhofer, R. Weiss, V. Dubourg, J. Vanderplas, A. Passos, D. Cournapeau, M. Brucher, M. Perrot, and Édouard Duchesnay, “Scikit-learn: Machine learning in python,” *Journal of Machine Learning Research*, vol. 12, no. 85, pp. 2825–2830, 2011.

[123] M. D. McKay, R. J. Beckman, and W. J. Conover, “A comparison of three methods for selecting values of input variables in the analysis of output from a computer code,” *Technometrics*, vol. 21, no. 2, pp. 239–245, 1979.

[124] J. R. Kalagnanam and U. M. Diwekar, “An efficient sampling technique for off-line quality control,” *Technometrics*, vol. 39, no. 3, pp. 308–319, 1997.

[125] S. R. Furlanetto, M. Zaldarriaga, and L. Hernquist, “The effects of reionization on Lyα galaxy surveys,” *Monthly Notices of the Royal Astronomical Society*, vol. 365, pp. 1012–1020, Jan. 2006.

[126] J. R. Pritchard and A. Loeb, “21 cm cosmology in the 21st century,” *Reports on Progress in Physics*, vol. 75, p. 086901, Aug. 2012.

[127] G. Harker, S. Zaroubi, G. Bernardi, M. A. Brentjens, A. G. de Bruyn, B. Ciardi, V. Jelić, L. V. E. Koopmans, P. Labropoulos, G. Mellema, A. Offringa, V. N. Pandey, A. H. Pawlik, J. Schaye, R. M. Thomas, and S. Yatawatta, “Power spectrum extraction for redshifted 21-cm Epoch of Reionization experiments: the LOFAR case,” *Monthly Notices of the Royal Astronomical Society*, vol. 405, pp. 2492–2504, July 2010.

[128] P. A. Shaver, R. A. Windhorst, P. Madau, and A. G. de Bruyn, “Can the reionization epoch be detected as a global signature in the cosmic background?,” *Astronomy and Astrophysics*, vol. 345, pp. 380–390, May 1999.

[129] M. Sokolowski, S. E. Tremblay, R. B. Wayth, S. J. Tingay, N. Clarke, P. Roberts, M. Waterson, R. D. Ekers, P. Hall, M. Lewis, M. Mossammaparast, S. Padhi, F. Schlagenhaufer, A. Sutinjo, and J. Tickner, “BIGHORNS - Broadband Instrument for Global HydrOgen ReioNisation Signal,” *Publications of the Astronomical Society of Australia*, vol. 32, p. e004, Feb. 2015.

[130] N. Patra, R. Subrahmanyan, A. Raghunathan, and N. Udaya Shankar, “SARAS: a precision system for measurement of the cosmic radio background and signatures from the epoch of reionization,” *Experimental Astronomy*, vol. 36, pp. 319–370, Aug. 2013.

[131] J. L. Pawsey, L. L. McCready, and F. F. Gardner, “Ionospheric thermal radiation at radio frequencies,” *Journal of Atmospheric and Terrestrial Physics*, vol. 1, pp. 261–277, Jan. 1951.

[132] W. R. Steiger and J. W. Warwick, “Observations of Cosmic Radio Noise at 18 Mc/s in Hawaii,” *Journal of Geophysical Research*, vol. 66, pp. 57–66, Jan. 1961.

[133] J. V. Evans and T. Hagfors, *Radar astronomy.* 1968.

[134] K. Davies, *Ionospheric Radio.* Electromagnetic Waves, Institution of Engineering and Technology, 1990.

[135] W. D. Jennings, C. A. Watkinson, F. B. Abdalla, and J. D. McEwen, “Evaluating machine learning techniques for predicting power spectra from reionization simulations,” *Monthly Notices of the Royal Astronomical Society*, vol. 483, pp. 2907–2922, Mar. 2019.

[136] M. Choudhury, A. Datta, and S. Majumdar, “Extracting the 21-cm power spectrum and the reionization parameters from mock data sets using artificial neural networks,” *Monthly Notices of the Royal Astronomical Society*, vol. 512, pp. 5010–5022, June 2022.

[137] A. Cohen, A. Fialkov, R. Barkana, and R. A. Monsalve, “Emulating the global 21-cm signal from Cosmic Dawn and Reionization,” *Monthly Notices of the Royal Astronomical Society*, vol. 495, pp. 4845–4859, July 2020.

[138] H. T. J. Bevins, W. J. Handley, A. Fialkov, E. de Lera Acedo, and K. Javid, “globalemu: a novel and robust approach for emulating the sky-averaged 21-cm signal from the cosmic dawn and epoch of reionization,” *Monthly Notices of the Royal Astronomical Society*, vol. 508, pp. 2923–2936, 09 2021.

[139] C. H. Bye, S. K. N. Portillo, and A. Fialkov, “21cmVAE: A Very Accurate Emulator of the 21 cm Global Signal,” *The Astrophysical Journal*, vol. 930, p. 79, May 2022.

[140] S. Hassan, A. Liu, S. Kohn, and P. La Plante, “Identifying reionization sources from 21 cm maps using Convolutional Neural Networks,” *Monthly Notices of the Royal Astronomical Society*, vol. 483, pp. 2524–2537, Feb. 2019.

[141] J. Chardin, G. Uhlrich, D. Aubert, N. Deparis, N. Gillet, P. Ocvirk, and J. Lewis, “A deep learning model to emulate simulations of cosmic reionization,” *Monthly Notices of the Royal Astronomical Society*, vol. 490, pp. 1055–1065, Nov. 2019.

[142] D. Korber, M. Bianco, E. Tolley, and J.-P. Kneib, “PINION: physics-informed neural network for accelerating radiative transfer simulations for cosmic reionization,” *Monthly Notices of the Royal Astronomical Society*, vol. 521, pp. 902–915, 02 2023.

[143] N. Gillet, A. Mesinger, B. Greig, A. Liu, and G. Ucci, “Deep learning from 21-cm tomography of the cosmic dawn and reionization,” *Monthly Notices of the Royal Astronomical Society*, vol. 484, pp. 282–293, Mar. 2019.

[144] X. Zhao, Y. Mao, and B. D. Wandelt, “Implicit Likelihood Inference of Reionization Parameters from the 21 cm Power Spectrum,” *The Astrophysical Journal*, vol. 933, p. 236, July 2022.

[145] J. Mirocha, S. Skory, J. O. Burns, and J. H. Wise, “Optimized Multi-frequency Spectra for Applications in Radiative Feedback and Cosmological Reionization,” *The Astrophysical Journal*, vol. 756, p. 94, Sept. 2012.

[146] G. J. A. Harker, J. Mirocha, J. O. Burns, and J. R. Pritchard, “Parametrizations of the 21-cm global signal and parameter estimation from single-dipole experiments,” *Monthly Notices of the Royal Astronomical Society*, vol. 455, pp. 3829–3840, Feb. 2016.

[147] G. Bernardi, M. McQuinn, and L. J. Greenhill, “Foreground Model and Antenna Calibration Errors in the Measurement of the Sky-averaged λ21 cm Signal at z∼20,” *The Astrophysical Journal*, vol. 799, p. 90, Jan. 2015.

[148] S. A. Wouthuysen, “On the excitation mechanism of the 21-cm (radio-frequency) interstellar hydrogen emission line.,” *The Astronomical Journal*, vol. 57, pp. 31–32, Jan. 1952.

[149] J. Mirocha, “Decoding the X-ray properties of pre-reionization era sources,” *Monthly Notices of the Royal Astronomical Society*, vol. 443, pp. 1211–1223, Sept. 2014.

[150] G. J. A. Harker, “Selection between foreground models for global 21-cm experiments.,” *Monthly Notices of the Royal Astronomical Society*, vol. 449, pp. L21–L25, Apr. 2015.

[151] A. de Oliveira-Costa, M. Tegmark, B. M. Gaensler, J. Jonas, T. L. Landecker, and P. Reich, “A model of diffuse Galactic radio emission from 10 MHz to 100 GHz,” *Monthly Notices of the Royal Astronomical Society*, vol. 388, pp. 247–260, July 2008.

[152] D. K. Bailey, “On a new method for exploring the upper ionosphere,” *Terrestrial Magnetism and Atmospheric Electricity (Journal of Geophysical Research)*, vol. 53, p. 41, Jan. 1948.

[153] A. R. Thompson, J. M. Moran, and J. Swenson, George W., *Interferometry and Synthesis in Radio Astronomy, 2nd Edition.* 2001.

[154] H. C. Hsieh, “Characteristics of ionospheric thermal radiation,” *Journal of Atmospheric and Terrestrial Physics*, vol. 28, pp. 783–788, Aug. 1966.

[155] S.-R. Zhang, J. M. Holt, A. M. Zalucha, and C. Amory-Mazaudier, “Midlatitude ionospheric plasma temperature climatology and empirical model based on Saint Santin incoherent scatter radar data from 1966 to 1987,” *Journal of Geophysical Research (Space Physics)*, vol. 109, p. A11311, Nov. 2004.

[156] S. R. Furlanetto, S. P. Oh, and F. H. Briggs, “Cosmology at low frequencies: The 21 cm transition and the high-redshift Universe,” *Physics Reports*, vol. 433, pp. 181–301, Oct. 2006.

[157] A. Chatterjee, P. Dayal, T. R. Choudhury, and A. Hutter, “Ruling out 3 keV warm dark matter using 21 cm EDGES data,” *Monthly Notices of the Royal Astronomical Society*, vol. 487, pp. 3560–3567, Aug. 2019.

[158] D. Bilitza, “International reference ionosphere 2000: Examples of improvements and new features,” *Advances in Space Research*, vol. 31, no. 3, pp. 757–767, 2003. Description of the Low Latitude and Equatorial Ionosphere in the International Reference Ionosphere.

[159] S. Singh and R. Subrahmanyan, “The Redshifted 21 cm Signal in the EDGES Low-band Spectrum,” *The Astrophysical Journal*, vol. 880, p. 26, July 2019.

[160] R. Hills, G. Kulkarni, P. D. Meerburg, and E. Puchwein, “Concerns about modelling of the EDGES data,” *Nature*, vol. 564, pp. E32–E34, Dec. 2018.

[161] D. Rapetti, K. Tauscher, J. Mirocha, and J. O. Burns, “Global 21 cm Signal Extraction from Foreground and Instrumental Effects. II. Efficient and Self-consistent Technique for Constraining Nonlinear Signal Models,” *The Astrophysical Journal*, vol. 897, p. 174, July 2020.

[162] K. Tauscher, D. Rapetti, B. D. Nhan, A. Handy, N. Bassett, J. Hibbard, D. Bordenave, R. F. Bradley, and J. O. Burns, "Global 21 cm Signal Extraction from Foreground and Instrumental Effects. IV. Accounting for Realistic Instrument Uncertainties and Their Overlap with Foreground and Signal Models," *The Astrophysical Journal*, vol. 915, p. 66, July 2021.

[163] H. T. J. Bevins, W. J. Handley, A. Fialkov, E. de Lera Acedo, L. J. Greenhill, and D. C. Price, "MAXSMOOTH: rapid maximally smooth function fitting with applications in Global 21-cm cosmology," *Monthly Notices of the Royal Astronomical Society*, vol. 502, pp. 4405–4425, Apr. 2021.

[164] M. F. Morales and J. S. B. Wyithe, "Reionization and Cosmology with 21-cm Fluctuations," *Annual Review of Astronomy and Astrophysics*, vol. 48, pp. 127–171, Sept. 2010.

[165] G. B. Field, "The time relaxation of a resonance-line profile.," *The Astrophysical Journal*, vol. 129, p. 551, May 1959.

[166] S. Zaroubi, "The Epoch of Reionization," in *The First Galaxies* (T. Wiklind, B. Mobasher, and V. Bromm, eds.), vol. 396 of *Astrophysics and Space Science Library*, p. 45, Jan. 2013.

[167] J. D. Bowman, A. E. E. Rogers, R. A. Monsalve, T. J. Mozdzen, and N. Mahesh, "An absorption profile centred at 78 megahertz in the sky-averaged spectrum," *Nature*, vol. 555, pp. 67–70, Mar 2018.

[168] S. Singh, N. T. Jishnu, R. Subrahmanyan, N. Udaya Shankar, B. S. Girish, A. Raghunathan, R. Somashekar, K. S. Srivani, and M. Sathyanarayana Rao, "On the detection of a cosmic dawn signal in the radio background," *Nature Astronomy*, vol. 6, pp. 607–617, Feb. 2022.

[169] H. Shimabukuro and B. a Semelin, "Analysing 21cm signal with artificial neural network," in *Peering towards Cosmic Dawn* (V. Jelić and T. van der Hulst, eds.), vol. 333, pp. 39–42, May 2018.

[170] X. Zhao, Y. Mao, C. Cheng, and B. D. Wandelt, "Simulation-based Inference of Reionization Parameters from 3D Tomographic 21 cm Light-cone Images," *The Astrophysical Journal*, vol. 926, p. 151, Feb. 2022.

[171] X. Zhao, Y. Mao, and B. D. Wandelt, "Implicit Likelihood Inference of Reionization Parameters from the 21 cm Power Spectrum," *The Astrophysical Journal*, vol. 933, p. 236, July 2022.

[172] D. Prelogović and A. Mesinger, "Exploring the likelihood of the 21-cm power spectrum with simulation-based inference," *Monthly Notices of the Royal Astronomical Society*, vol. 524, pp. 4239–4255, Sept. 2023.

[173] A. Saxena, A. Cole, S. Gazagnes, P. D. Meerburg, C. Weniger, and S. J. Witte, "Constraining the X-ray heating and reionization using 21-cm power spectra with Marginal Neural Ratio Estimation," *Monthly Notices of the Royal Astronomical Society*, vol. 525, pp. 6097–6111, 09 2023.

[174] B. Greig, D. Prelogović, Y. Qin, Y.-S. Ting, and A. Mesinger, "Inferring astrophysical parameters using the 2D cylindrical power spectrum from reionization," *Monthly Notices of the Royal Astronomical Society*, vol. 533, pp. 2530–2545, Sept. 2024.

[175] X. Zhao, Y. Mao, S. Zuo, and B. D. Wandelt, "Simulation-based Inference of Reionization Parameters from 3D Tomographic 21 cm Light-cone Images – II: Application of Solid Harmonic Wavelet Scattering Transform," *arXiv e-prints*, p. arXiv:2310.17602, Oct. 2023.

[176] B. Greig and A. Mesinger, "Simultaneously constraining the astrophysics of reionization and the epoch of heating with 21CMMC," *Monthly Notices of the Royal Astronomical Society*, vol. 472, pp. 2651–2669, Dec. 2017.

[177] A. Cohen, A. Fialkov, R. Barkana, and M. Lotem, "Charting the parameter space of the global 21-cm signal," *Monthly Notices of the Royal Astronomical Society*, vol. 472, pp. 1915–1931, Dec. 2017.

[178] B. Semelin, E. Eames, F. Bolgar, and M. Caillat, "21SSD: a public data base of simulated 21-cm signals from the epoch of reionization," *Monthly Notices of the Royal Astronomical Society*, vol. 472, pp. 4508–4520, Dec. 2017.

[179] S. R. Furlanetto, "Theoretical framework: The fundamentals of the 21 cm line," in *The Cosmic 21-cm Revolution*, 2514-3433, pp. 1–1 to 1–17, IOP Publishing, 2019.

[180] J. Mirocha, "Decoding the X-ray properties of pre-reionization era sources," *Monthly Notices of the Royal Astronomical Society*, vol. 443, pp. 1211–1223, Sept. 2014.

[181] G. J. A. Harker, J. Mirocha, J. O. Burns, and J. R. Pritchard, "Parametrizations of the 21-cm global signal and parameter estimation from single-dipole experiments," *Monthly Notices of the Royal Astronomical Society*, vol. 455, pp. 3829–3840, Feb. 2016.

[182] A. Chatterjee, P. Dayal, T. R. Choudhury, and A. Hutter, "Ruling out 3 keV warm dark matter using 21 cm EDGES data," *Monthly Notices of the Royal Astronomical Society*, vol. 487, pp. 3560–3567, 05 2019.

[183] Planck Collaboration, R. Adam, N. Aghanim, M. Ashdown, J. Aumont, C. Baccigalupi, M. Ballardini, A. J. Banday, R. B. Barreiro, N. Bartolo, S. Basak, R. Battye, K. Benabed, J. P. Bernard, M. Bersanelli, P. Bielewicz, J. J. Bock, A. Bonaldi, L. Bonavera, J. R. Bond, J. Borrill, F. R. Bouchet, F. Boulanger, M. Bucher, C. Burigana, E. Calabrese, J. F. Cardoso, J. Carron, H. C. Chiang, L. P. L. Colombo, C. Combet, B. Comis, F. Couchot, A. Coulais, B. P. Crill, A. Curto, F. Cuttaia, R. J. Davis, P. de Bernardis, A. de Rosa, G. de Zotti, J. Delabrouille, E. Di Valentino, C. Dickinson, J. M. Diego, O. Doré, M. Douspis, A. Ducout, X. Dupac, F. Elsner, T. A. Enßlin, H. K. Eriksen, E. Falgarone, Y. Fantaye, F. Finelli, F. Forastieri, M. Frailis, A. A. Fraisse, E. Franceschi, A. Frolov, S. Galeotta, S. Galli, K. Ganga, R. T. Génova-Santos, M. Gerbino, T. Ghosh, J. González-Nuevo, K. M. Górski, A. Gruppuso, J. E. Gudmundsson, F. K. Hansen, G. Helou, S. Henrot-Versillé, D. Herranz, E. Hivon, Z. Huang, S. Ilić, A. H. Jaffe, W. C. Jones, E. Keihänen, R. Keskitalo, T. S. Kisner, L. Knox, N. Krachmalnicoff, M. Kunz, H. Kurki-Suonio, G. Lagache, A. Lähteenmäki, J. M. Lamarre, M. Langer, A. Lasenby, M. Lattanzi, C. R. Lawrence, M. Le Jeune, F. Levrier, A. Lewis, M. Liguori, P. B. Lilje, M. López-Caniego, Y. Z. Ma, J. F. Macías-Pérez, G. Maggio, A. Mangilli, M. Maris, P. G. Martin, E. Martínez-González, S. Matarrese, N. Mauri, J. D. McEwen, P. R. Meinhold, A. Melchiorri, A. Mennella, M. Migliaccio, M. A. Miville-Deschênes, D. Molinari, A. Moneti, L. Montier, G. Morgante, A. Moss, P. Naselsky, P. Natoli, C. A. Oxborrow, L. Pagano, D. Paoletti, B. Partridge, G. Patanchon, L. Patrizii, O. Perdereau, L. Perotto, V. Pettorino, F. Piacentini, S. Plaszczynski, L. Polastri, G. Polenta, J. L. Puget, J. P. Rachen, B. Racine, M. Reinecke, M. Remazeilles, A. Renzi, G. Rocha, M. Rossetti, G. Roudier, J. A. Rubiño-Martín, B. Ruiz-Granados, L. Salvati, M. Sandri, M. Savelainen, D. Scott, G. Sirri, R. Sunyaev, A. S. Suur-Uski, J. A. Tauber, M. Tenti, L. Toffolatti, M. Tomasi, M. Tristram, T. Trombetti, J. Valiviita, F. Van Tent, P. Vielva, F. Villa, N. Vittorio, B. D. Wandelt, I. K. Wehus, M. White, A. Zacchei, and A. Zonca, "Planck intermediate results. XLVII. Planck constraints on reionization history," *Astronomy and Astrophysics*, vol. 596, p. A108, Dec. 2016.

[184] K. K. Rogers, H. V. Peiris, A. Pontzen, S. Bird, L. Verde, and A. Font-Ribera, "Bayesian emulator optimisation for cosmology: application to the Lyman-alpha forest," *Journal of Cosmology and Astroparticle Physics*, vol. 2019, p. 031, Feb. 2019.

[185] S. Kucherenko, D. Albrecht, and A. Saltelli, "Exploring multi-dimensional spaces: A comparison of latin hypercube and quasi monte carlo sampling techniques," *arXiv preprint arXiv:1505.02350*, 2015.

[186] A. Mazumder, A. Datta, A. Chakraborty, and S. Majumdar, "Observing the reionization: effect of calibration and position errors on realistic observation conditions," *Monthly Notices of the Royal Astronomical Society*, vol. 515, pp. 4020–4037, Sept. 2022.

[187] P. Dayal and A. Ferrara, "Early galaxy formation and its large-scale effects," *Physics Reports*, vol. 780-782, pp. 1–64, 2018. Early galaxy formation and its large-scale effects.

[188] S. Bharadwaj and S. K. Sethi, "HI Fluctuations at Large Redshifts: I–Visibility correlation," *Journal of Astrophysics and Astronomy*, vol. 22, pp. 293–307, Dec. 2001.

[189] M. F. Morales, "Power Spectrum Sensitivity and the Design of Epoch of Reionization Observatories," *The Astrophysical Journal*, vol. 619, pp. 678–683, Feb. 2005.

[190] M. Zaldarriaga, S. R. Furlanetto, and L. Hernquist, "21 Centimeter Fluctuations from Cosmic Gas at High Redshifts," *The Astrophysical Journal*, vol. 608, pp. 622–635, June 2004.

[191] G. Paciga, T.-C. Chang, Y. Gupta, R. Nityanada, J. Odegova, U.-L. Pen, J. B. Peterson, J. Roy, and K. Sigurdson, "The GMRT Epoch of Reionization experiment: a new upper limit on the neutral hydrogen power spectrum at z $\approx$ 8.6," *Monthly Notices of the Royal Astronomical Society*, vol. 413, pp. 1174–1183, 04 2011.

[192] F. G. Mertens, M. Mevius, L. V. E. Koopmans, A. R. Offringa, S. Zaroubi, A. Acharya, S. A. Brackenhoff, E. Ceccotti, E. Chapman, K. Chege, B. Ciardi, R. Ghara, S. Ghosh, S. K. Giri, I. Hothi, C. Höfer, I. T. Iliev, V. Jelić, Q. Ma, G. Mellema, S. Munshi, V. N. Pandey, and S. Yatawatta, "Deeper multi-redshift upper limits on the Epoch of Reionization 21-cm signal power spectrum from LOFAR between z=8.3 and z=10.1," *arXiv e-prints*, p. arXiv:2503.05576, Mar. 2025.

[193] V. Jelić, S. Zaroubi, P. Labropoulos, R. M. Thomas, G. Bernardi, M. A. Brentjens, A. G. De Bruyn, B. Ciardi, G. Harker, L. V. E. Koopmans, V. N. Pandey, J. Schaye, and S. Yatawatta, "Foreground simulations for the LOFAR–epoch of reionization experiment," *MNRAS*, vol. 389, pp. 1319–1335, 09 2008.

[194] V. Jelić, S. Zaroubi, P. Labropoulos, G. Bernardi, A. G. de Bruyn, and L. V. E. Koopmans, "Realistic simulations of the Galactic polarized foreground: consequences for 21-cm reionization detection experiments," *MNRAS*, vol. 409, pp. 1647–1659, 12 2010.

[195] E. Chapman, A. Bonaldi, G. Harker, V. Jelic, F. B. Abdalla, G. Bernardi, J. Bobin, F. Dulwich, B. Mort, M. Santos, and J. L. Starck, "Cosmic dawn and epoch of reionization foreground removal with the ska," in *Advancing Astrophysics with the Square Kilometre Array (AASKA14)*, p. 5, Apr 2015.

[196] T. Di Matteo, B. Ciardi, and F. Miniati, "The 21-cm emission from the reionization epoch: extended and point source foregrounds," *Monthly Notices of the Royal Astronomical Society*, vol. 355, pp. 1053–1065, Dec. 2004.

[197] S. Choudhuri, S. Bharadwaj, S. S. Ali, N. Roy, H. T. Intema, and A. Ghosh, "The angular power spectrum measurement of the Galactic synchrotron emission in two fields of the TGSS survey," *Monthly Notices of the Royal Astronomical Society: Letters*, vol. 470, pp. L11–L15, 05 2017.

[198] A. Chakraborty, N. Roy, A. Datta, S. Choudhuri, K. K. Datta, P. Dutta, S. Bharadwaj, H. Intema, M. Choudhury, S. Pal, and T. R. Choudhury, "Detailed study of ELAIS N1 field with the uGMRT – II. Source properties and spectral variation of foreground power spectrum from 300–500 MHz observations," *Monthly Notices of the Royal Astronomical Society*, vol. 490, pp. 243–259, 10 2019.

[199] A. Mazumder, A. Chakraborty, A. Datta, S. Choudhuri, N. Roy, Y. Wadadekar, and C. H. Ishwara-Chandra, "Characterizing EoR foregrounds: a study of the Lockman Hole region at 325 MHz," *Monthly Notices of the Royal Astronomical Society*, vol. 495, pp. 4071–4084, 05 2020.

[200] E. Chapman, S. Zaroubi, F. B. Abdalla, F. Dulwich, V. Jelić, and B. Mort, "The effect of foreground mitigation strategy on EoR window recovery," *Monthly Notices of the Royal Astronomical Society*, vol. 458, pp. 2928–2939, 03 2016.

[201] N. Thyagarajan, D. C. Jacobs, J. D. Bowman, N. Barry, A. P. Beardsley, G. Bernardi, F. Briggs, R. J. Cappallo, P. Carroll, B. E. Corey, A. de Oliveira-Costa, J. S. Dillon, D. Emrich, A. Ewall-Wice, L. Feng, R. Goeke, L. J. Greenhill, B. J. Hazelton, J. N. Hewitt, N. Hurley-Walker, M. Johnston-Hollitt, D. L. Kaplan, J. C. Kasper, H.-S. Kim, P. Kittiwisit, E. Kratzenberg, E. Lenc, J. Line, A. Loeb, C. J. Lonsdale, M. J. Lynch, B. McKinley, S. R. McWhirter, D. A. Mitchell, M. F. Morales, E. Morgan, A. R. Neben, D. Oberoi, A. R. Offringa, S. M. Ord, S. Paul, B. Pindor, J. C. Pober, T. Prabu, P. Procopio, J. Riding, A. E. E. Rogers, A. Roshi, N. U. Shankar, S. K. Sethi, K. S. Srivani, R. Subrahmanyan, I. S. Sullivan, M. Tegmark, S. J. Tingay, C. M. Trott, M. Waterson, R. B. Wayth, R. L. Webster, A. R. Whitney, A. Williams, C. L. Williams, C. Wu, and J. S. B. Wyithe, "FOREGROUNDS IN WIDE-FIELD REDSHIFTED 21 cm POWER SPECTRA," *The Astrophysical Journal*, vol. 804, p. 14, apr 2015.

[202] N. Thyagarajan, D. C. Jacobs, J. D. Bowman, N. Barry, A. P. Beardsley, G. Bernardi, F. Briggs, R. J. Cappallo, P. Carroll, A. A. Deshpande, A. de Oliveira-Costa, J. S. Dillon, A. Ewall-Wice, L. Feng, L. J. Greenhill, B. J. Hazelton, L. Hernquist, J. N. Hewitt, N. Hurley-Walker, M. Johnston-Hollitt, D. L. Kaplan, H.-S. Kim, P. Kittiwisit, E. Lenc, J. Line, A. Loeb, C. J. Lonsdale, B. McKinley, S. R. McWhirter, D. A. Mitchell, M. F. Morales, E. Morgan, A. R. Neben, D. Oberoi, A. R. Offringa, S. M. Ord, S. Paul, B. Pindor, J. C. Pober, T. Prabu, P. Procopio, J. Riding, N. U. Shankar, S. K. Sethi, K. S. Srivani, R. Subrahmanyan, I. S. Sullivan, M. Tegmark, S. J. Tingay, C. M. Trott, R. B. Wayth, R. L. Webster, A. Williams, C. L. Williams, and J. S. B. Wyithe, "CONFIRMATION OF WIDE-FIELD SIGNATURES IN REDSHIFTED 21 cm POWER SPECTRA," *The Astrophysical Journal*, vol. 807, p. L28, jul 2015.

[203] I. Hothi, E. Chapman, J. R. Pritchard, F. G. Mertens, L. V. E. Koopmans, B. Ciardi, B. K. Gehlot, R. Ghara, A. Ghosh, S. K. Giri, I. T. Iliev, V. Jelić, and S. Zaroubi, "Comparing foreground removal techniques for recovery of the LOFAR-EoR 21cm power spectrum," *Monthly Notices of the Royal Astronomical Society*, vol. 500, pp. 2264–2277, 11 2020.

[204] E. de Lera Acedo, C. M. Trott, R. B. Wayth, N. Fagnoni, G. Bernardi, B. Wakley, L. V. Koopmans, A. J. Faulkner, and J. G. bij de Vaate, "Spectral performance of SKA Log-periodic Antennas I: mitigating spectral artefacts in SKA1-LOW 21 cm cosmology experiments," *Monthly Notices of the Royal Astronomical Society*, vol. 469, pp. 2662–2671, 04 2017.

[205] C. M. Trott, E. de Lera Acedo, R. B. Wayth, N. Fagnoni, A. T. Sutinjo, B. Wakley, and C. I. B. Punzalan, “Spectral performance of Square Kilometre Array Antennas – II. Calibration performance,” *Monthly Notices of the Royal Astronomical Society*, vol. 470, pp. 455–465, 05 2017.

[206] R. C. Joseph, C. M. Trott, and R. B. Wayth, “The bias and uncertainty of redundant and sky-based calibration under realistic sky and telescope conditions,” *The Astronomical Journal*, vol. 156, p. 285, nov 2018.

[207] W. Li, J. C. Pober, B. J. Hazelton, N. Barry, M. F. Morales, I. Sullivan, A. R. Parsons, Z. S. Ali, J. S. Dillon, A. P. Beardsley, J. D. Bowman, F. Briggs, R. Byrne, P. Carroll, B. Crosse, D. Emrich, A. Ewall-Wice, L. Feng, T. M. O. Franzen, J. N. Hewitt, L. Horsley, D. C. Jacobs, M. Johnston-Hollitt, C. Jordan, R. C. Joseph, D. L. Kaplan, D. Kenney, H. Kim, P. Kittiwisit, A. Lanman, J. Line, B. McKinley, D. A. Mitchell, S. Murray, A. Neben, A. R. Offringa, D. Pallot, S. Paul, B. Pindor, P. Procopio, M. Rahimi, J. Riding, S. K. Sethi, N. U. Shankar, K. Steele, R. Subrahmanian, M. Tegmark, N. Thyagarajan, S. J. Tingay, C. Trott, M. Walker, R. B. Wayth, R. L. Webster, A. Williams, C. Wu, and S. Wyithe, “Comparing redundant and sky-model-based interferometric calibration: A first look with phase II of the MWA,” *The Astrophysical Journal*, vol. 863, p. 170, aug 2018.

[208] N. Barry, B. Hazelton, I. Sullivan, M. F. Morales, and J. C. Pober, “Calibration requirements for detecting the 21 cm epoch of reionization power spectrum and implications for the SKA,” *Monthly Notices of the Royal Astronomical Society*, vol. 461, pp. 3135–3144, 06 2016.

[209] C. M. Trott and R. B. Wayth, “Spectral calibration requirements of radio interferometers for epoch of reionisation science with the ska,” *Publications of the Astronomical Society of Australia*, vol. 33, p. e019, 2016.

[210] A. Ewall-Wice, J. S. Dillon, A. Liu, and J. Hewitt, “The impact of modelling errors on interferometer calibration for 21 cm power spectra,” *Monthly Notices of the Royal Astronomical Society*, vol. 470, pp. 1849–1870, 05 2017.

[211] A. H. Patil, S. Yatawatta, L. V. E. Koopmans, A. G. de Bruyn, M. A. Brentjens, S. Zaroubi, K. M. B. Asad, M. Hatef, V. Jelić, M. Mevius, A. R. Offringa, V. N. Pandey, H. Vedantham, F. B. Abdalla, W. N. Brouw, E. Chapman, B. Ciardi, B. K. Gehlot, A. Ghosh, G. Harker, I. T. Iliev, K. Kakiichi, S. Majumdar, G. Mellema, M. B. Silva, J. Schaye, D. Vrbanec, and S. J. Wijnholds, “Upper limits on the 21 cm epoch of reionization power spectrum from one night with LOFAR,” *The Astrophysical Journal*, vol. 838, p. 65, mar 2017.

[212] J. S. Dillon, S. A. Kohn, A. R. Parsons, J. E. Aguirre, Z. S. Ali, G. Bernardi, N. S. Kern, W. Li, A. Liu, C. D. Nunhokee, and J. C. Pober, “Polarized redundant-baseline calibration for 21cm cosmology without adding spectral structure,” *Monthly Notices of the Royal Astronomical Society*, vol. 477, pp. 5670–5681, 04 2018.

[213] J. Kumar, P. Dutta, and N. Roy, “Calibration requirements for epoch of reionization 21-cm signal observations – I. Effect of time-correlated gains,” *Monthly Notices of the Royal Astronomical Society*, vol. 495, pp. 3683–3694, 05 2020.

[214] C. H. Jordan, S. Murray, C. M. Trott, R. B. Wayth, D. A. Mitchell, M. Rahimi, B. Pindor, P. Procopio, and J. Morgan, “Characterization of the ionosphere above the Murchison Radio Observatory using the Murchison Widefield Array,” *Monthly Notices of the Royal Astronomical Society*, vol. 471, pp. 3974–3987, 07 2017.

[215] C. M. Trott, C. H. Jordan, S. G. Murray, B. Pindor, D. A. Mitchell, R. B. Wayth, J. Line, B. McKinley, A. Beardsley, J. Bowman, F. Briggs, B. J. Hazelton, J. Hewitt, D. Jacobs, M. F. Morales, J. C. Pober, S. Sethi, U. Shankar, R. Subrahmanyan, M. Tegmark, S. J. Tingay, R. L. Webster, and J. S. B. Wyithe, “Assessment of ionospheric activity tolerances for epoch of reionization science with the murchison widefield array,” *The Astrophysical Journal*, vol. 867, p. 15, oct 2018.

[216] S. K. Pal, A. Datta, and A. Mazumder, “Ionospheric effect on the synthetic Epoch of Reionization observations with the SKA1-Low,” *arXiv e-prints*, p. arXiv:2407.17573, July 2024.

[217] D. R. DeBoer, A. R. Parsons, J. E. Aguirre, P. Alexander, Z. S. Ali, A. P. Beardsley, G. Bernardi, J. D. Bowman, R. F. Bradley, C. L. Carilli, C. Cheng, E. de Lera Acedo, J. S. Dillon, A. Ewall-Wice, G. Fadana, N. Fagnoni, R. Fritz, S. R. Furlanetto, B. Glendenning, B. Greig, J. Grobbelaar, B. J. Hazelton, J. N. Hewitt, J. Hickish, D. C. Jacobs, A. Julius, M. Kariseb, S. A. Kohn, T. Lekalake, A. Liu, A. Loots, D. MacMahon, L. Malan, C. Malgas, M. Maree, Z. Martinot, N. Mathison, E. Matsetela, A. Mesinger, M. F. Morales, A. R. Neben, N. Patra, S. Pieterse, J. C. Pober, N. Razavi-Ghods, J. Ringuette, J. Robnett, K. Rosie, R. Sell, C. Smith, A. Syce, M. Tegmark, N. Thyagarajan, P. K. G. Williams, and H. Zheng, “Hydrogen epoch of reionization array (HERA),” *Publications of the Astronomical Society of the Pacific*, vol. 129, p. 045001, mar 2017.

[218] M. F. Morales and J. Hewitt, “Toward epoch of reionization measurements with wide-field radio observations,” *The Astrophysical Journal*, vol. 615, pp. 7–18, nov 2004.

[219] A. Datta, S. Bhatnagar, and C. L. Carilli, “DETECTION OF SIGNALS FROM COSMIC REIONIZATION USING RADIO INTERFEROMETRIC SIGNAL PROCESSING,” *The Astrophysical Journal*, vol. 703, pp. 1851–1862, sep 2009.

[220] J. S. Dillon and A. R. Parsons, “Redundant Array Configurations for 21 cm Cosmology,” *The Astrophysical Journal*, vol. 826, p. 181, Aug. 2016.

[221] R. Byrne, M. F. Morales, B. Hazelton, W. Li, N. Barry, A. P. Beardsley, R. Joseph, J. Pober, I. Sullivan, and C. Trott, “Fundamental limitations on the calibration of redundant 21 cm cosmology instruments and implications for HERA and the SKA,” *The Astrophysical Journal*, vol. 875, p. 70, apr 2019.

[222] R. Byrne, M. F. Morales, B. J. Hazelton, and M. Wilensky, “A unified calibration framework for 21 cm cosmology,” *Monthly Notices of the Royal Astronomical Society*, vol. 503, pp. 2457–2477, May 2021.

[223] C. J. Schmit and J. R. Pritchard, “Emulation of reionization simulations for Bayesian inference of astrophysics parameters using neural networks,” *Monthly Notices of the Royal Astronomical Society*, vol. 475, pp. 1213–1223, Mar. 2018.

[224] H. Tiwari, A. K. Shaw, S. Majumdar, M. Kamran, and M. Choudhury, “Improving constraints on the reionization parameters using 21-cm bispectrum,” *Journal of Cosmology and Astroparticle Physics*, vol. 2022, p. 045, Apr. 2022.

[225] W. Li, H. Xu, Z. Ma, R. Zhu, D. Hu, Z. Zhu, J. Gu, C. Shan, J. Zhu, and X.-P. Wu, “Separating the EoR signal with a convolutional denoising autoencoder: a deep-learning-based method,” *Monthly Notices of the Royal Astronomical Society*, vol. 485, pp. 2628–2637, May 2019.

[226] E. Beohar, A. Datta, A. Tripathi, S. K. Pal, and R. Sagar, “Mitigating gain calibration errors from EoR observations with SKA1-Low AA*,” *arXiv e-prints*, p. arXiv:2510.25886, Oct. 2025.

[227] S. Murray, B. Greig, A. Mesinger, J. Muñoz, Y. Qin, J. Park, and C. Watkinson, “21cmFAST v3: A Python-integrated C code for generating 3D realizations of the cosmic 21cm signal.,” *The Journal of Open Source Software*, vol. 5, p. 2582, Oct. 2020.

[228] M. McQuinn, S. P. Oh, and C.-A. Faucher-Giguère, “On Lyman-limit Systems and the Evolution of the Intergalactic Ionizing Background,” *The Astrophysical Journal*, vol. 743, p. 82, Dec. 2011.

[229] E. Sobacchi and A. Mesinger, “Inhomogeneous recombinations during cosmic reionization,” *Monthly Notices of the Royal Astronomical Society*, vol. 440, pp. 1662–1673, May 2014.

[230] E. Sobacchi and A. Mesinger, “How does radiative feedback from an ultraviolet background impact reionization?,” *Monthly Notices of the Royal Astronomical Society*, vol. 432, pp. 3340–3348, July 2013.

[231] A. Fialkov, R. Barkana, E. Visbal, D. Tseliakhovich, and C. M. Hirata, “The 21-cm signature of the first stars during the Lyman-Werner feedback era,” *Monthly Notices of the Royal Astronomical Society*, vol. 432, pp. 2909–2916, July 2013.

[232] S. R. Furlanetto, M. Zaldarriaga, and L. Hernquist, “The Growth of H II Regions During Reionization,” *The Astrophysical Journal*, vol. 613, pp. 1–15, Sept. 2004.

[233] S. R. Furlanetto, S. P. Oh, and F. H. Briggs, “Cosmology at low frequencies: The 21 cm transition and the high-redshift Universe,” *Physics Reports*, vol. 433, pp. 181–301, Oct. 2006.

[234] A. Bonaldi, M. Bonato, V. Galluzzi, I. Harrison, M. Massardi, S. Kay, G. De Zotti, and M. L. Brown, “The Tiered Radio Extragalactic Continuum Simulation (T-RECS),” *Monthly Notices of the Royal Astronomical Society*, vol. 482, pp. 2–19, 09 2018.

[235] *Wide Field Astronomy & Technology for the Square Kilometre Array*, Jan. 2009.

[236] *Wide Field Astronomy & Technology for the Square Kilometre Array*, Jan. 2009.

[237] A. R. Parsons, J. C. Pober, J. E. Aguirre, C. L. Carilli, D. C. Jacobs, and D. F. Moore, “A Per-baseline, Delay-spectrum Technique for Accessing the 21 cm Cosmic Reionization Signature,” *The Astrophysical Journal*, vol. 756, p. 165, Sept. 2012.

[238] M. F. Morales, A. Beardsley, J. Pober, N. Barry, B. Hazelton, D. Jacobs, and I. Sullivan, “Understanding the diversity of 21 cm cosmology analyses,” *Monthly Notices of the Royal Astronomical Society*, vol. 483, pp. 2207–2216, Feb. 2019.

[239] G. Mellema, L. V. E. Koopmans, F. A. Abdalla, G. Bernardi, B. Ciardi, S. Daiboo, A. G. de Bruyn, K. K. Datta, H. Falcke, A. Ferrara, I. T. Iliev, F. Iocco, V. Jelić, H. Jensen, R. Joseph, P. Labroupoulos, A. Meiksin, A. Mesinger, A. R. Offringa, V. N. Pandey, J. R. Pritchard, M. G. Santos, D. J. Schwarz, B. Semelin, H. Vedantham, S. Yatawatta, and S. Zaroubi, “Reionization and the Cosmic Dawn with the Square Kilometre Array,” *Experimental Astronomy*, vol. 36, pp. 235–318, Aug. 2013.

[240] D. W. Hogg, “Distance measures in cosmology,” *arXiv e-prints*, pp. astro–ph/9905116, May 1999.

[241] F. Pedregosa, G. Varoquaux, A. Gramfort, V. Michel, B. Thirion, O. Grisel, M. Blondel, A. Müller, J. Nothman, G. Louppe, P. Prettenhofer, R. Weiss, V. Dubourg, J. Vanderplas, A. Passos, D. Cournapeau, M. Brucher, M. Perrot, and É. Duchesnay, “Scikit-learn: Machine Learning in Python,” *Journal of Machine Learning Research*, vol. 12, pp. 2825–2830, Oct. 2011.

[242] J. Akeret, S. Seehars, A. Amara, A. Refregier, and A. Csillaghy, "CosmoHammer: Cosmological parameter estimation with the MCMC Hammer," *arXiv e-prints*, p. arXiv:1212.1721, Dec. 2012.

[243] J. Goodman and J. Weare, "Ensemble samplers with affine invariance," *Communications in Applied Mathematics and Computational Science*, vol. 5, pp. 65–80, Jan. 2010.

[244] G. Mellema, L. V. E. Koopmans, F. A. Abdalla, G. Bernardi, B. Ciardi, S. Daiboo, A. G. de Bruyn, K. K. Datta, H. Falcke, A. Ferrara, I. T. Iliev, F. Iocco, V. Jelić, H. Jensen, R. Joseph, P. Labroupoulos, A. Meiksin, A. Mesinger, A. R. Offringa, V. N. Pandey, J. R. Pritchard, M. G. Santos, D. J. Schwarz, B. Semelin, H. Vedantham, S. Yatawatta, and S. Zaroubi, "Reionization and the Cosmic Dawn with the Square Kilometre Array," *Experimental Astronomy*, vol. 36, pp. 235–318, Aug. 2013.